Hydro-mechanical risk analysis of submarine tunnels with segments lining crossing faults or fractured formations

Kyeunghye Ahn

To cite this version:

Kyeunghye Ahn. Hydro-mechanical risk analysis of submarine tunnels with segments lining crossing faults or fractured formations. Géotechnique. École des Ponts ParisTech, 2023. English. NNT : 2023ENPC0019 . tel-04269781

HAL Id: tel-04269781

https://pastel.hal.science/tel-04269781v1

Submitted on 3 Nov 2023

THÈSE DE DOCTORAT
de l’École des Ponts ParisTech

Hydro-mechanical risk analysis of submarine tunnels with segments lining crossing faults or fractured formations

École doctorale N° 531, Sciences, Ingénierie et Environnement (SIE)

Spécialité du doctorat : Géotechnique

Thèse préparée au laboratoire Navier

Thèse soutenue la date prévue le 23 mai 2023, par
Kyeung-Hye AHN

Composition du jury :

Jean SULEM Professeur, Ecole des Ponts Paris Tech	*Président*
Mountaka SOULEY Ingénieur de recherche, HDR, INERIS	*Rapporteur*
Philippe COSENZA Professeur, Université de Poitier	*Rapporteur*
Laetita PAVEL Ingénieure, ARCADIS	*Examinateur*
Pooneh MAGHOUL Associate Professor, Polytechnique Montréal	*Examinateur*
Baptiste LAROCHE Ingénieur, Bouygues Construction	*Examinateur*
Amade POUYA Directeur de recherche, Université Gustave Eiffel	*Directeur de thèse*
Gye-chun CHO Professeur, KAIST	*Co-Directeur de thèse*
Minh-ngoc VU Docteur, ANDRA	*Invité*
Francois LAIGLE Docteur, BG Ingénieurs Conseils	*Invité*

Appreciation

I am profoundly grateful to a multitude of individuals and organizations whose unwavering support, guidance, and contributions have been pivotal in the successful completion of this doctoral thesis. Their dedication and encouragement have undoubtedly enriched my academic journey, and I wish to extend my heartfelt appreciation to each and every one of them.

Foremost, my deepest gratitude goes to my esteemed supervisors Professor Amade POUYA and Gye-Chun CHO, whose expert guidance, insightful feedback, and relentless commitment have been the cornerstone of this research endeavor. Your mentorship has not only shaped the direction of this thesis but has also enriched my understanding of the subject matter.

My professor, Amade POUYA, has guided and mentally supported me from the beginning of my master's program until now. I would not have been able to imagine myself today without your support and advice when I was struggling in another country. I will always be in awe and grateful to you, and I will do my best to be your proud student.

In addition, Prof Gye-Chun CHO gave me a lot of guidance despite the time difference between Korea and France, and you personally attended my defense from Korea to far away France, and always gave me a lot of advice and introduced me to new paths. It was an honor to be your student.

I am indebted to the members of my thesis committee, for their invaluable insights, thoughtful critiques, and constructive suggestions. Your collective expertise has elevated the quality of this work and has broadened my horizons as a researcher.

I am a Korean national scholarship recipient, so my PhD financial funding has been provided by the Korean government for the last 3 years. In the last 9 months, it has also been supported by the Ecole des Ponts. The financial support provided by National institute for international education played a pivotal role in enabling the execution of this research. I am thankful for their investment in my academic endeavors.

I would like to thank my colleagues. I would like to thank my fellow lab navigators, our colleagues have always been supportive, caring, and friendly, not just coworkers, but friends and family. I love our lab navigators for always supporting each other.

Last but not least, I would like to thank my most beloved friends and my mom and dad. My best friends, Eunyoung and Jieun, you are my best friends and my forever big sisters. I know I say it all the time, but thank you for being there. And Sungtae, my eternal support, thank you is not enough, but thank you again.

For my parents, Dad, I miss you so much, and even at your advanced age, you always support me from a far and wish me the best. I am so happy and grateful to be your daughter. You are always my superman.

Finally, Mom. My mom who always loves me the most in the world, I am grateful and love you too. Your prayers, always praying for me no matter where you are, are the reason I am here.

In conclusion, the completion of my PhD thesis was possible because of the support and encouragement of many people. I would like to thank everyone once again.

Abstract

In countries with many islands (Korea, Singapore, Japan, the Philippines, etc.), as a means of connecting land to land, submarine tunnel are needed and their design highly challenging due to high water pressures existing around the tunnel and ignorance of the ground environment. The «Busan-Tsushima» submarine tunnel project, the shortest distance from Korea to Japan, meets the Yangsan submarine fault zone (active fault). Therefore, it is essential to consider the fault zone when designing this submarine tunnel.

This research was initiated with an investigation of geographic and geophysical properties (empirical method) of the Busan-Tsushima seabed between Korea and Japan.

To analyze hydraulic pressure effects, we proceeded to find an appropriate method in numerical modelling with adequate load paths (drainage & non-drainage) by using a Finite Element code (Disroc-FEM).

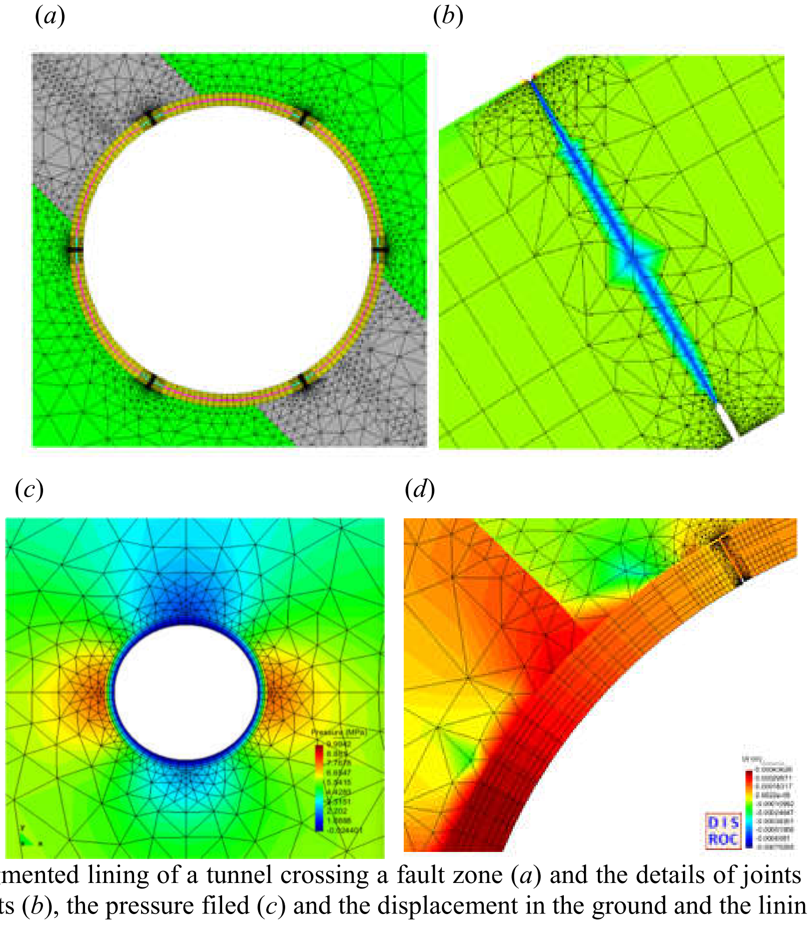

Figure: Segmented lining of a tunnel crossing a fault zone (*a*) and the details of joints between the segments (*b*), the pressure filed (*c*) and the displacement in the ground and the lining (*d*)

First, we compared the theoretical results and numerical analysis modelling results according to various conditions and focused on the estimation of the amount of inflow into the tunnel for different hydraulic properties of the lining and the ground.

In addition, a theoretical study made it possible to improve the analytical solutions for the ground-lining interaction. The existing solutions were limited to the cases of *perfect-bonding* or a *perfect-slip* between the ground and the lining, and we could extend them to the case of a linear elastic contact.

The modelling considers a sophisticated tunnel segment-joint model in in which the segment lining is modeled as a bulk material rather than a single beam model often used in existing 2D simulations. This model has the advantage of performing a more complete numerical analysis of the lining behavior and take into account elastoplastic ground behavior. As a matter of fact, existing studies in the literature were limited to elastic soil behavior. The volume-type continuum segment lining was modeled and first compared to existing theoretical models and then to the numerical analysis results for one-ring lining. Theses comparisons showed the advantages of bulk lining model compared to the beam model. Then, in response to the convergence stage (deconfinement ratio) of excavation with bulk segment lining, the influence of the interface (grouting, tail void gap) between the lining and the ground was analyzed. In this part, a comparative analysis was performed for different classes of rock properties and different horizontal earth pressure ratios. It was found that the non-linear stress-strain relationship between for the soil-lining contact could control the final load supported by the lining. Finally, the effects of the joint properties between segment elements of the lining were analyzed.

For long-term analysis of low-depth soft ground tunnel under drained and undrained conditions, the effects of the hydraulic properties of the interface and the ground with different Biot coefficients were analyzed. This analysis provided also the stress evolution around the tunnel with taking into account the segment's joints with highly non-linear mechanical behavior.

Due to complex geological conditions, an analysis of segmented tunnels with different locations in respect to the fault zone was performed. Fault zones with very poor mechanical properties, compared to the ground properties around the tunnel, were considered under different hydraulic and conditions and the related hydraulic and mechanical integrity risks were analyzed. The results of this analysis can pave the road for a design of the lining structure to prevent some unexpected risk situations.

The hydromechanical analyses for undrained conditions were performed for elastic behavior of the lining and the ground. The evolution under undrained conditions for elastoplastic materials showed some numerical difficulties the investigation of which constitutes the perspective of the present work.

Résumé

Le projet de tunnel sous-marin «Busan-Tsushima», la plus courte distance de la Corée au Japon, rencontre la zone de faille sous-marine de Yangsan (faille active). Par conséquent, il est essentiel de considérer la zone de faille lors de la conception de ce tunnel sous-marin.

Cette recherche a été initiée par une étude des propriétés géographiques et géophysiques (méthode empirique) du fond marin de Busan-Tsushima entre la Corée et le Japon.

Pour analyser les effets de la pression hydraulique, nous avons procédé à la recherche d'une méthode appropriée dans la modélisation numérique avec des chemins de charge adéquats (drainée et non-drainée) en utilisant un code aux éléments finis enrichis aux éléments joints (Disroc-JFEM).

Dans un premier temps, nous avons comparé les résultats théoriques et les résultats de la modélisation numérique selon diverses conditions et nous nous sommes concentrés sur l'estimation du débit d’exhaure dans le tunnel pour différentes propriétés hydrauliques du revêtement et du sol.

L’analyse effectuée considère un modèle sophistiqué de joint de voussoir dans lequel le revêtement en voussoirs est modélisé comme un matériau volumique plutôt qu'un modèle de poutre souvent utilisé dans les simulations 2D existantes. Ce modèle a l'avantage de réaliser une analyse numérique plus complète du comportement du revêtement et de prendre en compte le comportement élastoplastique du sol. En fait, les études existantes dans la littérature se sont limitées au comportement élastique du sol. Le revêtement de matériau volumique continu a été modélisé et comparé, d’abord, aux modèles théoriques existants, puis, aux modèles de revêtement en poutre. Ces comparaisons ont montré les avantages du modèle de revêtement massif par rapport au modèle de poutre. Ensuite, pour les différentes étapes de convergence (taux de déconfinement de l'excavation) avec le revêtement en voussoir du tunnel, l'influence de l'interface (vide annulaire) entre le revêtement et le sol a été analysée. Dans cette partie, une analyse comparative a été effectuée pour différentes classes de propriétés rocheuses et différents rapports des contraintes horizontale et verticale in situ. Il a été constaté que la relation contrainte-déformation non linéaire pour le contact sol-revêtement pouvait contrôler la charge finale supportée par le revêtement. Enfin, les effets des propriétés des joints entre les éléments de voussoir du revêtement ont été analysés.

Pour l'analyse à long terme d'un tunnel en sol mou et de faible profondeur dans des conditions drainées et non drainées, les effets des propriétés hydrauliques de l'interface et du sol avec

différents coefficients de Biot ont été pris en compte. Cette analyse a également fourni l'évolution des contraintes autour du tunnel en prenant en compte les joints à comportement mécanique fortement non linéaire.

Pour examiner des conditions géologiques complexes, une analyse de tunnels avec revêtement en voussoir et différents emplacements du tunnel par rapport à la zone de faille a été réalisée. Des zones de failles aux propriétés mécaniques très médiocres, par rapport aux propriétés du sol autour du tunnel, ont été considérées avec différentes conditions hydrauliques, et les risques associé l'intégrité hydraulique et mécanique du tunnel ont été analysés. Les résultats de cette analyse peuvent ouvrir la voie à une conception de la structure de revêtement pour permettant d'éviter certaines situations à risque imprévues.

Les analyses hydromécaniques en conditions non drainées ont été réalisées pour le comportement à court terme du revêtement et du sol. L'évolution due à la diffusion hydraulique en conditions drainées et avec des matériaux élastoplastiques a montré quelques difficultés numériques dont l'investigation constitue la perspective du présent travail.

TABLE OF CONTENT

GENERAL INTRODUCTION

The countries with many islands have been concentrating on the construction of infrastructures in the underground to overcome the geological challenges. But these infrastructures have been much located mostly in inland and mountainous areas.

Nowadays, with the increase in active trade exchanges between East Asian countries, these countries are interested in a more efficient distribution system than in the past. Research on submarine tunnels between Korea and Japan or China is related to this situation.

However, there are many parts that need to be considered in subsea ground construction, from precise subsea ground properties investigations to methods of supporting with unexpected ground conditions and to appropriate construction methods. And, since it is difficult to investigate the ground of undersea due to the special environmental conditions and to water pressure, a much higher stability is required than a land tunnel. In addition, in most submarine tunnel construction, it is important to consider safety issues related to faults, fracture zones, and the resulting water pressure and inflow. For example, the «Busan-Tsushima» submarine tunnel project, the shortest distance from Korea to Japan, meets the Yangsan submarine fault zone (active fault). This is why it is essential to consider the fault zone when designing this submarine tunnel.

Therefore, in this thesis, project “Hydro-mechanical risk analysis of submarine tunnels with segments lining crossing faults or fractured formations” is introduced with the following chapter 1~6 structure.

Chapter 1: Many construction areas are covered with seawater, which can have significant layers of silt on the seafloor. Submarine tunnels are more uncertainty, according to many results of researches, than in normal land tunnels. Therefore, there is necessity of clearer ground investigation and design. But, in fact, there are many difficulties because cost and time for seabed ground investigation and cooperation by national circumstances are required. As an alternative to this, it is possible to economically obtain the necessary local ground physical properties using an empirical model. First, this part will introduce the analysis of the modelling of the submarine tunnel by applying the geographical and ground conditions of the submarine tunnel project that can be built in East Asia (Korea-Japan).

Chapter 2: One of the biggest influencing factors in submarine tunnels is the problem of hydraulic pressure. Since the hydraulic effect is an important part on the design of the submarine tunnel, we proceeded to find an appropriate method in numerical modelling with possible elements in the numerical analysis program (Disroc) we used. Here, we compared the theoretical results and numerical analysis modelling results regarding various conditions and focused on the estimation of the amount of inflow into the tunnel according to the permeability coefficient of the lining and the ground.

Chapter 3: As a first step to understand the mechanical behavior of the tunnel and lining, a theoretical analysis of the interaction between the lining and the ground was conducted. After researching the existing theoretical formulations of the interaction condition of the existing ground and lining of the continuum base, a theoretical study made it possible to improve the analytical solutions for the ground-lining interaction. The existing solutions were limited to the cases of perfect-bonding or a perfect-slip between the ground and the lining, and we could extend them to the case of a linear elastic contact. And then, when we compared our theoretical formulas and existing formulas with numerical analysis results by Disroc, it could give more reasonableness to our results.

Chapter 4: When constructing an submarine tunnel, a closed TBM construction method is often introduced. This means that the segment linings are assembled immediately upon excavation of the tunnel with already formed "pre-casted segment" pieces. Therefore, the modelling of each segment is an important part, in particular, the joint between segments.

The modelling considers a sophisticated tunnel segment-joint model, which is modeled as a bulk material rather than a single beam model often used in existing 2D simulations. This model takes the advantage of performing a more complete numerical analysis of the lining behavior and takes into account elastoplastic ground behavior. In response to the convergence stage (convergence confinement method: load ratio) of excavation with bulk segment lining, the influence of the interface (grouting, tail void gap) between the lining and the ground was analyzed. In this part, a comparative analysis was performed for different classes of rock properties and different horizontal earth pressure ratios. In addition, it was found that the non-linear stress-strain relationship for the ground-lining contact could control the final load supported by the lining. Finally, the effects of the joint properties between segment elements of the lining were analyzed.

Chapter 5: Substantial layers of soil and sand are deposited on the shallow seabed at the entrance of the subsea tunnel. This means that it is necessary to investigate the hydraulic-mechanical linkage depending on the unsaturated ground conditions. For long-term analysis of low-depth soft ground tunnel under drained and undrained conditions, the effects of the hydraulic properties of the interface and the ground with different Biot coefficients were analyzed. This analysis provided also the stress evolution around the tunnel, taking into account the segment's joints with highly non-linear mechanical behavior.

Chapter 6: Segment lining behaviour, including joints, can be analyzed through hydraulic-mechanics coupled analysis in complex ground, and modelling of various grounds such as fault zones, fracture zones, and earthquake impact ranges will be possible.

Due to complex geological conditions, an analysis of segmented tunnels with different locations in respect to the fault zone was performed. Fault zones with very poor mechanical properties, compared to the ground properties around the tunnel, were considered under different hydraulic and conditions. Moreover, the related hydraulic and mechanical integrity risks were analyzed. The results of this analysis can pave the road for a design of the lining structure to prevent some unexpected risk situations.

LIST OF NOTATIONS (CH 1)

Symbol	**Definition**
C	Skempton’s coefficient
K_0, K_{fr}	Bulk modulus drained
K_u ;K	Bulk modulus undrained
K_s	Bulk modulus of solid grains
K_f	Bulk modulus of pore fluid
K_n, K_t	Normal and tangent stiffness between lining and ground
b_{biot}	Biot coefficient
γ	Specific weight
e	Layer width
φ	Friction angle
G	*Shear modulus*
E	*Young's modulus*
E_0	*Young's modulus drained*
E_u	*Young's modulus undrained*
ν	Poisson’s ratio
ν_0	Poisson’s ratio drained
ν_u	Poisson’s ratio undrained
H	*Plan wave modulus*
M	Storage modulus
λ	*Lame coefficient*
V_p	P-wave velocity
V_s	S-wave velocity
AI	Acoustic impedance
ρ	Density
ρ_s	Density of solid
ρ_w	Density of water
ρ_f	Density of fluid
ρ_{sat}	Density of saturation framework
ϕ	porosity
B_s	Skempton’s B parameter

1. Geological conditions and geotechnical properties of sub-marine ground

1.1. Introduction

In order to design a submarine tunnel, it is necessary to estimate the parameters of appropriate subsea rocks. But that is not easy because the data from ground surveys on subsea sections are more difficult to be observed and we have fewer opportunities than surveys on land tunnels. Since Q-system and RMR method (the general rock classification method) are experiential classification methods, it may be more overestimated (conservative evaluation) than actual rock grade when high water pressure applies to the surface ground (Bae et al., 2014).

Unexpected situations also due to ground conditions that were not identified in the design of subsea tunnels are left with many challenges (Shin, Society and Information, 2009; Heur, 1995; Foose et al., 1996; Holmøy, 2009).

In general, the most reliable environmental parameters can be obtained from long-core sediments. However, in the course of geoacoustic modelling, it suffers from a lack of relevant long-core data (Kim et al., 2012; Ryang et al., 2014).

In particular, the construction of submarine tunnels between countries has many requirements like detailed examination in terms of construction technology between the two countries, social issues such as economy, politics, and territories, as well as public sentiment and military aspects. These conditions also cause the limitations of permitting subsea drilling investigations.

Geo-acoustic and Physical properties on the subsea section are estimated by a seismic survey (ex: OBS) and exploration data (ex: Borehole) data. Geo-acoustic models of the seafloor are fundament to underwater acoustics and to marine geological and geophysical studies of the earth's crust (HAMILTON EL, 1970; Hamilton, 1980; Jackson et al., 2007; Ryang et al., 2014).

Therefore, we need to study about geo-acoustic properties for parameters and geometries around expected submarine tunnels.

In this chapter, the major ground properties model of the route of the East Asian super-long submarine tunnel, especially for the route connecting Korea and Japan, is described and analyzed by using the results of physical and geoacoustic properties of surface sediments based on the empirical method.

In addition, since the fault passing through this area also extends to the seabed, tunnel modelling for the existence of an uncertain fault is necessary when designing the tunnel. Therefore, the physical properties of major faults that may exist in this area are also researched through reference literature.

Introducing routes that are mentioned as expected submarine tunnels in Korea is shown in Table 1 below (Shin et al., 2009).

Table 1. Introduction of the possibility of subsea tunnel project in Korea

1.Korea-Japan	Geoje -Tsushima(top)-Iki- Karatsu	Buans -Tsushima(down)-Iki-Karatsu	Geoje -Tsushima(down)-Iki-Karatsu
2.Korea-China	Inchon -Weihai	Hwaseong-Weihai	Pyeongtaek-Weihai
3.Honam-Jeju	Bokil – Chuja - Jeju		

The purpose of this study is to derive parameters that can be applied to the design by analyzing the main ground properties of the subsea tunnel connecting Korea and Japan among these tunnel routes.

1.2. Projected localization subsea tunnel (Korea- Japan)

It can be divided into Geoje-Tsushima Line and Busan-Tsushima Line as expected routes of the Korea-Japan subsea tunnel (Figure 1). Their average length of the route is about 135 km, with a maximum depth of 155 to 220 m. In the Korea Strait area (Korea-Tsushima), the sea distance is about 50km and the average depth is 160 ~ 230m. The longitudinal profile of the tunnel was examined according to the state of the seabed.

As active faults that are expected to affect the design of the subsea tunnels are Yangsan faults in the Korea Strait. In addition, there is a trough (the deepest depth is 230m) alongside Tsushima Island which is expected to be the weakest point of the tunnel. (Shin et al., 2009)

Our modelling example would be part of the Korea Strait. Lots of researchers have studied the submarine geology in the Korea Strait using seismic reflection profiles partly associated with drilling data. (Minami, 1979; Inoue, 1982; Katsura and Nagano, 1982; Korea Institute Energy and Resources, 1982; Choi and Park, 1985)

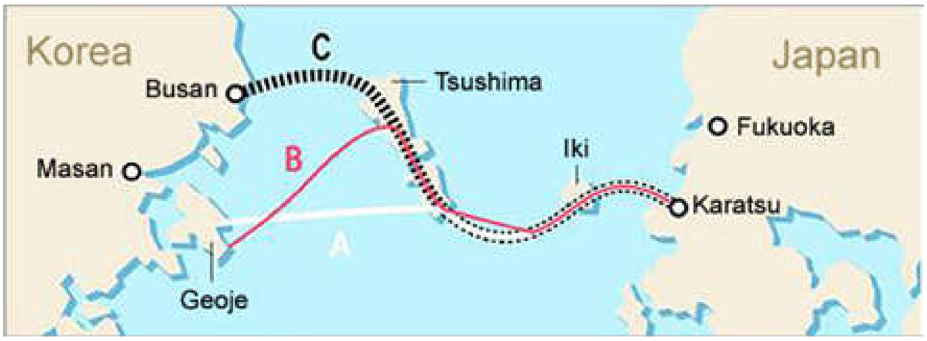

Figure 1 Korea-Japan tunnel expected route.

- **<u>Previous researches on the properties of this area</u>**

The properties of the surface of the seafloor are required in geoacoustic modelling. To evaluate the properties of the deep subsea ground, we want to refer to the data of the surface properties that have been studied. Generally, these properties can be determined from in situ measurements accompanied by core-boring or laboratory measurements corrected to in situ values.

According research by Kim et al., (2009, 2001) and Yoo et al., (2017), the surface in this area (Busan and Geoje sea) can be divided into three physiographic regions based on seafloor gradients and bottom sediments: (1) inner shelf: Province1 (shallower than 80m, covered mud from the Nakdong and Seomjin rivers). (2) mid-shelf : Province 2 (80-120m depth, the gradient of about 0.12°, thin sandy sediments with gravels), and (3) outer shelf: Province 3 (deeper than 120m depth) (Figure 2).

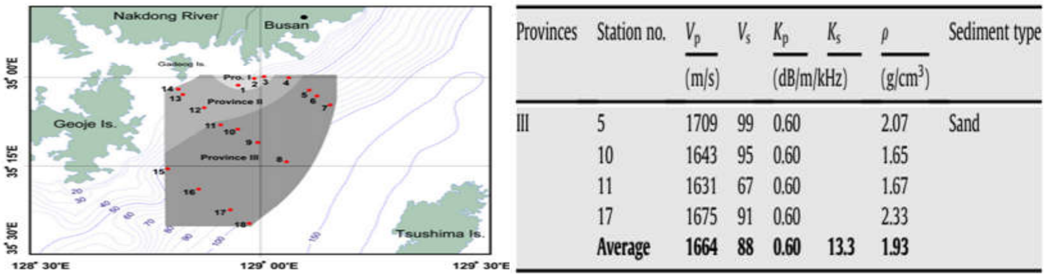
(a)

(b)

Provinces	Station no.	V_p (m/s)	V_s	K_p (dB/m/kHz)	K_s	ρ (g/cm^3)	Sediment type
III	5	1709	99	0.60		2.07	Sand
	10	1643	95	0.60		1.65	
	11	1631	67	0.60		1.67	
	17	1675	91	0.60		2.33	
	Average	**1664**	**88**	**0.60**	**13.3**	**1.93**	

Figure 2. (a) Grouping of the study area by sediment textural parameters and acoustic and physical properties (Kim et al., 2005). (b) Geoacoustic provinces 3 of surface sediments in the study area

(Kim et al., 2011)

As another research, BRIGGS, K et al., (1991) modelled four regions of 17 provinces (Figure 3). Province 8 is found at water depths between approximately 70 and 120m off the Korean peninsula and it can be identified by four sediments layers (sand-silt-clay, medium sand, semi consolidated silt sand, and basement)

In our study, I refer to the results of their research:

Province 3 (Kim et al., 2011) and Province 8 (BRIGGS, K et al., 1991).

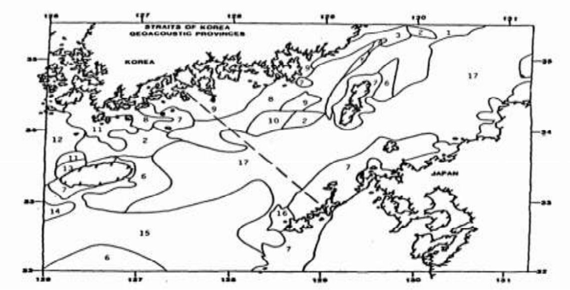

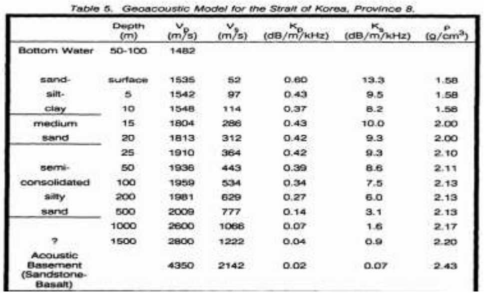
Table 5. Geoacoustic Model for the Strait of Korea, Province 8.

	Depth (m)	V_p (m/s)	V_s (m/s)	K_p (dB/m/kHz)	K_s (dB/m/kHz)	ρ (g/cm^3)
Bottom Water	50-100	1482				
sand-	surface	1535	52	0.60	13.3	1.58
silt-	5	1542	97	0.43	9.5	1.58
clay	10	1548	114	0.37	8.2	1.58
medium	15	1804	286	0.43	10.0	2.00
sand	20	1813	312	0.42	9.3	2.00
	25	1910	364	0.42	9.3	2.10
semi-	50	1936	443	0.39	8.6	2.11
consolidated	100	1959	534	0.34	7.5	2.13
silty	200	1981	629	0.27	6.0	2.13
sand	500	2009	777	0.14	3.1	2.13
	1000	2600	1066	0.07	1.6	2.17
?	1500	2800	1222	0.04	0.9	2.20
Acoustic Basement (Sandstone-Basalt)		4350	2142	0.02	0.07	2.43

Figure 3. Map of the 17 geoacoustic provinces of the Strait of Korea as defined in this technical note and geoacoustic model for Province 8 (BRIGGS, K et al.,1991)

- **Previous studies on the Geometry of this area**

Minami (1979) and Inoue (1982) divided the sedimentary package above the acoustic basement into four layers, ranging from Paleogene to Holocene in age (X: coastal and volcanic deposited, N: marine sediment deposited, K: shallow marine deposits with some volcanic and intrusive rocks, and D from the bottom upward as looking for Figure 4 (a)).

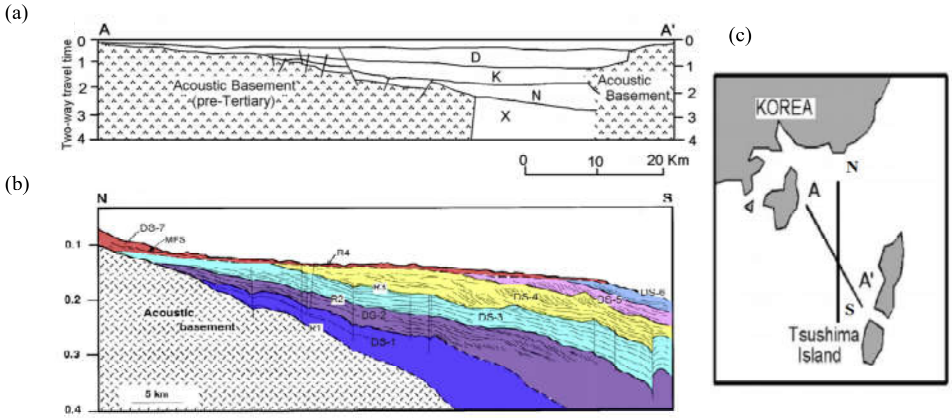

Figure 4. (a) A general stratigraphy across the shelf based on interpretation of seismic reflection profiles by Minami (1979) and Inoue (1982), (b) individual sequence forms by Yoo (2017).

(c) observation area.

At the D layer, strong deformations of the underlying strata have resulted in many anticlinal structures, including faults and folding structures in this area.

Therefore, much research has been done in this area. Minami (1979) and Inoue (1982) revisited this section for four distinctive formations (A, B, C, and D).

Yoo et al., (2017) also modeled the part corresponding to layer D as shown in figure 4(b). According to his studies, the shelf sequences above the acoustic basement consist of seven depositional sequences separated by erosional unconformities depending on falls in sea level. Seven depositional sequences were identified in the Korea Strait by interpretation of the high-resolution seismic profiles. The seven stacked sequences, each with different seismic facies and geometries, are referred to as DS-1 to DS-7 from oldest to youngest respectively.

Table 2. Stratigraphic correlation around the Korea strait of depositional sequences at layer D

Layer	Minami(1979) , Inoue(1982)	Yoo(2017)	Continuity	Material
D	A formation	DS-7	Discontinuous and continuous	Mud and sand with some gravels and shell debris
	B formation	DS-4,5,6	Continuous	Semi- consolidated sand and mud with gravels
	C formation	DS-3	Continuous	Marine sandstone and mudstone
	D formation	DS-1,2	Discontinuous	Non-marine or nearshore sediments

1.3. Rock physics modelling by elastic wave propagation

A “Geoacoustic model” is defined as a model of the real sea floor with emphasis on measured, extrapolated, and predicted values of those properties important in underwater acoustics and those aspects of geophysics, including sound transmission. (Hamilton et al.,1971, 1976, 1978, 1979, 1980).

In order to comprehend the relationship between the results of seafloor seismic survey data obtained by geoacoustic modelling and rock properties, it is necessary to understand the theories of rock physics. In this part, some basic theories of rock physics and their applications are examined. As a method to derive the various properties and components of the geoacoustic model, it is necessary to understand and analyze about elastic wave propagation.

Elastic physical properties given as a result of elastic waves by interpreting the relationship between P-wave velocity (*Vp*), S-wave velocity (*Vs*), and acoustic impedance (*AI*) are quantitatively presented and used to predict storage properties from elastic properties (e.g. Biot-Gassmnn’s equation). Such rock physics has been developed along with the improvement of seismic wave acquisition and processing technology due to the need for hydrocarbon exploration reservoir characteristics research and amplitude analysis for reservoir monitoring for decades (DVORKIN et al., 1999; Avseth et al., 2005).

To relate the elastic modulus of sediment to porosity, pore fluid compressibility, mineralogy, and effective pressure, we first model the elastic modulus of the dry rock frame. And then, in the case of the elastic modulus of saturated sediments, they are calculated from sediments of the dry frame using Gassmnn's (1951) equation (DVORKIN et al., 1999).

In the isotropic solid case, with at least two independent elastic modules, (from among these: Bulk modulus *K*, Shear modulus *G*, Young's modulus *E*, lame coefficient λ, Poisson's ratio ν, Plan wave modulus *H*) it can be used many times, depending on the application to find out the elastic wave propagations of *Vp, Vs*.

Two solutions (P-wave: compression, longitudinal, primary Eq.1) (S-wave: shear, transverse, secondary Eq.2)

$$V_p = \sqrt{\frac{\lambda + 2G}{\rho}} = \sqrt{\frac{K + \frac{4}{3}G}{\rho}} = \sqrt{\frac{\frac{E(1-\nu)}{(1-2\nu)(1+\nu)}}{\rho}} \tag{1}$$

$$V_s = \sqrt{\frac{G}{\rho}} \tag{2}$$

G=0 for fluids; hence *E*=0 and ν=0.5.

In other words, all isotropic elastic modulus can derive from measurements of *Vp, Vs* and density ρ.

$$K = \rho V_p^2 - \frac{4}{3}\rho V_s^2 \tag{3}$$

$$G = \rho V_s^2 \tag{4}$$

$$E = \rho V_s^2 \frac{3V_p^2 - 4V_s^2}{V_p^2 - V_s^2} \tag{5}$$

$$\nu = \frac{V_p^2 - 2V_s^2}{2(V_p^2 - V_s^2)} \tag{6}$$

$$\lambda = \rho V_P^2 - 2\rho V_s^2 \tag{7}$$

The velocity of elastic waves in seafloor rocks is affected by the fluid contained in the pores. In order to calculate the elastic properties of the field state, especially in the seafloor ground, fluid-saturated data (*Vp, Vs*, density) are required. Based on these data, the following equations (Eq1~Eq3) are used to derive the bulk modulus and shear modulus of elasticity of the rock.

When designing an undersea tunnel, if poroelastic is considered, it is necessary to mention the Biot theory. In general, this theory is significant when referring to drained, undrained, or unjacketed conditions, which is regarded as a necessary condition when explaining drained, undrained design conditions in tunnel design. In other words, the undrained strength is used in the short-term stability problem immediately after tunnel construction, and the drainage condition is applied in the design of the long-term problem.

Here are some poroelastic coefficients needed.

$$
\left[\begin{array}{l}
E_0,\ \nu_0 \\
K_0 = \dfrac{E_0}{3\left(1-2\nu_0\right)} \\
b_{biot} = \dfrac{C}{M} = 1 - \dfrac{K_0}{K_s} = 1 - \dfrac{K_{fr}}{K_s} \\
\dfrac{1}{M} = \dfrac{\phi}{K_f} + \dfrac{b-\phi}{K_s} \\
B_s = \dfrac{Mb_{biot}}{K_u} = \dfrac{K_u - K_0}{b_{biot} K_u} \\
K_u = K_0 + Mb^2{}_{biot} \\
E_u = \dfrac{1+\nu_u}{1+\nu_0} \times E_0 \\
\nu_u = \dfrac{\nu_0 E_0 + \left(1+\nu_0\right)\left(1-2\nu_0\right) Mb^2{}_{biot}}{E_0 + 2\left(1+\nu_0\right)\left(1-2\nu_0\right) Mb^2{}_{biot}}
\end{array}\right]
$$

b_{biot}: Biot coefficient (drained experiment *ΔVp/ΔV*). *M:* storage modulus describing released fluid volume during a pore pressure decrease, keeping constant bulk volume. *C/K= Bs* describes the pore pressure change during undrained loading and is also known as Skempton's *B* parameter.

The Biot-Gassmann equation is a useful tool to predict the mechanical properties of subsurface rocks and soils. For example, it can be used to anticipate the seismic velocity of a sedimentary rock by accounting for the porosity and composition of the rock. Similarly, it can be used to calculate the shear modulus of a reservoir rock, which is important for estimating the strength of a reservoir. It would also be used to calculate the stress required to produce a given strain in a reservoir rock, which is useful for predicting the response of a reservoir to a given pressure.

So, Biot-Gassmann's relation, which is a quantitative expression of the change in the modulus of elasticity of a rock according to the change of the fluid in the void, can be applied.

- Biot-Gassmann's Equation is a representative rock physics model

Isotropic solids (base in Gassmann’s equation)

$$\frac{1}{K}=\frac{\phi}{K_f}+\frac{1-\phi}{K_s},\ G=0$$

$$K=K_{fr}+\frac{K_f}{\phi}\frac{b^2{}_{biot}}{1+\phi\dfrac{K_f}{K_s}(b_{biot}-\phi)}$$

$$\frac{K}{K_s-K}=\frac{K_{fr}}{K_s-K_{fr}}+\frac{K_{fr}}{\phi\left(K_s-K_f\right)}$$

$$\rho=\phi\rho_f+(1-\phi)\rho_s$$

$$\rho_{sat}=\phi S_w\rho_w+(1-\phi)\rho_s$$

$(Dry\ K_f=0,\ \text{Seawater}\ K_f=2.34GPa)$

Biot-Gassmann permits fluid substitution by isolating the effect of the saturating fluid. Biot-Gassmann is strictly valid only at low frequency.

1.4. Geoacoustic modelling (Empirical model)

Geoacoustic and physical properties on the subsea section are estimated by using a seismic survey (ex: OBS) and exploration data (ex: Borehole) data. Geo-acoustic models of the seafloor are basic to underwater acoustics and to marine geological and geophysical studies of the earth’s crust (Hamilton, 1980, 1987; Jackson and Richardson, 2007, Ryang et al., 2014). The geoacoustic property of marine sediments has been of a great interest in various fields such as seafloor engineering, sedimentology, marine geophysics, and underwater acoustics (Hamilton, 1970, 1980; Hamilton and Bachman, 1982; Richardson et al., 2002; Kim et al., 2007, 2011).

What can be seen in the studies of several geoacoustic modelling is that the empirical relationship between mean grain size and velocity suggested by Hamilton was used for the calculation of p-wave velocity. In order to characterize geoacoustic provinces of the South Sea shelf of Korea, sediment texture, physical, and geoacoustic properties (P-wave velocity) were measured and calculated based on approximately 350 core samples collected from the study area (Kim et al., 2012, Ryang et al., 2014). In their studies, the geoacoustic model was reconstructed for 7 geoacoustic units of the core sediments, based on the measurements of 125 P-wave velocities and 121 attenuations. The P-wave speed was compensated to in-situ depth below the sea floor using the Hamilton method.

The South Sea shelf of Korea is characterized by various sediment types caused by recent sea level changes. Direct physical and acoustic property measurements in the study area are relatively rare. Briggs and Fischer (1991) indirectly suggested geoacoustic provinces for the South Sea shelf using an empirical equation based on limited texture data. And, Kim et al. (2001) reported three different geoacoustic provinces (individual models for Namhae, Busan, and Ulsan areas) for the South Sea of Korea.

As a ground investigation of the expected area of the Korea-Japan submarine tunnel in East Asia, an extended investigation was conducted from shallow ground to deep ground using the Hamilton Empirical model based on the research data of The South Sea shelf of Korea (Kim et al., 2012, Ryang et al., 2014).

- <u>Empirical method</u>

Hamilton's Empirical Model (HEM) is a method used to investigate the physical properties of the seafloor through geo-acoustic modelling. This method is related to a combination of acoustic data and sediment samples to create a model of the seafloor. The model is then used to predict the acoustic properties of the seafloor, such as sound speed, attenuation, and reverberation.

Pros:	Cons:
• HEM is a relatively simple and cost-effective method for investigating the physical properties of the seafloor. • HEM can be used to accurately predict the acoustic properties of the seafloor. • HEM can be used to identify areas of sediment accumulation and erosion.	• HEM is limited in its ability to accurately predict the physical properties of the seafloor in areas with complex geology. • HEM is limited in its ability to accurately predict the acoustic properties of the seafloor in areas with high levels of sedimentation. • HEM is limited in its ability to accurately predict the acoustic properties of the seafloor in areas with high levels of biological activity.

Unknown parameters according to depth are calculated by applying Hamilton's equation data to the parameters of the shallow ground area found above. We applied the data to Hamiton's equation from inverse calculation.

As the empirical method, Hamilton (1979) established velocity gradients in the top parts of the first sediment layers by fixing the sonobuoy regression equations to an independently derived, sediment surface velocity. The velocity gradients can be used to compute layer thicknesses and identify the correlation between sediment and rock layers. It is convenient for purposes of comparison and to compute thicknesses to express these gradients as positive, linear increases of velocity with depth in m/s.

To explain in more detail,

1) Following Hamilton's method, it starts with the P velocity value at the bottom of the seawater. This value is called the initial velocity $Vp0$.

2) Then, the first upper surface is obtained by applying different ratio values according to the type of ground, as suggested by Hamilton.

The velocity ratio of sediment relative to bottom water (Hamilton, 1980)

Silty clay : 0.994

Sand-silt- clay : 1.036

Silty sand : 1.078

Shelly fine to medium sand : 1.20

Rock : 3.43

3) And the *Vp* value regarding the depth of the layer is obtained by applying the formula found through the experiment (Hamilton, 1980).

4) At the next layer, the constant K^H is first found on each layer.

This value shows the values tested by Hamilton in a laboratory by taking 5 cm sample for each type of ground. However, if this is also not known exactly, an approximate constant K^H value can be obtained from the value in the previous layer.

5) After that, it is obtained by multiplying the constant K^H value and the value proportional to the depth.

Depending on the compression velocity value, several gradient equations of compression wave velocity have been proposed as non-linear by Hamilton.

Vp and shear wave velocity *Vs* in km/s

From $V_p = 1.512$ to $V_p = 1.555$ km/s $V_s = 3.884V_p - 5.757$

From $V_p = 1.555$ to $V_p = 1.650$ km/s $V_s = 1.137V_p - 1.485$

From $V_p = 1.650$ to $V_p = 2.150$ km/s $V_s = 0.991 - 1.136V_p + 0.47V_p^{\ 2}$

V_p greater than 2.150km/s $V_s = 0.78V_p - 0.962$

To investigate a very deep rock part, it would be calculated with the linear velocity gradient for thick sediment z. It is used by linear velocity gradient in the top and bottom because of assuming the velocity gradient as it is linear and the same as in thick sections of similar rock at equivalent depths.

Table 3, 4 show the methods we used to find *Vp, V*

Table 3. Properties of the sediment by Geo-acoustic model from mud (Hamilton et al.,1970,1979,1980,1982)

	Depth (m)	**V_p (m/s)**	**V_s (m/s)**	**ρ_{bulk} (g/cm3)**	
Bottom water	80~150	1482~1500	0		The sound velocity of bottom water is approximated as $V_{bw}=1482\ m/s\ \left(BRIGGS,\ K.B\ et\ al.,\ 1991\right)$ $V_{bw}=1500\sim1510\ m/s\ \left(Hamilton\ 1980\right)$
Mud **(Silt clay)**	Surface	1482*0.994 =1473.1	31	1.48	$V_{p0}=ratioV\times V_{bw}$ Velocity ration of silt clay :0.994 (Hamilton 1979) For the Japanese data (Ohta and Goto 1978) When z=0.05m, $V_s=78.98D^{0.312}$
		1486	58		For the soft sediment cf: 0~500m (Hamilton1977) $\rho=1.135V_p-0.190$ $(V_p:km/s)$ $z:depth(km)$
	20	1498.88	115 (201)	1.51	$V_p=A+Bz+Cz^2+Dz^3$ Case : Terrigenous sediments (Hamilton 1980) $V_p=V_0+1.304z-0.741z^2+0.257z^3$ When the sediment surface V_p <1.51km/s, the shear wave velocity approximated $V_s={}^{V_p}\!/_{13}$ (Hamilton, 1979) For the Japanese data (Ohta and Goto 1978) $V_s=78.98D^{0.312}$
Medium sand	100	1850	497 (332)	2.03	For medium sand (Hamilton 1971,1976,1980) $K^H=1727$ $(K^H:coeffient\ const)$ $V_p=K^Hz^{0.015}$ From V_p =1650m/s to 2000~2150m/s

					$V_s = 0.991 - 1.136V_p + 0.47V_p^2$ For the japanese data (Ohta and Goto 1978) $V_s = 78.98D^{0.312}$ Density of sand as given by Hamilton (1980) us 2.03g/cm^3
Coarse Semi-consolidated	200	1981	585 (412)	2.08	For Coarse (Hamilton 1980) $K^H = 1830$ $(K^H : coeffient\ const,\ z : depth)$ $V_p = K^H z^{0.015}$ From V_p =1650m/s to 2000~2150m/s $V_s = 0.991 - 1.136V_p + 0.47V_p^2$ Or $V_s = 0.78V_p - 0.962$ greater than 200~2150m/s For medium and coarse sand in Japan z:>100m (Ohta and Goto 1978) $V_s = 78.98D^{0.312}$ For mudstone-shale expectable at depth below about ~600m (Hamilton1977) $\rho = 0.917 + 0.744V_p - 0.08V_p^2$ $(V_p : km/s)$

Table 4. Properties of the sediment by Geo-acoustic model from sand (Hamilton et al.,1970,1979,1980,1982)

	Depth (m)	**V_p (m/s)**	**V_s (m/s)**	**ρ_{bulk} (g/cm3)**	
Bottom water	80~150	1482~1500	0		The sound velocity of bottom water is approximated as $V_{bw} = 1482\ m/s\ \left(BRIGGS,\ K.B\ et\ al.,\ 1991\right)$ $V_{bw} = 1500 \sim 1510\ m/s\ \left(Hamilton\ 1980\right)$
Sand	Surface	1482*1.080 =1600	55.32 (D:0.05m)	1.62	$V_{p0} = ratio V \times V_{bw}$ ` Velocity ratio sand silt :1.08 (Hamilton 1979) For fine Sand z:<20m (Hamilton, 1976) $V_s = 128z^{0.28}$ For the soft sediment cf: 0~500m (Hamilton1977) $\rho = 1.135V_p - 0.190 \quad (V_p : km/s)$ $z : depth(km)$
	20	1626	296 (265)	2.03	$V_p = A + Bz + Cz^2 + Dz^3$ Case : Terrigenous sediments (Hamilton 1980) $V_p = V_0 + 1.304z - 0.741z^2 + 0.257z^3$ For fine Sand z:<20m (Hamilton, 1976) $V_s = 128z^{0.28}$ For medium and coarse sand in Japan z:<20m (Ohta and Goto 1978) $V_s = 104.33D^{0.312}$
Medium sand	100	1860	504 (332)	2.03	For medium sand (Hamilton 1971,1976,1980) $K^H = 1736$ $(K^H : coeffient\ const)$ $V_p = K^H z^{0.015}$ From V_p =1650m/s to 2000~2150m/s $V_s = 0.991 - 1.136V_p + 0.47V_p^2$

					For the japanese data (Ohta and Goto 1978) $V_s = 78.98D^{0.312}$ Density of sand as given by Hamilton (1980) us 2.03g/cm^3
Coarse Semi-consolidated	200	2014	608 (412)	2.3	For Coarse (Hamilton 1980) $K^H = 1860$ $(K^H : coeffient\ const)$ $V_p = K^H z^{0.015}$ For the deeper stratum of unidentified lithology or V_p greater than 2000m/s $V_s = 0.78V_p - 0.962$ For the japanese data (Ohta and Goto 1978) $V_s = 78.98D^{0.312}$ For mudstone-shale expectable at depth below about ~600m (Hamilton 1977) $\rho = 0.917 + 0.744V_p - 0.08{V_p}^2 \quad (V_p : km/s)$

1.5. Determination of the properties of underwater rocks and fault and the formation fracture

Based on the research data of the acoustic model of the shallow ground of the south sea shelf of Korea (Kim et al., 2012, Ryang et al., 2014), the acoustic model of the seabed under the deep sea was finally derived based on Hamilton's empirical theory, and finally, the material properties of the deep ground (in Table 5, 6) were discovered using rock physics (Eq.1~Eq.7).

In the Korean continental margin of the south sea deep, two geoacoustic models were reconstructed (shallow ground: mud, sand) in Table 5, 6.

However, these studies were limited to regional areas and/or resulted from theoretical data. Thus, these research need to be reassessed using new data measured directly from specimens collected from the seafloor

Table 5. Examples of expected ground sediment and rock layer properties in the Korea-Japan Submarine Tunnel (Mud)

	Depth (m)	V_p (m/s)	V_s (m/s)	ρ_{bulk} (g/cm3)	E_{dyn} (MPa)	K (MPa)	ν	$C_{cohesion}$ (kPa)	$\Phi_{friction\ angle}$	$k_{permeability}$ (m/s)	Φporo (%)	Water content (%)	S_w (saturation)	B (Biot)
Bottom water	20~80	1482~1500												
Mud (Sity clay)	Surface	1473.1	31	1.48	4.2	K:3209								
	20	1498.88	115	1.51	60	K :3366								
A. R. Kim et al., 2017; Bae et al., 2014; D. C. Kim et al., 2012; G. Y. Kim et al., 2011		1486~1515	50~60	1.45~1.65	15~20	K : Ks : K_{fr} :	0.35	30~40	$22_{\circ}$	2E-09	60~70	40~50	1	0.65
Medium sand	100	1850	497	2.03	1465 (5 class)	K:6279	0.25	50 (5 class)	30	2E-08				0
Coarse Semi-consolidated	200	1981	585	2.08	2067 (4 class)	K:7213	0.25	200 (4 class)	32	2E-08				0

Table 6. Examples of expected ground sediment and rock layer properties in the Korea-Japan Submarine Tunnel (Sand)

	Depth (m)	V_p (m/s)	V_s (m/s)	ρ_{bulk} (g/cm3)	E_{dyn} (MPa)	K (MPa)	ν	$C_{cohesion}$ (kPa)	$\Phi_{friction\ angle}$	$k_{permeability}$ (m/s)	Φporo (%)	Water content (%)	S_w (saturation)	B (Biot)
Bottom water	80~150	1482~1500												
Sand	Surface	1600	55.32	1.62	15	K:4140								
	20	1626	265	2.03	423	K:5177								
A. R. Kim et al., 2017; Bae et al., 2014; D. C. Kim et al., 2012; G. Y. Kim et al., 2011		1630~1850	~100	1.7~2	15~20	K : Ks : K_{fr} :	0.25	30~40	$25_{\circ}$	2E-09 1.75E-06 (without hydrate)	40~50	20~30	65 (partie hydrate) Or 1	0.43
Medium sand	100	1860	504	2.03	1506 (4~5 class)	K:6335	0.25	50 (5 class)	30	2E-08				0
Coarse Semi-consolidated	200	2013.85	608	2.3	2465 (4 class)	K:8194	0.25	200 (4 class)	32	2E-08				0

Fault fracture zones exist between rock sections with severe weathering and crushing, and cause excessive displacement and collapse during tunnel excavation. Therefore, when designing and constructing a tunnel, it is necessary to determine the distribution of the fracture zone through a ground investigation and to reflect it appropriately.

The fault zone is divided into the fault core and the damaged zone according to the degree of damage of the constituent materials, as shown in figure (5), and the fault core is divided into breccias, cataclasite, and fault gouge (Fig. 5; modified from Caine et al., 1996; Heynekamp et al., 1999; Faulkner et al., 2003; Choi et al., 2009; Gudmundsson et al., 2010). The ground parameters applied to the numerical analysis are unit weight, cohesive, friction angle, deformation modulus, and Poisson's ratio.

Although it is difficult to determine the parameters of the fault zone, in the study of Song et al (2016), the fault zone was subdivided into the fault core part and the fault zone using the existing test results and design experience, and then the parameters were applied.

It shows more reliable fault property values than the parameters of other studies (Korea High Speed Fail Construction corporation 1999; Kang et al., 2020).

However, it was necessary to refer to other papers for the values of hydraulic properties (Table 7).

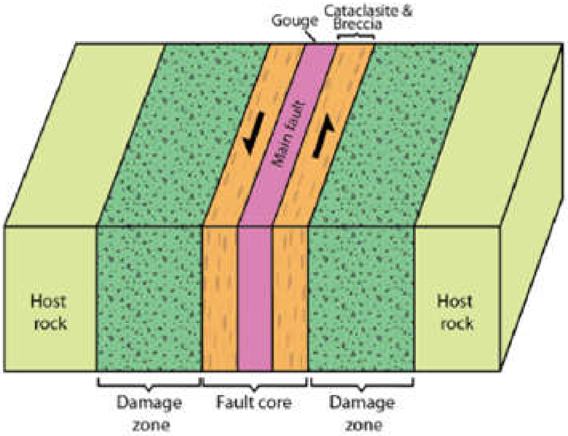

Figure 5. Conceptual model of a (strike-slip) fault including fault gouge, fault breccias, and fault damage zone (Song et al.,2016)

Table 7. Physical properties of the fault area through several research data.

Properties of fault 1 (Korea High Speed Rail Construction Corporation1999 : Yang San fault)

E-deformation (MPa)	Permeability (m/s)	Cohesion (KPa)	φ (。)	γ (kN/m3)	ν	e (m)	*Kt (KPa/m)*	*Kn* (KPa/m)
100	6.3E-07~09	80	30	19.5	0.27	2	19,500	62,000

Properties of fault 2 (Song et al., 2016)

	E-deformation (Mpa)	Cohesion (kPa)	φ (。)	γ (kN/m3)	ν	e (m)	Kt (KPa/m)	Kn (KPa/m)
Gouge	9	12.3	22	19.7	0.34	0.5	6,716	27,705
Breccia	50	15.7	44	19.8	0.36	0.5*2	36,764	168,067
Damage zone	290	60	44.1	22.1	0.4	2*2	51,785	310,714

Properties of fault 3 (Kang et al., 2020: fault fracture zone with gouge experiment labo)

	E-deformation (Mpa)	Permeability (m/s)	Cohesion (KPa)	φ (。)	ν	γ(kN/m3)
With gouge	15	1.0E-4	16	26.5	0.39	19
Without gouge	75	7.0E-03	0.8	35	0.32	21.3

LIST OF NOTATIONS (CH 2)

Symbol	**Definition**
$\underline{v}$	Fluid velocity
ϕ	Total hydraulic head
v_r	Radial fluid velocity
Q, q	Water flow
q_r	Radial water flow
r_i	Radius intrados of tunnel
r_0	Radius extrados of tunnel
γ_w	Unity weight of water
g	Gravitational acceleration
P_0	Bottom sea pressure
k	Permeability
k_s	Permeability of ground
k_L	Permeability of lining
h_s	Depth of ground
h_w	Depth of groundwater
H_w	Total depth

2. Hydraulic pressure evaluation of the underwater tunnel modelling

The flow of groundwater flowing into the tunnel is an essential understanding part of designing and constructing underground excavation (El Tani, 2003; Huangfu *et al.*, 2010). The construction of a tunnel below the groundwater affects the hydraulic environment of the surrounding ground and encounters water infiltration into the tunnel. Also the permeability of the aquifer, its supply, and the method of tunneling and lining all influence the relationship between the groundwater in a rock mass and the excavation of tunnels (Reuter et al., 2000).

For example, water pressure does not have an effect on the lining in a tunnel with the flow characteristics of a completely drained condition. However, the inflow of water into the tunnel generates a penetration force, which increases the effective stress of the surrounding ground, and a displacement, which generates additional stress in the lining.

In addition, groundwater flow in bedrock is governed by the characteristics of joints (fault). In general, since it is difficult to reflect the characteristics of all joints (fracture zone, fault) in the analysis, there would be a tendency to focus on the analysis by replacing the joints with a medium assumed to be a continuum.

However, in this chapter of this paper, we also try to understand the hydraulic behavior of the deep tunnel passing through the fracture zone modeled as a single interface under the assumption of a homogeneous isotropic continuum rock medium.

We present the overall process of hydraulic flow in tunnel design. First, the theoretical background of hydraulic behavior in tunnels is described. The method of modelling and analysis of water inflow into the tunnel through the numerical code DISROC used for this purpose is presented. Finally, the results obtained from various geological conditions are presented and discussed. We also comprehend the hydraulic behavior in the deep tunnel passing through the fracture zone modeled as a single interface under the assumption of a homogeneous isotropic continuum rock medium.

2.1. Theoretical study

Analytic methods usually allow simplify the geostructural setting and rock mass assemblage, and only a few simple input data are included (Coli and Pinzani, 2014) Analytical solutions take the advantages of convenience and are suitable for direct application to tunnel inflow estimate or validation and comparison of numerical models (Huangfu et al., 2010).

Harr (1962) and Goodman (1964) obtained the pore pressure distribution in the ground surrounding a tunnel based on a mirror-image and in deep tunnels where the cover and water level are five times more than the diameter of the tunnel. In addition, the groundwater flow near the tunnel wall is assumed to be a radial flow (Figure 6). They used the equations of KOCHINA (1962) that are identical to the equations developed by Muskat (1938)

Figure 6a) shows an ideal analytical model of inflow in a circular tunnel in a semi-infinite isotropic and homogenous formation. The tunnel (source) and the mirror-image sink can be considered to be equidistant from the existing groundwater level before excavation. Thus the distance, L, can be approximated as twice the depth of the tunnel below the ground level, h_s (Figure 6a). It shows the flow network occurring under steady-state in seepage between the two wells at the groundwater level is in equilibrium with the ground slope. These flow net lines intersect the same potential line set by the existing groundwater's seepage level at 90 degrees.

A prediction of groundwater inflow into a drained tunnel can be analytically obtained based on several simple assumptions:

1) Homogenous and isotropic permeability
2) Steady flow, circular tunnel cross-section,
3) Hold at constant hydraulic potential

The method suggested by Goodman (1964) is described below as an example.

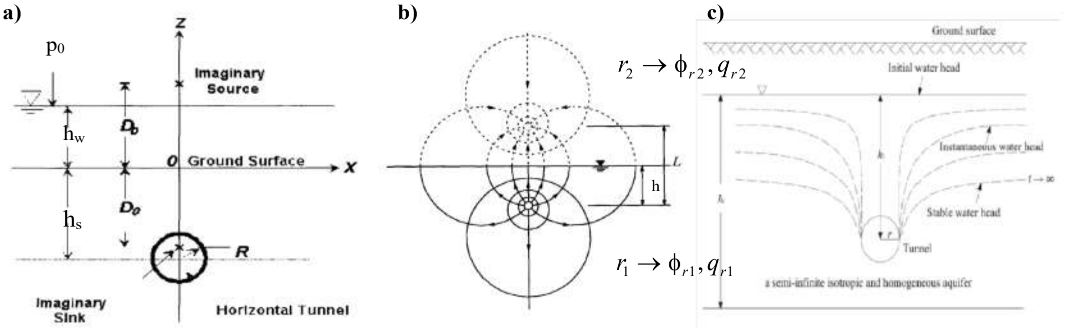

Figure 6. a) Tunnel profile (Shizhong Lei 1999. b) Image method (Fernandez 1994)
c) Idealized analytical model of tunnel inflow (Xiao-Xue Liu 2018)

First, according to Darcy's law and mass conservation, the two-dimensional flow around the tunnel is described by the following Laplace equation.

$$\underline{v} = -k\nabla\phi \tag{8}$$

$$\nabla.\underline{v} = 0$$

$$\Rightarrow \Delta\phi = 0$$

$$\frac{\partial^2\phi}{\partial^2 x^2} + \frac{\partial^2\phi}{\partial^2 z^2} = 0 \tag{9}$$

Using polar coordinates for the flow around the circular tunnel, we confirm the radial component of the fluid velocity:

$$v_r = -k\frac{\partial\phi_r}{\partial r} \tag{10}$$

$$\frac{\partial\phi_r}{\partial r} = \frac{1}{k}\frac{q_r}{2\pi r_0} \tag{11}$$

With the assumption of a deep tunnel (diameter small compared to the depth), we can suppose that the pressure is the same at all the points on the tunnel wall. In this case, v_r is constant around the tunnel and is related to the water inflow in the tunnel by:

$$q_r = 2\pi v_r(r_0) \tag{12}$$

The boundary condition at the ground surface is p_0 (bottom sea pressure)

$$z = 0; \qquad \phi = p_0 = \gamma_w g h_w \tag{13}$$

$$z \to \infty; \qquad \phi(x,z) \to \phi(\mathrm{r}) = -k\,\mathrm{H} = -k(\mathrm{z}+ {p_0}/{\gamma_w}) \tag{14}$$

So the boundary condition for the flow problem on the tunnel wall becomes:

$$r = r_0; \qquad \frac{\partial\phi}{\partial r} = \frac{1}{k}\left(\frac{q}{2\pi r_0}\right) \tag{15}$$

When the method of mirror source (Figure 6b)) is used (Goodman's method), the equation becomes:

(The last equation and substituting the boundary conditions and integrate)

$$r_1 \rightarrow \phi_{r1}, q_{r1},\ r_2 \rightarrow \phi_{r2}, q_{r2} \tag{16}$$

$$\phi_{r1} = +\frac{q_{r1}}{2\pi k}\ln r_1 + c_1$$

$$\phi_{r2} = -\frac{q_{r2}}{2\pi k}\ln r_2 + c_2$$

Applying the superposition principle of the solution,

$$\phi = \phi_{r1} + \phi_{r2} = \frac{q_{r1}}{2\pi k}\ln r_1 + c_1 - \frac{q_{r2}}{2\pi k}\ln r_2 + c_2 \tag{17}$$

In the tunnel excavation surface

At Figure 6 (a), (b), we can see *h=h_s= distance* from the ground surface of rock and soil to the center of the tunnel. $(x = r_0, \mathrm{z} = \pm h)$

$$r_1 = \sqrt{x^2 + (\mathrm{z}+h)^2} = r_0 \tag{18}$$

$$(h >> r_0)$$

$$r_2 = \sqrt{x^2 + (\mathrm{z}-h)^2} = \sqrt{r_0^{\ 2} + (2h)^2} \approx 2h$$

$$\phi = +\frac{q_{r1}}{2\pi k}\ln\sqrt{x^2 + (\mathrm{z}+h)^2} - \frac{q_{r2}}{2\pi k}\ln\sqrt{x^2 + (\mathrm{z}-h)^2}$$

$$\textit{free drainage}(q_{r1} = q_{r2} = q_0)$$

$$\phi = \frac{1}{2\pi k}\ln\frac{r_0}{2h}q_0$$

In the case of submarine tunnel

(P₀ exists on the ground surface by h_w, $\phi \Rightarrow H_w = h_s + h_w$)

$$q_0 = 2\pi k\frac{H_w}{\ln(2h_s / r_0)} \tag{19}$$

$$(q : m^3 / \mathrm{sec}/ m, \quad k : \mathrm{m/\,sec})$$

(:total potential, P_0=bottom water pressure, γ_w=unit weight of water, h_w=distance from the water surface to the ground surface of rock, h_s=distance from the boundary of rock and soil to center of the tunnel, k=permeability conductivity, q=water inflow, r1: distance from the imaginary sink, r2: distance from the imaginary source)

- Comparison of different analytical solutions for tunnel inflow

Many researchers have proposed approximate solutions for the equation presented in the previous section to obtain analytical-theoretical formulas for tunnel inflow. The results of their equations are difficult to compare because the given assumptions are different, but we introduce each formula analysis and the corresponding assumptions in order to select and apply the appropriate conditions for our model.

Polubarinova-KOCHINA (1962) derived an approximate expression for a horizontal tunnel in a fully saturated, semi-infinite homogeneous medium. And it was assumed that $r \ll D$, the equipotential produced by the sink imaginary (Figure 6a) at the tunnel's centerline ($z=-D_0$) and a source at $z=D_0$, means almost a circle at the tunnel perimeter.

The most well-known Goodman's equations (1964) and research equations by Lei (1999) reviewed the work of Polubarinova-KOCHINA (1962) to analyze and provide numerical solutions for transient flows.

Goodman (1964) and Lei (1999) supposed the presence of a constant head boundary to predict groundwater inflow to a tunnel. The paper of Goodman et al. (1964) concerns experimental tests on tunnel driving in water tanks. One of their interesting comments is the slow increase in the water inflow with the tunnel diameter. The solution discovered by Lei (1999) predicts very large values for the water inflow when the tunnel is close to the water table and unrealistic values for the seepage forces near the tunnel edge.

ZHANG et al. (1993) extended Goodman's steady-state model by taking into account the commonly observed hydraulic conductivity gradient. It is found that the error between the analytical solution Q_a and numerical results Q_n, for example, the difference $(Q_a - Q_n)/Q_a$, is less than 6% if the ratio of rock cover to tunnel diameter L/d is less than 2.

Two attempts were proposed for a formal study of the calculation of tunnel inflow water. There are El-Tani' works (1999), (2003). The former (1999) showed that two terms truncated single-layer approximations. The latter (2003) adopted the mobius transformation and Fourier series to analyze the water inflow problem of a circular tunnel in a semi-infinite aquifer.

By compiling the exact and approximate solutions by many researchers, we can see the difference in the prediction of groundwater inflow. Looking at Figure 7, the error increases as the radius of the shallow tunnel increases compared to the depth of the ground surface. At least the depth of the tunnel should be twice more than the diameter of the tunnel so that the error is within 10%. When the water depth is five times deeper than the tunnel radius, the El-Tani (1999) equation presents a reliable result. However, it should be noted that the formula may underestimate the amount of inflow during less than 20% of h_s/r .

Kolymbas and Wagner(2006) proposed an analytical expression that applies to both deep and shallow tunnels with variable groundwater heads around the tunnel and at the surface.

Park et al. (2008) noted that, in a homogeneous aquifer, leakage, and seepage forces are proportional, and their ratio is the permeability. They extend the validity range of the analytical leakage equation in El Tani (2003) to structural analysis and tunnel stability, such as for submarine tunnels. (Table 8)

Table 8. Some general theoretical equations used to model groundwater inflow in submarine tunnels.

Reference	Equation	Annotation
Polubarinova-Kochina (1962) Goodman (1964) L.ZHANG et al(1993) Park et al (2008)	$q_{o\max} = 2\pi k \frac{H_w}{\ln(2h_s / r_0)}$	- In the case of an undersea tunnel, h_w is greater than h_s. q_{0max} = maximum water inflow per metre (m3/s·m) $q_{0stable}$ = stable water inflow per metre (m3/s·m) k = hydraulic conductivity (m/s); H_w = distance from centre of tunnel to water head (m) h_s = distance from boundary of rock and soil to center of tunnel (m) h_w = distance from water surface head to boundary of rock and soil (m) $H_w=h_w+h_s$ if existence, h_a = water head of tunnel (m) r_o = tunnel radius (m).
Lei (1999)	$q_o = 2\pi k \frac{H_w}{\ln\left[\frac{h_s}{r} + \sqrt{\frac{h_s^2}{r^2} - 1}\right]}$	
El-Tani (1999) El-Tani (2003)	$q_o = 2\pi k \frac{\lambda^2 - 1}{\lambda^2 + 1} * \frac{H_w}{\ln \lambda}$ $\lambda = \frac{H_w}{r} - \sqrt{\frac{H_w^2}{r^2} - 1}$	
For $H_w>>r_o$ we can think this way $h_s + \sqrt{h_s^2 - r^2} \approx 2h$ Then, El-Tani's equation and Lei's equation are similar to Goodman's.		
Lombardi (2002)	$q_0 = \frac{2\pi k_s H_w}{\left(1 + 0.4\left(\frac{r_0}{H_{filterL}}\right)^2\right) \ln\left(2H_{filterL} \big/ r_0\right)}$	
Kolymas et al (2006)	$q_o = 2\pi k \frac{H_w - h_a}{\log(2h_s / r_0)}$ $h_a = const$	

As mentioned earlier, these formulas are made under the following assumptions. (Lei., 1999)

- The tunnel is horizontal with a circular cross-section and is located in a fully saturated, homogeneous, isotropic, and semi-infinite porous aquifer.

- The flow is in steady-state

- The fluid is incompressible

- The hydraulic head at the ground surface and that at the tunnel perimeter are both constant.

However, these equations are inferred based on the assumptions of the idealized analytic model and therefore are not valid in certain situations. Moreover, these analytical solutions only provide predictive equations for maximum or stable groundwater inflow per meter. To compensate for these limitations, Xiao-Xue Liu (2017) presented a predictive approach for time-dependent groundwater inflow into tunnels in not only anisotropic but isotropic-constrained aquifers.

$Q_{MG}=2\pi k\dfrac{h}{\ln\left(\dfrac{2h}{r}\right)}$	Muskat (1937), Goodman et al. (1965)
$Q_{Ka}=2\pi k\dfrac{h}{\ln\left(\dfrac{2h}{r}-1\right)}$	Karlsrud (2001)
$Q_{SL}=2\pi k\dfrac{h}{\ln\left(\dfrac{h}{r}+\sqrt{\dfrac{h^2}{r^2}-1}\right)}$	Rat (1973), Schleiss (1988), Lei (1999)
$Q_{Lo}=2\pi k\dfrac{h}{\left(1+0.4\left(\dfrac{r}{h}\right)^2\right)\ln\dfrac{2h}{r}}$	Lombardi (2002)
$Q_{T2}=2\pi kh\dfrac{1-3\left(\dfrac{r}{2h}\right)^2}{\left[1-\left(\dfrac{r}{2h}\right)^2\right]\ln\dfrac{2h}{r}-\left(\dfrac{r}{2h}\right)^2}$	Two terms truncated single layer, El Tani (1999)

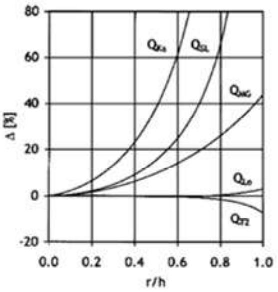

Figure 7. Relative differences of the various approximations to tunnel inflow equations.
(El Tani., 2003)

Since tunnel construction involves excavation and installation of support materials (linings), the groundwater flow path flowing from the drainage tunnel into the tunnel gets resistance as it passes through the support materials. Fernandez (1994) and Kolymas(2005) attempted to derive the relationship between the lining and ground influence according to these drainage conditions. Kolymbas et al. (2006) recognize the existence of a water head difference in the tunnel. This means the difference in the water pressure inside and outside the tunnel.

So, first, let's revisit the equation of Goodman (1964) in Table 8. The problem is to determine the hydraulic head drop hl between the extrados and intrados of the lining.

We determine it by writing the mass conservation and by writing the equality of the total inflow on the extrados (Rock) and intrados (Lining) surfaces: In Figure 8, there is the hydraulic head difference due to the presence of the lining. Subtracting this head difference from the existing flow equation, the formula below is calculated.

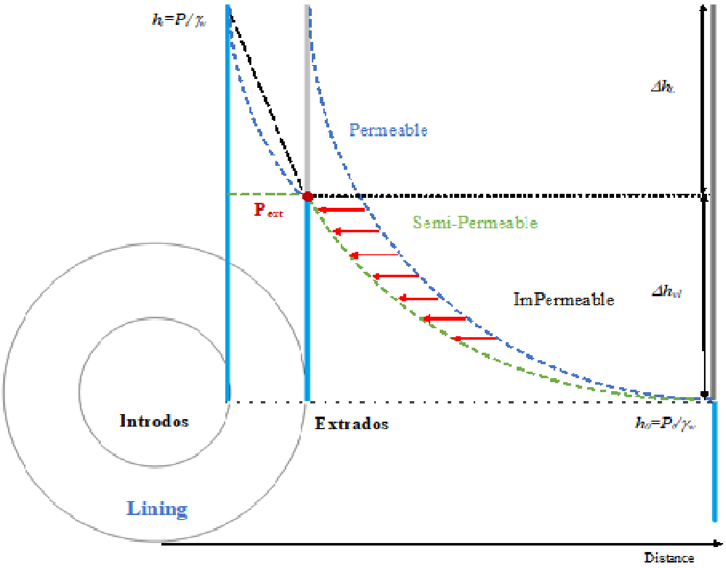

Figure 8. Hydraulic head as a function of distance x

Theoretical equation with lining

$$q_o = 2\pi k \frac{H_w - h_a}{\log(2h_s / r_0)} \qquad (20)$$

$$h_a = const$$

$$q_{Lining}=\frac{2\pi k_L\Delta h_l}{\ln\left({}^{r_0}\!\big/_{r_i}\right)}=q_{Rock}=\frac{2\pi k_s(H_w-\Delta h_l)}{\ln\left({}^{2h_s}\!\big/_{r_0}\right)}$$

$$A=\frac{2\pi k_L}{\ln\left({}^{r_0}\!\big/_{r_i}\right)}\ ,B=\frac{2\pi k_s}{\ln\left({}^{2h_s}\!\big/_{r_0}\right)}\ ,BH_w=q_{0Goodman}$$

$$\Rightarrow q_{Lining}=\frac{2\pi k_L\Delta h_l}{\ln\left({}^{r_0}\!\big/_{r_i}\right)}=\frac{2\pi k_s(H_w-\Delta h_l)}{\ln\left({}^{2h_s}\!\big/_{r_0}\right)}$$

$$=A\Delta h_l=BH_w-B\Delta h_l$$

$$\Rightarrow \Delta h_l=q_{0Goodman}\frac{1}{A+B}$$

$$\Rightarrow q_{Lining}=A\Delta h_l=q_{0Goodman}\frac{A}{A+B}=q_{0Goodman}\left(\frac{1}{1+{}^{B}\!\big/_{A}}\right)$$

$$=q_{0Goodman}\frac{1}{1+\dfrac{k_s}{k_L}\dfrac{\ln\left({}^{r_0}\!\big/_{r_i}\right)}{\ln\left({}^{2h_s}\!\big/_{r_0}\right)}}$$

$$\Rightarrow q_{Lining}=q_{0Goodman}\frac{1}{1+\dfrac{k_s}{k_L}\dfrac{\ln\left({}^{r_0}\!\big/_{r_i}\right)}{\ln\left({}^{2h_s}\!\big/_{r_0}\right)}} \qquad (21)$$

2.2. Numerical analysis of Hydraulic behaviour by DISROC

In complex hydrogeological conditions, numerical methods can be adapted to analyze ground water flow around tunnel. A numerical flow model is a simplified representation of an aquifer, and its construction requires first formulating a conceptual model, which is a qualitative description of the main properties of the flow system (Berkowitz 2002; Samardzioska and Popov 2005; Gustafson 2012).

In this part, numerical analysis was conducted under various conditions, as well as a comparison with the result of the theoretical formula. The numerical modelling of the seepage and the flow based on Darcy's law is done by using the Finite Element Analysis code DISROC.

In our study, the materials models required for hydraulic numerical analysis of tunnels are Ground, Support (lining), and Faults.

Ground material:

Bulk material (Ground) is modeled by an isotropic permeability model according to the law of Darcy.

$$v = -k\nabla p \tag{22}$$

$$\underline{v} = -k\nabla\left(p + \gamma_f z\right)$$

(v: *fluid velocity*, p: *fluid pressure*, γ_f: *fluid unit weight*, k: *conductivity coefficient*)

<u>Lining support</u>

The lining can be mechanically represented by volumetric elements or by shell, or in 2D by beam elements. In our modelling, we have represented the lining by beam elements. However, the beam element is not perfectly bonded to the rock formation, and so a contact interface is introduced between the lining and the rock formation. This corresponds with the code DISROC to a type of element called “bolt element”. This element is comprised of a beam element (steel rod of a bolt with the property of bending) attached to the surrounding material by a joint or contact interface.

For the case where there is a lining corresponding to a concrete ring with a thickness *e* and a permeability *k:*

We take

Element “BEAM”: $C_n = k/e$

Element “Bolt”: $C_n = k/e$ and $C_t = ke$

In these relations, C_t represents the hydraulic conductivity of the tube depending on its section, and C_n shows the coefficient of exchange between the inside and outside of the tube depending on the permeability and thickness of the tube wall (Figure 9). *(*q_{tube}*: debit in the tube,* $p_{outside}$*: pressure outside the tube,* p_{inside}*: pressure inside the tube, delta p: fluid pressure gradient along the tube).*

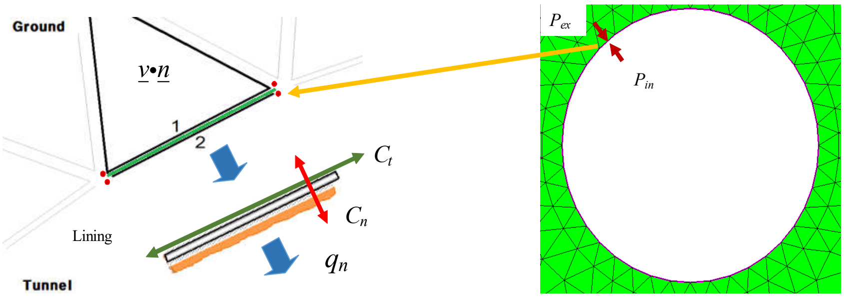

Figure 9. Hydraulic flow when the tunnel lining is considered a thin layer

The constitutive equation for this element includes the flow along the tube denoted by q_t and fluid mass exchange between the tube and the surrounding rock denoted by Q_n. The first one is related to the pressure gradient along the tube and the second one to the difference between the tube pressure inside the tube and the pressure outside of the tube in the surrounding rock by the following equations:

$$q_t = -C_t \nabla_t p \qquad (23)$$
$$q_n = C_n (p_{outside} - p_{inside})$$

The mass conservation law for the tube expresses the variation of the flow alone. The tube is compensated by its fluid exchange with the outside. The masse conservation equation reads:

$$\nabla(C_t \nabla p) + C_n (p_{outside} - p_{inside}) = 0 \qquad (24)$$

So this model depends on two parameters C_t, the tube longitudinal conductivity, and C_n, the tube-through conductivity, which should be determined. Actually, the problem is independent of the C_t value, and we can take it equal to zero. So, we can consider only the parameter C_n tube-through conductivity.

We need an explanation to calculate *q,* the flow rate going into the tunnel.

$$q = \int \underline{v}\underline{n}\; ds \rightarrow q_n = C_n (p_{outside} - p_{inside}) \qquad (25)$$

(q_{joint}: debit in the joint, ∇p : fluid pressure gradient along the joint, k: permeability, e: thickness of the joint)

(If the interface line of the fault contacts the tunnel boundary)

$$q_{joint} = -C_t \nabla p \qquad (26)$$
$$C_t = k_{joint} e_{joint}$$

In modelling of hydraulic behaviour in Disroc, the actual applied permeability coefficient must be converted to the Disroc applied permeability coefficient.

In Disroc, it is explained as follows:

$$\underline{v} = -k_{Disroc}\nabla p \tag{27}$$

The speed v is in m/s. But in Darcy's law, the hydraulic head ψ is used by the height of water

$$\underline{v} = -k_{Darcy}\nabla\Psi \tag{28}$$

for a water column of height h and water density ρ_e g gravity acceleration

$$\begin{aligned} &p = \rho_e g h \\ &\rho_e g = 9.81 * 10^3\, Pa/m \\ &p = \rho_e g h = \rho_e g \Psi \\ &\nabla p = \rho_e g \nabla\Psi \end{aligned} \tag{29}$$

Here, if we compare the Disroc permeability k_{Disroc} and the Darcy permeability k_{Darcy}.

$$\begin{aligned} &\underline{v} = -k_{Disroc}\nabla p = -k_{Disroc}\rho_e g \nabla\Psi \\ &k_{Disroc}\rho_e g = k_{Darcy} \\ &k_{Disroc} = \frac{k_{Darcy}}{\rho_e g} \end{aligned} \tag{30}$$

That is the units taken

$$k_{Disroc} = \frac{k_{Darcy}}{9.81} \approx \frac{k_{Darcy}}{10} \tag{31}$$

In order to perform the numerical analysis of the submarine tunnel, the boundary condition is applied to the hydraulic load according to the vertical gravity gradient.

There is the boundary of the model divided into four sides (top, bottom, and two lateral sides), which are employed in different cases of hydraulic load applied on these sides. The different cases considered are as follows the Table 8 and Figure 10.

Table 8. Various boundary conditions applied cases

N.1	Apply hydraulic pressure only to the top surface.
N.2	Apply water pressure to all 4 sides, top, bottom, left, and right.
N.3	Apply water pressure to only 3 sides excluding the bottom side.

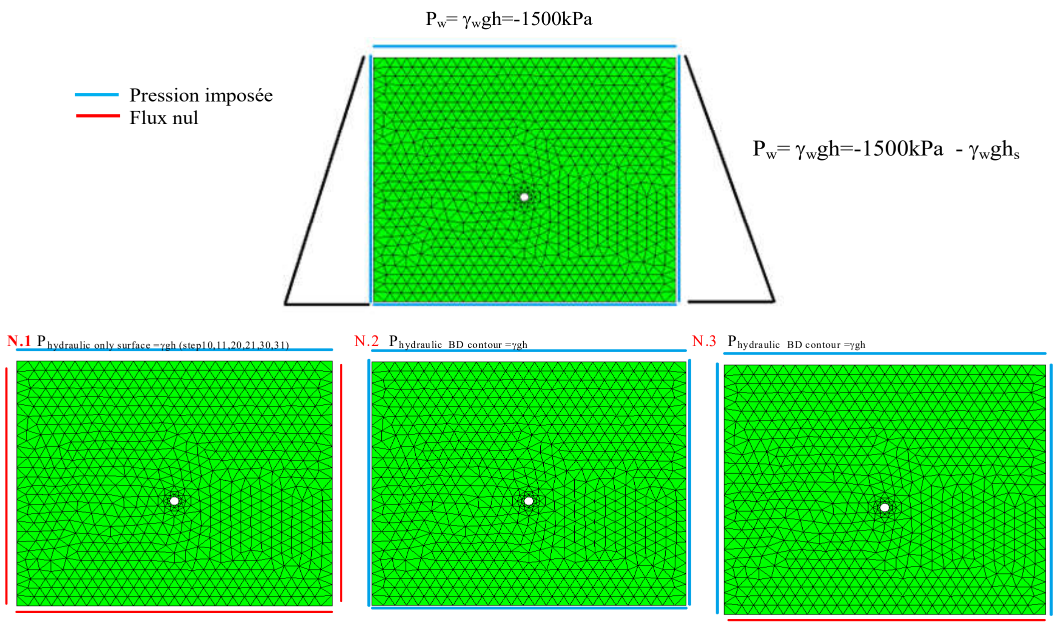

Figure 10. Boundary conditions on geometry of tunnel

Also important is the hydraulic pressure conditions applied inside the tunnel on the lining.

On each lining element in Figure 9, there are four nodes, two of them representing the intrados and the others the extrados or the rock-face.

First, in the case where there is Non-lining in Table 8, in this case, the pressure outside and inside the tube is the same as zero, we can produce this condition in two different ways:

- Imposing the same pressure outside and inside the model. In this case, the C_n value has No effect.
- Imposing only the inside pressure and we take $C_n = \infty$ (numerically a great value, or small value of e lining's thickness in the equation).

Table 9. Lining conditions applied cases.

Case1. Desactive lining (free drainage)	Hydraulic pressure of lining P(in)=0 Hydraulic pressure of lining P(ex)=0 Conductivity of lining C_t=0
Case 2. Impermeability (non drainage)	Conductivity of lining C_t=0 Conductivity of lining C_n= very small value
Case 3. Active lining (drainage-non drainage)	Hydraulic pressure of lining P(in)=0

2.3. Tunnel Model's Loading/ Boundary condition

In our hydraulic model, models with three different geometry conditions are presented.

First of all, Tunnel HB conceived an ideal geometry environment simply suitable for the theoretical equation in order to compare the numerical analysis and the theoretical equation.

Secondly, after the basic model of Tunnel HB was introduced earlier, fault conditions according to different locations have been added.

It shows the numerical analysis according to the ground conditions of the submarine tunnel in the East Sea of Korea.

Those Figures below show the geometry conditions of each model.

1) Tunnel HB

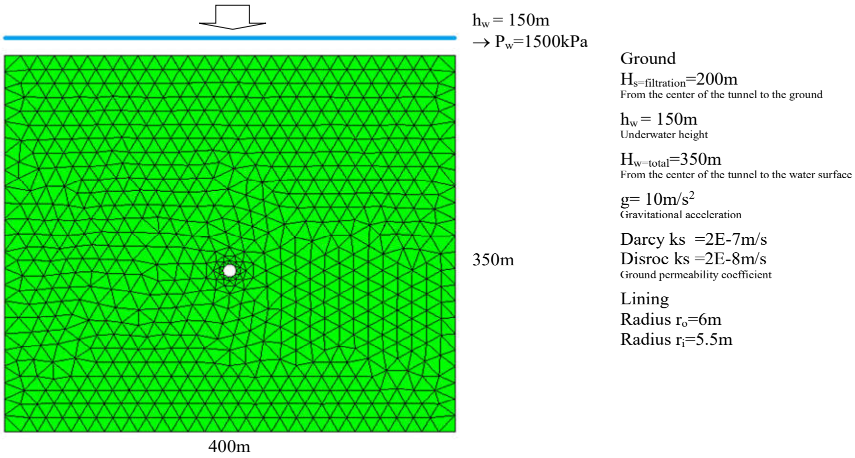

Figure 11. Hydraulic simple model condition Tunnel HB

2) Tunnel HBF1, HBF2, HBF3

Tunnel HBF Model (Figure 12) added one fault in the Tunnel HB basic model introduced, and analysed the results according to the fault's location.

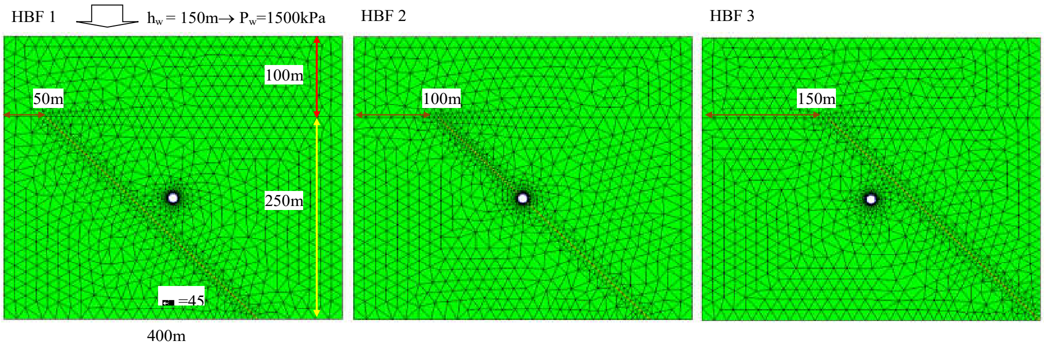

Figure 12. Hydraulic simple model condition Tunnel HBF1, HBF2, HBF3

3) Tunnel H1, H2, H3

Tunnel H1,2,3 (Figure 13) also has no significant structural difference from the previous model, but there are two layers with different parameters in the upper layer of the ground.

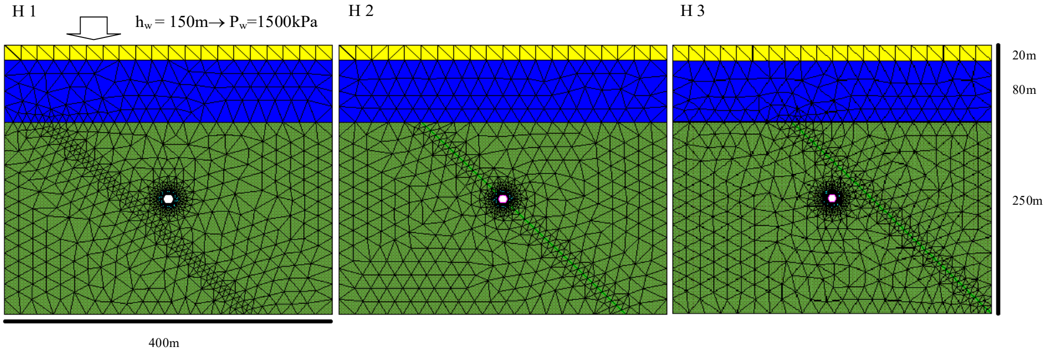

Figure 13. Hydraulic simple model condition Tunnel H1, H2, H3

2.4. Comparison of numerical analysis and theoretical results for the simple tunnel HB model

The tunnel HB model is a single-layer homogeneous isotropic model. With this model, the numerical analysis result and the theoretical formula result of the same condition were compared.

In Figure 14, it can be seen that theoretical results and numerical analysis under N.3, boundary conditions that applied water pressure to only three sides, excluding the bottom side (Table 8), fit well.

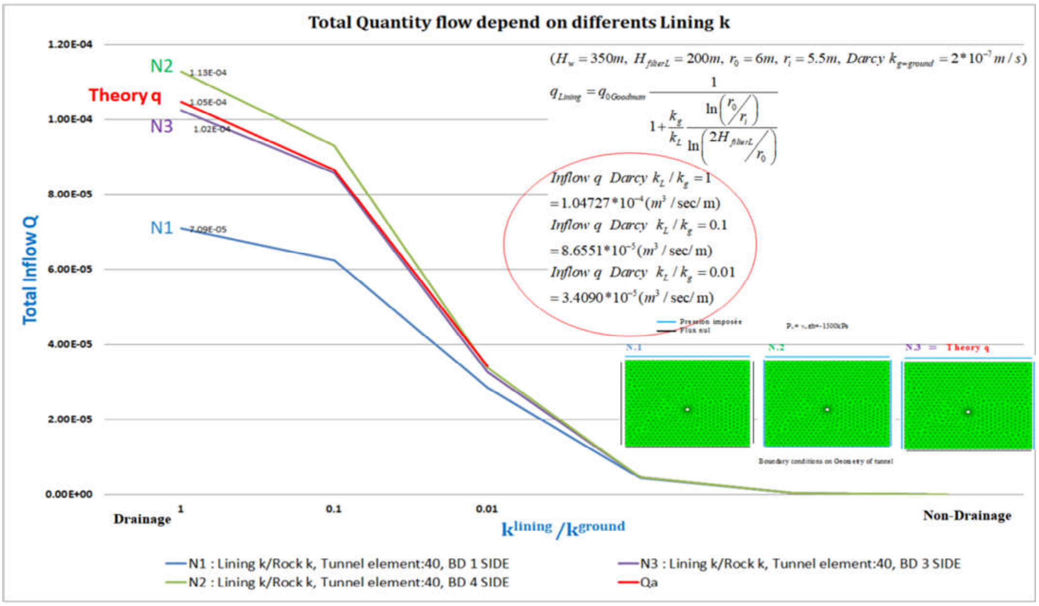

Figure 14. Comparison of total Quantity flow according to lining conditions of N1, N2, and N3

In the case of N3, which is the most suitable condition for comparison with the theoretical value, the difference between the numerical analysis result and the theoretical value is as follows (Table 10).

$$\frac{q^0_{N3} - q^0_{(Goodman's)}}{q^0_{(Goodman's)}} = 2 \sim 3\%$$

Therefore, this seems to be affected by the selection of the surrounding ground size/tunnel size ratio during numerical analysis. Therefore, it would be necessary to select appropriate boundary conditions to apply to the theoretical formula and numerical analysis.

Under the assumption of isotropic and homogeneous ground, the N3 boundary condition was suitable for comparing the theoretical value and the numerical analysis *q-flow* result. However, it cannot be concluded that these results are the cases we may face in actual construction. Because the theoretical formula (ex Goodman's) we used is generally more overestimated than the actual value, it's good to simply evaluate it before construction.

Table 10. Error value between the numerical value of the Q flow analysis and the theoretical value.

Hypothese		Numerical analysis q flow result (m^3/sec/m)	Numerical Analysis and Goodman's Equation Error $\frac{q_N - q_L}{q_L}$
Lining k_l/Rock k_R ($C_t=k_l*e$, $C_n=k_l/e$, $P_{inside}=0$, $e=0.5m$)			
N.2	1	1.13E-04	7.90%
	0.1	9.30E-05	7.45%
	0.01	3.38E-05	-0.85%
N.3	1	1.02E-04	-2.60%
	0.1	8.58E-05	-0.87%
	0.01	3.27E-05	-4.08%

2.5. Tunnel analysis in which faults are added

Tunnel modelling with a fault is shown in Figures 12 and 13, depending on the fault location.

If we focus on Tunnel HBF1 and Tunnel HBF2 (Figure 12), we can see that Tunnel HBF1 simulates passing through the lower part of the tunnel, and Tunnel HBF 2 passes through the centre of the tunnel.

Looking at the case where the fault line is in contact with the tunnel boundary (Tunnel HBF2), there are two kinds of modelling where the fault line is in contact with the lining boundary (Figure15 b), or there is a space between the lining boundaries (Figure 15a).

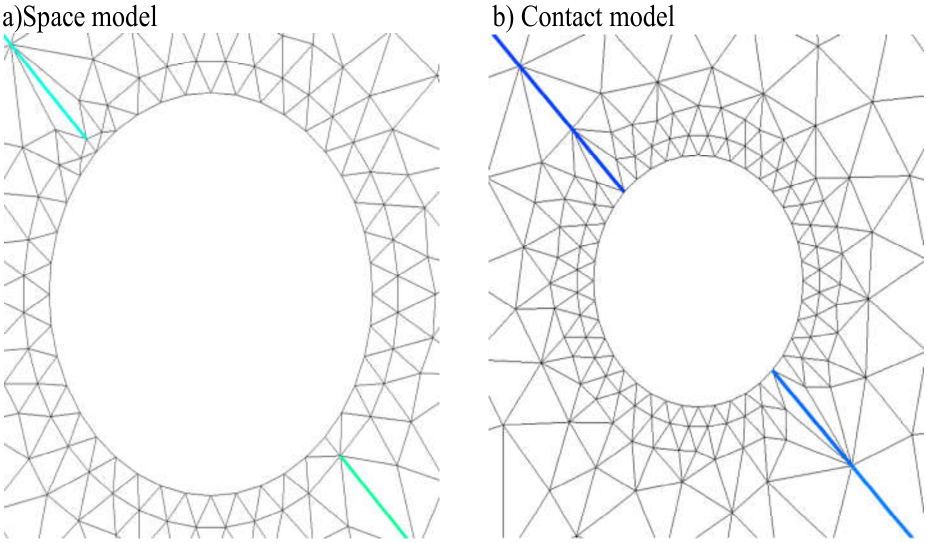

Figure 15. Contact of the location of the fault line and lining line.

The difference when calculating the two models is that the space model can calculate the Q flow in the tunnel with only the elements of the lining line.

(The parameters C_t, C_n of the Beam element are described in detail in chapter 2.2.)

$$
\begin{aligned}
Q_a &= \int \underline{v}\underline{n}\, ds + \sum q_{joint} \\
q_{joint} &= -C_t \nabla p \\
C_t &= k_{joint} e_{joint}
\end{aligned}
\tag{32}
$$

However, the contact model must calculate the Q flow coming from the end of the fault line in contact with the tunnel and add it to the Q flow flowing through the lining, as shown in the equation below. Figure 16 shows the Q flow in the tunnel according to the orientation of the circular tunnel. The Q flow of all tunnels is greatest in the part where the shortest distance to the fault is close. And looking at the tunnels HBF1 and HBF2, a larger inflow was found as the depth of the ground was deeper due to water pressure gravity. (Figure 16-a, b, c, d)

Looking at Tunnel HBF2 in Figure 16, the largest Q inflow is seen in the two parts, where the fault contacts the tunnel boundary. However, the flow rate values of the lower and upper parts are not the same, and the lower part is seen to be larger. This is due to the difference in water pressure depending on the height, as mentioned above.

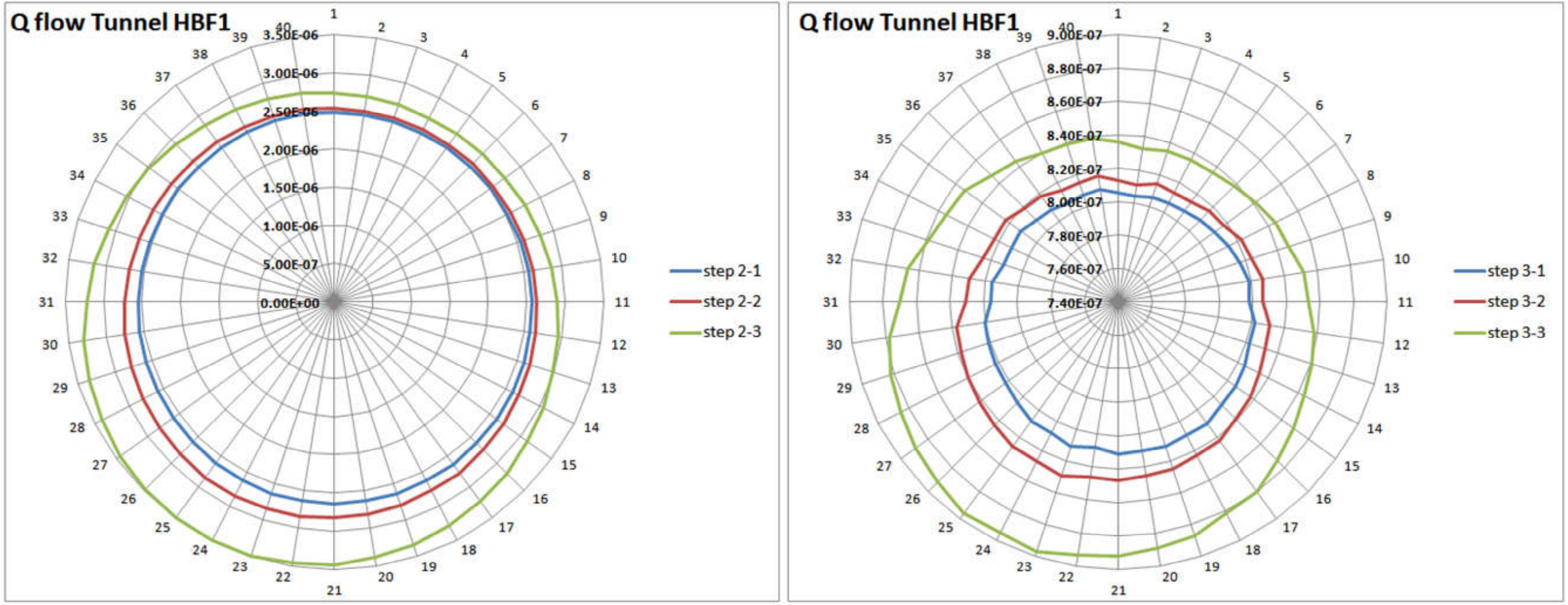

a) Free drainge (Q flow m^3/sec/m)

b) Lining effect active (Q flow m^3/sec/m)

Figure 16. Q flow according to tunnel orientation

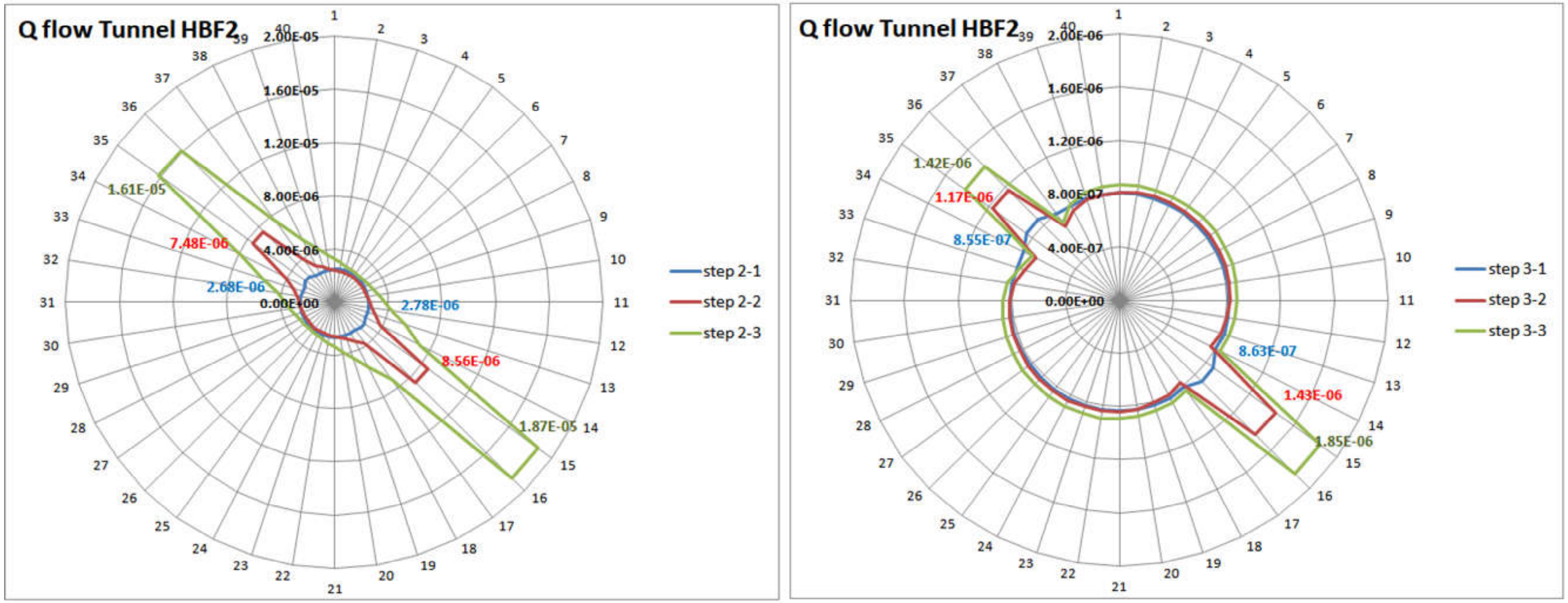

c) Free drainge (Q flow m^3/sec/m)

d) Lining effect active (Q flow m^3/sec/m)

Figure 16. Q flow according to tunnel orientation

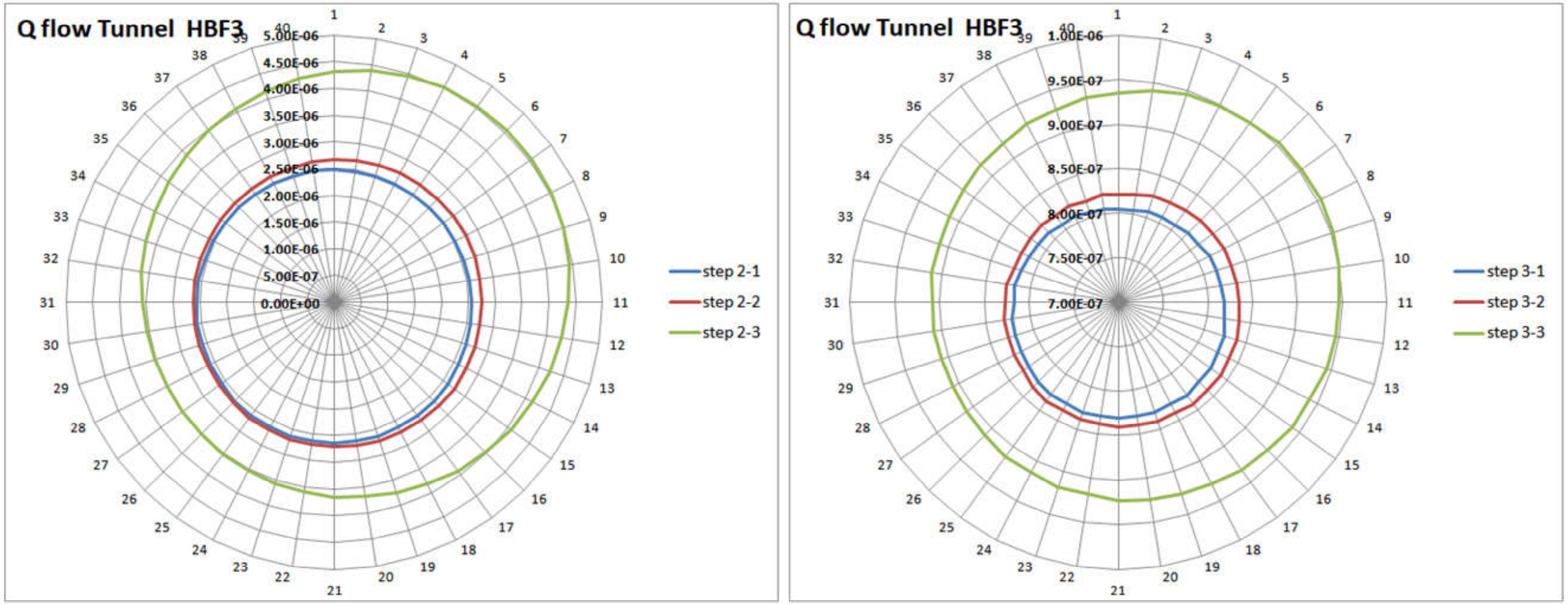

e) Free drainge (Q flow $m^3/sec/m$) **f) Lining effect active (Q flow $m^3/sec/m$)**

Figure 16. Q flow according to tunnel orientation

These problems should be solved as coupling (Mechanics + Hydraulic) problems. This is because, in the tunnel construction process, displacement (M) and hydraulic pressure (H) often interact as cause and effect, and low hydraulic pressure is often accompanied by an increase in displacement (Shu-cai Li., 2016). But first, in our study, the groundwater was analyzed by separating the basic non-coupled processes (Next step H+M modelling shown in Chapter 5). This will help to better understand tunnel behavior and prepare to model the coupled processes.

LIST OF NOTATIONS (CH 3)

Symbol	**Definition**
C	Compressibility ratio
c	Cohesion c
$\tilde{c}$	Cohesion transformed
E	Young's modulus
$E\,\mathrm{g}$	Young's modulus of ground
E^L	Elastic modulus of lining
E_b	Young’s modulus of the beam material (ex; concrete)
ε^g ,ε^L	Elongation strain of ground and strain of lining
F	Flexibility ratio
θ	Referenced central angle of lining
K_0	Earth pressure coefficient
K_n, K_t	Normal and tangent stiffness between lining and ground
μ	Shear modulus of elasticity
M	Bending moment of lining
N	Axial force of lining
V	Tangent of lining
ν	Poisson’s ratio of ground
ν_b	Poisson ratio of the beam material (ex; concrete)
σ_v, σ_h	Vertical and horizontal stress
$\sigma_r, \sigma_\theta, \tau_{r\theta}$	Radial, tangential stresses and shear stress by the Airy function
$\sigma_{rr}, \sigma_{\theta\theta}, \sigma_{r\theta}$	Radial, tangential stresses and shear stress in general solution
$\tilde{\sigma}_{rr}$, $\tilde{\sigma}_{r\theta}$	Transformed radial, shear stress in general solution
S	Area of lining section (segment)
s (ds)	Circumferential direction lying on the curvilinear middle plane of the beam.
U_r, U_θ	Radial, tangential displacements by Airy function
u_r, u_θ	Radial, tangent displacements in general solution
u_r^g, u_θ^g	Radial, tangent displacements of ground
u_r^L, u_θ^L	Radial, tangent displacements of lining
ϕ	Airy function
φ	Friction angle
$\tilde{\varphi}$	Friction angle transformed
ω^g, ω^L	Elongation rotation of ground and lining
r	Radial distance
R	Radius of the curvilinear tunnel hole

f_n , f_t	Normal force and tangent force

3. Mechanical modelling of continuous support-lining

In this part, it is preparing to publish a journal article.

3.1. Theoretical background

This chapter focuses on ground-lining interaction in tunnel modelling by investigating analytical solutions and introducing a contact interface between the lining and the ground. Analytical solutions are attractive because they make a possibly quick estimation of lining member forces. They can provide reference values for lining analysis even if they generally do not cover all the complexity of real structures and need to be completed by numerical methods (Marwan *et al.*, 2021). They can also serve as validation references for numerical methods (Guan *et al.*, 2015).

The distribution of thrust and bending moment in the lining of a circular tunnel, modelled as an elastic shell, started to be considered by Voellmy (1937), Engelberth (1957), and Morgan (1961), who assumed a priori that the circular lining deforms into an elliptical mode. In this way, the tangent stresses and corresponding deformations are omitted (Duddeck and Erdmann 1985). In the English-speaking world of tunnel design, the most commonly used and cited solution is that proposed by Curtis (1976). But according to Duddeck and Erdmann (1985) and Asche, Ireland (2013), the same solutions were achieved independently by the Norwegian and German authors Duddeck and Erdmann (1985).

Muir Wood (1975) established a corrected version of Morgan's more intuitive approach by taking into account tangential ground stresses and also the effect of fluid pressure in an approximate way. But the effects of tangential ground stresses on radial deformations were still omitted. They were included in the more complete Curtis's (1976) solution. A more advanced approach, including the plane deformability of the shell (longitudinal deformability of the beam in 2D), was proposed by Einstein & Schwartz (1979). The interaction between the ground and the lining needed still more investigation because, in all these works, it remained restricted to the two extreme cases of perfect bonding between the ground and lining or of perfect slip (no shear stress) between them. However, the real ground/lining contact can be more complex and include elastic deformation and even non-linearity like plasticity and friction. For instance, the presence of grouting material or void-tail can make the gap between the ground and the lining closed (example: closed-TBM) and is a very common situation in the lining design which cannot be modelled by the two extreme cases of perfect bonding or perfect slip.

The solution for an elastic contact between the lining and the ground introduced in this paper attempts to improve the existing solutions by deriving a closed-form solution for member forces in the lining for an elastic ground-lining contact. We will first see the governing equations of the problem, including the circular beam deformation theory, the elastic interface model, the ground constitutive model, and the equilibrium conditions. Then, a set of Airy functions providing basic potential solutions for the stress and displacement in the ground are presented and their parameters are identified to build the final solution for different cases.

M.J.Pender (1980) investigated the lining displacements under two different loading conditions, which are called, in the sequel, the *shell inclusion* (Case 1) and *tunnel excavation* (Case 2). In the former, the hole exists in the infinite medium at zero stress, and then the far-field stress is applied. This case is called active load. The latter case corresponds to the classical tunnel excavation problem in which the hole is excavated in a pre-stressed medium, and it is called passive load. The elastic interaction between the lining and the ground is carefully analysed for these two cases in the following.

The new analytical solutions obtained in this paper are then discussed and compared to the solutions existing in the literature. They are also compared to numerical solutions obtained by the FEA code Disroc (Fracsima, 2016), which includes adequate shell lining elements with elastic contact with the ground.

The closed-form solution of tunnel behaviour can be obtained from the theoretical model that simplified and idealized the tunnel condition. Besides, the theoretical solution is useful for gaining engineering intuition about the tunnel behaviour. Simple and ideal assumptions for theoretical analysis are, for example, homogeneous ground, isotropic or orthogonal loads, and the assumptions of (axis) symmetric geometrically circular cross-sections. The analytical solutions for tunnels normally rely on 2D plan strain conditions and circular tunnel cross-sections. In this part, the tunnel stress theory of elasticity is showed and then theoretical methods of lining member force, as usually known researched, is presented. Finally, we would like to introduce a new theoretical method by regarding the interrelationship between the ground and lining.

In general, there may be two mentioned load methods in lining behaviour analysis by loading modes imposed by surrounding ground of tunnel. i.e. active loading mode and passive- loading model.

1) Active loading model means that the surrounding ground applies the earth/water pressures to the lining structure actively, which are calculated by theoretical or empirical formulas.

2) Passive-loading mode is that the ground-lining interaction with the earth/water pressures transferred by the excavation force to the lining is calculated.

3.2. General solution for stress and displacement around a circular tunnel

The general solution for the stress and displacement fields around a circular hole in an infinite plane and in plane strain conditions can be deduced from the Airy functions. The Airy function sufficiently general for the problem with finite stresses at infinite boundary can be considered in the following form:

$$\phi = A\ln r + Cr^2 + \left\{ Br^2 + Gr^{-2} + H \right\}\cos 2\theta \tag{33}$$

Where *A, C, B, G* and *H* are arbitrary constants. The stress and displacement solutions have the following expressions:

$$\begin{aligned}
\sigma_r &= \frac{1}{2}\frac{\partial\phi}{\partial r} + \frac{1}{r^2}\frac{\partial^2\phi}{\partial\theta^2} = 2C + \frac{A}{r^2} - (2B + \frac{6G}{r^4} + \frac{4H}{r^2})\cos 2\theta \\
\sigma_\theta &= \frac{\partial^2\phi}{\partial r^2} = 2C - \frac{A}{r^2} + (2B + \frac{6G}{r^4})\cos 2\theta \\
\tau_{r\theta} &= \frac{1}{r^2}\frac{\partial\phi}{\partial\theta} - \frac{1}{r}\frac{\partial^2\phi}{\partial r\partial\theta} = (2B - \frac{6G}{r^4} - \frac{2H}{r^2})\sin 2\theta
\end{aligned} \tag{34}$$

$$\frac{U_r}{R}=\frac{1+v}{E}\left[2C(1-2v)-\frac{A}{r^2}-\left\{2B-\frac{2G}{r^4}-(1-\mathrm{v})\frac{4H}{r^2}\right\}\cos 2\theta\right] \tag{35}$$

$$\frac{U_\theta}{R}=\frac{1+v}{E}\left[\left\{2B+\frac{2G}{r^4}-2(1-2\,\mathrm{v})\frac{H}{r^2}\right\}\sin 2\theta\right]$$

It is more convenient for the present problem to define, instead of *A, C, B, G* and *H,* 5 dimensionless parameters a_s, a_D, a_1, a_2, a_3 related to them in the following way:

$$A=-2\mu a_1R^2,\quad C=\mu a_s,\quad B=\mu a_D,\quad G=\mu a_2R^4,\quad H=\mu a_3R2$$

The two parameters a_s, a_D are determined directly from the isotropic and deviatory part of the stress at the infinite boundary. If the vertical and horizontal stresses are denoted by σ_v and σ_h respectively, then:

$$a_s=\frac{\sigma_v+\sigma_h}{4\mu}\ ,\qquad a_D=\frac{\sigma_v-\sigma_h}{4\mu} \tag{36}$$

The coefficients a_1, a_2, a_3 are determined from the conditions at the borehole wall (*r=R*). The general solution of the stress and displacement at the borehole wall (*r=R*) takes the following form:

$$\begin{aligned}\sigma_{rr}(R,\theta)&=2\mu\left(a_s-a_1\right)-2\mu\left(a_D+3a_2+2a_3\right)\cos 2\theta\\ \sigma_{\theta\theta}(R,\theta)&=2\mu\left(a_s+a_1\right)+2\mu\left(a_D+3a_2\right)\cos 2\theta\\ \sigma_{r\theta}(R,\theta)&=2\mu\left[a_D-3a_2-a_3\right]\sin 2\theta\end{aligned} \tag{37}$$

$$\begin{aligned}\frac{u_r(R,\theta)}{R}&=a_s(1-2\nu)+a_1+\left[-a_D+a_2+2a_3(1-\nu)\right]\cos 2\theta\\ \frac{u_\theta(R,\theta)}{R}&=\left[a_D+a_2-a_3(1-2\nu)\right]\sin 2\theta\end{aligned} \tag{38}$$

It is able to be noticed that, for a tunnel with free wall i.e., $\sigma_{rr}=0$, $\sigma_{r\theta}=0$ at *r=R,* the above equations provide :

$$a_1=a_s\ ,\quad a_2=a_D\ ,\quad a_3=-2a_D \tag{39}$$

And the Kirsch solution for the stress field around circular tunnels is recovered in this way (Kirsch, 1898; Li and Wang, 2008; Vitali, Celestino and Bobet, 2018).

Let us note that two different cases of problems can be considered for the displacement field solution.

The displacement given by (38) corresponds to the case in which the hole exists in the infinite medium at zero stress and then the far-field stress (σ_h, σ_v) is applied. This problem is different from the classical tunnel excavation problem in a pre-stressed medium. The solution (38) can be applied to different cases of problems, for instance, to the problem of a circular inclusion in an infinite matrix considered for heterogeneous materials. The solution given by (38) is called the "Inclusion" solution. The "Inclusion" type solution can be used also when circular pipelines are placed in the ground and then a vertical load is applied on the soil or when the ground stress changes around an existing tunnel due to, for instance, digging the layers above the tunnel. The displacements induced by these changes in the far-field stress must be calculated from the "Inclusion" solution.

For a tunnel excavated in a ground with the initial stresses σ_h, σ_v and the displacement at the tunnel wall due to the excavation is related to the changes in the ground stress field as the excavation force or the difference between the stresses after and before excavation. This means that the displacement must be removed from the above solution because of the uniform stress (σ_h, σ_v) existing in the ground before excavation. This displacement is the part which does not tend to zero when $r \to \infty$ in (35). The consequence for (38) consists in removing $a_s(1-2\nu)-a_D\cos 2\theta$ in u_r/R and $a_D\sin 2\theta$ in $u\theta/R$ n this equation and we call this displacement solution the "Tunnel Excavation" solution.

In the two cases, the parameters a_1, a_2, a_3 have to be determined from the conditions at the wall of the borehole, which can include the existence of a lining.

To unify the equations for the two cases, we note $u^g(\theta)$ the displacement at $r=R$ in the ground(rock) formation, to be distinguished from the displacement in the lining which will be introduced farther and denoted by $u^L(\theta)$. Then, starting from (38), we write the solution for the two cases in the following form:

$$\frac{u_r^g(\theta)}{R} = \beta_s a_s + a_1 + \left[-\beta_D + a_2 + 2a_3(1-\nu)\right]\cos 2\theta \tag{40}$$

$$\frac{u_\theta^g(\theta)}{R} = \left[\beta_D a_D + a_2 - a_3(1-2\nu)\right]\sin 2\theta$$

With:

I) “Shell Inclusion” solution: $\beta_S = 1\text{-}2\nu$ $\beta_D = 1$
II) “Tunnel Excavation” solution: $\beta_S = 0$, $\beta_D = 0$

To solve the problem in the presence of a lining and to determine the parameters a_1, a_2, a_3 for this case, we have to introduce the equations governing the mechanical behavior of the lining and of the contact between the lining and the tunnel (ground).

3.3. Circular beam governing equations

The lining is modelled as a circular beam undergoing the forces *f* resulting from its interaction with the ground (rock) and the displacements designated by u^L. The general theory of curved beams (TIMOSHENKO, S., 1970; Reddy, Wang and Lee, 1997; SALENCON, 2012) establishes the following relations for the momentum and forces balance of the beams:

$$\frac{dN}{ds}-\frac{V}{R}+f_t=0, \qquad \frac{dV}{ds}+\frac{N}{R}+f_n=0, \qquad \frac{dM}{ds}+V+m=0 \tag{41}$$

Where s designates the curvilinear abscissa and *R* the curvature radius of the beam, (f_n , f_t) the normal and tangent components of the force applied to the unit surface and (N, V, M) the axial and tangent force and the bending moment respectively.

The same type of equations has been used for curved beam modeled as Winkler type elastic media (Huang et al., 2021). Almost all the works on the tunnel lining modelling, staring from the early works of Morgan (1961) up to the more recent works of Shi et al. (2018) and Huang et al., (2021) have considered the Euler beam theory for deformations of the curved beam.

In this theory, member forces *N* and *M* are related to elastic deformations by:

$$N = E^L S\,\varepsilon^L, \qquad M = E^L I\frac{d\omega^L}{ds} \tag{42}$$

In these equations, the elongation strain ε^L and the rotation ω^L are related to the normal and tangent displacements by:

$$\varepsilon^L = \frac{du_t^L}{ds}-\frac{u_n^L}{R}, \qquad \frac{d\omega^L}{ds}=\frac{d^2u_n^L}{ds^2}+\frac{1}{R}\frac{du_t^L}{ds} \tag{43}$$

For a lining in a circular tunnel, we take the following notations (see Figure 17):

$$\underline{n} = -\underline{e}_r\,, \qquad \underline{t} = \underline{e}_\theta\,, \qquad u_n^L = -u_r^L\,, \qquad u_t^L = u_\theta^L\,, \qquad ds = Rd\theta \tag{44}$$

The E^L represents the Young's modulus of the beam. However, note that under plane strain conditions for the tunnel liner, it is more appropriate to take, following H. Einstein and C. W. Schwartz (1979), the liner parameter E^L as:

$$E^L = \frac{E_b}{1-\nu_b^2} \tag{45}$$

(E_b and ν_b are the Young's modulus and the Poisson ratio of the beam material generally concrete for tunnels.)

The stress vector continuity subsists even in the presence of contact interface between the lining and the ground. The force $\underline{f}$ applied on the lining is the opposite of the external force $\underline{\sigma} = \boldsymbol{\sigma}.\underline{n}$ applied on the tunnel wall, and so:

$$\underline{f} = -\boldsymbol{\sigma}.\underline{n}, \qquad f_n = \underline{f}.\underline{n} = -\sigma_{rr}\,, \qquad f_t = \underline{f}.\underline{t} = \sigma_{r\theta} \tag{46}$$

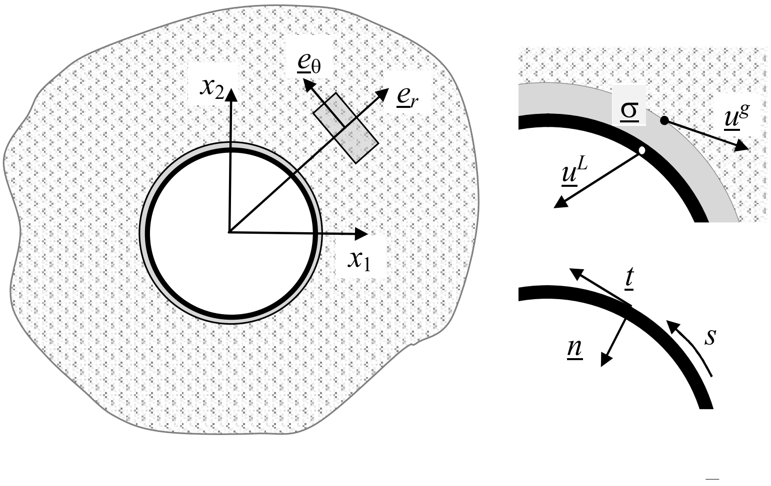

Figure 17. Elastic contact between a circular beam and the ground

And since the curvature R is constant in (43), we can write:

$$M = E^L I \frac{d\omega'^L}{ds}, \qquad \omega'^L = -\frac{du_r^L}{Rd\theta} + \frac{u_\theta^L}{R} \tag{47}$$

Now, by elimination of *V* in equations (41) and replacing in it by (46) for $\underline{f}$, we obtain:

$$\frac{d^2N}{Rd\theta^2}+\frac{N}{R}-\sigma_{rr}+\frac{\partial\sigma_{r\theta}}{\partial\theta}=0, \qquad \frac{dM}{R^2d\theta}+\frac{dN}{Rd\theta}+\sigma_{r\theta}=0 \tag{48}$$

By replacing for *N* and *M* from (43) and (47), introducing the auxiliary parameters:

$$k_s^L=\frac{E^LS}{2\mu R}, \qquad k_D^L=\frac{E^LI}{2\mu R^3} \tag{49}$$

Where μ designates the ground shear modulus, we obtain the following equations:

$$k_s^L\left(1+\frac{d^2}{d\theta^2}\right)\varepsilon^L-\frac{\sigma_{rr}}{2\mu}+\frac{1}{2\mu}\frac{\partial\sigma_{r\theta}}{\partial\theta}=0 \tag{50}$$

$$k_D^L\frac{d^2\omega'^L}{d\theta^2}+k_s^L\frac{d\varepsilon^L}{d\theta}+\frac{1}{2\mu}\sigma_{r\theta}=0 \tag{51}$$

We described the equations above in details in order to be capable of explaining the differences between our results and previous works. Morgan (1961) pioneer analysis has been at the basis of the works of Muir Wood (1975) and Curtis (1976), which followed it. Morgan deduced the maximum bending moment in the lining from the change in the curvature of circular beam which becomes an ellipse after deformation. He used the following relation in which *R* is the radius of the circular beam and R_1 the small diameter of the ellipse:

$$\varepsilon^L=\frac{u_r^L}{R}, \qquad \frac{d\omega^L}{ds}=\frac{1}{R_1}-\frac{1}{R}=-\frac{d^2u_r^L}{R^2d\theta^2} \tag{52}$$

Comparing these equations with Eq.(43), we note that du_t/ds is missing in Morgan's equations. Muir Wood (1975) used the same equations and, with Morgan (1961), assumed that only normal pressure could be transmitted through the interface between the lining and the ground. As the result, tangential stress and the corresponding deformation are omitted in these works. In addition, this approach underestimates the bending moment as it can be seen farther in this part. The approach was improved in Curtis (1976) work which included the axial deformations due to tangential stresses. However, Curtis (1976) considered only the two extreme cases of *full bond*ing between the lining and the tunnel and of *perfect slip*. Although this work improved the

Muir Wood's solution, it omits some interactions, which make it possible to underestimate the radial displacements as it will be shown farther in this part. Einstein & Schwartz (1979) took into account a compressibility ratio between the liner and the ground, which was supposed to be infinite in Curtis (1976). This lets the Einstein & Schwartz (1979) approach the closest to ours. But their solutions are correct only for the case of perfect slip and infinite compressibility ratio as it will be seen farther in this section.

The intermediate cases of the contact between the lining and the tunnel in which the interaction force depends on the relative displacement between the lining and the ground were not considered in previous works. To extend the modelling to these cases, first, the *Elastic Contact* model is introduced in the following section.

3.4. Elastic contact model for ground-liner interface

In the elastic interface model, the interaction force between the two faces depends on the relative displacement. With the notations of the Figure 17, the general relationship equation for the elastic contact is the following:

$$\begin{aligned} \sigma_{rr} &= K_n\left(u_r^g - u_r^L\right) \\ \sigma_{r\theta} &= K_t\left(u_\theta^g - u_\theta^L\right) \end{aligned} \tag{53}$$

K_n and K_t are the normal and tangent contact stiffness. Determination of K_n and K_t for real cases is a challenging problem. Assimilation of the contact surface to a thin layer of highly deformable elastic material generally can obtain some estimates for the stiffness parameters K_n and K_t. Let us notice that the contact model between the lining and the ground is generally highly non-linear and the unilateral contact condition can also have great effects. The contact properties depend on the roughness of the contact surface between the lining and the ground and can be different at the different points of the wall around the tunnel. Therefore, the model presented by (53) contains the great simplifications as elastic module. However, if analytical solutions are sought, this simplified model makes it possible to go further than previous works.

The two extremes cases considered in previous works are the following special or limit cases of this model (Figure 18):

Perfect bonding: the limit case of $K_n \to \infty$ and $K_t \to \infty$

$u_r^L = u_r^g, \quad u_\theta^L = u_\theta^g$

Prefect sliding: the limit case $K_n \to \infty$ and $K_t \to 0$ which implies $\sigma_{r\theta} = 0$

$u_r^L \neq u_r^g, \quad u_\theta^L \neq u_\theta^g$

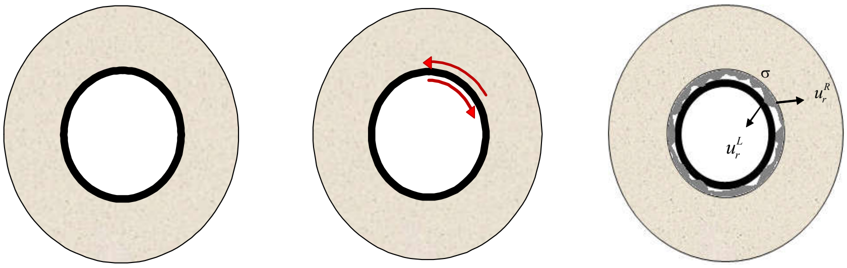

Perfect Bonding	*Perfect Sliding*	*Elastic Contact*
$u_r^L = u_r^g, \quad u_\theta^L = u_\theta^g$	$\sigma_{r\theta} = 0$ $(u_r^L \neq u_r^g, \quad u_\theta^L \neq u_\theta^g)$	$\sigma_{rr} = K_n\left(u_r^g - u_r^L\right)$ $\sigma_{r\theta} = K_t\left(u_\theta^g - u_\theta^L\right)$

Figure 18. Interface between the boundary of the tunnel lining and the ground

3.5. Solutions for different cases

3.5.1. Interaction with the ground

To solve the system of equations described here-above, we express all the variables in the equilibrium equation (50) of the lining function of the variables and parameters of the general solution (37) and (40). To do this, it is useful to define first two auxiliary variables ε^g and ω'^g from the ground (rock) displacement in the same way that ε^L and ω'^L for the lining:

$$\varepsilon^g = \frac{u_r^g}{R} + \frac{d}{d\theta}\frac{u_\theta^g}{R}, \qquad \omega'^g = -\frac{d}{d\theta}\frac{u_r^g}{R} + \frac{u_\theta^g}{R} \tag{54}$$

The expression of these variables can be deduced from (40):

$$\varepsilon^g = \frac{u_r^g}{R} + \frac{d}{d\theta}\frac{u_\theta^g}{R} = \beta_s a_s + a_1 + \left(\beta_D a_D + 3a_2 + 2\nu a_3\right)\cos 2\theta \tag{55}$$

$$\omega'^g = -\frac{d}{d\theta}\frac{u_r^g}{R} + \frac{u_\theta^g}{R} = \left[-\beta_D a_D + 3a_2 + a_3(3-2\nu)\right]\sin 2\theta \tag{56}$$

Then, the combination of (43), (47), (53) and (54) provided:

$$\varepsilon^L = \varepsilon^g - \frac{\sigma_{rr}}{RK_n} - \frac{1}{RK_t}\frac{d\sigma_{r\theta}}{d\theta}, \qquad \omega'^L = \omega'^g + \frac{1}{RK_n}\frac{d\sigma_{rr}}{d\theta} - \frac{\sigma_{r\theta}}{RK_t} \tag{57}$$

With the notation:

$$\kappa_n = \frac{2\mu}{RK_n}, \quad \kappa_t = \frac{2\mu}{RK_t} \tag{58}$$

We found:

$$\varepsilon^L = \begin{bmatrix} (\beta_s - \kappa_n)a_s + (1+\kappa_n)a_1 \\ +\left[(\beta_D + \kappa_n - 2\kappa_t)a_D + (3+3\kappa_n+6\kappa_t)a_2 + (2\nu + 2\kappa_n + 2\kappa_t)a_3\right]\cos 2\theta \end{bmatrix} \tag{59}$$

$$\omega'^L = \left[(-\beta_D + 2\kappa_n - \kappa_t)a_D + (3+6\kappa_n+3\kappa_t)a_2 + (3-2\nu+4\kappa_n+\kappa_t)a_3\right]\sin 2\theta \tag{60}$$

And so, for the bending moment and axial force deduced from (43) and (47) we obtain:

$$M = 2\frac{E^L I}{R}\left[(-\beta_D + 2\kappa_n - \kappa_t)a_D + (3+6\kappa_n+3\kappa_t)a_2 + (3-2\nu+4\kappa_n+\kappa_t)a_3\right]\cos 2\theta \tag{61}$$

$$\begin{aligned} N &= N_s + N_D \cos 2\theta \\ N_s &= E^L S\left[(\beta_s - \kappa_n)a_s + (1+\kappa_n)a_1\right] \\ N_D &= E^L S\left[(\beta_D + \kappa_n - 2\kappa_t)a_D + (3+3\kappa_n+6\kappa_t)a_2 + (2\nu+2\kappa_n+2\kappa_t)a_3\right] \end{aligned} \tag{62}$$

And, from (53) we deduce:

$$\begin{aligned} \frac{u_r^L(\theta)}{R} &= \beta_s a_s + a_1 - \kappa_n(a_s - a_1) + \left[-\beta_D a_D + a_2 + 2a_3(1-\nu) + \kappa_n(a_D + 3a_2 + 2a_3)\right]\cos 2 \\ \frac{u_\theta^L(\theta)}{R} &= \left[\beta_D a_D + a_2 - a_3(1-2\nu) - \kappa_t(a_D - 3a_2 - a_3)\right]\sin 2\theta \end{aligned} \tag{63}$$

The solutions must be calculated separately for the general case and the two limit cases defined in Figure 18. For each case, the two subcases of “shell inclusion” and “tunnel excavation” defined here-above can be considered.

3.5.2. General Case Solution

By replacing for ε^L in (51) from (59), we obtain an expression $J + Q\cos 2\theta = 0$ which should be true for every θ, so this provides two equations *J=0* and *Q=0* for the three unknown parameters a_1, a_2 and a_3. Then by substituting for ω'^L in (51) from (60) we obtain an expression $T\sin 2\theta = 0$ which provides a third equation *T=0* for these parameters. It can be noted also that only a_1 is involved in the first equation *J= 0* which provides:

$$a_1 = \frac{1 - k_s^L\left(\beta_s - \kappa_n\right)}{1 + k_s^L\left(1 + \kappa_n\right)} a_s \tag{64}$$

And the two equations *Q*=0 and *T*=0 involve the two parameters unknown a_2, and a_3 in the following form:

$$\begin{aligned} m_1 a_2 + m_2 a_3 &= m_3 a_D \\ m_4 a_2 + m_5 a_3 &= m_6 a_D \end{aligned} \tag{65}$$

Where:

$$\begin{aligned} &m_1 = 1 + 3k_s^L\left(1 + \kappa_n + 2\kappa_t\right),\ \ m_2 = 2k_s^L\left(\nu + \kappa_n + \kappa_t\right), \\ &m_3 = 1 - k_s^L\left(\beta_D + \kappa_n - 2\kappa_t\right),\ \ m_4 = 1 + 12k_D^L\left(1 + 2\kappa_n + \kappa_t\right), \\ &m_5 = 1 + 4k_D^L(3 - 2\nu + 4\kappa_n + \kappa_t),\ \ m_6 = -1 + 4k_D^L\left(\beta_D - 2\kappa_n + \kappa_t\right) \end{aligned} \tag{66}$$

And so the solution reads:

$$a_2 = \frac{m_3 m_5 - m_2 m_6}{m_1 m_5 - m_2 m_4} a_D\ , \qquad a_3 = \frac{m_1 m_6 - m_3 m_4}{m_1 m_5 - m_2 m_4} a_D \tag{67}$$

Now we can check several special cases of these equations with their physical meaning which recover previous studied cases. First, if the lining stiffness is zero, the condition of stress-free tunnel wall and the Kirsch solution must be recovered. As a matter of fact, if we put $k_s^L = k_D^L = 0$ the equations (64) to (66), it provides (39). We could also consider the case of zero stiffness of the contact between the lining and the ground. In this case, the lining is non-existent and so the stress in the ground must be the same for the free wall or the Kirsch solution. However, this case cannot be obtained as special case of the solution (64) -(66) because these equations are based on the lining displacement (equations (51), (59), (60)), which remains undetermined when there is no contact between the ground and the lining. Note that the equations (64) to (64) become degenerate for $\kappa_n \to \infty$, $\kappa_t \to \infty$. Also, the problem for perfect slip must be solved separately as it will be seen in the sequel. The physical parameters applied in our study are described in Table 11.

Table 11. Applied proprieties parameters for Ground and Lining in the study

	Shell inclusion	*Tunnel Excavation*
R (m)	6	
E^g (kPa)	8.5E+5	
v (Poisson)	0.35	
E^L (kPa)	3E+7	
$E^L I$ (kNm^2)	3.12E+5	
$E^L S$ (kN)	1.5E+7	
σ_v *(kPa)*	-1500	-5424
σ_h *(kPa)*	-795	-2929

3.5.3. Elastic slip

The above general solution dose not ensure that the radial displacement of the ground be less, in absolute value, than the liner radial displacement. So, in some cases, there can be overlapping of the ground and the liner ($u_r^g < u_r^L < 0$). Different treatments can be proposed for this problem. For instance, if it is supposed that the physical distance between the liner and the ground is about *e* but that the overlapping does not exceed *e*, the solution is acceptable. Another way would be to introduce unilateral contact between the ground and liner. But this case cannot be treated with analytical solutions. Another solution consists in taking $\kappa_n = 0$ which ensure $u_r^g = u_r^L$ and avoid overlapping. This assumption corresponds also to what has been considered in the literature for the solutions that will be discussed below. We call this intermediate case of $\kappa_n = 0$ but κ_t taking finite values the *elastic slip* case. We will see that all the solutions proposed in the literature are special cases of this case for witch $\kappa_t = 0$ or $\kappa_t = \infty$.

The general *elastic slip* solution is obtained by taking $\kappa_n = 0$ in (64) to (67), and so to take:

(67)

$$a_1 = \frac{1-k_s^L \beta_s}{1+k_s^L} a_s$$

(36)

a_2 and a_3 given by (67) with:

$$m_1 = 1 + 3k_s^L\left(1 + 2\kappa_t\right), \;\; m_2 = 2k_s^L\left(\nu + \kappa_t\right), \tag{68}$$
$$m_3 = 1 - k_s^L\left(\beta_D - 2\kappa_t\right), \;\; m_4 = 1 + 12k_D^L\left(1 + \kappa_t\right), \tag{37}$$
$$m_5 = 1 + 4k_D^L(3 - 2\nu + \kappa_t), \;\; m_6 = -1 + 4k_D^L\left(\beta_D + \kappa_t\right)$$

The results given by this solution will be compared with other analytical solutions as well as numerical solutions in the sequel.

3.5.4. Perfect-Bonding Solution

The equation (66) provides the solution for the case of perfect bonding by taking $\kappa_n = \kappa_t = 0$. We find:

$$a_1 = \frac{1 - k_s^L\beta_s}{1 + k_s^L} a_s \tag{69}$$
$$a_2 = \frac{(1 - \beta_D k_s^L)\left[1 + 4k_D^L(3 - 2\nu)\right] - (2vk_s^L)(-1 + 4\beta_D k_D^L)}{(1 + 3k_s^L)\left[1 + 4k_D^L(3 - 2\nu)\right] - (2vk_s^L)(1 + 12k_D^L)} a_D \tag{38}$$
$$a_3 = \frac{(1 + 3k_s^L)(-1 + 4\beta_D k_D^L) - (1 - \beta_D k_s^L)(1 + 12k_D^L)}{(1 + 3k_s^L)\left[1 + 4k_D^L(3 - 2\nu)\right] - (2vk_s^L)(1 + 12k_D^L)} a_D$$

The maximum value of the bending moment and the extreme values of axial force N in (61) and (62) are obtained for $\theta = 0$ and $\pi/2$ and by replacing in these equations from (69).

If the case of “Tunnel Excavation” ($\beta_s = 0$, $\beta_D = 0$) is considered, the maximum bending moment is found to be:

$$M_{Max} = 4\mu k_D^L R^2 \frac{(3 - 4\nu) + 3(3 - 4\nu)k_s^L}{1 + k_s^L\left(3 - 2\nu\right) + 4k_D^L\left(3 - 2\nu\right) + 12k_s^L k_D^L\left(3 - 4\nu\right)} a_D \tag{70}$$
$$M_{Max} = \frac{1 + 3k_s^L}{1 + k_s^L\left(3 - 2\nu\right) + 4k_D^L\left(3 - 2\nu\right) + 12k_s^L k_D^L\left(3 - 4\nu\right)} (3 - 4\nu) \frac{E^L I}{2\mu R}\left(\sigma_v - \sigma_h\right) \tag{39}$$

<u>Comparison with other solutions (Perfect bonding)</u>

The general perfect bonding solution (70) is different from what is found by Muir

Wood (1975) and Curtis (1976) and Einstein & Schwartz (1979) (see APPENDIX A.). To analyze the reason for the differences, let examine the assumptions and equations of previous works. The difference from Curtis is mainly due to the assumption of longitudinal compressibility of the liner, designated by $k^L{}_s$ in this paper, which was supposed infinite by Curtis. Einstein & Schwartz (1979) carried out a more advanced approach by considering finite compressibility of the liner. However, their solution is different from our solution in the general case. The comparison between their results and ours demands a deep investigation because they considered different equilibrium equations and used different dimensionless variables from ours. They start by more general Airy functions than (33) but after elimination of useless terms, it arrives finally to (33). They use two dimensionless variables called the compressibility and flexibility ratios which were also used later by (Einstein, H.H., Schwartz, 1979; Do *et al.*, 2014):

$$C=\frac{E^g R(1-\nu_b^2)}{E^b S(1-\nu^2)}, \qquad F=\frac{E^g R^3(1-\nu_b^2)}{E^b I(1-\nu^2)} \tag{71}$$

These ratios are related to our dimensionless parameters by the following relations:

$$C(1-\nu)=(k_s^L)^{-1} \qquad F(1-\nu)=(k_D^L)^{-1} \tag{72}$$

They used different stress-displacement relations for the beam deformation which, according to Flugge's shell model, read as follows(1966)(FLÜGGE, 1966; Einstein, H.H., Schwartz, 1979):

$$\frac{\partial u_\theta^g}{\partial\theta}+u_r^g+\frac{EI}{ESR^2}\left[\frac{\partial^4 u_r^g}{\partial\theta^4}+2\frac{\partial^2 u_r^g}{\partial\theta^2}+u_r^g\right]=\frac{(1-v^2)R^2}{ES}\sigma_{rr} \tag{73}$$

$$\frac{\partial^2 u_\theta^g}{\partial\theta^2}+\frac{\partial u_r^g}{\partial\theta}=-\frac{(1-v^2)R^2}{ES}\sigma_{r\theta} \tag{74}$$

If we replace (51) by the beam deformation equation (43) and (47) we obtain:

$$\frac{E^L I}{R^4}\left(-\frac{d^3u_r^L}{d\theta^3}+\frac{d^2u_\theta^L}{d\theta^2}\right)+\frac{E^L S}{R^2}\left(\frac{d^2u_\theta^L}{d\theta^2}+\frac{du_r^L}{d\theta}\right)+\sigma_{r\theta}=0 \tag{75}$$

This last equation must be compared to the (74) used by Einstein & Schwartz.

It can be noted that our equation (75) is a third rank differential equation on the displacement whereas (74) is a second rank. If in (75) the first term depending on I is removed, the two equations are exactly the same considering the definition (45) of E^L. So the equation (74) used by Einstein & Schwartz neglects the lining's moment of inertia when expressing the effect of shear stress $\sigma_{r\theta}$. Unfortunately, we could not access to Flugge's work cited by Einstein & Schwartz in order to determine the origin of the error. But if $\sigma_{r\theta}$ is null *(perfect slip)* and $k_s^L \to \infty$ ($C= 0$) then the same equations are obtained. So, Einstein & Schwartz solutions do not agree with our results for the general case of perfect bonding (Figure 19), but only for a special case of perfect slip which will be seen in the following section.

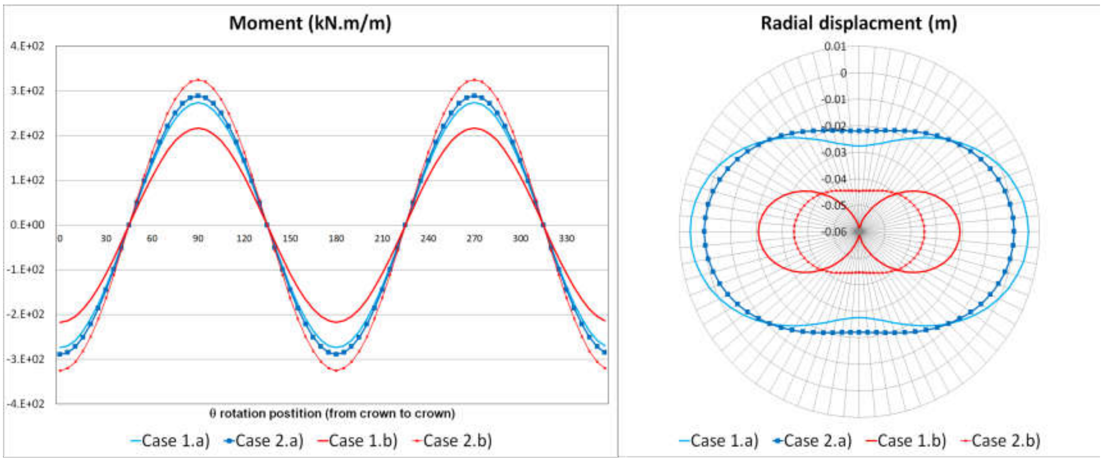

Figure 19. Comparison of bending moment and displacement between the new solution (NS) and Einstein & Schwartz (1979) (E&S) for perfect bonding with two assumptions compressibility ratio (k^L_s). →Infinite k^L_s: Case 1.a) NS, Case 2.a) E&S, Infinite k^L_s: Cas1 1.b) NS, Case 2.b) E&S)

However, for finite values of k^L_s, Einstein & Schwartz results are closer to our results than Curtis because this last work does not take into account finite k^L_s values (Figure 20).

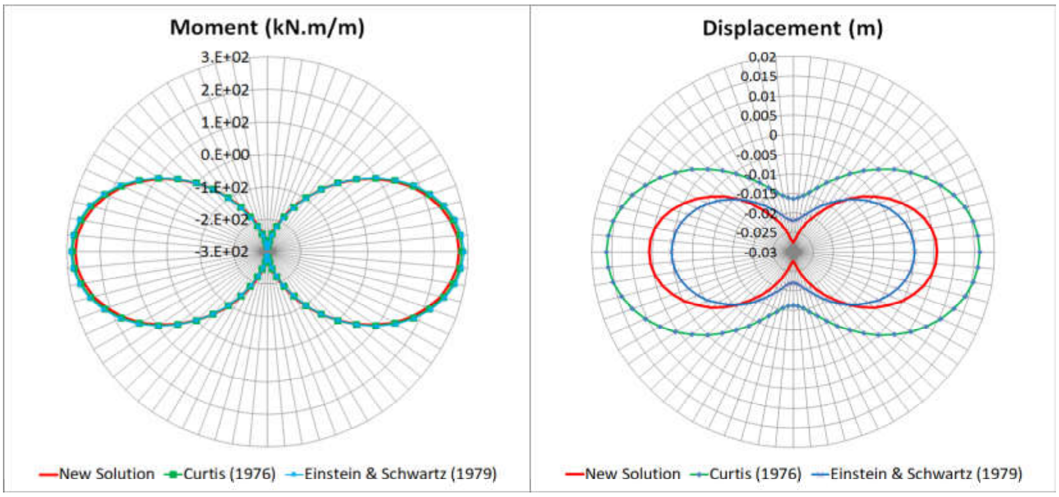

Figure 20. Comparison of Moment and radial displacement for the cases perfect bonding and finite $k^L{}_s$ of Curtis (1976), Einstein & Schwartz (1979) and our solution.

Now, if the limit case of incompressible liner ($k_s^L \to \infty$) is considered, Einstein & Schwartz's results remain different from ours because their basic equations have been different but the Curtis (1976) solution is exactly the same as ours solution base. To estimate the effect of this assumption, let take the limit of the bending moment (70) for $k_s^L \to \infty$.

It provides:

$$M_{Max}^{\infty} = \frac{12(3-4\nu)\mu\, k_D^L R^2}{\left(3-2\nu\right)+12k_D^L\left(3-4\nu\right)} a_D \tag{76}$$

If we replace $k^L{}_D$ and a_D from (49) and (36) with $\mu = E^g / 2(1+\nu)$ where E^g and the ground elastic parameters, we found exactly the Muir Wood (1975) & Curtis (1976) result which reads:

$$M_{Max} = \frac{(\sigma_v - \sigma_h)R^2}{4 + \dfrac{(3-2\nu)E^g R^3}{3(1+\nu)(3-4\nu)E^L I}} \tag{77}$$

The ratio $M_{Max} / M_{Max}^{\infty}$ calculated from the Eqs (70) and (76) to estimate the approximation is included in the Curtis (1976) formulae. If *e* designates the lining thickness, then for the unit length of the tunnel *S =e* and *I=e³/12*. Typically in tunnels, *e/R* is smaller than 1/10, so k_D^L can be neglected compared to k_s^L . Also, with *e/R<1*,

k_D^L will be negligible compared to 1 even if the lining Young's modulus is 10 times greater than the ground Young's modulus. So we can simplify the *Eq*. (70) in:

$$M_{Max}^{s} = 4\mu k_D^L R^2 \frac{1+3k_s^L}{1+k_s^L\left(3-2\nu\right)}(3-4\nu)a_D$$

And we find the ratio:

$$\frac{M_{Max}^{s}}{M_{Max}^{\infty}} = \frac{\left(3-2\nu\right)\left(1+3k_s^L\right)}{3+3k_s^L\left(3-2\nu\right)} \tag{78}$$

This ratio is an increasing function of k_s^L varying from 1-2*v*/3 for $k_s^L = 0$ to 1 for $k_s^L \to \infty$. If the typical value of *v*=0, then the ratio becomes 0.8 and for typical value of $k_s^L = 1$ and the ratio is found to be 0.94. Therefore, we deduce that the approximation consisting to consider the limit $k_s^L \to \infty$, or to neglect the axial deformability of the lining leads to overestimate the bending moment for value 5 to 20%.

When the limit $k_s^L \to \infty$ of this solution is considered, we obtain the same result that Curtis's (1976):

$$N_s = N_s^{Curtis} = \frac{(\sigma_v + \sigma_h)R}{2 + \dfrac{2E^g R}{(1+\nu)E^L S}} \tag{79}$$

$$\lim_{k_s^L \to \infty} N_D = N_D^{Curtis} = R\frac{1+\dfrac{E^g R^3}{12(1+\nu)E^L I}}{2+\dfrac{\left(3-2\nu\right)E^g R^3}{6(3-4\nu)(1+\nu)E^L I}}\left(\sigma_v - \sigma_h\right)$$

For the displacement solution also, if the limit $k_s^L \to \infty$ in our solution is considered then the same expression for the Max $u_r^L(\theta)$ given by Curtis (1976) is found (See Appendix A):

$$\lim_{k_s^L \to \infty} u_{r\,\max}^{L} = u_{r\,\max}^{L,Curtis} = \frac{\dfrac{R^4}{E^L I}}{12+\dfrac{\left(3-2v\right)E^g R^3}{\left(3-4v\right)(1+v)E^L I}}\left(\sigma_2 - \sigma_1\right) \tag{80}$$

3.5.5. Perfect-Slip Solution

The solution for the case of perfect slip cannot be obtained by taking the limit of $\kappa_t \rightarrow \infty$ in the above general case solution. As a matter of fact, by taking the limit of $\kappa_t \rightarrow \infty$ in equations (66)-(67) the solution becomes degenerate. We show first how and why this solution becomes degenerate and then explain how to derive the solution for the perfect slip in a proper way.

The expression m_i (i=1,6) are first degree functions of κ_t that we can write *as* $m_i = p_i + q_i \kappa_t$ for instance for m_1, according to (66), we have:

$$p_1 = 1 + 3k_s^L \left(1 + \kappa_n\right), \quad q_2 = 6k_s^L$$

So the numerator and denominator of the fractions (67) are a priori quadratic functions of κ_t. However, we can notice that the quadratic terms of theses expression coming from $q_i q_j$ vanish all. For instance, for the quadratic term in numerator of a_2 in (67), we find $q_3 q_5 - q_2 q_6 = 0$. Therefore, the limit for $\kappa_t \rightarrow \infty$ is obtained by taking only the first degree terms in κ_t. The first degree terms in κ_t in these expressions come from the cross terms $p_i q_j + p_j q_i$ and this allows easily evaluation of the limit for $\kappa_t \rightarrow \infty$ of the solution. For instance, we find:

$$\lim_{\kappa_t \rightarrow \infty} a_2 = \frac{p_3 q_5 + q_3 p_5 - p_2 q_6 - q_2 p_6}{p_1 q_5 + q_1 p_5 - p_2 q_4 - q_2 p_4} a_D \tag{81}$$

In this way, we find well the solution given by (85) for the perfect slip. However, the displacement solution for this case remains partially undetermined. As a matter of fact, if we consider the solution u_θ^L in (63), we find that it is undetermined for the perfect slip case because it contains the term $\kappa_t \left(a_D - 3a_2 - a_3\right)$ with $\left(a_D - 3a_2 - a_3\right) \rightarrow 0$ and $\kappa_t \rightarrow \infty$. The undermined part in this solution will be specified below.

To solve the problem for the case of perfect slip, it is preferable and is more certain to calculate the solution in a direct way and not as the limit of the general case.

For this case, we can start by $\sigma_{r\theta} = 0$ in (37) which provides:

$$a_3 = a_D - 3a_2 \tag{82}$$

Then, by taking (82) into account, the liner deformation (59) -(60) become:

$$\varepsilon^L = (\beta_s - \kappa_n) a_s + (1 + \kappa_n) a_1 + \left[(\beta_D + \kappa_n) a_D + (3 + 3\kappa_n) a_2 + (2\nu + 2\kappa_n) a_3 \right] \cos 2\theta \tag{83}$$

$$\omega'^L = \left[(-\beta_D + 2\kappa_n) a_D + (3 + 6\kappa_n) a_2 + (3 - 2\nu + 4\kappa_n) a_3 \right] \sin 2\theta \tag{84}$$

When replacing by (83) in the first equation of (51), that is, no more depending on κ_t,, we obtain an expression $J + Q\cos 2\theta = 0$ which should be true for every ×and so provides two equations $J = 0$ and $Q = 0$ for the three unknown parameters a_1, a_2, a_3. One of these equations provides a_1 by the same expression (64) which is, in fact, independent of κ_t. The other one provides $3k_s^L a_2 + k_s^L a_3 = k_s^L a_D$ which is the same that (82). Also, by replacing (84) in the second equation of (51) the same result (82) is obtained in the form $3k_D^L a_2 + k_D^L a_3 = k_D^L a_D$. This shows well the degeneracy of the solution if we base it on the liner displacements ((52) -(53)).

To solve the problem, we start with the interface constitutive model (53) in which the second equation is simply replaced by $\sigma_{r\theta} = 0$.

The first equation $\sigma_{rr} = K_n \left(u_r^R - u_r^L \right)$ with the general expression (37) and (38) for implies that we can write $u_r^L = J_r + Q_r \cos 2\theta$ where J_r and Q_r are two constants.

The first equation of (51) with $\sigma_{r\theta} = 0$ and of the σ_{rr} given by (37) imposes an expression $\varepsilon^L = J_1 + Q_1 \cos 2\theta$ with J_1 and Q_1 two constants. Comparing this to the general expression of the liner deformation (43), we deduce the expression $u_\theta^L = T_\theta \sin 2\theta + C^*$ where T_θ and C^* are two constants. The three parameters J_r , Q_r and T_θ , and, by the way, the three parameters a_1, a_2 and a_3, can be determined from the two equations (51), but C^* remains undetermined. The solution a_1 found in this way is the same (64). The two other parameters are given by.

$$a_2 = \frac{k_s^L + k_D^L + 3k_D^L k_s^L (-\beta_D + 2 - 2\nu + 3\kappa_n)}{k_s^L + k_D^L + 3k_D^L k_s^L \left(5 - 6\nu + 3\kappa_n\right)} a_D \tag{85}$$

$$a_3 = \frac{3k_D^L k_s^L (3\beta_D - 1 - 6\kappa_n) - 2\left(k_D^L + k_s^L\right)}{k_s^L + k_D^L + 3k_D^L k_s^L \left(5 - 6\nu + 3\kappa_n\right)} a_D$$

This allows calculation of the member forces of the liner by:

$$M_{\max}=\frac{-E^L I}{R}\left[\frac{(3\beta_D+9-12v)k_s^L}{k_s^L+k_D^L+3k_D^L k_s^L\left(5-6\nu+3\kappa_n\right)}\right]a_D \tag{86}$$

$$N_s=E^L S\left[\frac{1+\beta_s}{1+(1+\kappa_n)k_s^L}\right]a_s$$

$$N_D=E^L S\left[\frac{(3\beta_D+9-12v)k_D^L}{k_s^L+k_D^L+3k_D^L k_s^L\left(5-6\nu+3\kappa_n\right)}\right]a_D$$

The radial displacement is also fully determined but the tangent displacement u_θ^L remains undetermined for a global rotation *C**.

They have the following expressions:

$$\frac{u_r^L}{R}=\frac{a_s-a_1}{k_s^L}-\frac{k_D^L+k_s^L}{9k_D^L k_s^L}\left(a_D+3a_2+2a_3\right)\cos 2\theta \tag{87}$$

$$\frac{u_\theta^L}{R}=\left(a_D+3a_2+2a_3\right)\left(\frac{4k_D^L+k_s^L}{18k_D^L k_s^L}\right)\sin 2\theta+C^*$$

The fact that indetermination of u_θ^L can be understood since there is no shear force interaction between the liner and the ground and so a global rotation of the circular liner around the tunnel center does not induce any stresses and remains free. This degeneracy of the solution has not been underlined in previous works. However, it can be noted that it has no practical effects and can be simply removed by assuming $u_\theta^L=0$ for $\theta=0$, i.e., by taking $C^*=0$.

Comparison with other solutions (Perfect slip)

The solutions given for the case of perfect slip by Curtis (1976) and Einstein & Schwartz (1979) assume implicitly that the liner and the ground keep contact and can only slide relative to each other. This means that, to recover their solution from our solution, we have to assume $\kappa_n=0$ in order to ensure that $u_r^L=u_r^R$. Also their solutions consider the case of “Tunnel Excavation” ($\beta_S = 0$, $\beta_D = 0$). With these assumptions, we find the following expressions for the parameters:

$$a_1 = \frac{a_s}{1 + k_s^L} \tag{88}$$

$$a_2 = \left[\frac{k_D^L + k_s^L + 6k_D^L k_s^L (1 - \nu)}{k_D^L + k_s^L + 3k_D^L k_s^L \left(5 - 6\nu\right)} \right] a_D$$

$$a_3 = \left[\frac{-2\left(k_D^L + k_s^L\right) - 3k_D^L k_s^L}{k_D^L + k_s^L + 3k_D^L k_s^L \left(5 - 6\nu\right)} \right] a_D$$

And for member forces we find:

$$M_{\max} = \frac{E^L I}{R} \left[\frac{3(3 - 4\nu)k_s^L}{k_D^L + k_s^L + 3k_D^L k_s^L (5 - 6\nu)} \right] a_D \tag{89}$$

$$N_s = \frac{2\mu R k_s^L}{1 + k_s^L} a_s = \frac{(\sigma_v + \sigma_h)R}{2 + \dfrac{2E^g R}{(1 + \nu)E^L S}} \tag{90}$$

$$N_D = 6\mu R k_s^L \left[\frac{(3 - 4\nu)k_D^L}{k_s^L + k_D^L + 3k_D^L k_s^L \left(5 - 6\nu\right)} \right] a_D$$

At this stage, only the solution for radial displacement given by Einstein & Schwartz (1979), as listed in *Appendix A*, is the equal to our solution. The member forces are different. As a matter of fact, we explained above that their equilibrium equations (74) are different, and we think, erroneous, but apparently, the radial displacement is not affected by the error. Now, if again we take the limit $k_s^L \to \infty$ then we find the same solution as Einstein & Schwartz (1979) for bending moment and radial displacement as listed in *Appendix A* and shown in Figure 21.

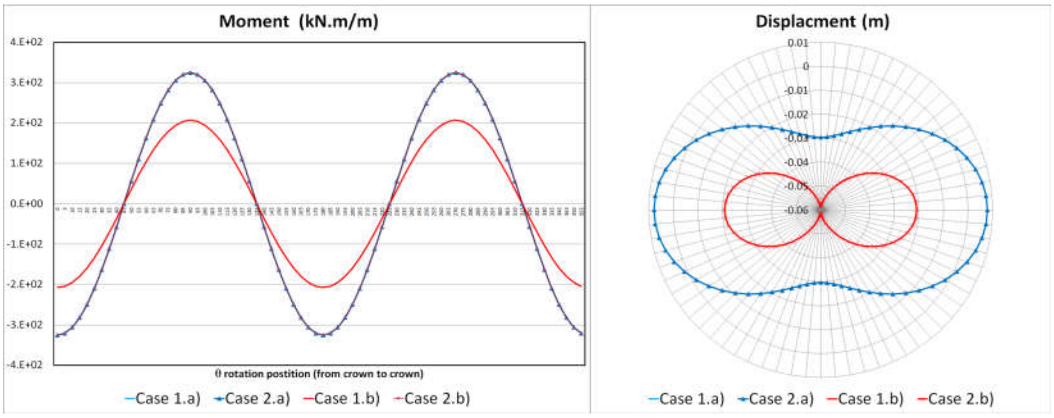

Figure 21. Comparison the result of Moment and displacement for the cases Perfect slip between our solution and Einstein & Schwartz (1979)

Curtis (1976) does not take into account finite k_s^L . If we take the limit $k_s^L \to \infty$, we find the same solution as Curtis (1976) as well as Einstein & Schwartz (1979) for bending moment and displacement as listed in *Appendix A* but not for the axial forces. Concerning the bending moment and displacement, we have:

$$M_{Max}^{\infty} = \lim_{k_s^L \to \infty} M_{\max} = \frac{E^L I}{R}\left[\frac{3(3-4v)}{1+3k_D^L(5-6\nu)}\right] a_D \tag{91}$$

Or, also with more common notations:

$$M_{Max}^{\infty} = \frac{(\sigma_v - \sigma_h)R^2}{\dfrac{10-12\nu}{3-4v} + \dfrac{2E^g R^3}{3E^L I(1+v)(3-4v)}} \tag{92}$$

$$u_{r\max}^{L\infty} = \lim_{k_s^L \to \infty} u_{r\max}^{L} = \frac{\left(\sigma_v - \sigma_h\right) R^4 / E^L I}{\dfrac{2E^g R^3}{\left(1+\nu\right)\left(3-4\nu\right)E^L I} + \dfrac{6\left(5-6\nu\right)}{3-4\nu}} \tag{93}$$

These are the same solution found by Curtis (1976) as well as Einstein & Schwartz. Concerning axial forces, N_s is independent from k_s^L and has the same expression than Curtis:

$$N_s = 2\mu R a_s = \frac{(\sigma_v + \sigma_h)R}{2 + \dfrac{2E^g R}{(1+\nu)E^L S}} \tag{94}$$

About N_D, if the take the limit $k_s^L \to \infty$, we find the same solution than Curtis:

$$\lim_{k_s^L \to \infty} N_D = 6\mu R\left[\frac{(3-4v)k_D^L}{1+3k_D^L\left(5-6\nu+3\kappa_n\right)}\right] a_D = \frac{\left(\sigma_v - \sigma_h\right)R}{\dfrac{\left(10-12\nu\right)}{(3-4v)} + \dfrac{2E^g R^3}{3(\nu+1)(3-4v)E^L I}} \tag{95}$$

These solutions for axial forces are different from that given Einstein & Schwartz (1979) as listed in *Appendix A*.

3.6. Comparison between analytical solutions and numerical results

In this section, the new analytical solution established in previous sections is compared to the results of the numerical modelling for different cases of contact properties. The finite element code Disroc (Fracsima 2016) is used for this purpose. In this code, the liner can be represented, in 2D geometry, by beam elements which have given contact properties with the ground. The linear elastic contact is supposed for this comparison in accordance with our analytic solution.

First, the cases of perfect bonding and perfect slip are considered for the Shell Inclusion loading. The parameters values for the comparison are the same in the Table 11. The results for the bending moment and radial displacement are shown in Figure 22. The dotted lines represent the numerical results and the full line our analytical solution. A perfect agreement is observed between the analytical and the numerical results.

The comparison for the elastic slip uses considers $\kappa_n = 0$ (numerically great value for K_n) and two cases of tangent stiffness values given in Table 12. The numerical results for this case are also in perfect agreement with our analytical solution as shown in Figure 23.

In the general case of elastic contact, we have compared the relative errors for the maximum bending moment, axial force and radial displacement given by different analytical solutions with the numerical results for the case of Tunnel Excavation loading. The numerical parameters for this comparison are those given in Table 11. The results are given in Table 13. It can be seen that, in all cases, our analytical solutions give negligible differences from the numerical results while for other analytical solutions, Curtis (1976) and Einstein & Schwartz (1979) greater differences are obtained for some cases. Only for the axial force in the case of perfect slip, the difference between our new analytical solution and the numerical result is slightly greater than for other analytical solution, but we think that in this case probably the numerical solution is less accurate.

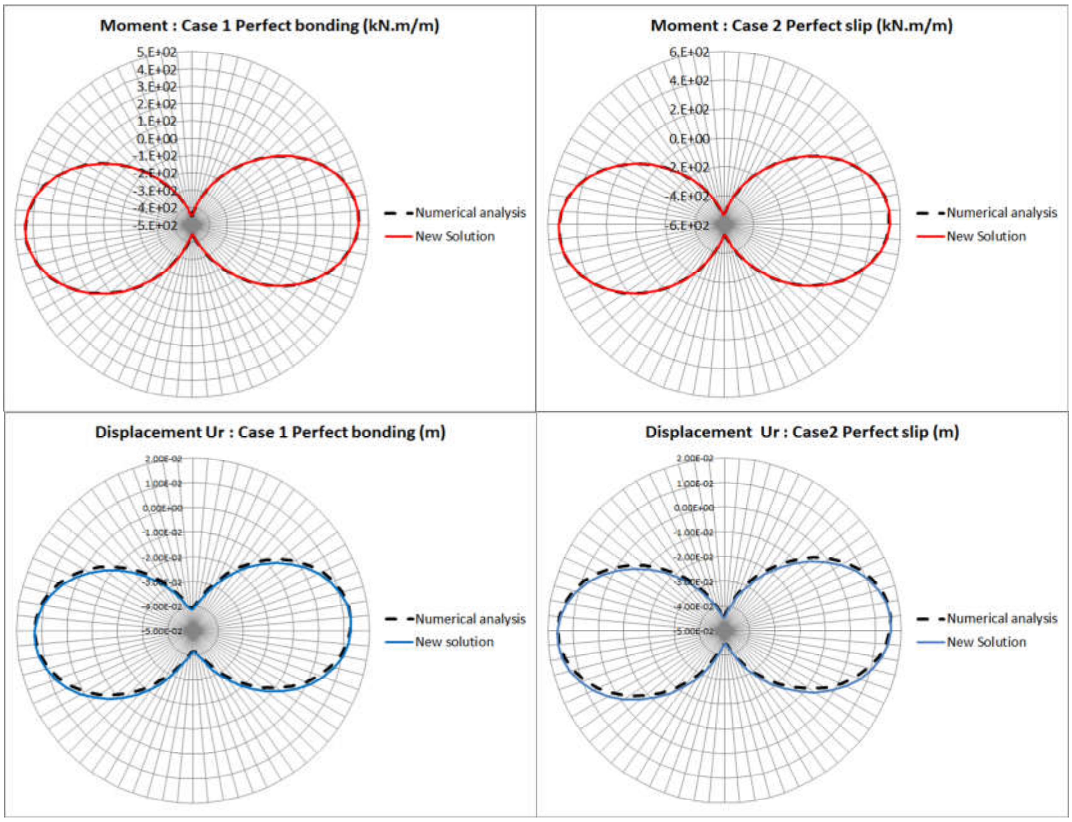

Figure 22. Comparison the result Moment and displacement between Numerical analysis and our solution (Elastic Contact model) for case of the Shell inclusion.

Table 12. Different conditions of interface parameters for Elastic Slip

Interface stiffness	K_t *(kPa/m)*	κ_t	K_n *(kPa/m)*$= \infty$ $\kappa_n=0$
N 1	1.0×10^8	1.05×10^{-3}	
N 2	1.0×10^5	1.05	

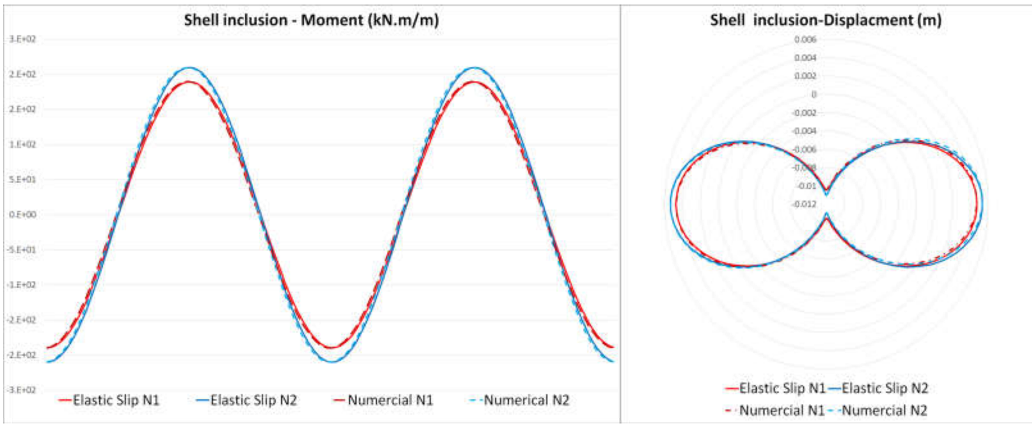

Figure 23. Comparison of bending moment and displacement between the new solution for Elastic Slip according to two different condition of κ_t.

Table 13. Maximum results of member Force in the case of Tunnel excavation with different analysis.

Case	Maximum Values	Numerical analysis	New Solution	Curtis (1976)	Einstein Schwartz (1979)
Case 3 **Perfect-bonding** (k_n, k_t= ∞)	Bending Moment (kN.m/m)	274.5	274	283.08	289
		R.E (%)	0.18	3.12	5.28
	Axial Force (kN/m)	22198	22663	23331.5	22697
		R.E (%)	2.1	5.1	2.3
	Radial Displacement (m)	0.0265	0.0278	0.0163	0.022
		R.E (%)	4.9	38.5	17
Case 4 **Perfect-Slip** (k_n = ∞, k_t=0)	Bending Moment (kN.m/m)	306	325.17	325.42	325.34
		R.E (%)	6.2	6.34	6.32
	Axial Force (kN/m)	17988	18351	18145	18246.68
		R.E (%)	2	0.87	1.44
	Radial Displacement (m)	0.0283	0.0296	0.0187	0.0296
		R.E (%)	4.6	34	4.6
Case 5 **Elastic Slip** (k_n =∞, k_t=1×10^5)	Bending Moment (kN.m/m)	295	305		
		R.E (%)	3.4		
	Axial Force (kN/m)	19550	19971.3		
		R.E (%)	2.15		
	Radial Displacement (m)	0.0276	0.0289		
		R.E (%)	4.7		
Case 6 **Elastic Contact** (k_n =2×10^7, k_t=1×10^5)	Bending Moment (kN.m/m)	294	305.4		
		R.E (%)	3.8		
	Axial Force (kN/m)	19481	19901		
		R.E (%)	2.1		
	Radial Displacement (m)	0.0277	0.0286		
		R.E (%)	3.2		

3.7. A forward perspective of applying the limit frictional criterion (Mohr-Coulomb criterion)

We presented the general solution which shows the effect of the interaction between the lining and the ground by a simple model of linear elastic contact However, there is a limit to the analysis by applying the elastoplastic behaviour or limiting failure criterion. A linear elastic interaction is about a gross approximation, which prepares fundament for future analyses, in the view of the study, to elastoplastic or frictional contact.

Table 14. Simple model parameters applied to the Mohr-Coulomb criterion

	Tunnel Excavation
R (m)	6
E^g (kPa)	1500,000
ν (Poisson)	0.27
Cohesion (kPa)	200
Friction angle (°)	27
E^L (kPa)	3E+7
E^LI (kNm^2)	3.12E+5
E^LS (kN)	1.5E+7
K_0 (when σ_v=-5424kPa)	0.6, 0.5, 0.4
σ_v (kPa) (when K_0=0.5)	-5000, -3000, -1500

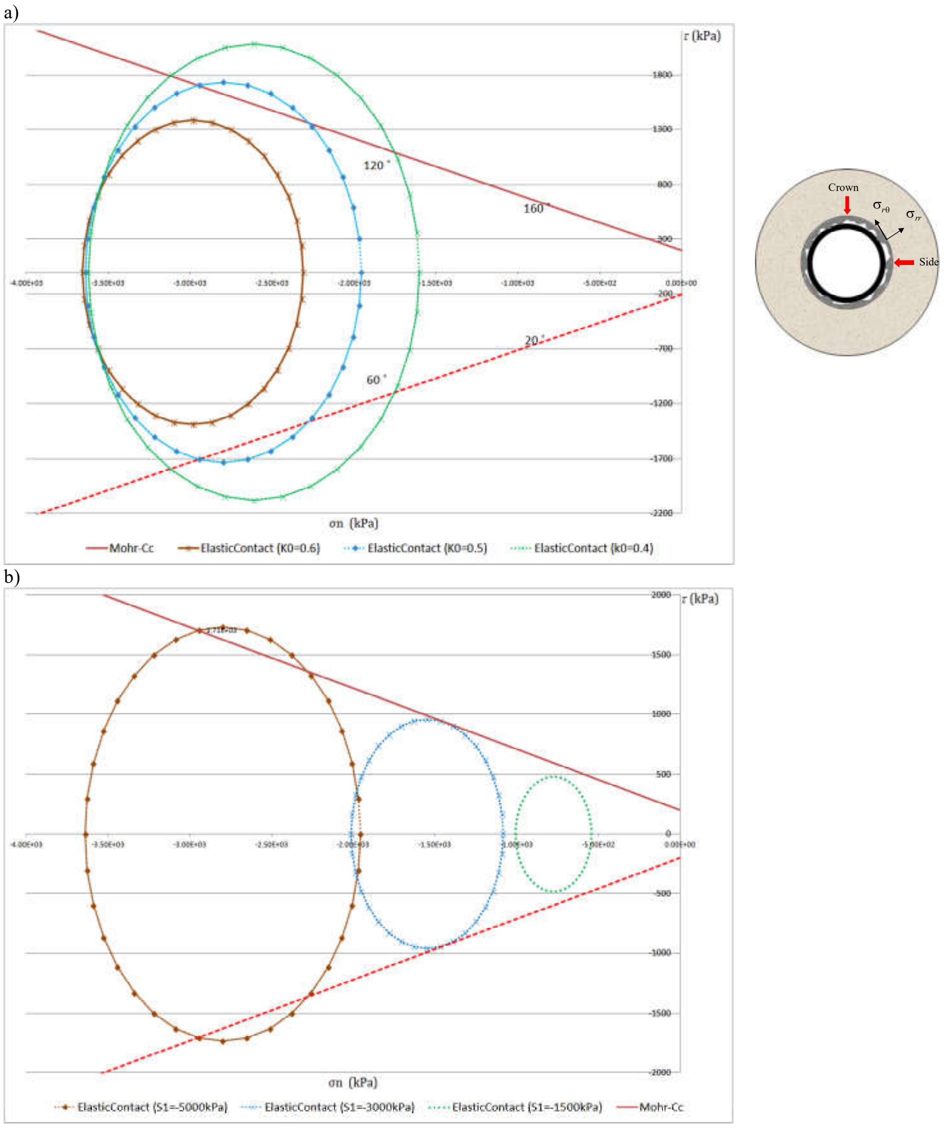

Figure 24. a) Radial and tangential stresses in a tunnel in an elastic contact solution for different earth pressure coefficients (K_0=0.6, 0.5, 0.4), and considering the Mohr-Coulomb criterion. b) Radial and tangential stresses in the tunnel of elastic contact solutions for different maximum principal stresses (S1=σ_v -5000, -3000, -1500 kPa, K_0 = 0.5 constant) and regarding to compare to the Mohr-Coulomb criterion.

The need for advanced analysis of such elastoplastic or frictional contact can be realized through a simple example analysis as shown below.

By adding cohesion and friction angle, which are necessary parameters for the basic linear Mohr-coulomb limit model (Table 14), we analyzed the behavior of the radial stress and tangential stress (Eq.37) of the tunnel obtained by our elastic contact solution. (Figure 24)

Figure 24 a) shows the Mohr-Coulomb limit criterion of the set friction angle (Table 14) and the anisotropic stress field of the tunnel where different earth pressure coefficients (K_0: 0.6, 0.5, 0.4) are applied to the same normal stress of the elastic contact solution. Here, if the static earth pressure coefficient (K_0) is less than 0.5, it exceeds the limit standard, and it is expected that there will be a part where elastoplastic or ground failure will occur.

After closer observation, in the case of K_0=0.4, the largest portion exceeded the limit. As a result of finding out which part of the tunnel was beyond that, it was found that the limit was exceeded between ± 20 degrees to ±60 degrees and ±120 degrees to ±160 degrees based on the crown point of the tunnel.

Figure 24 b) shows the radial and tangential stress behaviors of the tunnel when the maximum principal stress, that is, the normal stress, is applied differently at the same earth pressure coefficient (K_0=0.5).

The case where the initial normal stress before tunnel excavation is the largest (σ_v :-1500 kPa) already shows a stress behavior that exceeds the limit criterion. When an initial normal stress of less than that is given, it can be said to be in the elastic behavior by enduring the solidity of the ground.

Transformation normalized of elliptical stress behavior of general solution into circular behavior

The stress ($\sigma_{rr} - \sigma_{r\theta}$) behavior of the general solution in Figure 25 shows the result of an elliptical shape. If this elliptical stress behavior is converted into a circular behavior, the Mohr-Coulomb limit criterion must also be converted into appropriate parameters. This process is explained below.

First of all, recall the Eq. (37) of the general solution, and summarize it like Eq. (96).

$$\begin{bmatrix} \sigma_{rr}(R,\theta) = 2\mu\left(a_s - a_1\right) - 2\mu\left(a_D + 3a_2 + 2a_3\right)\cos 2\theta \\ \sigma_{r\theta}(R,\theta) = 2\mu\left[a_D - 3a_2 - a_3\right]\sin 2\theta \end{bmatrix} \tag{96}$$

$$\rightarrow \begin{bmatrix} \sigma_{rr} = A_0 + A_1\cos 2\theta \\ \sigma_{r\theta} = A_2 \sin 2\theta \\ A_0 = 2\mu\left(a_s - a_1\right) \\ A_1 = -2\mu\left(a_D + 3a_2 + 2a_3\right) \\ A_2 = 2\mu\left[a_D - 3a_2 - a_3\right] \end{bmatrix}$$

The stress ($\sigma_{rr} - \sigma_{r\theta} \Leftrightarrow \sigma_n - \tau$) behavior forms an ellipse as shown in Figure 25 for ElasticContact. This is based on the elliptic equation below Eq. (66). And this elliptic equation has already exceeded the Mohr-Coulomb criterion (Mohr-Cc) of the soil parameters in Table 14 shown above for the stress behavior.

$$\frac{\left(\sigma_{rr} - A_0\right)^2}{A_1^2} + \frac{\sigma_{r\theta}^2}{A_2^2} = 1 \tag{97}$$

In order to replace the existing elliptical stress $\sigma_{rr} - \sigma_{r\theta}$ behavior with circular stress $\tilde{\sigma}_{rr} - \tilde{\sigma}_{r\theta}$ behavior, the stress behavior was converted as follows Eq. (98).

$$\begin{aligned} \tilde{\sigma}_{rr} &= \sigma_{rr} = A_0 + A_1\cos 2\theta \\ \tilde{\sigma}_{r\theta} &= \frac{A_1}{A_2}\sigma_{r\theta} = A_1 \sin 2\theta \end{aligned} \tag{98}$$

After this transformation, the following circular equation (99) stress behavior can be found.

$$\left(\tilde{\sigma}_{rr} - A_0\right)^2 + \tilde{\sigma}_{r\theta}^2 = A_1^2 \tag{99}$$

Also, if the transformed stresses (98) are applied again to the Mohr-Coulomb criterion (Mohr-Cc), it can be seen that (100) is obtained.

$$\begin{cases} |\tau| + \sigma_n \tan\varphi - c \le 0 \\ |\sigma_{r\theta}| + \sigma_{rr} \tan\varphi - c \le 0 \end{cases} \rightarrow \left. \begin{array}{l} \left|\left(A_2/A_1\right)\tilde{\sigma}_{r\theta}\right| + \tilde{\sigma}_{rr} \tan\varphi - c \le 0 \\ \left|\tilde{\sigma}_{r\theta}\right| + \tilde{\sigma}_{rr} \tan\tilde{\varphi} - \tilde{c} \le 0 \end{array} \right\} \tag{100}$$

Here, parameters applied to the previous Mohr-Coulomb criterion (Mohr-Cc) are replaced with appropriate parameters "$\tilde{\varphi}$" and "$\tilde{c}$" in the transformed criterion.

$$\left|\frac{A_1}{A_2}\right| \tan\varphi = \tan\tilde{\varphi} \rightarrow \tilde{\varphi} = \tan^{-1}\left(\left|\frac{A_1}{A_2}\right| \tan\varphi\right), \qquad \left|\frac{A_1}{A_2}\right| c = \tilde{c} \tag{101}$$

Figure 25 shows the results of the relationship between the existing elliptical stress behavior (ElasticContact) and the Mohr-Coulomb criterion (Mohr-Cc) and the relationship between the substituted circular stress behavior (TS-ElasticContact) and the transformed Mohr-Coulomb criterion (TS-Mohr-Cc).

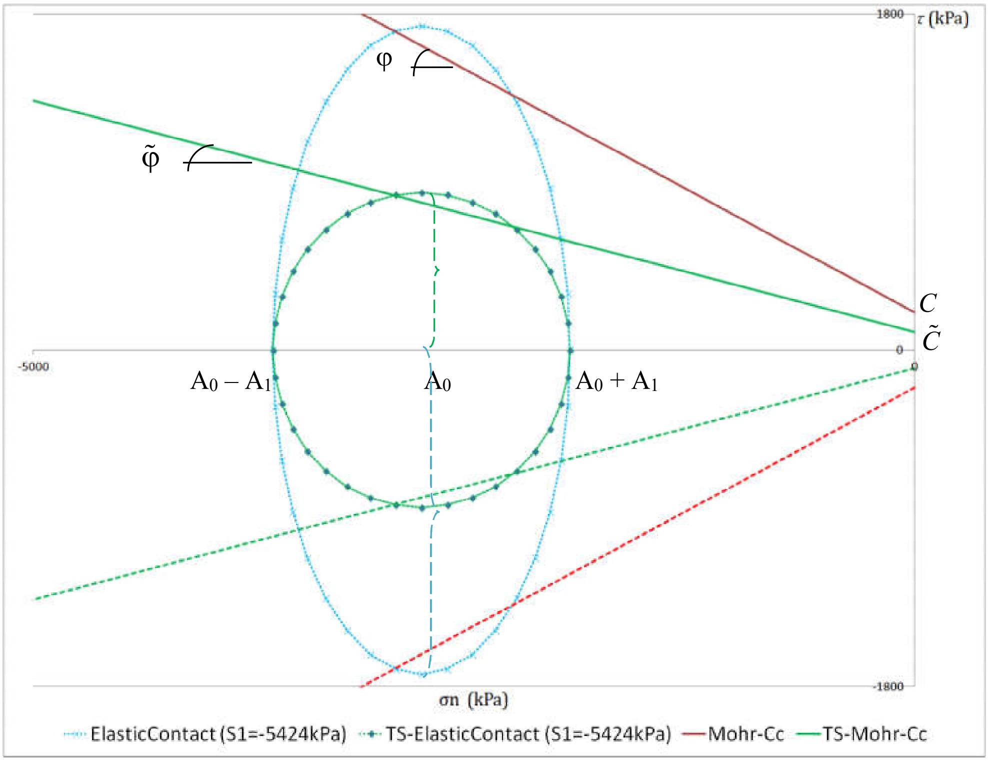

Figure 25. Relationship between the stress behavior of the original and transformed general solution (ElasticContact) and the Mohr-Coulomb criterion. (General solution: ElasticContact (S1=-5424kPa), general solution transformed to circular behavior: TS-ElasticContact (S1=-5424kPa), original Mohr-Coulomb standard: Mohr-Cc, transformed Mohr-Coulomb standard: TS-Mohr -Cc), initial stress: -5424 kPa, Ko: 0.5.

3.8. Conclusion and perspectives

In this Chapter, we introduced the effect of the interaction between the lining and the ground by a simple model of linear elastic contact. In fact, the existing solutions in the literature were limited to the two extreme cases of perfect bonding between the lining and the ground or to perfect slide which means no shear stress in the contact surface. We showed that the general solution obtained here covers the solutions existing in the literature as special limit cases and also brings some corrections. The main comparison points between our solutions and the most advanced previous solutions can be summarized as follows.

Einstein & Schwartz's solution takes into account the longitudinal deformability of the circular lining with some complex relations but finally the result is not correct for all aspects: concerning the radial displacement of the lining, there are perfect agreements between our solution and that of Einstein & Schwartz (1979) in the case of perfect slip but not in the case of perfect bonding. We explained why the latter solution is erroneous and also showed that our solution is closer to numerical solution results obtained by FEA.

We introduced dimensionless coefficients for the deformability of the lining (bending and axial deformation) compared to the ground stiffness. The displacement solution given by Curtis (1976) is different from us because it assumes implicitly a lining infinitely stiffer than the ground. In all cases, the progress in our solution is that it extends the existing solution to the elastic contact between the ground and the lining.

An interesting extension of the present work for application to tunnels would be the introduction of an excavation load ratio before setting up the lining. The solutions presented here allow more accurate modelling of the member forces than the previous ones if a relevant contact model can be determined for the ground-lining interaction, for instance in case of tunnels excavated by tunnelling boring machine (TBM).

A linear elastic interaction is surely a gross approximation, but it prepares the terrain for more advanced analyses, in the perspective of the present work, to elastoplastic or frictional contact. Moreover, the extension to elastoplastic ground as well as to segment lining could be considered.

APPENDIX A. Theoretical tunnel member force formula (Curtis., 1976),(Einstein and Schwartz .,1979)

<table>
<tr><th rowspan="1">Curtis (1976)
Perfect Slip</th><th>Curtis (1976)
Perfect Bonding</th><th>Einstein and Schwartz (1979)
Perfect Slip</th><th>Einstein and Schwartz (1979)
Perfect Bonding</th></tr>
<tr>
<td rowspan="2">$M_{max} = \dfrac{(\sigma_v - \sigma_h)R^2}{\dfrac{10\text{-}12\nu}{3\text{-}4\nu} + \dfrac{2E^g R^3}{3(1+\nu)(3\text{-}4\nu)E^L I}}$

$N_{const} = \dfrac{(\sigma_v + \sigma_h)R}{2 + \dfrac{2E^g R}{(1+\nu)E^L S}}$

$N_{max} - N_{const} = \dfrac{(\sigma_v - \sigma_h)R}{\dfrac{10\text{-}12\nu}{3\text{-}4\nu} + \dfrac{2E^g R^3}{3(1+\nu)(3\text{-}4\nu)E^L I}}$

$U_{max\text{-}r} = \dfrac{(\sigma_v - \sigma_h)R^4 / E^L I}{\dfrac{6(5\text{-}6\nu)}{3\text{-}4\nu} + \dfrac{2E^g R^3}{(1+\nu)(3\text{-}4\nu)E^L I}}$</td>
<td rowspan="2">$M_{max} = \dfrac{(\sigma_v - \sigma_h)R^2}{4 + \dfrac{(3-2\nu)E^g R^3}{3(1+\nu)(3-4\nu)E^L I}}$

$N_{const} = \dfrac{(\sigma_v + \sigma_h)R}{2 + \dfrac{2E^g R}{(1+\nu)E^L S}}$

$N_{max} - N_{const} =$
$\dfrac{(\sigma_v - \sigma_h)R\left[1 + \dfrac{E^g R^3}{12(1+\nu)E^L I}\right]}{2 + \dfrac{(3-2\nu)}{6(1+\nu)(3-4\nu)} \dfrac{E^g R^3}{E^L I}}$

$U_{max-r} = \dfrac{(\sigma_v - \sigma_h)R^4 / E^L I}{12 + \dfrac{(3-2\nu)E^g R^3}{(1+\nu)(3-4\nu)E^L I}}$</td>
<td>$M_{max} = \dfrac{(\sigma_v - \sigma_h)R^2(1-2a_2^*)}{2}$

$N - N_{const} =$
$R\dfrac{(\sigma_v + \sigma_h)(1-a_0^*) + (\sigma_v - \sigma_h)(1-2a_2^*)}{2}$

$\dfrac{U_r E^g}{R(1+\nu)}_{max} =$
$\dfrac{(\sigma_v + \sigma_h)a_0^* - (\sigma_v - \sigma_h)\left[(5+6\nu)a_2^* - (1-\nu)\right]}{2}$</td>
<td>$M_{max} = \dfrac{(\sigma_v - \sigma_h)R^2}{4}(1-2a_2^* + 2b_2^*)$

$N - N_{const}$
$= R\dfrac{(\sigma_v + \sigma_h)(1-a_0^*) + (\sigma_v - \sigma_h)(1+2a_2^*)}{2}$

$\dfrac{U_r E_g}{R(1+\nu)}_{max}$
$= \dfrac{(\sigma_v + \sigma_h)a_0^* + (\sigma_v - \sigma_h)\left[4(1-\nu)b_2^* - 2a_2^*\right]}{2}$</td>
</tr>
<tr>
<td colspan="2">$Compressibility\ \ ratio: C = \dfrac{E^g\ R(1-\nu_l^2)}{E^L\ S(1-\nu^2)}, \quad Flexibility\ \ ratio: F = \dfrac{E^g\ R^3(1-\nu_l^2)}{E^L\ I(1-\nu^2)}$

$Dimensionless\ \ coefficients$
$a_0^* = \dfrac{CF(1-\nu)}{C + F + CF(1-\nu)}, \quad a_2^* = \dfrac{(F+6)(1-\nu)}{2F(1-\nu) + 6(5-6\nu)} or\ \beta b_2^*$
$\beta = \dfrac{(F+6)C(1-\nu) + 2F\nu}{3F + 3C + 2CF(1-\nu)} = \dfrac{(F+6)C(1-\nu) + 2F\nu}{3F + 3C + 2CF(1-\nu)}$
$b_2^* = \dfrac{C(1-\nu)}{2\left[C(1-\nu) + 4\nu - 6\beta - 3\beta C(1-\nu)\right]}$</td>
</tr>
</table>

LIST OF NOTATIONS (CH 4)

Symbol	**Definition**
R	Tunnel radius
E	Young's modulus
ν	Poisson's ratio of ground
E^{g}	Young's modulus of ground
E^{L}	Elastic modulus of lining
$E^{L}I$	Elastic modulus of lining * moment of inertia
$E^{L}S$	Elastic modulus of lining * section
σ_v, σ_h	Vertical and horizontal stress
$\sigma_{rr}, \sigma_{\theta\theta}, \sigma_{r\theta}$	Radial, tangential stresses and shear stress
S_{rr}	Radial, tangential stresses
U_r, U_θ	Radial, tangential displacements
K_0	Earth pressure coefficient
$k_{0n},\ k_0$	Initial normal of interface
k_{0t}	tangent stiffness of interface
$K_n,\ K_t$	Normal and tangent stiffness of interface
e	Gap of interface
U_r^{total}	Total radial displacement
U_r^{s}	Radial displacement of segment
U_r^{I}	Radial displacement of interface
$u_n,\ u_r,\ u_\theta$	Normal, radial, tangent displacements
$R_n^{segment}, R_n$	Segment strength
P_s	Segment pressure
P_0	Initial pressure (stress)
P_i	Internal pressure (stress)
$u_r^g,\ u_\theta^g$	Radial, tangent displacements of ground
$u_r^L,\ u_\theta^L$	Radial, tangent displacements of lining

4. Numerical modelling of segments volume lining with joints

In this chapter 4, we will present the research on the modelling of segment lining with joints. It is attempted to model the volumetric segment lining, and this analysis provides an opportunity to compensate for the limitations encountered in the previous model analysis, and, furthermore, to analyse the effects of joints between segments.

In this analysis study, segments are first bulk modelled in real size on geometry. In addition, interfaces between lining and ground can be analysed with the various stiffness of material grouting and with the Gap parameters as well by difference between the diameter of the excavation and of the segment installations in actual boring tunnel (TBM) construction.

Here, it would be shown that we have largely derived three analyses sequentially.

1) Suitability of the volumetric continuum lining model

2) Analysis of the influence of the interface gap (ex: tail void) due to the interaction between the lining and the ground

3) Joint segment modelled and analysis by joint impact depending on horizontal earth pressure coefficient

After revealing the appropriateness of the use of the volumetric continuum model, based on the recognition that the primary volume loss in the construction of the shield tunnel is caused by the tail void gap between the segment lining and the ground skin, the tail void gap is modelled as an interface element to analyse the effect of segment lining by stiffness values and spacing 'e' of the interface. These results were evaluated by the member force analysis of a lining and the Convergence confinement method.

If the tail void(gap) interface becomes larger between the segment lining and the ground and the stiffness value is lower, even if the gap grouting process and the installation of the segment are performed simultaneously, the support stiffness of the actual segment lining is expressed afterward the stiffness combination of the segment lining and the interface. In conclusion, this analysis is required to control the load on the lining.

Currently, there are limitations in modelling analysis considering various ground conditions along with joint modelling of linings. This is because it is often used to analyse the lining behavior due to joints in elastic ground like the beam-spring model or to analyse the ground behavior by simplifying the lining. However, since both are important parts that influence each other, it can be said that modelling analysis is appropriate when analysed together. If it is possible to analyse the segment lining behaviour, including joints, and even under the complex ground, we can model various ground, such as fault zone conditions, fracture zones, or seismic impact ranges. To do so, while performing a continuum numerical analysis of the complex ground, a modelling analysis is also required that goes beyond the method of analysing the ground only with elasticity like the single-beam model or the beam-spring model for segment lining.

In the Disroc (FEM) numerical analysis code we used, the segment is designed as a bulk model and, at the same time, in order that the mechanical behavior of this bulk continuum lining is calculated, we suggest the method of geometries in Figure 26.

4.1. Suitability of model as volumetric continuum segment lining

In this analysis study, segments are first bulk modelled in real size on geometry (Figure 26-b)) and then, the lining beam model in Figure 26 a)-A is installed in the middle between the bulk segments. This is to analyse the beam behavior while modelling the lining as a bulk model. The physical properties of the lining beam model are derived from the lining segment physical properties, but the scale is calculated to be 1/1000. (Table 15)

Table 15. Applied proprieties parameters for Ground and Lining in the study
(Kwak et al. 2016; Salemi, Esmaeili, Sereshki 2015)

	Shell inclusion	*Tunnel Excavation*
R (m)	6	
E^g *(kPa)*	8.5E+5	
v (Poisson)	0.35	
E^L *(kPa)*	3E+7	
v^L *(Poisson)*	0.2	
$E^L I/1000$ *(kNm^2)*	312	
$E^L S/1000$ *(kN)*	1.5E+4	
σ_v *(kPa)*	-1500	-5424
σ_h *(kPa)*	-795	-2929

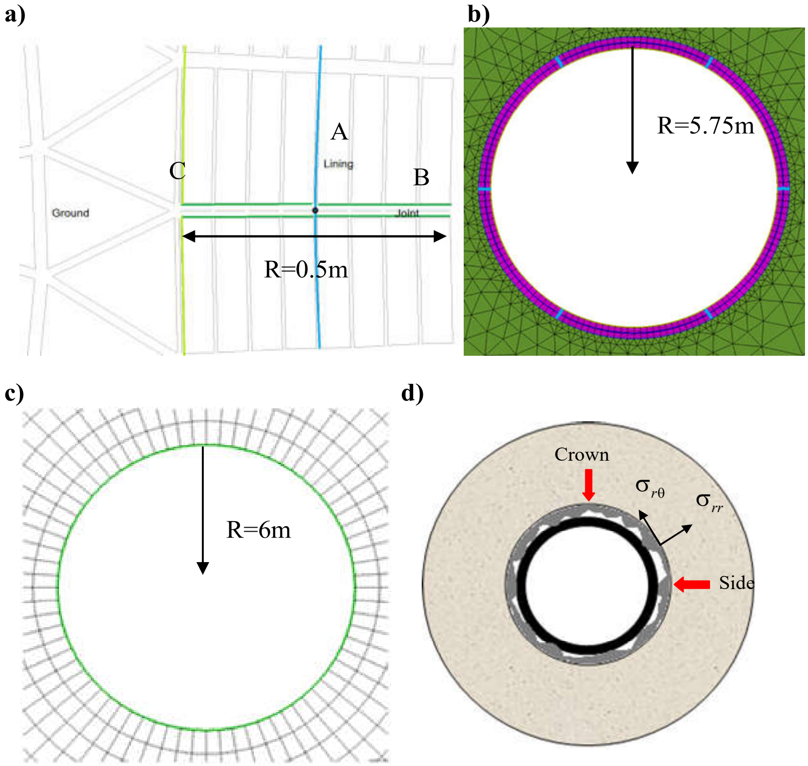

Figure 26.a) A: Phantom beam element, B: Interface joint between each segment longitudinal, C: Interface between ground and lining. b) Geometry of bulk segment model by GID, c) Geometry of one beam model by GID, d) Segment lining and tail void illustration.

In Figure 26 a)-B, joints between segments were also simulated together, but, the joint effect is little different from that of a continuum model if the stiffness of joints between segments is quite large under isotropic conditions. Therefore, this analysis of joint would be more mentioned at the next section (Ch 4.3). Since a)-C is the interface that can model the gap between the volume lining and the ground, this element can simulate tunnel grouting or gap effect of tail void.

First of all, to find out the suitability of the volumetric lining model, we compared the results of the previous study of mechanical elastic ground lining behavior. According to the two methods of applying tunnel stress that have already been introduced (CH. 3), they are divided into "Shell inclusion" and "Tunnel Excursion".

In Table 16, we can see the maximum member force (Moment, Axial force, Ur) depending on the two tunnel stress application methods.

This result shows the comparison of the volumetric continuous lining model, the new theoretical solution as introduced in the previous chapter and the result when the lining is modelled as a single beam when the interrelationship of lining-ground is "Perfect bonding" or "Perfect slip". As a result, the applicability of the volume lining model can be seen (Table 16).

Shell inclusion: the hole exists in the infinite medium at zero stress and then the far-field stress is applied (active load).

Tunnel excavation: this case corresponds to the classical tunnel excavation problem in which the hole is excavated in a pre-stressed medium (passive load).

Table16. Comparison of volume type lining model with other elastic models at tunnel crown point

Maximum		Shell inclusion			Tunnel excavation		
		General solution	One beam	Bulk lining	General solution	One beam	Bulk Lining
Perfect bonding	Moment (kN.m/m)	189	189	184	412	388	379
	Axial force (kn/m)	4980	4980	4629	14300	15054	14159
	Ur (m)	0.0104	0.0104	0.0105	0.0245	0.0215	0.00196
Perfect slip	Moment (kN.m/m)	223	221	202	526	450	410
	Axial force (kn/m)	7110	7112	5419	18600	19753	15856
	Ur (m)	0.0114	0.0114	0.0099	0.02383	0.0233	0.0205

4.2. Numerical modelling method of annular grouting in tunnels tail void with gap by an interface element.

The analysis of the interrelationship between the ground and lining in terms of the tunnel design method is important for tunnel design. Conventional excavation methods and shield tunneling (TBM) methods are well established. In particular, TBM tunneling methods under complex ground conditions require an improved numerical analysis of segment lining due to the influence of the interface behavior as gap (tail void) parameters between the ground and the lining (Ziegler, Oh 2014; Vu, Broere, Bosch 2016; Vonk 2020; Oh, Ziegler 2014; Ding et al. 2021). The technique of shield tunneling is characterized by active support, and the stress behavior accepted by the segment must be interpreted through the grouting process for the gap (tail void) between the excavation ground skin and the segment lining (Ziegler, Oh 2014).

In TBM tunneling, an annular cavity exists between the lining and the surrounding soil after the lining segment is installed as one of the volume losses because of ground subsidence. In general, grouting is performed immediately on the tailgating gap at the same time as excavation, but the surrounding soil may be pressed into the gap depending on the stiffness of the grouting material (Vu, Broere, Bosch 2016; Ding et al. 2021). In general, tail void for annular grouting is usually the preferred method for controlling surface settlement. Therefore, it is necessary to analyze whether segment behavior due to increased or decreased stiffness of the grouting variable affects the radial displacement into the tunnel regarding the physical properties of ground. As one of the factors influencing the load of the lining, the thickness (spacing) of the annular grouting (backfilling) is not known a priori but depends on the properties squeezed by the deformation of the profile between the tunnel excavation skin and the segment(Ramoni, M., Anagnostou 2010).

The radial stress of the soil towards the tail void causes the ground to push into the tail void and collapse. To overcome this problem, when the gap of tail void is completely filled with grouting, grouting particles can support the role instead (Vonk, 2020). Initially after grouting, the action of the ground load around the lower half of the liner is promoted and no excessive pressure is accumulated. In other words, the expansion of tail void gap due to grouting does not compensate for surface settlement (Teachavorasinskun 2018). Therefore, many material studies are being conducted on the stiffness and strength of the behavior of the grouting material to be filled in the tail void cavity (Peila, Borio, Pelizza 2011). This is inevitable for the ground to settle by the tail void that occurs during TBM tunneling operation, but if it is well controlled, the stress effect on the load transmission capability of the lining (segment) can be investigated.

In this numerical analysis by two-dimensional, tail void grouting was simulated as an interface model between ground skin and segment lining after tunnel excavation. Moreover, the main purpose is to analyze the behavior of segment lining depending on interface rigidity. Our research examines the interface element of Bandis Elastic non-linear in the finite element code of DISROC (Fracsima, 2016). This element's stiffness value changes based on the gap 'e,' allowing us to simulate the impact of the interface gap interval on segment lining behavior.

In this paper, we conducted parameter studies of the interface model depending on the stage of excavation ground load ratio under the rock conditions of Grade 2, 3 or Grade 4 isotropic ground. As a result of the analysis, the member force (axial force, radial displacement) analysis of the segment lining is carried out and, the behavior of the interface model for tail void grouting by the Convergence Confirmation Method is described.

4.2.1. Annular grouting (tail void) interface model

In general, the difference between the rigidity of the structure and of the ground is 100 to 10000 times. As a result, if the strength is exceeded at the connection between the ground and the lining, relative displacement may occur. Since the boundary between the ground and the segment lining is in fact negligible in thickness, an interface model is used as ground element with zero thickness to consider this. Thus, ground and segment linings were simulated with bulk volume models, but gaps between them were modeled with interface elements simulating the grouting of tail void.

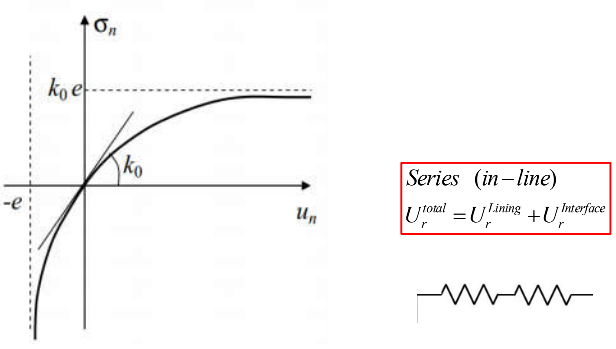

$Series \quad (in-line)$
$U_r^{total} = U_r^{Lining} + U_r^{Interface}$

21200 Non-linear hyperbolic elastic joint

Nb: 4
Param1 = k_{0t} (tangent stiffness)
Param2 = k_{0n} (normal stiffness)
Param3 = $K_{nt} = K_{tn}$ (non diagonal stiffness → dilatancy)
Param4 = e (maximum closure or physical thickness

Figure 27. Bandis Nonlinear hyperbolic elastic model applied to the interface element. (Fracsima/Disroc 2022)

To do a modelling of annular grouting was applied to the nonlinear elastic Bandis model for interface between ground and lining. (Fracsima, 2016) This is because

Nonlinear Bandis model is able to take into account the gap to this interface by actually modelling a physical distance "e" of the interface between the liner and the ground. Looking at Figure 27, this shows that the stiffness of the interface increases as the gap decreases due to the gradual closure at the initial interval e, taking into account the closure displacement of the gap between the ground and the liner. Besides, the radial displacement of the ground cannot go over the liner. (Eq 102)

The following Equation (102) indicates the interface stiffness in which the interface stiffness changes non-linearly regarding a given interval 'e'. In general, when several supports are installed at the same time, the stiffness of the support members resisting the ground load is combined in a parallel connection form to increase the support stiffness of the entire support.

$$\begin{bmatrix} K_n = \dfrac{k_{0n}}{1+u_n/e} \\ \sigma_n = K_n u_n \\ K_n = \dfrac{k_{0n}}{1+\dfrac{\sigma_n}{K_n e}} \\ K_n = k_{0n} - \dfrac{\sigma_n}{e} \end{bmatrix} \rightarrow \begin{bmatrix} K_t = \dfrac{k_{0t}}{1+u_n/e} \\ \\ K_t = \dfrac{k_{0t}}{1+\dfrac{\sigma_n}{K_n e}} = k_{0t}(1-\dfrac{\sigma_n}{k_{on}e}) \\ K_t = k_{0t} - \dfrac{k_{0t}}{k_{on}e}\sigma_n \end{bmatrix} \tag{102}$$

In this study, although segment lining and tail void grouting are performed simultaneously, the contact with the ground is first interface grouting and then segment lining. Therefore, the convergence of the process of supporting the ground load is performed in a series manner, that is, the sum of the respective internal displacements. (Eq. 103)

$$\textit{Combinaison Segment} - \textit{Interface} \tag{103}$$

$$\begin{bmatrix} U_r^S = \dfrac{P_s}{R_n^{segment}} \\ P_s = \sigma_\theta \dfrac{t}{r_0} = \dfrac{E_l}{1-\nu^2}\dfrac{U_r^L}{r_0}\dfrac{t}{r_0} \\ R_n^{segment} = \dfrac{E_l}{1-\nu^2}\dfrac{t}{r_0^2} \\ U_r^I = \dfrac{P_s}{K_n^{Interface}} = \dfrac{P_s}{k_{0n} - {P_s}/{e}} \end{bmatrix} \Rightarrow \begin{bmatrix} U_r^{total} = U_r^S + U_r^I \\ U_r^{total} = P_s \left[\dfrac{R_n + k_{0n} - {P_s}/{e}}{R_n\left(k_{0n} - {P_s}/{e}\right)} \right] \\ = \dfrac{P_s}{R_n} - e - \dfrac{k_{0n}e^2}{\left(P_s - k_{0n}e\right)} \\ = \dfrac{\left(P_s - k_{0n}e\right)}{R_n} + \dfrac{k_{0n}e}{R_n} - e - \dfrac{k_{0n}e^2}{\left(P_s - k_{0n}e\right)} \end{bmatrix}$$

As a simple example result, Figure 28 shows the maximum radial displacement value of the tunnel lining under the same stress (isotropic) condition according to various stiffness values (N 1~N 9, kPa) and gaps (e: 10cm or 1cm) of the lining-ground interface.

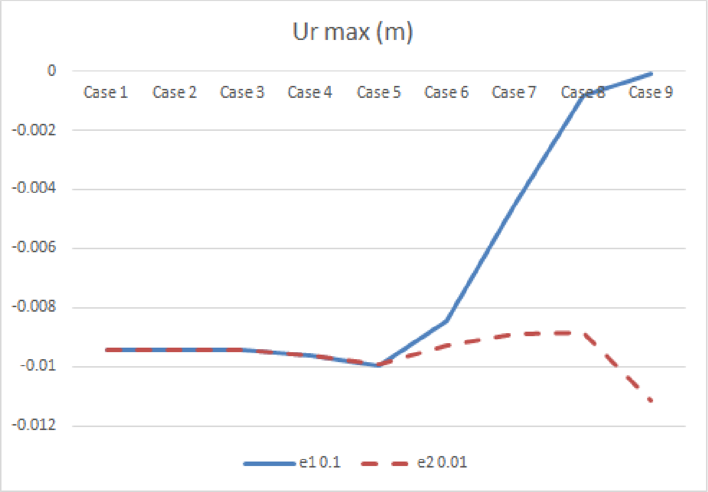

Distance	e
e1	10cm
e2	1cm

Interface stiffness kt, kn	
Case N 1	1E+9, 2E+9
Case N 2	1E+8, 2E+8
Case N 3	1E+7, 2E+7
Case N 4	1E+6, 2E+6
Case N 5	1E+5, 2E+5
Case N 6	1E+4, 2E+4
Case N 7	1E+3, 2E+3
Case N 8	1E+2, 2E+2
Case N 9	10, 20

Figure 28. Maximum radial displacement (ex: Shell inclusion load) depending on the interface stiffness change and the distance "e" between the lining and the ground

It may be seen that the radial displacement value differs depending on the interval "e" at decreasing the case from N5 stiffness of interface.

If the initial spacing is 10cm, the gap between the ground and the lining is relatively large. This is why the lower the stiffness of the interface, the less the direct impact of the lining. On the other hand, when the gap is 1 cm, it can be seen that the lining and the ground are almost in complete contact. Therefore, the less the stiffness of the interface decreases, the greater the impact of the lining from the ground it receives.

In the interface condition Case N7, let's look at the change in the radial displacement of the ground and the radial displacement of the lining. When the distance between the ground and e=1cm is completely closed, it can be shown that the displacement difference between the ground and the lining approaches e=1cm. This means the initial distance between them in complete contact. (Table 17)

Table 17. Radial displacement of the ground and lining according to the gap "e" of interface

Case N7 $u_{r-Max(crown)}$	$u_r^g\ (m)$	$u_r^L\ (m)$	$\left\|u_r^g - u_r^L\right\| < e$
$e1 = 0.1\ (m)$	-2.18E-02	-4.54E-03	0.01726
$e2 = 0.01\ (m)$	-1.87E-02	-8.89E-03	0.00981

4.2.2. Tunnel excavation with convergence confinement method by load ratio

Under the plane strain condition of the two-dimensional analysis, it should be noted that simulating tunnel excavation under 3D stress condition as a 2D plane deformation problem has the implication of simultaneously excavating the entire section of the tunnel rather than gradual excavation. For example, all ground displacements occur immediately after excavation, but, in actual tunnel excavation, less than the total displacement occurs immediately after excavation due to the arching effect and the displacement converges approximately four times the diameter of the tunnel. Therefore, when analyzing a tunnel in two dimensions, it should be assumed that the excavation force is not applied to the excavation surface at once, and only a part of the load is adapted depending on the degree of occurrence of the tunnel radial displacement.

In order to consider this analysis, load ratio is divided into stages based on the tunnel displacement according to the stage of excavation during the two-dimensional analysis, and the corresponding displacement is expressed as the ratio to the final displacement. The tunnel excavation load ratios performed are shown in Table 18 below.

In the resulting graph, load ratio 1 on the horizontal axis means 10% tunnel excavation convergence before the application of support materials.

Table 18. Load ratio of tunnel excavation force for segment installation

Load ratio ⌵	0.1	0.2	0.3	0.4	0.5	0.6	0.7	0.8	0.9
Excavation	Load ratio 1 → Load ratio 9 Convergence of α*100% internal displacement								
Support	(1-α)*100% support for remaining load displacement convergence								

In particular, tail void grouting and segment lining play a crucial role in supporting the significant load generated during shield tunneling, given the fast installation of segments and reduced internal displacement compared to conventional tunneling methods. Theoretically, at the total load P_0, stress release occurs as much as $P_i=(1-\alpha)P_0$ before the installation of the support, and the remaining stress αP_0 to be supported by the lining is released. If this load ratio is analyzed using Convergence Confinement Method, the adequacy of support stiffness, stability factor, and optimal support installation time can be determined. (Figure 29)

Many researchers have studied the interaction between excavation ground and support in tunnel design. These studies have been interpreted based on the well-known and widely used CCM. CCM is a two dimensional simplified approach that can be used to simulate three-dimensional problems as the rock-support interaction in tunnels. (Sulem, Panet, Guenot 1987; De La Fuente et al. 2019; Vlachopoulos, Diederichs 2009; Paraskevopoulou, Diederichs 2018)

GRC: Ground Reaction Curve. It is a characteristic line that records the decrease of an apparent internal support pressure. The GRC depends on the rock mass behavior. It is assumed to be linear for an elastic material but it varies if the material is elasto-plastic or visco-elastic etc. SCC: Support Characteristic Curve (Lining). The internal pressure P_i acts radically on the tunnel profile (from the inside) and represents the support resistance (SCC) needed to hinder any further displacement at that specific location. The ground reaction curve shows an increase in the internal displacement when the internal pressure P_i of the tunnel is decreased from the pressure P_0 of the original ground. In addition, the support member characteristic curve (SCC) shows an increase in the support pressure P acting on the support member as the internal displacement of the tunnel increases. The point where SCC and GRC meet each other is the stress equilibrium convergence point. (Figure 29)

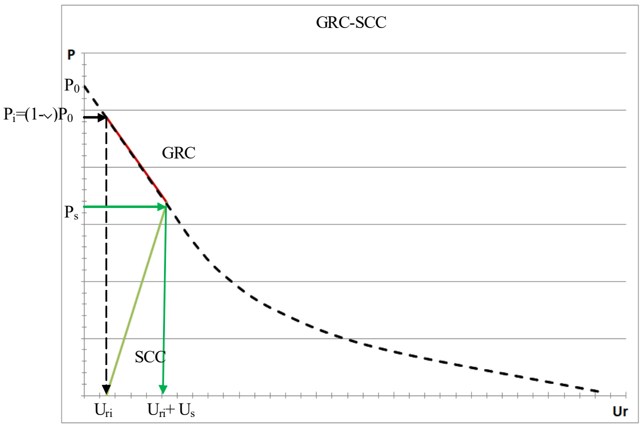

$$\alpha = Load \quad ratio$$
$$P_i = P_0(1-\alpha)$$
$$Lining \Rightarrow \quad P_0\alpha$$

Figure 29. Ground Reaction-Support Characteristic Curve by Convergence Confinement method according to load ratio.

Figure 30 shows the radial stress distribution in accordance with the load sharing rate immediately after tunnel excavation before installing the segment lining. In Figure 30-a) (α: 0.1), the displacement convergence rate is lower than that in Figure 30-b) (α: 0.9). This is because the rate accompanying the tunnel excavation force varies depending on the convergence stage.

Figure 30-b) shows that the displacement convergence has already progressed considerably, reducing the stress around the tunnel. On the other hand, this means that the influence of the force received by the lining would be not significant.

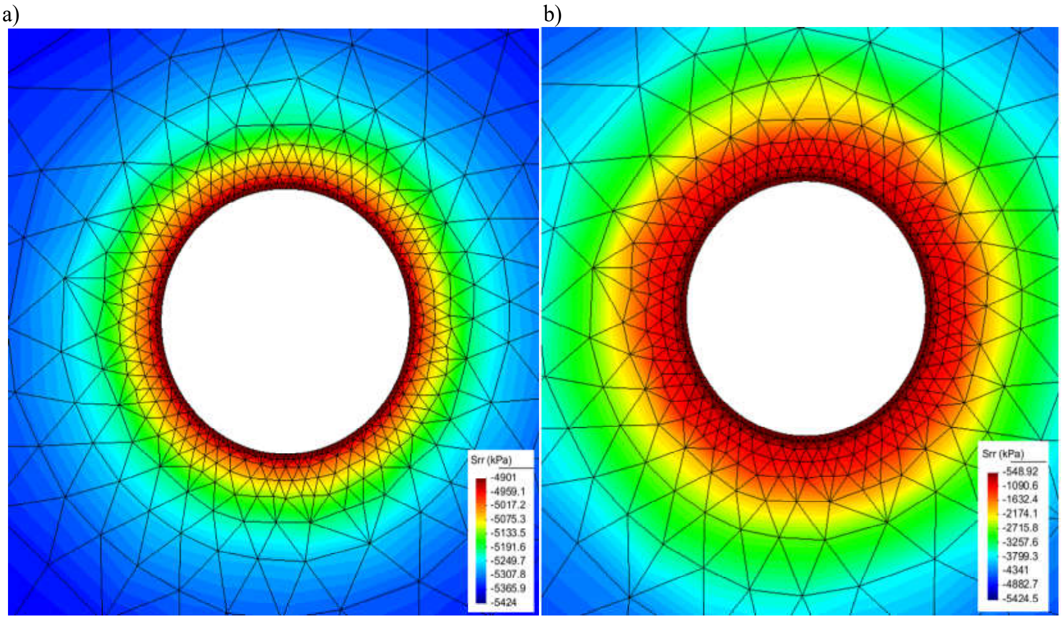

Figure 30. Radial stress distribution before installing the segment lining according to the displacement convergence step after excavating the tunnel a) α: 0.1 and b) α: 0.9, ground G4 in isotropy stress condition (Table 18 and Table 19).

The numerical simulation steps of tunnel excavation with Disroc code are as follows.

Stage 0: Application of stress conditions in the initial stage.
Before excavation, all the physical properties of the support part remain applied to the existing ground parameters and the physical properties of the beam-lining are set to zero.
Stage 1: Save the condition of stage 0.
It is essential to delete the geometries of segment and grouting interface

Stage 2: Application of first tunnel excavation force as load ratio α.

Save again excavation convergence stress
Stage 3: Recreation of all the geometries previously deleted (segments and grouting interface) and activation of their actual parameters.

Stage 4: Apply remaining (1-α) tunnel excavation force.

- **Tunnel Excavation by load ratio (Rock classification G2-G3-G4, Isotropy**

For the analysis of lining support, the evaluation of member force that means the axial force, moment, and radial displacement would be required.

In the case of an isotropic load, the difference regarding the presence or absence of a segment joint is not really important. The uniform convergence phenomenon is noticeable in the center of the tunnel, so the moment value is close to zero. Thus, the results of the axial force and radial displacement of the lining through the parameter study case of the interface between the lining and the ground are presented depending on the load ratio distribution conditions.

In this part, tunnel excavation simulations have been conducted in an isotropic stress field with three different classes (G2, G3 and G4) of rock properties depending on the stiffness (k_t , k_n) and spacing distance (e) of the interface between the lining and the ground. The material behavior of rock was modeled by means of Elasto-plastic with Mohr-Coulomb criterion. And, as previously mentioned, the interface between lining and ground used a non-linear hyperbolic elasticity Bandis model of which already explained stiffness values vary depending on the distance "e", the simulation of the tunnel excavation is performed in a step-by-step procedure of load ratio as well on the face. The applied material parameters are also described in Table 19.

Table 19. Properties applied of rock classification and interface between Ground-Lining for comparative analysis in this study (Kwak et al. 2016; Salemi, Esmaeili, Sereshki 2015)

<table>
<tr><th colspan="2">Classification</th><th>Unit Weight (kN/m^3)</th><th>Elastic modulus (MPa)</th><th>Poisson's ratio</th><th>Cohesion (kPa)</th><th>Friction angle (°)</th></tr>
<tr><td rowspan="3">Rock</td><td>G2</td><td>25.7</td><td>22,000</td><td>0.22</td><td>2,000</td><td>40</td></tr>
<tr><td>G3</td><td>24.7</td><td>8,000</td><td>0.24</td><td>700</td><td>38</td></tr>
<tr><td>G4</td><td>23.2</td><td>1,500</td><td>0.27</td><td>200</td><td>27</td></tr>
<tr><td colspan="2" rowspan="3">Segment Lining</td><td>23.0</td><td>30,000</td><td>0.2</td><td>-</td><td>-</td></tr>
<tr><td colspan="2">$E^L S/1000$ (kN)</td><td colspan="3">$E^L I/1000$ (kNm^2)</td></tr>
<tr><td colspan="2">15000</td><td colspan="3">312</td></tr>
<tr><td colspan="2">Interface G-L</td><td colspan="2">k_{0t} (kPa/m)</td><td>k_{0n} (kPa/m)</td><td>e 1 (m)</td><td>e 2 (m)</td></tr>
<tr><td colspan="2">Case N5</td><td colspan="2">1E+5</td><td>2E+5</td><td>0.1</td><td>0.01</td></tr>
<tr><td colspan="2">Case N6</td><td colspan="2">1E+4</td><td>2E+4</td><td>0.1</td><td>0.01</td></tr>
<tr><td colspan="2">Stress field</td><td colspan="5">Initial stress</td></tr>
<tr><td colspan="2">Isotropy</td><td colspan="3">P_0 (kPa)</td><td colspan="2">-5424</td></tr>
<tr><td colspan="2">Anisotropy</td><td colspan="2">σ_v (kPa)</td><td>-5424</td><td>σ_h</td><td>-2929</td></tr>
</table>

In Figure 31-a), c) and e), the axial forces at the crown (maximum) point of the 2G, 3G and 4G ground tunnels are represented according to the interface conditions.

The horizontal axis represents the load ratio distribution condition stage. It can be found that the larger the load distribution condition value (load ratio1→load ratio9), the less axial force of the lining supports because the internal displacement has already enough arrived to convergence before the lining is installed.

For example, under any rock classification condition, if the tunnel excavation convergence load ratio before lining installation (Load ratio from 1 to 9 in Table 18) increase and the interface property value (Case N5 > Case N6) is smaller, the results of the member force on the lining will have indicated smaller (Figure 31).

In addition, the results of these graphs show different results depending on the interface conditions (Case N5 to N6 and gap e1, e2 in Table 19).

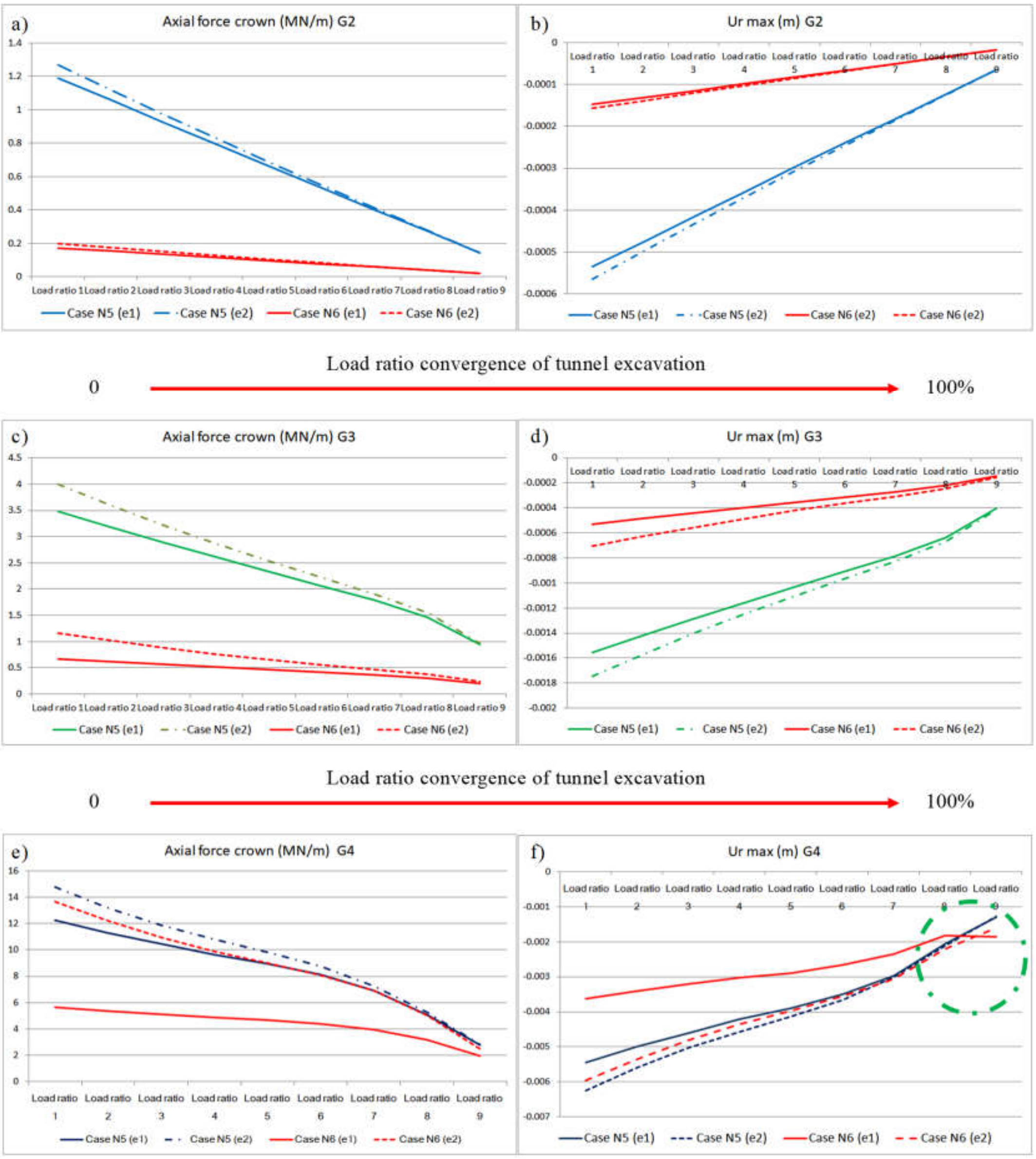

Figure 31. Analysis of volume-type lining member forces according to interface properties Case N5 and Case N6 e1=0.1m, e2=0.01m of interface gap 'e' in rock conditions of G2 a), b), G3 c), d) and G4 e), f)

The higher rock property value(G2), the less the effect of the distance of the interface between the ground and the lining. On the other hand, under relatively low grade rock conditions (G3, G4), interface's distance revealed many effects in the results. For example, the G3 class axial force results (Case N5, e1:0.1m, e2:0.01m) show a difference in axial force of approximately 0.5MN/m despite the same physical properties of the interface and different intervals (Figure 31 c)). So, although the stress supported by the ground due to the same load ratio is the same, the larger the interface's distance (e1>e2), the smaller the member force received by the lining. During the rock grade G4 in Figure 31-e) and f), more dynamic change results can be seen. This could be interpreted as a result of showing the plastic behavior from the early load ratio due to low grade rock.

In the interface relatively large stiffness values, there is little difference in the result value whether the given interface gap (e1>e2) is large or small. However, from the stiffness value Case N5, the axial force received by the lining varies depending on the value of the given interface gap ‘e’. In other words, the larger e-gap, the less axial force the lining supports even under the same ground, load ratio and interface conditions.

This phenomenon shows a more pronounced result as the load because of the load ratio (ex:α=0.1) increases. So, it can be said that the faster a lining is installed, the greater the effect of tail void conditions on the lining.

- **Convergence Confinement Method analysis (rock: 4G).**

As shown in Figure 31 results, the lining member force behavior in the ground 4G class is noticeable depending on the interface conditions. Therefore, in this part, numerical results were interpreted and compared through the Convergence Confirmation Method (GRC-SCC) for the results of the ground class G4 (rock) and the interface stiffness cases N5 and N6 conditions.

Looking at the GRC-SCC graph in Figure 32, it is found that the interface (bleu line) corresponding to the tail void grating affected by the segment rigidity has nonlinear behavior. This means that at the nonlinear behavior of the interface Case N5, it is more dominant than the linear behavior of the segment. As a result, segments taken at the same convergence stress of interface support smaller loads than without an interface and perform linear behavior (green lines) with the elastic rigidity they have.

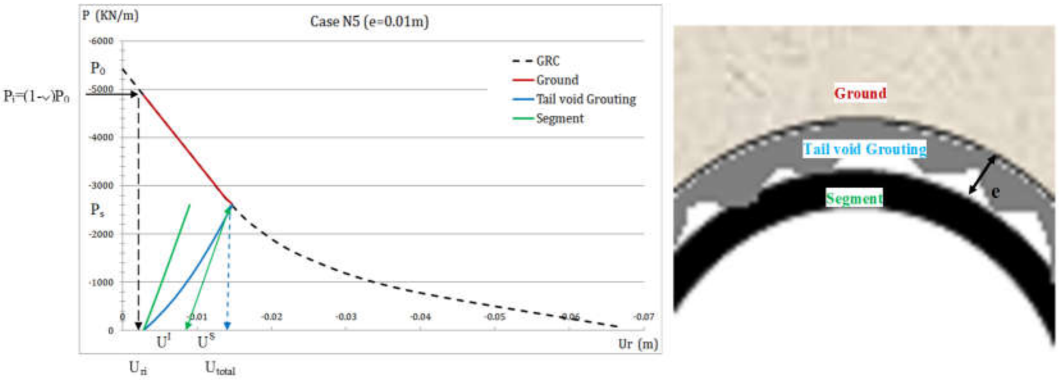

Figure 32. Based on ground 4G and interface Case N5 conditions, Ground Reaction-Support Characteristic Curve by Convergence Confinement method according to load ratio=0.1.

If the interface stiffness was sufficiently large, the two result lines would have been superimposed as the same displacement behavior and linear behavior. As the stiffness of the interface decreases, the two result lines show a difference in results. The larger the difference in the resulting behavior of these two elements (the interface of the tail void and the bulk segment lining), the smaller the convergence force supporting the ground load would be. And the displacement of the interface increases. As a result, segments under the same support load, such as the convergent support load of the interface, will be able to support the reduced load unlike what was expected.

In Figure 32, when the segment stiffness line (green) is moved to the interface behavior line of the tail void grouting (green arrow line), the displacement value of the interface can be determined by the displacement of the segment from the entire internal displacement. The difference between these two displacements does not exceed the preset gap 'e'. Therefore, if the behavior of tail void (blue line) is shown to have the same stiffness slope as the segment lining past the nonlinearity, this can be interpreted as full contact between the two elements. It means that if excess support is received, it may mean that the two elements are in perfect-contact and behave the same together, and furthermore, that the behavior of the interface would exceed the yield criterion.

Figure 33 a) illustrates the comparison of the results due to only the gap between the lining and the ground 'e' in the interface N5 case, i.e., when all the ground conditions are the same. The behavior of tail void grouting (blue line, blue dotted line) converges faster when the gap ‘e’ is narrower to support these large loads. And it also shows that the tangential slope (red arrow dotted line) at the equilibrium convergence support force becomes more similar to the segment lining stiffness slope value than when the gap is wide.

Figure 33 b) presents that the slope (Case N6, red arrow dotted line) at the final convergence support equilibrium point is the same as the segment lining stiffness gradient (blue arrow dotted line) when the interface gap 'e' is the same but the stiffness value (Case N6) of the interface is small in other cases. Here, in other words, rather than interpreting that the interface supports the ground, it can be interpreted that segment lining has begun to fully support the ground.

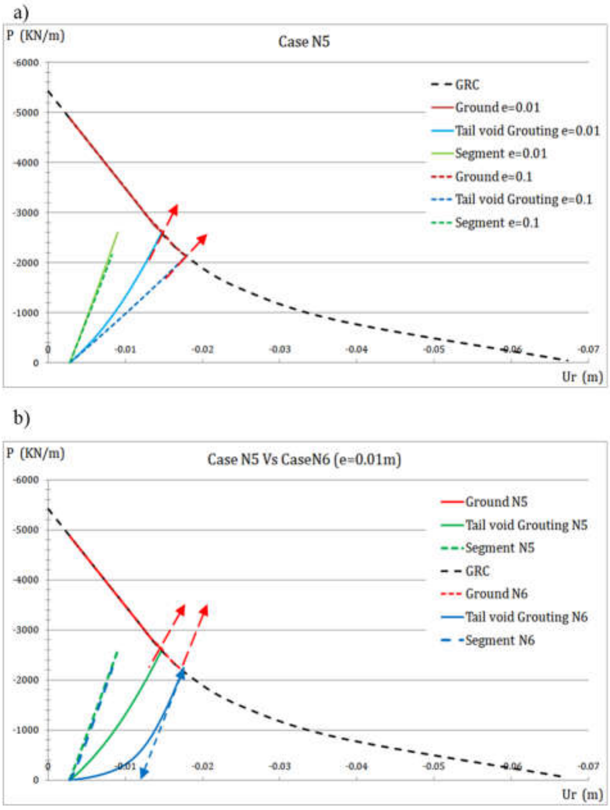

Figure 33. Comparative GRC-SCC analysis of a) different gap 'e' under interface Case N5 condition and analysis of b) different interface condition N5, N6 (4G, load ratio=0.1).

4.3. Evaluation of effort in segments on contact joints by numerical analysis

Segmental joints are the weakest points in the tunnel, and their design must be carefully considered to ensure that they can withstand the loads imposed by the tunneling process and must be designed to resist the loads from ground pressure, water pressure, and other external forces.

Furthermore, in the design of the segmental lining joints, the potential for differential settlement must also be considered, which can cause significant damage to the tunnel (Liu et al. 2017).

The segmental joint of infrastructures is characterized by several rings composed by precast segments in contact. So, the mechanical response of this type of lining is significantly influenced by the behavior of the joints (Lee et al. 2001; Andreotti et al. 2020; Do et al. 2013; Li et al. 2015; Zhang et al. 2019; Blom 2002).

In general, there are limitations in modelling analysis considering various ground conditions along with segment joint modelling of linings.

For example, joints modelling method on the effect of contact points in the structural analysis of segmental lining can be categorized into (Salemi, Esmaeili, Sereshki 2015).

Hinges model: beam elements considering perfect hinges in their contact locations. Disadvantage: more bending moment in the liner than other contact models. It does not simulate properly the actual construction conditions but considers joints as a hinge while ignoring partial moment transmitting capacity.

Reducing liner rigidity model: continuous ring with discounted rigidity by applying a reduction factor $\eta \leq 1$, to the bending stiffness (EI) of liners.

Disadvantage: although effective bending rigidity must only affect contact points, it affects the entire lining by ratio of the bending rigidity (Morgan 1961; Einstein, H.H., Schwartz 1979; Lee et al. 2001; Blom 2002).

Effective moment of inertial model: same length for each segment in the case of segment number of n>4 and introduced the effective moment of inertia of liners (Muir Wood 1975).

Disadvantage: segments have the same length in a ring.

Finally, Rotational springs model: segments are modeled by beam elements and longitudinal joints using rotational springs. It is often used to analyze the lining behavior due to joints in elastic ground like the beam-spring model or to analyze intensively the ground behavior by simplifying the lining.

However, since consideration of complex ground conditions (ex: fault, earthquakes, water pressure) and behavior analysis of segment by joints are both important parts that influence each other, it can be said that modelling analysis is appropriate when analyzed together. If it is possible to analyze the segment lining behavior including joints and even the complex ground, it would be possible to model various ground, such as fault zone conditions, fracture zones, or seismic impact ranges.

Segment joints can be divided into two parts and named according to the direction of the segment surfaces in contact. There are interring joints in the circumferential direction of the tunnel in Figure 34. In this part, it is needed to analyse the three-dimensional response of the lining by increasing the interaction between adjacent rings due to the force that advances in the transverse direction of the TBM (Tunnel Boring Machine) during construction. However, in long-term stress behavior analysis, the axial force in the joint tends to be significantly reduced (Arnau, Molins 2011; Zhang et al. 2019), so the interaction between adjacent rings becomes less important than radial loading. Under these conditions, a two-dimensional analysis is also reasonable because the mechanical behavior of the segment lining is affected by the solution of the radial joint (Figure 34) (Luttikholt, Vervuurt, den Uijl 2008; Li et al. 2015; Zhang et al. 2019).

In this study, as 2D numerical modelling, it has been attempted to model the volumetric segment lining by considering the effects of joints between segments, and this analysis provided an opportunity to compensate for the limitations encountered in the previous.

The indirect methods (previously mentioned methods: Hinges model, Reducing liner rigidity model, Effective moment of inertial model, Rotational springs model) simplify the tunnel lining into a ring of uniform stiffness and apply a reduction factor to the bending stiffness of the tunnel lining. Although this is computationally cost effective, it cannot reliably evaluate relative rotation and quantification of joint openings. In the direct method, each precast segment and joints are explicitly modelled. Classical interface models for longitudinal joints were developed by Gladwell (1980) and Janssen (1983) (Zhang et al. 2019; Andreotti et al. 2020). The fundamental assumptions of both models are linear material behavior of concrete and unreinforced interfaces. However, it is necessary to structurally apply and analyse the limit-damage model depending on the contact area of the segment joint and the transmitted load. Therefore, in this part, an attempt was made to evaluate the effect of the nonlinear behavior joint model in addition to the case studied in the previous part (evaluation of the interface effect of lining and ground).

First, after finding a clear relationship between the stiffness and normal stress of the interface in contact with the joints, the behavior of the segment was simulated by applying Bandis Elastic to a nonlinear interface element (FEM code: DISROC-Fracsima, 2016).

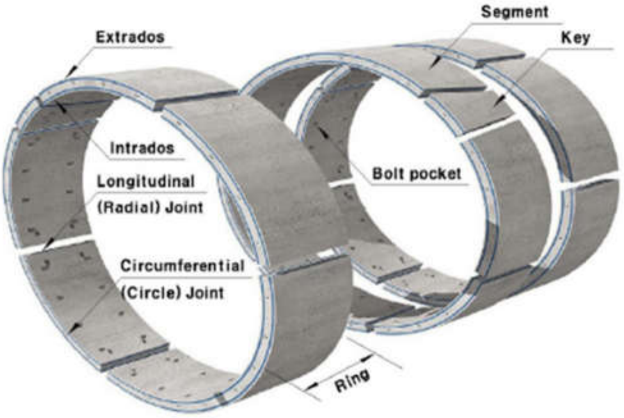

Figure 34. Illustration of segments and joints (Woo and Yoo., 2015)

4.3.1. Geometry of segment and joint parameters as non-linear interface

Since the lining of the segment tunnel has longitudinal joints, it is unreasonable to assume that it is a continuous ring-beam. Therefore, in order to approach the actual internal force displacement values of these joints, the effect of the segment joint material properties must be evaluated.

In the study of SALEMI.A et al (2015), the mechanical behavior of longitudinal joints in segmental lining was studied in order to find a definite relationship between stiffness of contact points and normal stress in contact locations. In other words, their research tried to develop a precise contact model based on experimental direct shear tests on the concrete samples of contact points in segments. We focus here on the results of the experimental tests they performed on concrete samples. Their experimental results are a good source to be applied to our numerical joint model.

In that research, the relation of the contact shear and normal reaction module in compression normal condition (Figure 35) was found.

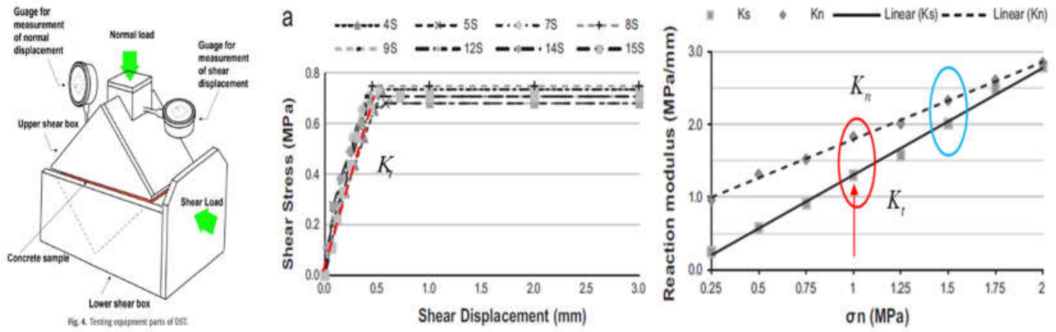

Figure 35. Experimental data on segment joint properties by SALEMI.A et al 2015 (Case -condition: the normal stress 1MPa without gasket)

The contact shear and normal reaction modules K_t and K_n were related to contact normal stress via two linear regression equations. The joint stiffness formula required for our joint model is as Eq(104).

$$\begin{bmatrix} K_n = 730100 + 1106380\sigma_n \quad kPa/m \\ K_t = \pm 168400 + 1472500\sigma_n \quad kPa/m \end{bmatrix} \tag{104}$$

(Salemi, Esmaeili, Sereshki 2015)

After referring to the research data by SALEMI, Akbar et al (2015),

In order to apply to our joint model, the Bandis nonlinear elastic model, the initial stiffness value, which is a parameter of the joint, is requested. To do so, if Eq (104) is replaced with the Bandis nonlinear model, initial stiffness parameter and "e"(gap of joint) are obtained.

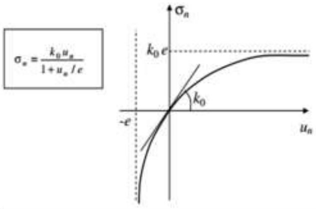

21200 Non-linear hyperbolic elastic joint

Nb: 4
Param1 = k_{0t} (tangent stiffness)
Param2 = k_{0n} (normal stiffness)
Param3 = $K_{nt} = K_{tn}$ (non diagonal stiffness → dilatancy)
Param4 = e (maximum closure or physical thickness

Bandis(1981,1983)

$$\begin{bmatrix} K_n = \dfrac{k_0}{1+u_n/e} \\ \sigma_n = -K_n u_n \\ K_n = \dfrac{k_0}{1-\dfrac{\sigma_n}{K_n e}} \\ K_n = k_0 + \dfrac{\sigma_n}{e} \end{bmatrix} \begin{bmatrix} K_t = \dfrac{k_{0t}}{1+u_n/e} \\ \sigma_t = K_t u_t \\ K_t = \dfrac{k_{0t}}{1+\dfrac{\sigma_t}{K_t e}} = k_{0t}(1-\dfrac{\sigma_n}{k_{on} e}) \\ K_t = k_{0t} - \dfrac{\sigma_t}{e} \end{bmatrix} \Leftrightarrow \begin{bmatrix} K_n = 730100 + 1106380\sigma_n \ kPa/m \\ K_t = \pm 168400 + 1472500\sigma_n \ kPa/m \\ e = 9E-7m \end{bmatrix}$$

Figure 36. Transformation process of relational form of shear and normal stress according to reaction coefficient of joint concrete sample test and Bandis nonlinear elasticity model (Disroc-FEM)

The joint gap "e" obtained here is 9E-7m, so it is very small. Looking at the non-linear hyperbolic graph in Figure 36, a very small "e" means a very large stiffness value. This has no discriminative power in evaluating the effect of the presence or absence of a joint. So we tried to simulate here two different cases for the joint spacing "e". This is an attempt to change the joint stiffness value depending on the normal stress.

The final total parameters applied to the numerical analysis performed in this section are shown in Tables 19, 20.

Table 20. Properties applied of rock classification, interface between Ground-Lining and joint for comparative analysis in this study (Kwak et al. 2016; Salemi, Esmaeili, Sereshki 2015)

Classification		Unit Weight (kN/m3)	Elastic modulus (MPa)	Poisson’s ratio	Cohesion (kPa)	Friction angle (°)
Rock	G3	24.7	8,000	0.24	700	38
	G4	23.2	1,500	0.27	200	27
Joint		k_{0t} (kPa/m)	k_{0n} (kPa/m)		e 1 (m)	
		730100	168400		9E-07	
Interface G-L		k_{0t} (kPa/m)	k_{0n} (kPa/m)		Case1 :e 1 (m)	Case2 :e 2 (m)
Case N3		1E+7	2E+7		0.1	0.01
Case N4		1E+6	2E+6		0.1	0.01
Case N5		1E+5	2E+5		0.1	0.01
Case N6		1E+4	2E+4		0.1	0.01

Figure 37 shows different geometries in accordance with the presence or absence of joints in the numerically analyzed segment lining. Except for the joint part, all other dimension conditions are the same.

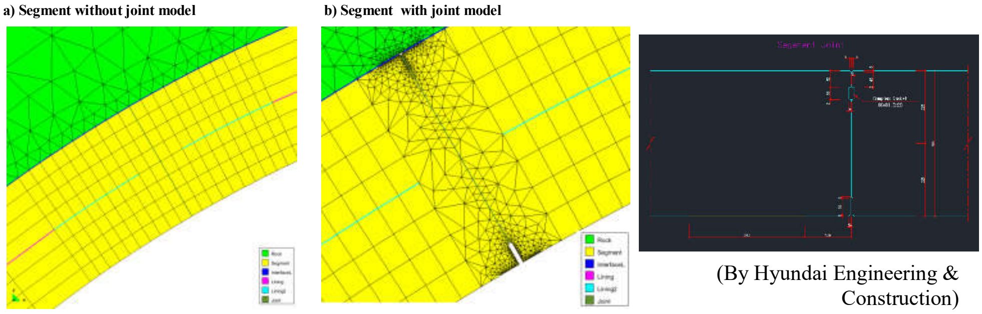
a) Segment without joint model

b) Segment with joint model

(By Hyundai Engineering & Construction)

Figure 37. Segment Lining Geometry By GID: a) Segment Lining Geometry without Joints, b) Geometry with Joints in Actual Segment Lining Design Parts by Hyundai E&C and Korea Expressway Corporation.

4.3.2. Numerical analysis result in isotropic and anisotropic stress field

- **<u>Analysis of the segment joint model in ISOTROPIC field (G3, G4)</u>**

This is the analysis of comparing the lining member force and radial displacement depending on the isotropic stress field of rock G3 and G4 grades with and without joints.

First, looking at the conditions considered for the analysis of the results, G3 and G4 different grades of ground conditions.

Second, by using an interface (as tail void) element, which is a nonlinear elastic model between the lining and the ground, the condition of the difference between the stiffness of case N3 ~ N4 and the gap between e1 and e2.

Third, the condition of the initial stress received by the outer wall of the lining due to the convergence of the tunnel excavation (load ratio).

And finally, the segment joint model condition.

The first to third conditions are the same as those in the previous analysis CH 4.2, but here are the results of comparative analysis according to the presence or absence of the joint model by applying the segment joint model.

In a deep isotropic stress field, it can be said that the axial force, Ur, of all linings is the same in all directions. And since the value of the bending moment of the lining in the isotropic stress field is close to zero, the moment result analysis is omitted.

Figure 38 shows the result analysis according to the different stiffness of the interface between each lining and the ground when the ground condition is G3 and Figure 38 is when the ground condition is G4.

In Figure 38 (a, b, e, f) and Figure 39 (a, b, e, f), a relatively large stiffness value (Case N3 to N4) was applied to the interface between the lining and the ground. Therefore, regardless of whether the interface gap value is large or small, and whether or not the segment joint model exists, the same result behaviors are shown according to the tunnel excavation convergence stage. However, if there is a difference, in G4, where the ground is relatively soft, non-linear results due to early elasto-plastic progression and greater axial force and consequently greater displacement can be seen.

In Figure 38 and Figure 39 (c, d, g, h), the stiffness of the interface between the lining and the ground varies depending on the gap between the interface intervals from Cases N5 and N6. However, it can be seen that the difference regarding the presence or absence of the joint is still not important. This is interpreted as the fact that the condition of the given ground is good, and the difference according to the presence or absence of the joint model is not large.

Therefore, in an isotropic stress field and in the case of a relatively good homogeneous rock mass, segment linings can be modeled as a continuum (ring) without considering the presence of joints.

But, from Case N6-Figure 38, 39 (d, h), the result value depending on the presence or absence of a joint starts to show a difference even though it is subtle. Although the most notable difference in Figures 38 and 39 (c, g, d, h) is in fact the different result values due to the interface gap (e1:0.1m, e2:0.01m), looking at the results of Case N6, the axial force of the Gap(e2)-joint model shows a larger value than the Gap(e2)-Cont continuum model. And, the difference in accordance with the presence or absence of the joint model in the isotropic stress field is not very noticeable, but in Figure 39 (h), when the interface gap is 0.1m (e1), if the lining is installed after the tunnel excavation displacement convergence step is 80% (load ratio 0.8), it starts to show a significant difference in the displacement results of the continuum model and the joint model.

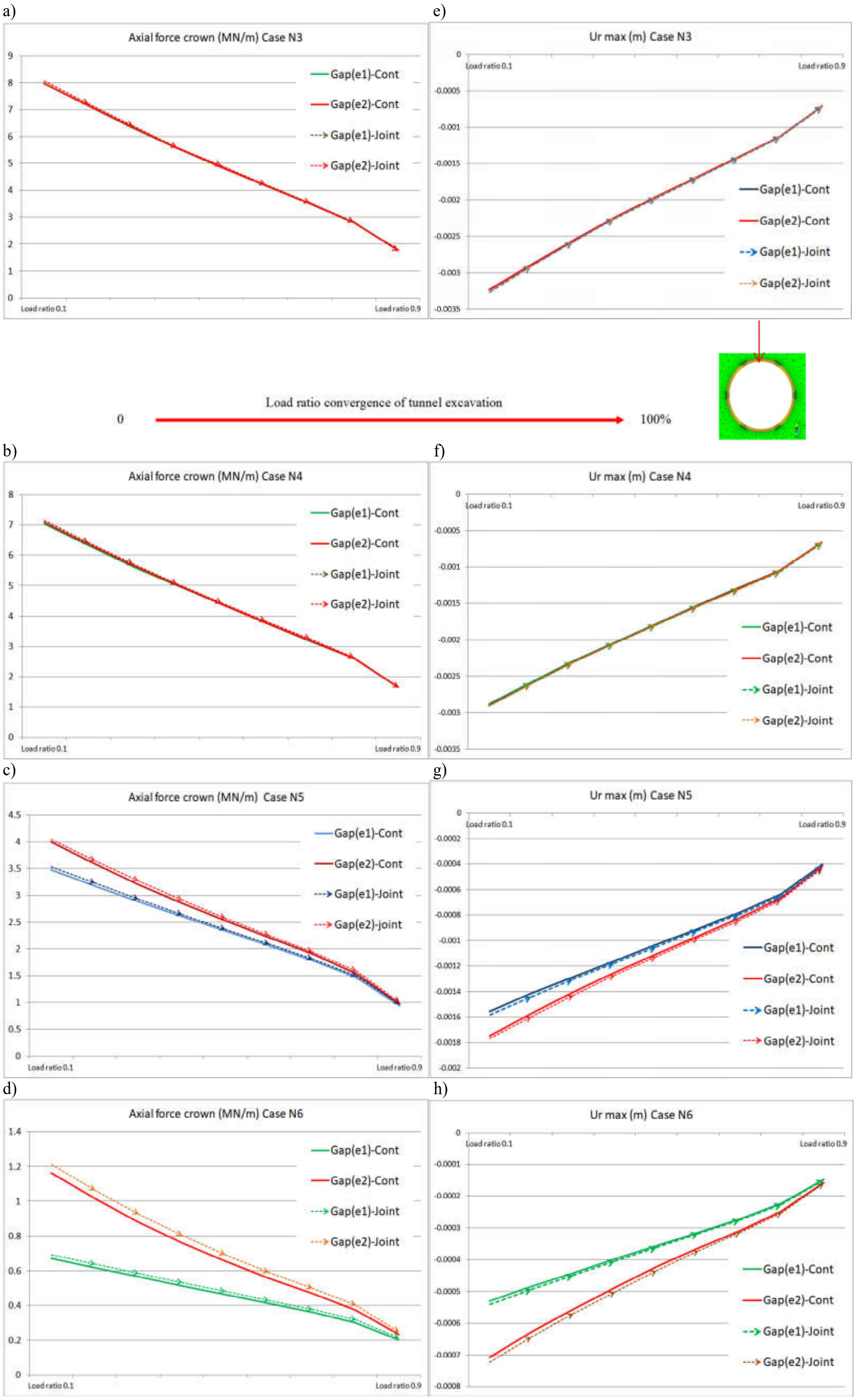

Figure 38. Analysis of the continuum or joint lining model for the 4 stiffness cases of the interface in the isotropic (G3) field. a),b),c),d): Axial force, e),f),g),h): Radial displacement. Gap(e1): gap of interface 0.1m, Gap(e1): gap of interface 0.01m. Cont: continuum lining, Joint: joint lining model.

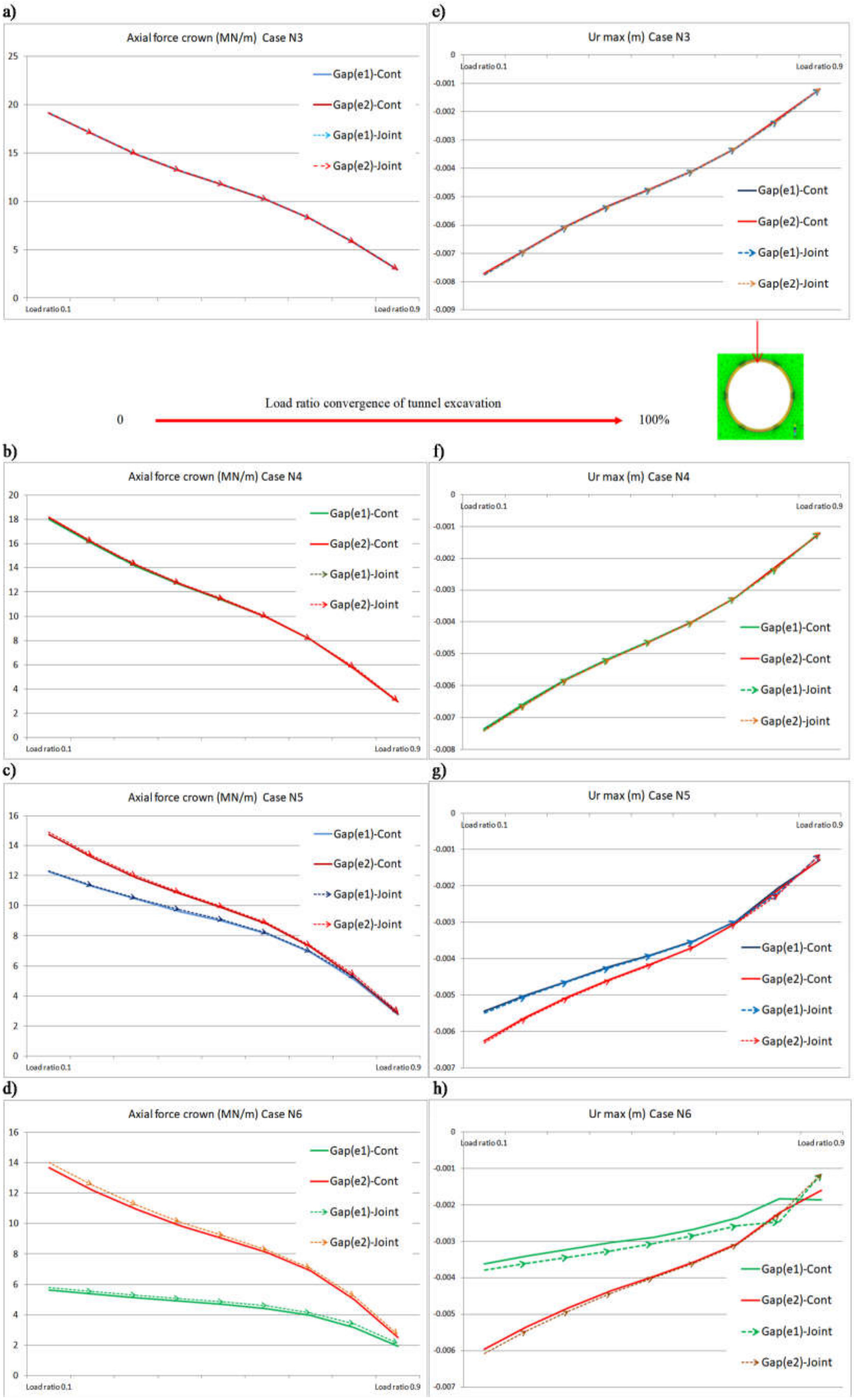

Figure 39. Analysis of the continuum or joint lining model for the 4 stiffness cases of the interface in the isotropic (G4) field. a),b),c),d): Axial force, e),f),g),h): Radial displacement. Gap(e1): gap of interface 0.1m, Gap(e1): gap of interface 0.01m. Cont: continuum lining, Joint: joint lining model.

- **Analysis of the segment joint model in ANISOTROPIC field (G3, G4)**

In the anisotropic stress field, unlike the isotropic stress field, the lining member force and displacement are clearly different in all directions of the tunnel circle. Therefore, the tunnel crown point, 45 degrees, and 60 degrees' points of the lining members were examined.

First of all, in the anisotropic stress field (earth pressure coefficient K0:0.5), Figures 40 (ground G3) and 41 (ground G4) are the axial force and displacement values of the lining at the crown point. When the ground grade is G3 (Figure 40), most of the results show a linear decrease in elastic behavior according to the tunnel excavation coefficient load ratio. The ground grade G4 (Figure 41) also shows a similar pattern. But, in Case N6 (Figure 41 (h)), a difference in displacement results due to the influence of interface properties can be seen.

This looks like the same as the result mentioned in the previous isotropic stress field. Looking at these two results (Figures 40 and 41), no significant difference was found between the results of the joint model and the continuum model at the crown point even in the anisotropic stress field.

In order to find a noticeable difference in results in the comparative analysis of the continuum lining model and the joint lining model, let's look at the lining member force at different points. For example, Figure 42 and Figure 43 are the results of the part at the 45° point in the clockwise direction of the tunnel for grade 3 and grade 4 ground. In the result analysis of interface cases N3 to N5, no significant difference was found, but in case N6 with a relatively low interface stiffness value (Figure 42, 43-d)), the joint lining model produced slightly larger axial force values than the continuum lining model. On the other hand, in the displacement results of Figure 42 (h), it can be seen that the value of negative radial displacement toward the inside of the tunnel has a lower value in the joint model. However, when the interface stiffness is low and the gap (e1: 0.1m) is large in the case of Figure 43 (h), at the soft ground (G4), irregular patterns are shown. In addition, this shows an irregular aspect as the tunnel excavation convergence step proceeds before the lining installation.

Figures 44 and 45 are the results at the 60° point in the clockwise direction of the tunnel. In the results of Figure 44 (g) and Figure 45 (g, h), it can be seen that the displacement at the 60-degree point changes direction according to the tunnel excavation convergence stage. When the tunnel convergence excavation stage is low (load ratio 0.1, lining installation after 10% tunnel excavation convergence), there is a pattern of displacement moving outside of the tunnel (positive displacement), but after the load ratio has passed considerably (about load ratio 0.5), we can see how the displacement moves inward (negative displacement).

Although those of results are very small, it can be seen that the results of the joint model and the continuum lining model are different aspect when the direction of movement changes. In particular, the analysis difference between the joint model and the continuum model begins to show in the soft ground when interface properties between the ground and the lining are lower.

In general, as shown in the previous results, the displacement decreases with the axial force at each stage of the load ratio. However, in Figure 45 (e, f, g, h), although the result value itself is small, it shows a different pattern of behavior.

This aspect is the reason why the lining installation time and the grouting properties should be considered at the same time when the grouting (interface) property values and behavior process are not clearly known. This is because the grouting hardening between the lining and the ground is not sufficiently hardened in the soft ground.

Figure 46 to Figure 49 show the results of the axial force, radial displacement, and moment of the lining in the circular direction of the tunnel. This makes it possible to see the lining behavior in the entire tunnel direction at a glance.

First of all, looking at Figures 46~49 (b), when the interface stiffness between the lining and the ground is low (Case N6), different axial force results due to the gap difference can be seen. And it can be seen that the axial force value of the joint model is slightly larger than the axial force value of the continuum model.

As an example, Figure 46 is the result of comparative analysis of interface stiffness values Case N3 and Case N6 when the load ratio is 0.1 (10% excavation convergence) in the G3 ground grade. The part where the difference between the continuum model (non-joint model) and the joint model can be clearly seen is the moment part. In the joint model, the moment was cut by the joint part, so the overall value is lower than that of the continuum model.

As the anisotropy characteristic of the lining in the hard ground increases, the difference between the moment values of the joint model and the continuum model becomes significant.

Therefore, when looking at the moment change, it is necessary to look at the anisotropy ratio of the axial force of the lining. For example, although Figure 47 (a) has a smaller axial force than Figure 48 (a) because the load ratio is 0.7, the anisotropy of vertical and horizontal forces is greater, so the difference between the moment value is more noticeable. And in the case of a good grade of ground and a good interface stiffness between the ground and the lining, there is little difference in axial force and displacement between the joint model and the continuum model, even considering tunnel excavation convergence.

However, the moment difference (Figure 46, 49(e)) of the joint model and the continuum model is shown a little bit. This difference is not significant in the relatively low grade of the ground.

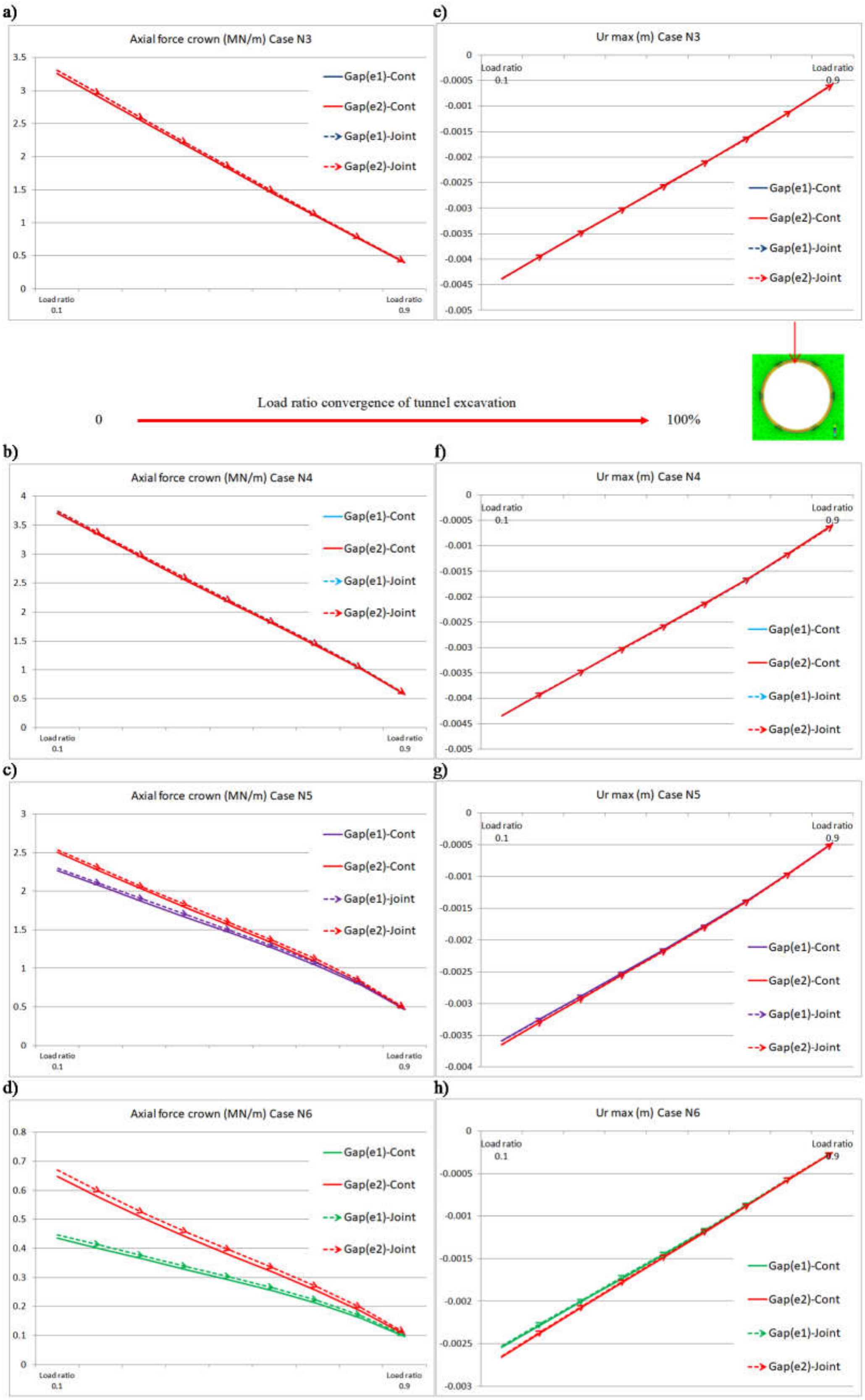

Figure 40. Analysis of the continuum or joint lining model for the 4 stiffness cases of the interface in the anisotropic (G3-Crown point) field. a),b),c),d): Axial force, e),f),g),h): Radial displacement. Gap(e1): gap of interface 0.1m, Gap(e1): gap of interface 0.01m. Cont: continuum lining, Joint: joint lining model.

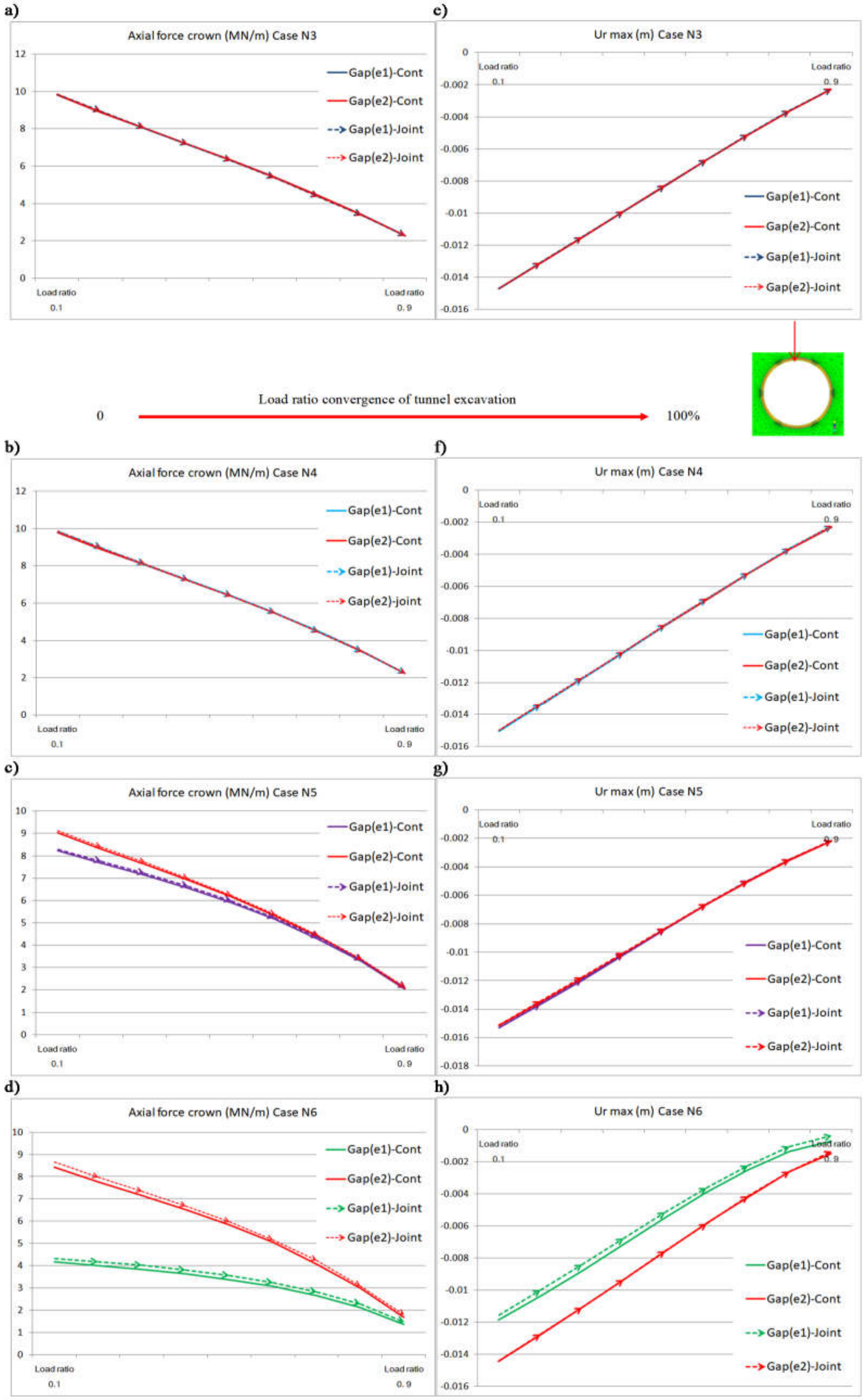

Figure 41. Analysis of the continuum or joint lining model for the 4 stiffness cases of the interface in the anisotropic (G4-Crown point) field. a),b),c),d): Axial force, e),f),g),h): Radial displacement. Gap(e1): gap of interface 0.1m, Gap(e1): gap of interface 0.01m. Cont: continuum lining, Joint: joint lining model.

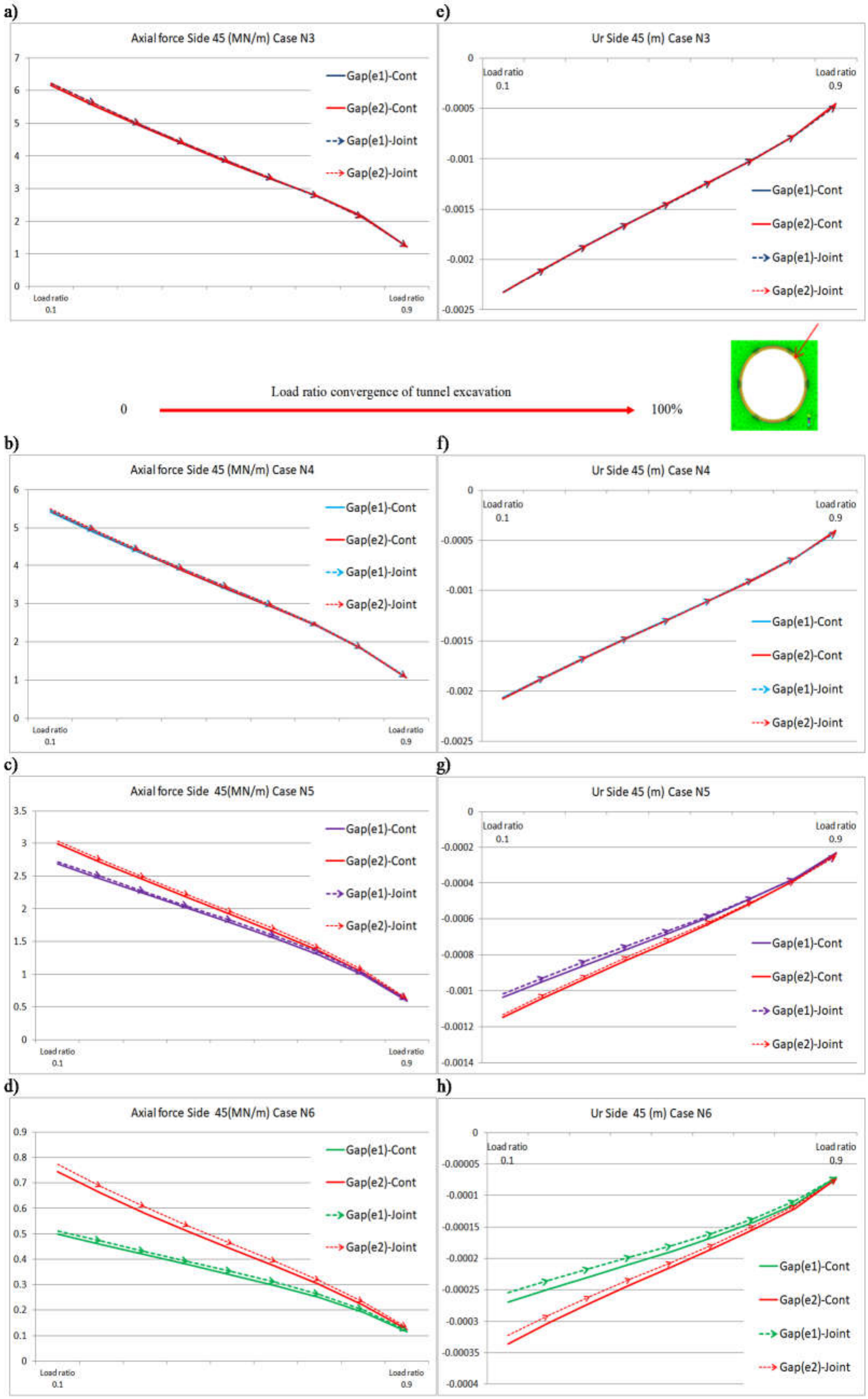

Figure 42. Analysis of the continuum or joint lining model for the 4 stiffness cases of the interface in the anisotropic (G3-45° point) field. a),b),c),d): Axial force, e),f),g),h): Radial displacement. Gap(e1): gap of interface 0.1m, Gap(e1): gap of interface 0.01m. Cont: continuum lining, Joint: joint lining model

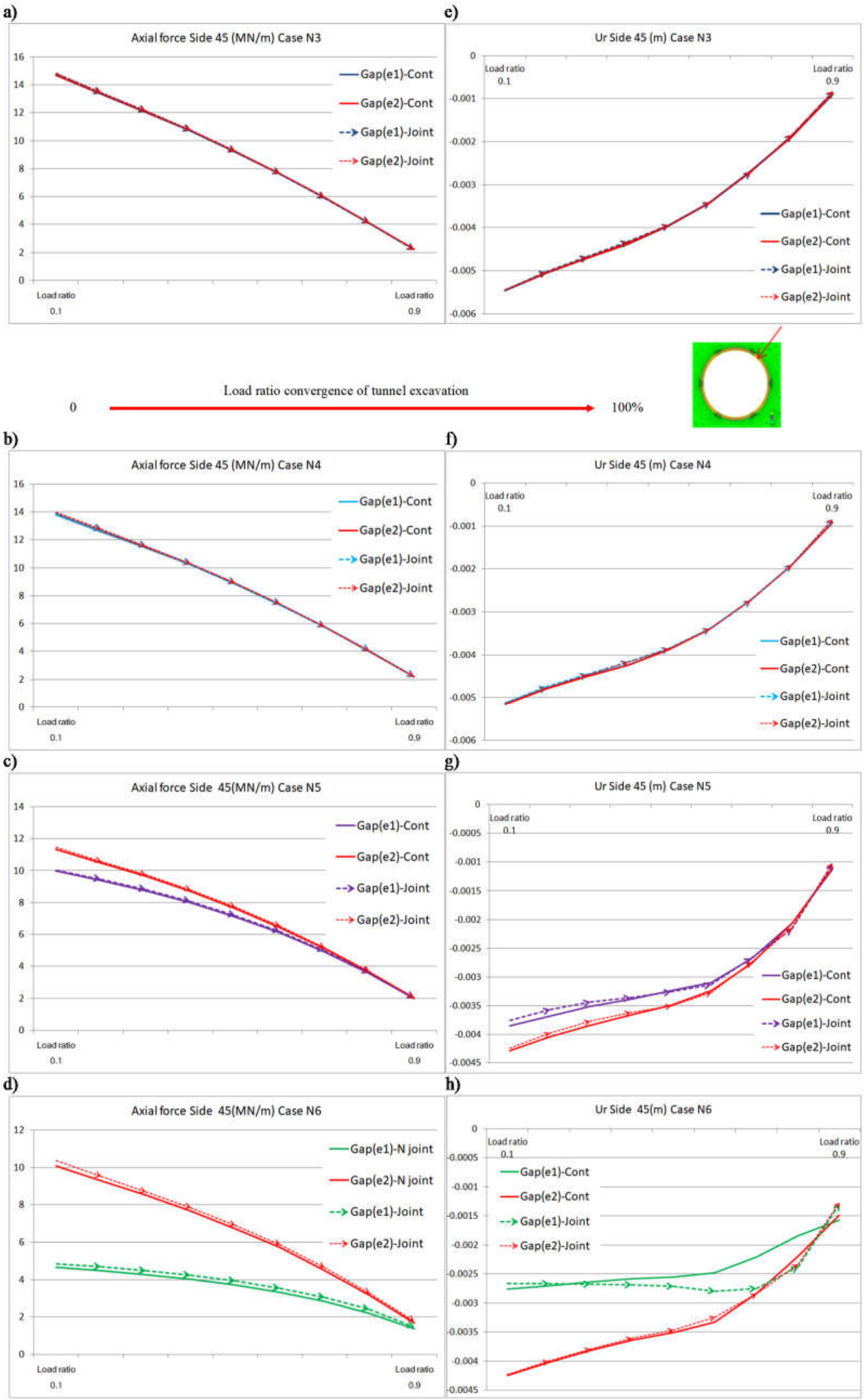

Figure 43. Analysis of the continuum or joint lining model for the 4 stiffness cases of the interface in the anisotropic (G4-45° point) field. a),b),c),d): Axial force, e),f),g),h): Radial displacement. Gap(e1): gap of interface 0.1m, Gap(e1): gap of interface 0.01m. Cont: continuum lining, Joint: joint lining model.

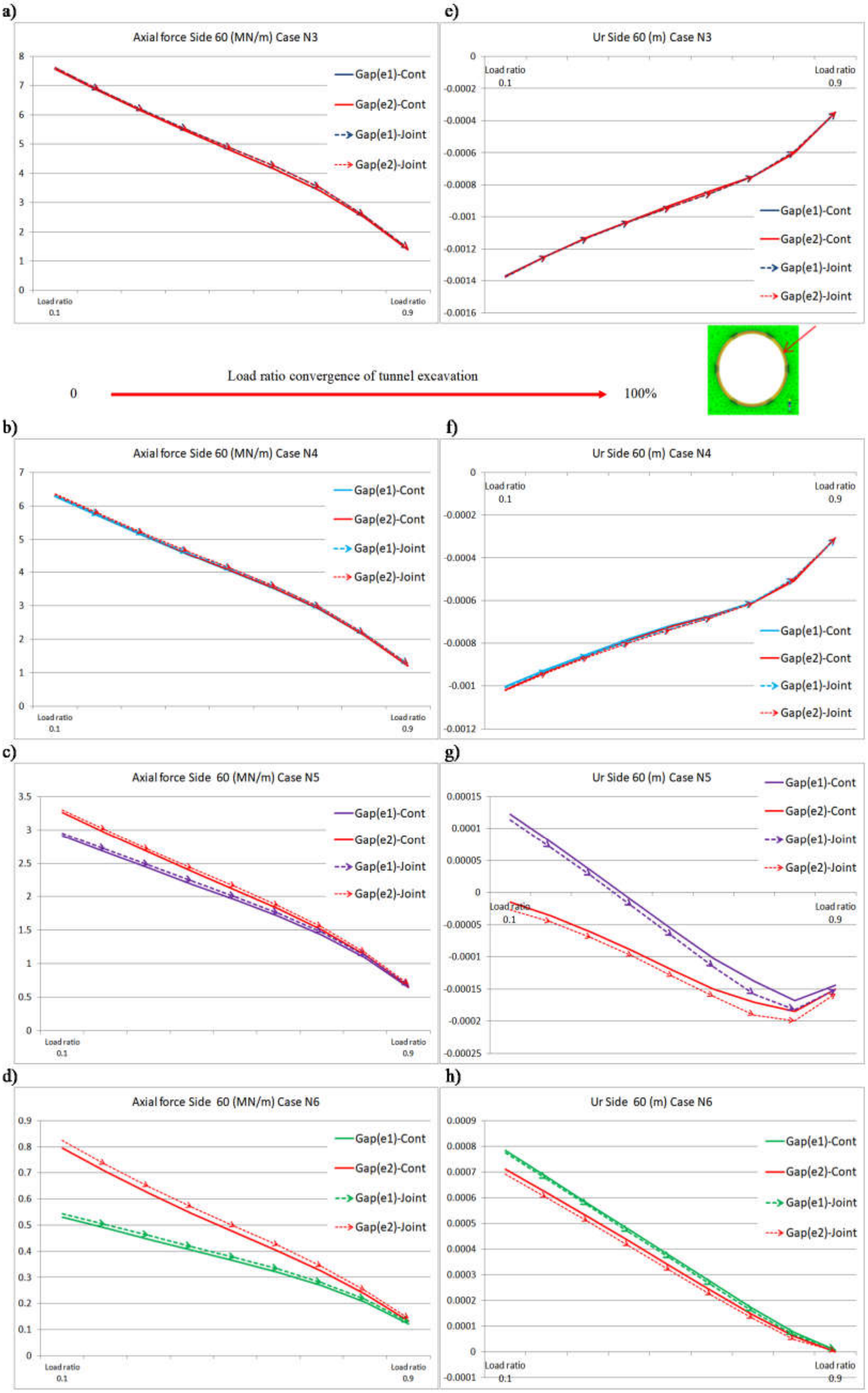

Figure 44. Analysis of the continuum or joint lining model for the 4 stiffness cases of the interface in the anisotropic (G3-60° point) field. a),b),c),d): Axial force, e),f),g),h): Radial displacement. Gap(e1): gap of interface 0.1m, Gap(e1): gap of interface 0.01m. Cont: continuum lining, Joint: joint lining model.

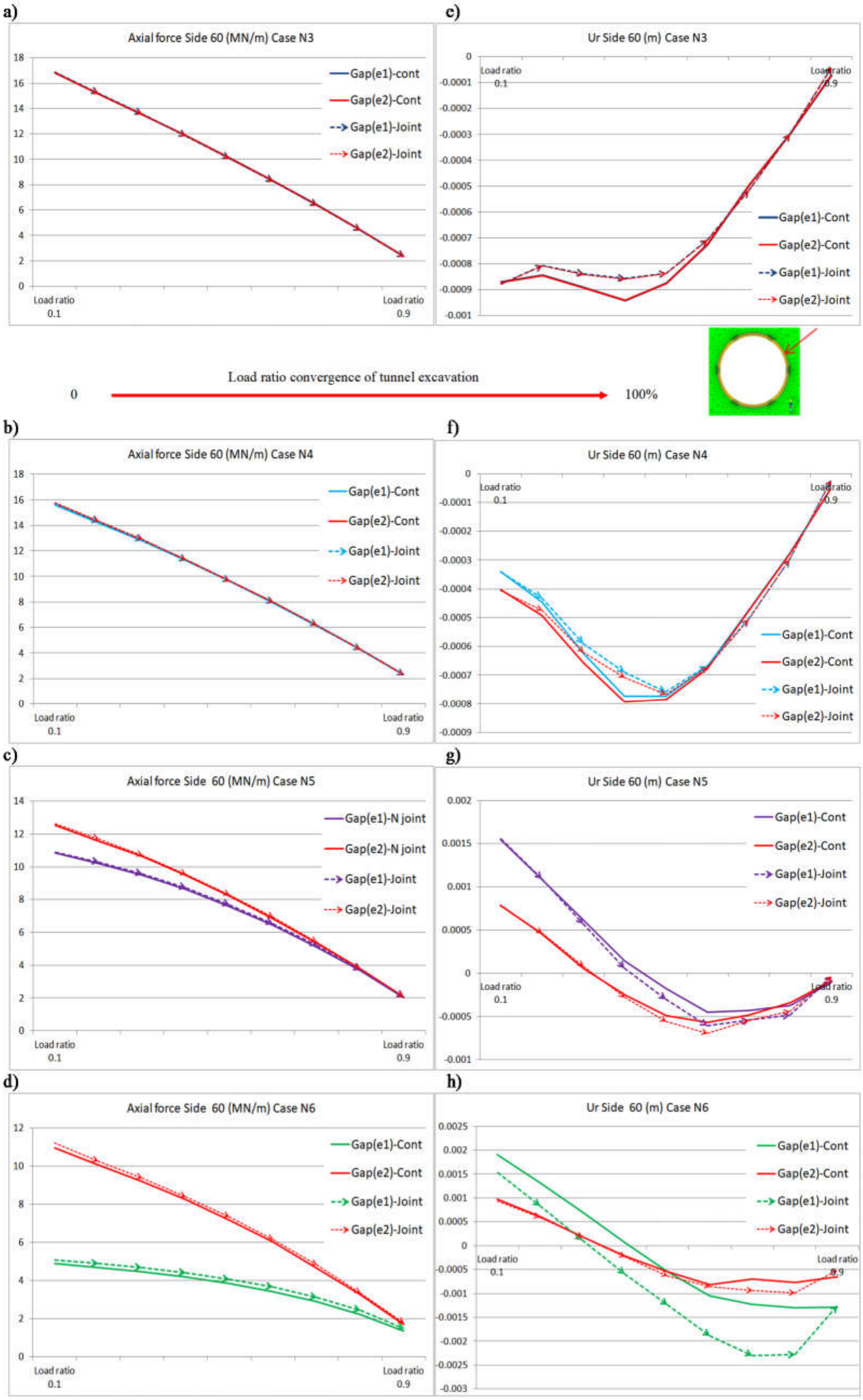

Figure 45. Analysis of the continuum or joint lining model for the 4 stiffness cases of the interface in the anisotropic (G4-60° point) field. a),b),c),d): Axial force, e),f),g),h): Radial displacement. Gap(e1): gap of interface 0.1m, Gap(e1): gap of interface 0.01m. Cont: continuum lining, Joint: joint lining model.

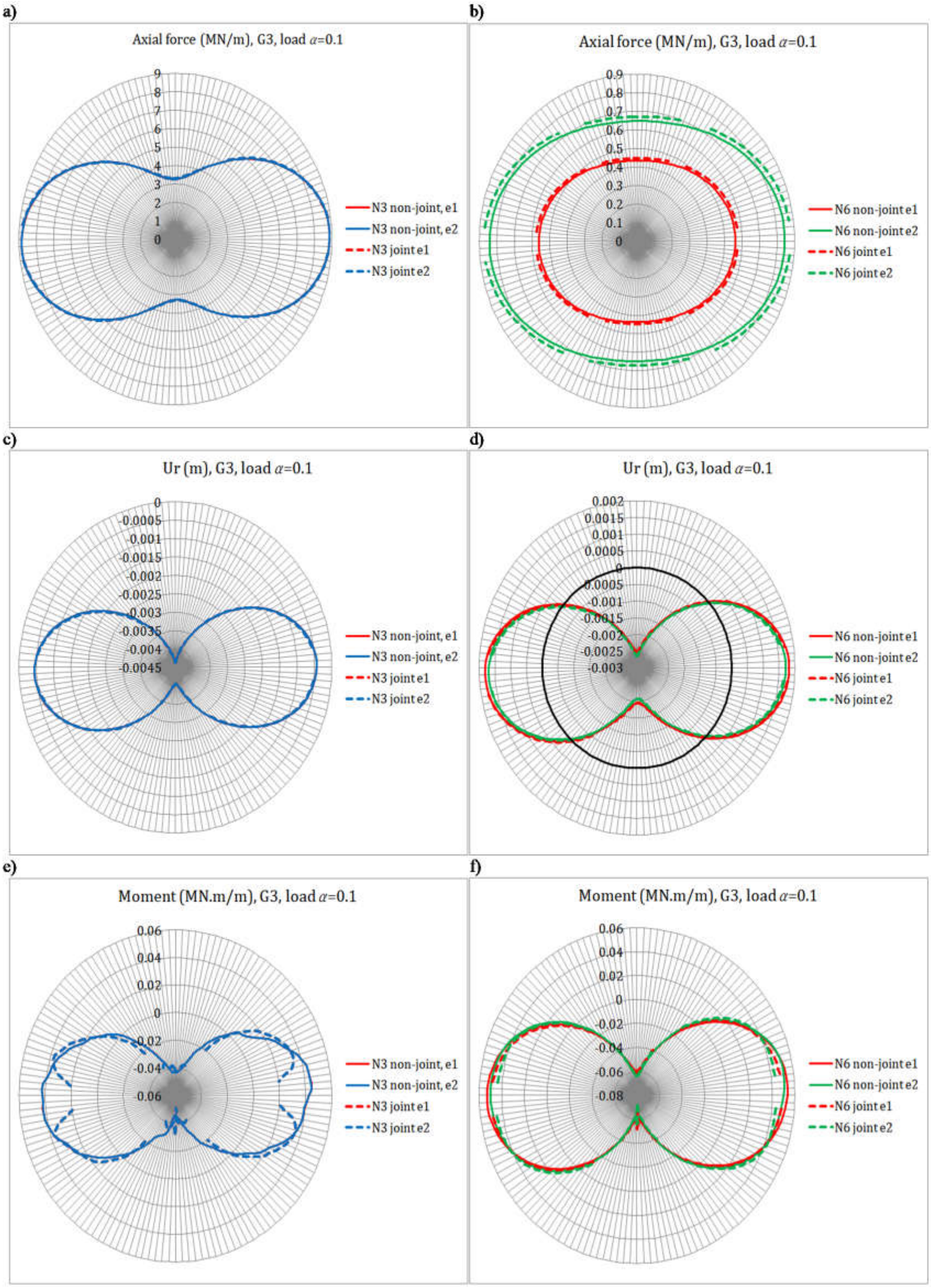

Figure 46. Axial force, radial displacement and moment of circular lining of tunnel according to interface stiffness (Case N3, N6) in ground G3, load ratio 0.1 (lining installation after 10% tunnel excavation convergence), non-joint: continuum model, joint: joint model, interface gap e1: 0.1 m, e2: 0.01 m

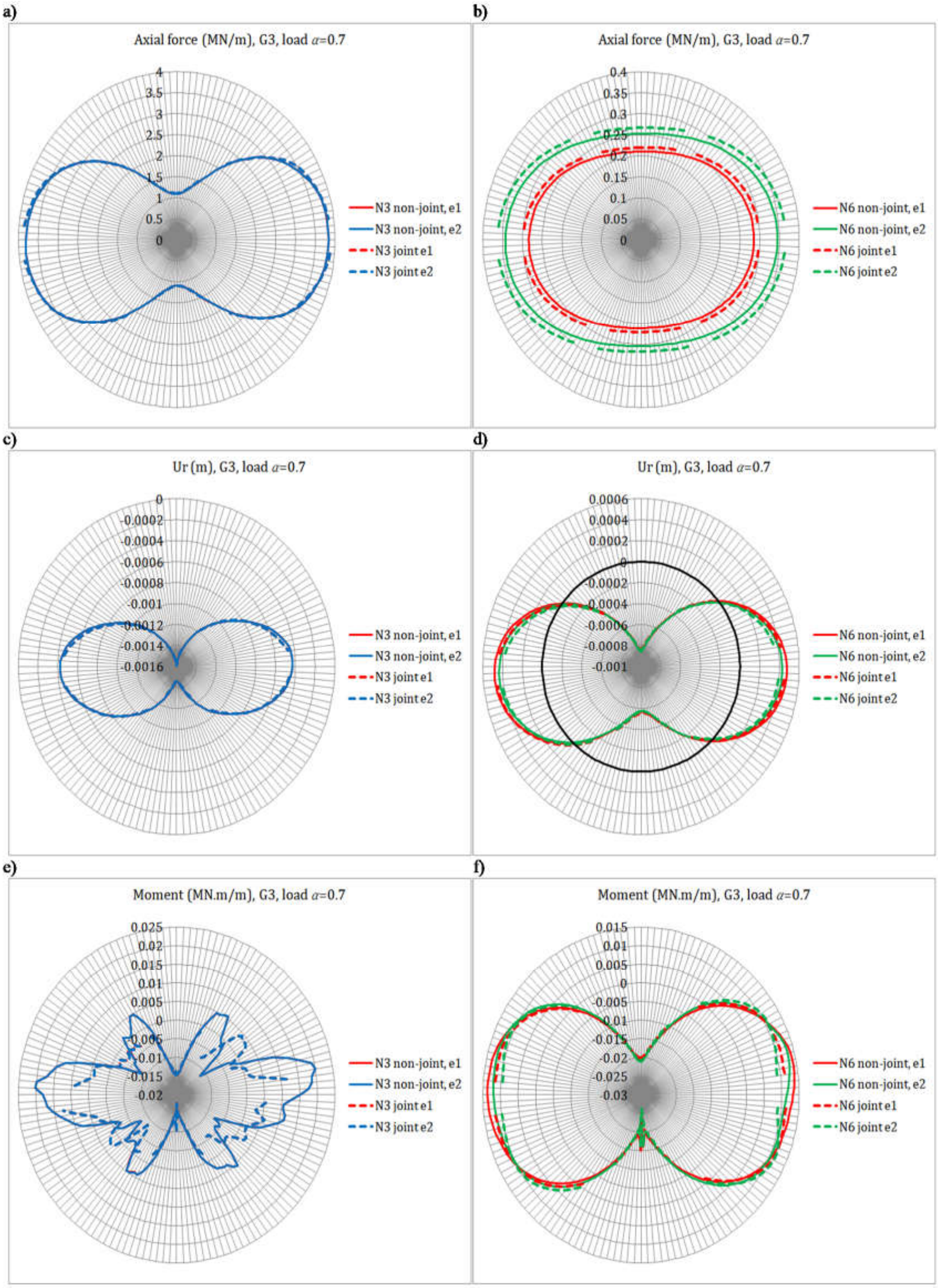

Figure 47. Axial force, radial displacement and moment of circular lining of tunnel according to interface stiffness (Case N3, N6) in ground G3, load ratio 0.7 (lining installation after 10% tunnel excavation convergence), non-joint: continuum model, joint: joint model, interface gap e1: 0.1 m, e2: 0.01 m

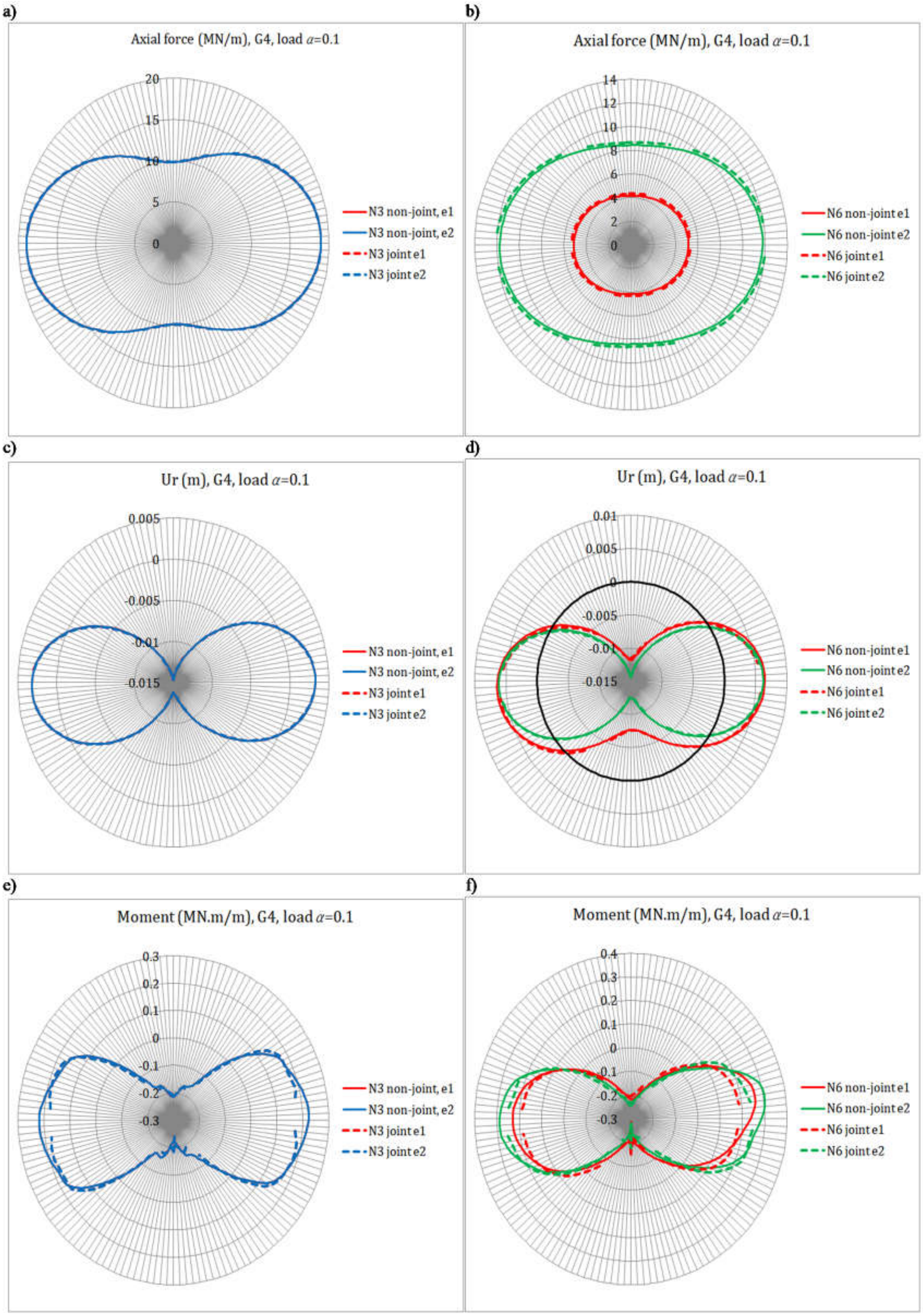

Figure 48. Axial force, radial displacement and moment of circular lining of tunnel according to interface stiffness (Case N3, N6) in ground G4, load ratio 0.1 (lining installation after 10% tunnel excavation convergence), non-joint: continuum model, joint: joint model, interface gap e1: 0.1 m, e2: 0.01 m

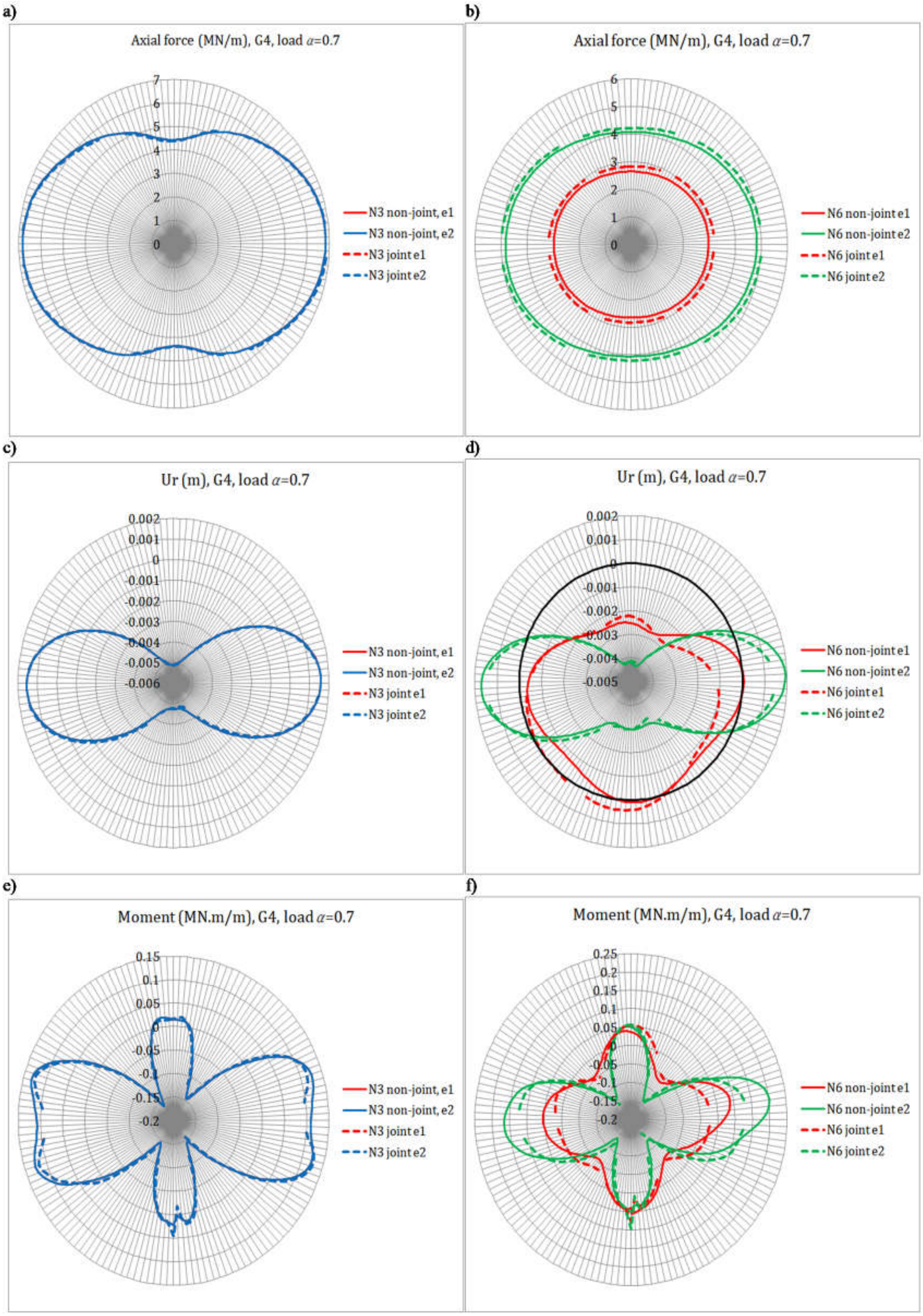

Figure 49. Axial force, radial displacement and moment of circular lining of tunnel according to interface stiffness (Case N3, N6) in ground G4, load ratio 0.7 (lining installation after 10% tunnel excavation convergence), non-joint: continuum model, joint: joint model, interface gap e1: 0.1 m, e2: 0.01 m

4.4. Conclusion and Perspective

In this chapter, first, we tried to describe the volume type segment lining, and then, the behavior of the tail void between the skin of the excavated ground and the segment lining was simulated as an interface element, and the behavior of the segment lining due to this interface was analyzed. Finally, segment joint modelling was performed in numerical analysis according to various study cases.

If the ground skin and segment lining are attached well and the grouting interface stiffness between them is large, the segment lining should support the load immediately after installation. However, in case of that, there is a gap due to void 'e' and insufficient stiffness of the grouting material, and the internal displacement occurs more in the given void, but the equilibrium support pressure where the Ground Reaction Curve meets the Support Characteristic Curve will decrease. The tail void grouting process and segment lining installation timing are the same right after the initial displacement occurs on the ground, but, in fact, the combination method of the support system supporting the ground load is considered to be sequentially serialized. It does not mean that each support system is installed separately, but at the same time, it affects the overall stiffness change. Furthermore, the stiffness of the overall support would eventually represent as support of the lining with the greatest stiffness considering that a system with relatively small support force is considered to have reached the yield first. Therefore, especially as soon as it is excavated, it is necessary to analyze it according to various conditions between the ground and the lining in order to control the load on the lining.

After studying joint modelling, when the interface between the lining and the ground is high, the higher the ground grade, the greater the moment difference between the joint model and the continuum model. And when the interface stiffness between the lining and the ground is low, the joint model exhibits slightly larger axial forces than the continuum model. Although it is not a noticeable result difference, it can be said that the displacement value is slightly smaller in the case of the joint model.

In Figures 48(f) to 49(d, f), there are some results that do not achieve symmetry, which shows the need for a more advanced model for micro errors in numerical analysis.

In fact, over all, since the already given joint stiffness is large, it was not easy to find a large difference in the results of the two models because it behaved almost completely in contact like the continuum model.

Therefore, one comparative result was tested. The resulting changes were examined by comparing the model to which the existing joint material property values were applied with the model to which 1000 times smaller material property values were applied.

In the results of Figure 50, a) two radial displacement result values according to the joint material properties are shown. To examine the visual change of the lining behavior, b) is the radial displacement result of the lining with the existing joint stiffness applied, and c) is the displacement result with the existing joint stiffness value multiplied by 1/1000.

Looking at Figure 50 a), obviously, the smaller the joint stiffness value, the smaller the overall lining displacement. However, looking more closely, it can be seen that the displacement at the crown point is small when the joint stiffness is high. This can be clearly noticed by comparing b) and c). It can be seen that the segment of the tunnel crown part slipped out due to the weak joint stiffness. This is a more conspicuous result for the better grade of the ground, that is, much greater is the anisotropy of the stress field in the ground around the tunnel.

As a result, if the stress field around the tunnel is clearly anisotropic (ground with less plasticity or convergence in early tunnel excavation), the joint effect evaluation needs to look at not only the overall behavior of the segment lining but also the specific risky part of the segment.

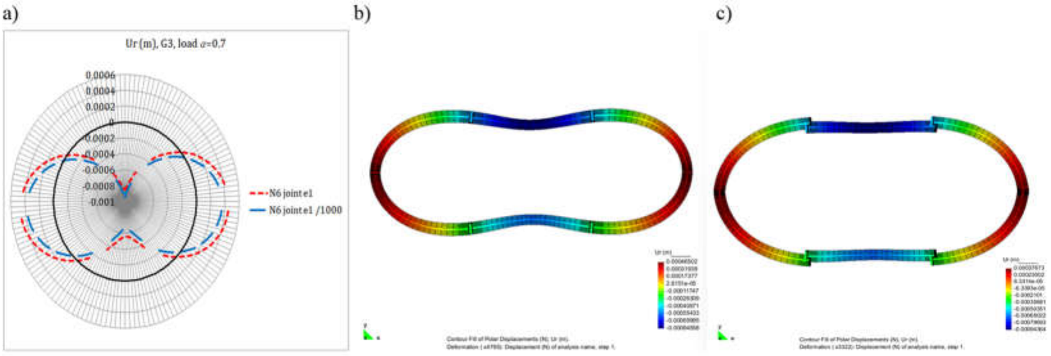

Figure 50. Lining radial displacement for different joint stiffness values at a load ratio of 0.7 (70%) in ground G3. a) N6 joint e1 Radial lining displacement when applying the existing joint stiffness or applying a joint stiffness 1/1000 times smaller. b) Displacement when applying an existing physical joint. c) Displacement when applying joint stiffness as small as 1/1000 (results b) c) by GID).

5. Hydro-mechanical coupling analysis with segments lining

5.1. Introduction

In this chapter, we conducted an analysis of hydraulic and mechanical coupling based on finite element numerical analysis (2D FEM-Disroc) to investigate the member force of segment lining caused by the loading of tunnel excavation convergence below the groundwater level.

When constructing tunnels below the groundwater level, the stress changes in the ground resulting from tunnel excavation can lead to alterations in the effective stress fields within the ground due to changes in pore pressure. This can decrease the load-bearing capacity of the ground surrounding the tunnel and increase ground deformation because of volume changes. Therefore, stress-pore pressure coupled analysis that takes into account both mechanical and hydraulic aspect is necessary to understand the behavior of the tunnel and the surrounding ground (Schleiss, 1986, 1997; Yoo., 2004; Graziani et al., 2012; Olumide, 2013; Zhou, Su, Wu 2015; Dadashi et al., 2017a).

Olumide and Marence (2012, 2013) suggested a way to model the interaction between water flow and mechanical forces in soil using a two-dimensional finite element analysis approach. They combined the results of consolidation and water flow analyses to obtain a coupled seepage stress.

Due to the limitations of the coupled analysis functions of tunnel analysis programs and technical difficulties in analysis modelling, there are not many examples that incorporate stress-pore pressure coupled (H+M coupling) analysis considering the interaction between drained-undrained states of excavation and water pressure during excavation by convergence stage in the design.

In this regard, this study will investigate the basic mechanism of the interaction between water pressure and mechanical-hydraulic relationship according to tunnel excavation convergence by taking into account drained-undrained states through numerical modelling using Disroc (FEM) finite element code.

The grouting interface between the segment lining and the surrounding rock mass can significantly affect the long-term stability of the excavation site. Therefore, we introduced a permeability coefficient to simulate the grouting interface.

In addition, we analysed the long-term behavior of the excavation site under different permeability coefficients.

The grouting interface between the segment lining and the surrounding rock mass plays a crucial role in the long-term stability of an excavation site (You., 2004; Kim et al., 2012).

Chapter 2 provides an analysis from a hydraulic perspective, while Chapters 3 and 4 present an analysis from a mechanical perspective. In this chapter, we conducted a numerical analysis using the segment-joint model presented in Chapter 4 and performed stress-hydraulic coupled analysis to investigate the excavation site's long-term behavior based on the grouting permeability coefficient and the Biot value of the ground.

5.2. H+M coupling tunnel excavation elastic model process

Understanding the interaction between ground properties, permeability, and pore water pressure distribution is essential in order to accurately model the hydraulic-mechanical response of the tunnel and its surrounding ground during excavation.

When excavating a tunnel, the stress distribution in the surrounding ground will change, which can cause pore water pressure to increase or decrease. Therefore, the pore water pressure due to the drainage and non-drainage characteristics of the ground can affect the behavior of the ground. In some cases, the ground may be able to drain excess pore water pressure relatively quickly, while in other cases it may take longer. If the ground is unable to drain excess pore water pressure, it may become more susceptible to failure, which can pose a significant risk to the safety of workers and the stability of the tunnel. In other words, the distribution of pore water pressure, or the pressure exerted by fluids in the pores of the ground, is an important factor that can affect the behavior of the ground, including its strength and deformation characteristics.

Poroelasticity, known as Biot theory, is a fundamental concept in geomechanics that describes the interaction between the solid matrix of a porous medium (such as rock or soil) and the fluid (usually water) that fills the pores.

The theory describes the mechanical behavior of the solid and the fluid in response to external loads, such as those induced by tunnel excavation.

Also, through this, under drained loading conditions, the model can simulate the deformation of the rock mass and the changes in the pore water pressure because of the drainage process. Then, the permeability and other hydraulic properties of the rock mass can also be considered, and the flow of water through the porous medium can be simulated.

Therefore, as a first example for modelling the hydraulic-mechanical coupling through the draining-non-draining process of the ground by tunnel excavation, a tunnel excavation model considering the Biot value of the ground was introduced through numerical analysis (FEM 2D-Disroc).

5.2.1. Parameters required for drained and undrained loading in tunnel excavation process

The relationship between geological and hydraulic properties around the tunnel is crucial in understanding the behavior of the surrounding ground during and after excavation. Parameters such as ground properties, permeability, and pore water pressure distribution play a significant role in the hydraulic-mechanical response of the surrounding ground

The Biot's coupling theory, known as the theory of poroelasticity, serves as the theoretical basis for hydro-mechanical coupling. Terzaghi (1943) developed the one-dimensional consolidation theory based on the concept of effective stress, which was later extended to three dimensions by Rendulic (1936). Biot (1955, 1956a, 1956b, 1956c, 1962, 1972, 1973) presented the governing equations for coupled three-dimensional fluid flow and deformation field for linear elastic porous media between 1955 and 1973. (Tan, Konietzky 2014)

Biot's coefficient represents the ratio of the fluid volume to the total volume of the porous medium. It characterizes the ability of the porous medium to transmit fluid pressure and is a measure of the compressibility of the porous medium. A higher value of 'b' indicates a more compressible and more porous medium.

The Biot's effective stress can be expressed as follows Eq(105):

$$\Delta\sigma^{'} = \Delta\sigma - b\Delta p_f \tag{105}$$

$$\Delta\sigma^{'} = K_{fr}\varepsilon_{vol}$$

Biot theory can be used to model both drained and undrained loading conditions. Under drained loading conditions, the model makes it possible to simulate the deformation of the ground and the changes in the pore water pressure due to the drainage process. Under undrained loading conditions, the model must account for the incompressibility of the pore fluid and the resulting high pore pressures that can occur during excavation.

The basic important parameter for tunnel excavation H+M numerical modelling (FEM-Disroc) with given Biot coefficients is introduced below.

Skempton's Bs coefficient describes the interaction between the solid and fluid phases of the porous medium. It represents the ratio of the change in effective stress to the change in pore water pressure. It(?) characterizes the drainage behavior of the porous medium and determines the rate at which the pore water pressure changes in response to changes in effective stress. Therefore, it(?) is an essential parameter in drainage behavior. To account for this parameter, a storage modulus (1/M = Cm) was applied to the ground (bulk material) in the Disroc finite element code (Table 2).

Under drained loading conditions, the model can incorporate Biot's theory to describe the mechanical behavior of the rock mass and the fluid in response to external loads and the changes in the pore water pressure that occur due to the drainage process. Skempton's B coefficient can be used to represent the degree to which the pore pressure changes in response to changes in the total stress applied to the rock mass.

The equations below represent physical properties relational expression of hydraulic and mechanical behaviors already discussed in Chapter 1.

$$\begin{bmatrix} K_0 = \dfrac{E_0}{3\left(1-2\nu_0\right)} \\ K_f = 2.2GPa \\ b_{biot} = 1 - \dfrac{K_0}{K_s} \end{bmatrix} \begin{bmatrix} \dfrac{1}{M} = \dfrac{\phi}{K_f} + \dfrac{b-\phi}{K_s} \\ B_s = \dfrac{Mb_{biot}}{K_u} = \dfrac{K_u - K_0}{b_{biot}K_u} \\ K_u = K_0 + Mb^2{}_{biot} \end{bmatrix}$$

Table 21. Given properties of the sample model

Sample	E_0 (MPa)	ν_0	n (porosity)	K_0 (MPa)	K_f (MPa)	b (biot)	k(permeability) (m/s)
Roche	1000	0.25	0.2	666.7	2200	0.4	2E-0.8
Beton	3000	0.2				0	2E-0.3 or 2E-14

Table 22 provided the physical properties required for the drainage and undrained loading analysis, which were obtained from the soil's physical properties and the Biot coefficient given in Table 21.

Table 22. Obtained properties for drainage loading analysis

Sample	K_s (MPa)	M (MPa)	1/M (C_M)	K_u (MPa)	B_s
Roche	1111	3691.2	0.00027	1257.3	1.2

5.2.2. Tunnel excavation modelling process through H+M coupling analysis

- **Steady state and transient analysis**

H+M coupled analysis is divided into steady-state analysis and transient analysis based on the application of the time concept. Steady-state analysis pertains to the state reached after infiltration occurs due to changes in the external environment. It should be noted that results regarding the process of reaching equilibrium cannot be obtained through this analysis. Nevertheless, it can be applied when evaluating the degree to which tunnel excavation affects the surrounding ground deformation.

On the other hand, transient analysis introduces the concept of time, and it allows for the acquisition of results at any point in time from the moment of infiltration towing to tunnel excavation until a steady state is achieved. This type of analysis can be used to understand the behavior of the tunnel and surrounding ground over time after tunnel excavation. Therefore, in coupled analysis, it is necessary to determine whether to use steady-state or transient analysis depending on the desired results from the analysis.

- **Sample model geometry, boundary and initial conditions**

To conduct a hydraulic pressure analysis, boundary conditions for hydraulic pressure must be assigned to the analysis area in the same manner as assigning boundary conditions for displacement in mechanical analysis. Furthermore, an anisotropic stress with normal stress of -10 and flat stress of -7 was applied with the given initial conditions. (Figure 51)

In situations where the groundwater level does not decrease despite the inflow of groundwater into the tunnel due to the continuous inflow of groundwater from the subsea tunnel or its surroundings, it is appropriate to analyze the conditions for maintaining the groundwater level. Figure 51 illustrates an example model where a tunnel with a diameter of 12m is constructed 50m below the ground surface, with the entire model measuring 100m in width and length. Since this model is a simple tunnel excavation model, a volume model of a concrete cylindrical (Beton) model with a thickness of 0.5 m was applied as a tunnel support.

Figure 52 depicts the flow of water pressure before the tunnel excavation.

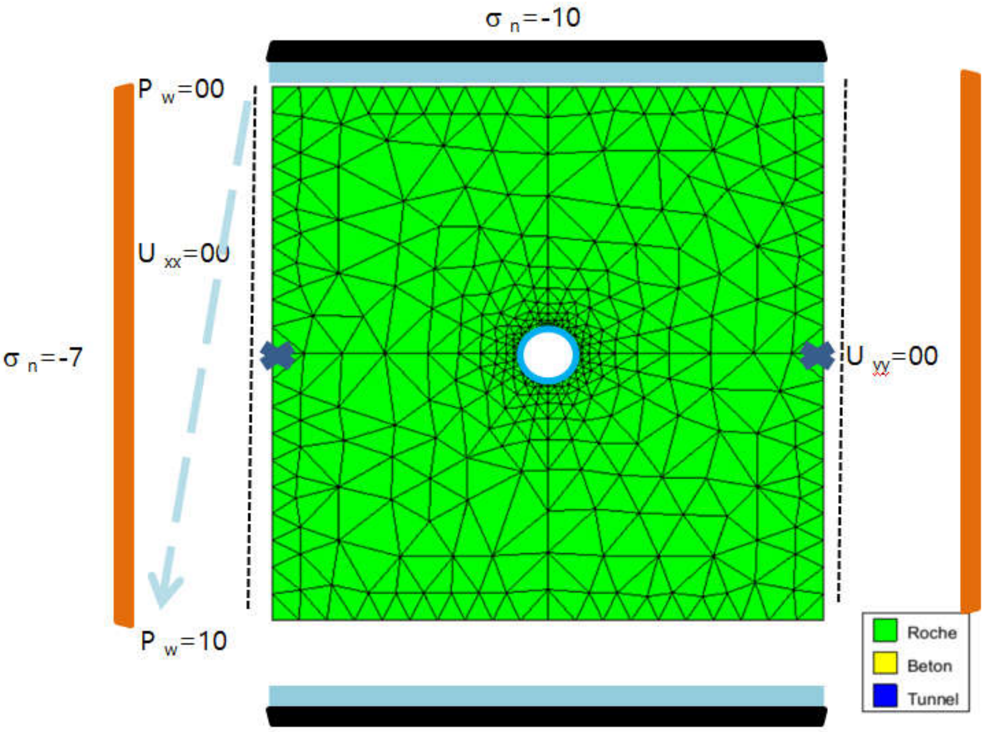

Figure 51. Sample model geometry and initial condition

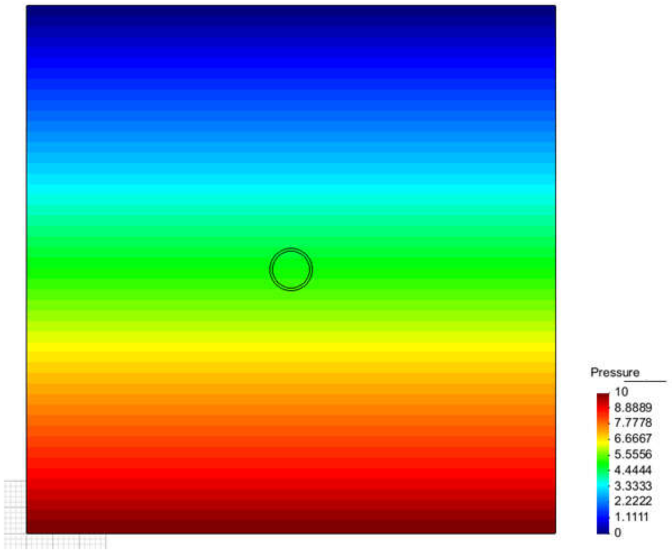

Figure 52. Hydraulic flow after initial condition loading by GID

- **Steps according to the undrained and drained of tunnel excavation**

In M+H coupled modelling, proper simulation of undrained and drained loading is necessary to accurately represent the tunnel excavation process.

The excavation modelling process follows the steps sequence outlined below.

Step 0-2: Initial and boundary conditions are applied to the tunnel excavation ground. And tunnel geometry pre-excavation step in which hydraulic behavior and initial stress conditions are maintained.

Step 3 or 4: The tunnel excavation force is applied according to the load ratio (tunnel excavation convergence ratio), and the H+M behavior is evaluated based on pore water pressure. (undrained stage, steady state analysis, and ground storage modulus Cm must be applied)

Step 30 or 40: Support (Beton) is adapted to the geometry.

Step 31 or 41: After applying the support material, the remaining tunnel excavation force (1-load ratio) is adapted, and the H+M behavior is evaluated based on pore water pressure. (undrained stage, steady state analysis, and ground storage modulus Cm must be applied)

Step 32, 33, or 42, 43: After installing the support, the water pressure of the boundary inside the support is applied as Po=0, and the long-term behavior is evaluated depending on the permeability coefficient of the support. (drainage stage, transient analysis condition)

The step-by-step modelling process are shown in Figures 53 and 54.

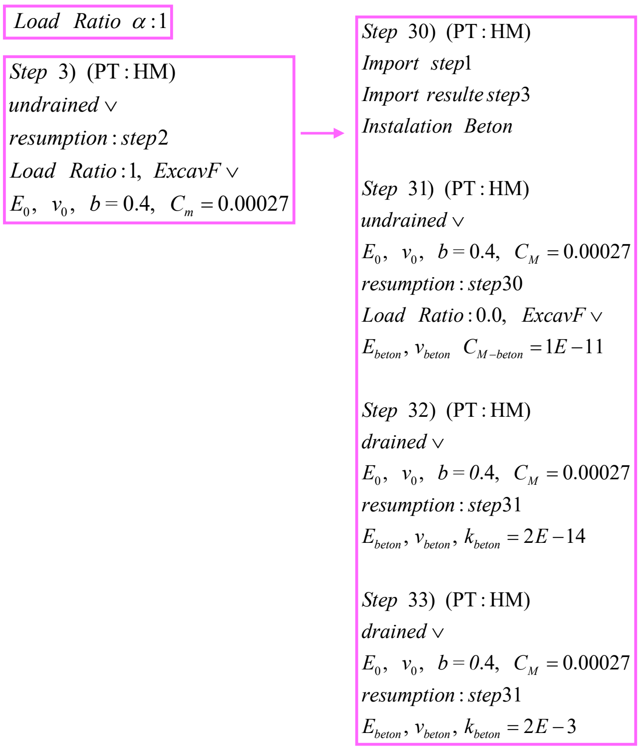

$Load\ \ Ratio\ \ \alpha:1$

$Step\ \ 3)\ \ (\mathrm{PT:HM})$
$undrained \vee$
$resumption: step2$
$Load\ \ Ratio:1,\ \ ExcavF \vee$
$E_0,\ \ v_0,\ \ b=0.4,\ \ C_m=0.00027$

$Step\ \ 30)\ \ (\mathrm{PT:HM})$
$Import\ \ step1$
$Import\ \ resulte\, step3$
$Instalation\ \ Beton$

$Step\ \ 31)\ \ (\mathrm{PT:HM})$
$undrained \vee$
$E_0,\ \ v_0,\ \ b=0.4,\ \ C_M=0.00027$
$resumption: step30$
$Load\ \ Ratio:0.0,\ \ ExcavF \vee$
$E_{beton},\ v_{beton}\ \ C_{M-beton}=1E-11$

$Step\ \ 32)\ \ (\mathrm{PT:HM})$
$drained \vee$
$E_0,\ \ v_0,\ \ b=0.4,\ \ C_M=0.00027$
$resumption: step31$
$E_{beton},\ v_{beton},\ k_{beton}=2E-14$

$Step\ \ 33)\ \ (\mathrm{PT:HM})$
$drained \vee$
$E_0,\ \ v_0,\ \ b=0.4,\ \ C_M=0.00027$
$resumption: step31$
$E_{beton},\ v_{beton},\ k_{beton}=2E-3$

Figure 53. Behavior analysis procedure after installation of support at initial excavation force

load ratio=1

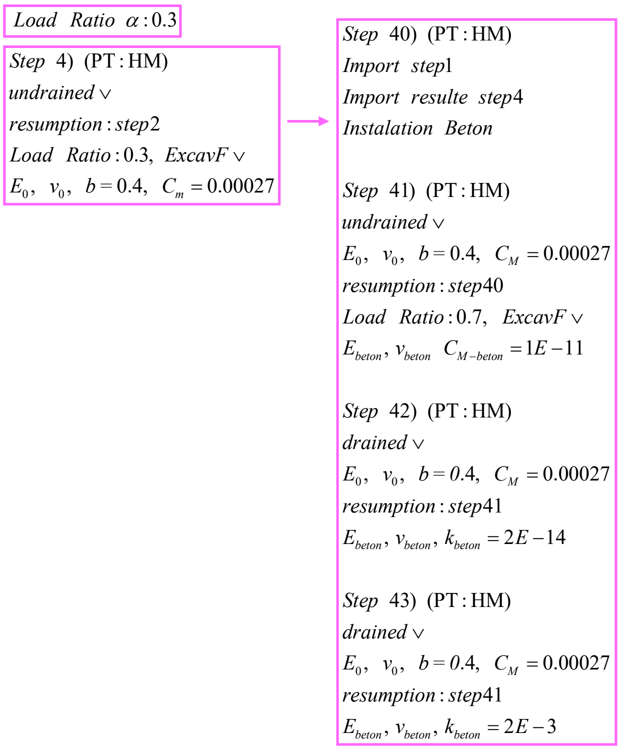

$Load\ \ Ratio\ \ \alpha : 0.3$

$Step\ \ 4)\ \ (\mathrm{PT:HM})$
$undrained \vee$
$resumption : step2$
$Load\ \ Ratio : 0.3,\ \ ExcavF \vee$
$E_0,\ \ v_0,\ \ b = 0.4,\ \ C_m = 0.00027$

$Step\ \ 40)\ \ (\mathrm{PT:HM})$
$Import\ \ step1$
$Import\ \ resulte\ \ step4$
$Instalation\ \ Beton$

$Step\ \ 41)\ \ (\mathrm{PT:HM})$
$undrained \vee$
$E_0,\ \ v_0,\ \ b = 0.4,\ \ C_M = 0.00027$
$resumption : step40$
$Load\ \ Ratio : 0.7,\ \ ExcavF \vee$
$E_{beton},\ v_{beton}\ \ C_{M-beton} = 1E-11$

$Step\ \ 42)\ \ (\mathrm{PT:HM})$
$drained \vee$
$E_0,\ \ v_0,\ \ b = 0.4,\ \ C_M = 0.00027$
$resumption : step41$
$E_{beton},\ v_{beton},\ k_{beton} = 2E-14$

$Step\ \ 43)\ \ (\mathrm{PT:HM})$
$drained \vee$
$E_0,\ \ v_0,\ \ b = 0.4,\ \ C_M = 0.00027$
$resumption : step41$
$E_{beton},\ v_{beton},\ k_{beton} = 2E-3$

Figure 54. Behavior analysis procedure after installation of support at initial excavation force load ratio=0.3

Let's examine whether the tunnel excavation modelling analysis followed the Biot theory of the H+M coupled model during these processes.

First, we looked at the change in pore pressure at a node after tunnel excavation using Skempton's B coefficient (Figure 55).

The theoretical Skempton's B principle states that the change in pore pressure can be expressed by the following equations Eq (106):

$$B_s = \frac{\Delta u_w}{\Delta \sigma_m} = \frac{(\Delta u_w - \Delta \sigma_3)}{(\Delta \sigma_1 - \Delta \sigma_3)} \tag{106}$$

$$(\Delta u_w = \Delta P_w)$$

$$\Delta P_w = \Delta P_{w0} + B_s \Delta \sigma_m$$

The green box in Figure 55 shows the initial pore water pressure and stresses, as well as the posterior pore water pressure Pw1 and the resulting changed stresses after tunnel excavation at node 322 (tunnel's 90-degree side point clockwise).

Through this numerical analysis, the Skempton's B value of 1.15 was obtained by examining the relationship between the changed stresses and the pore water pressure values. This value is very similar to the applied Skempton's B value of 1.2 (Table 22), which validates the validity of the numerical analysis process.

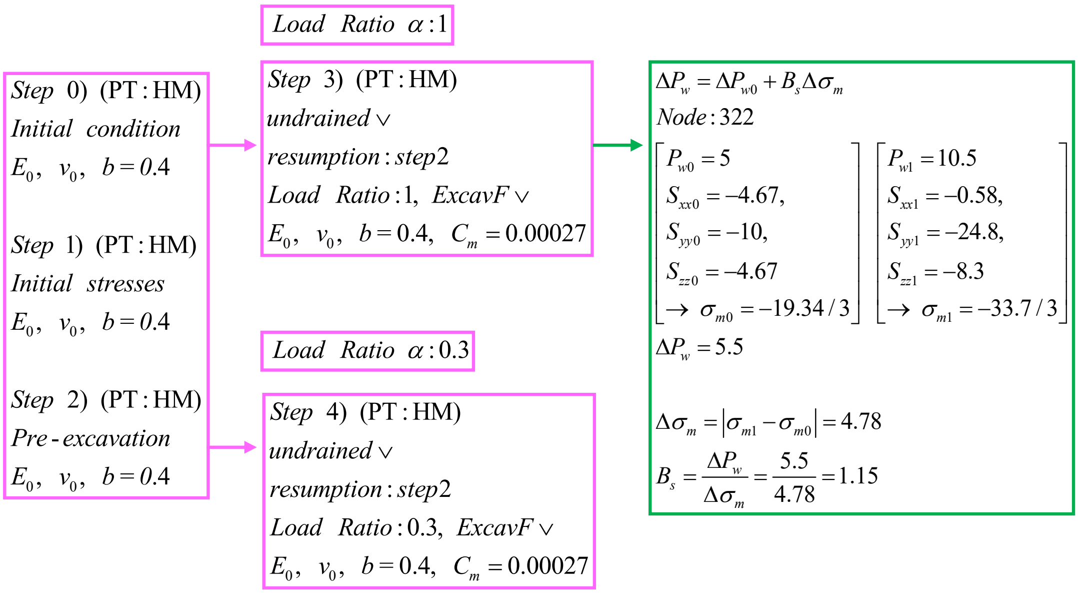

Figure 55. Example of analysis of surrounding behavior of excavated ground after initial tunnel excavation

- **<u>Post-process analysis result by GID</u>**

In Figure 56, the flow of pore water pressure after tunnel excavation is shown for different load ratios during the convergence stage. As the load ratio approaches 1 (Figure 56-a)), significant tunnel convergence occurs, which can cause significant changes in the surrounding stresses. Therefore, the pore water pressure changes during the excavation process in the undrained stage can be substantial.

Figure 57-b) shows a long-term behavior of pore water pressure after installing the support material (Beton). Since the support material has a higher permeability coefficient than the surrounding ground, the fluid flow can move into the tunnel and reduce the pore water pressure around it, as seen in the reduction of pore water pressure in Figure 57-b). In contrast, Figure 57-a) shows that the surrounding ground has a relatively higher pore water pressure as the support material almost acts as a waterproof barrier.

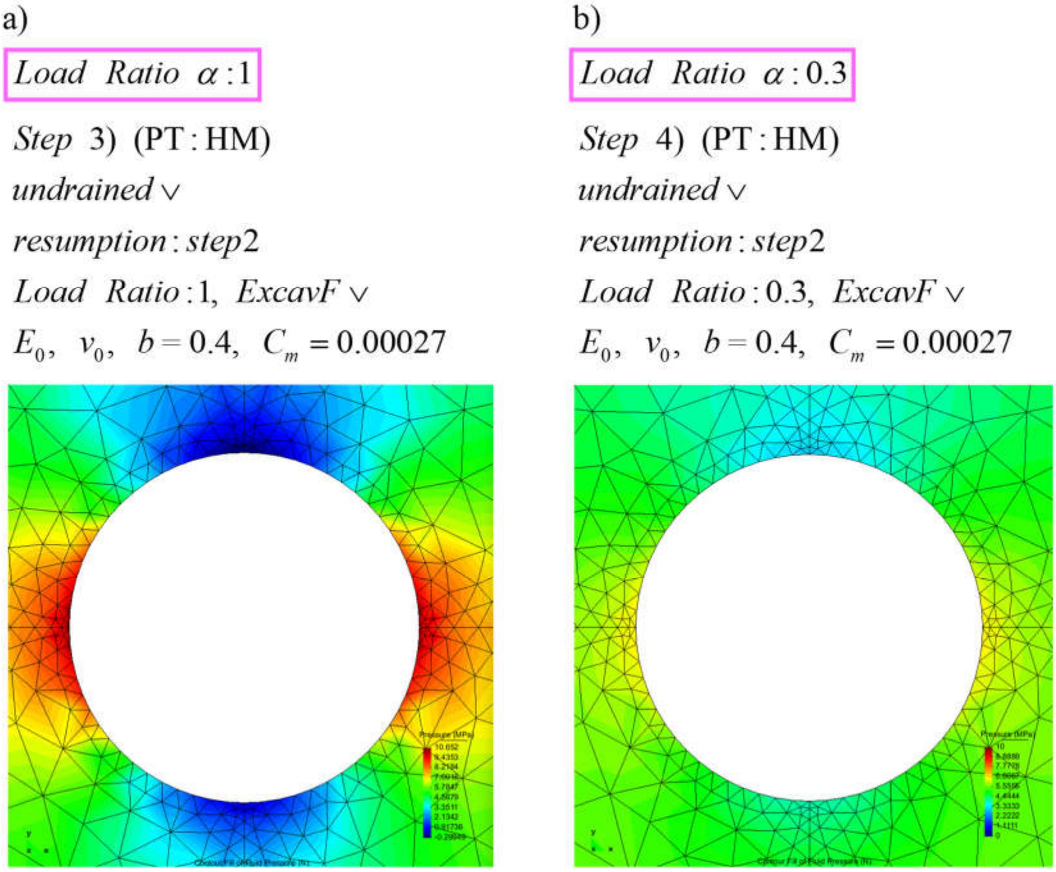

Figure 56. Hydraulic pressure according to convergence load ratio of tunnel excavation before support installation. a)load ratio , b): load ratio 0.3

In Figure 58, the Sxx (x-Stress) of the support material (Beton) is examined. Since the Biot coefficient of the support material is 0, the effective stress and total stress in this part are the same.

However, we found a difference in the stress of the support material depending on the permeability coefficient of the surrounding ground.

When comparing Figure 58-a) and b), it can be seen that the inner side Sxx (x-Stress) of the support material is more than four times larger when the permeability coefficient of the support material is larger than that of the surrounding ground.

Ex: figure 58 a) Side Sxx:-0.026, figure 8 b) Side Sxx:-0.113.

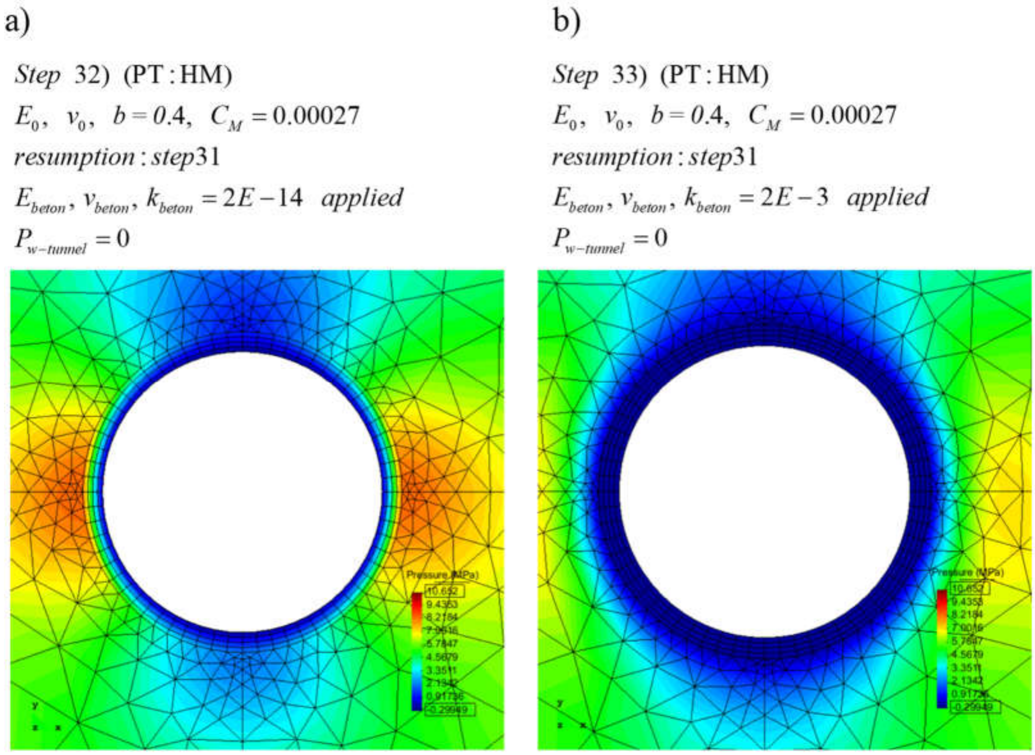

a)

$Step\ 32)\ (\mathrm{PT:HM})$
$E_0,\ v_0,\ b=0.4,\ C_M=0.00027$
$resumption: step31$
$E_{beton}, v_{beton}, k_{beton}=2E-14\ \ applied$
$P_{w-tunnel}=0$

b)

$Step\ 33)\ (\mathrm{PT:HM})$
$E_0,\ v_0,\ b=0.4,\ C_M=0.00027$
$resumption: step31$
$E_{beton}, v_{beton}, k_{beton}=2E-3\ \ applied$
$P_{w-tunnel}=0$

Figure 57. Hydraulic pressure according to the permeability coefficient of the support material (Beton) after installation of the support material. a) support material is impermeability. b) support material permeability is greater than ground.

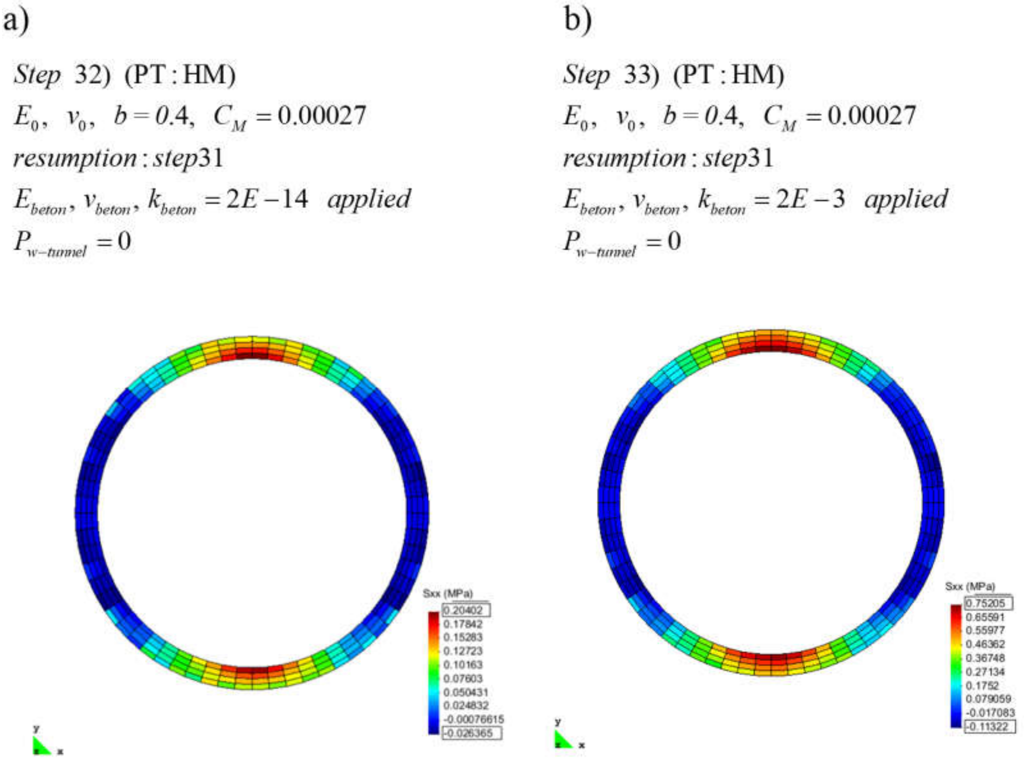

a)

$Step\ 32)\ (\mathrm{PT:HM})$
$E_0,\ v_0,\ b=0.4,\ C_M=0.00027$
$resumption: step31$
$E_{beton}, v_{beton}, k_{beton}=2E-14\ \ applied$
$P_{w-tunnel}=0$

b)

$Step\ 33)\ (\mathrm{PT:HM})$
$E_0,\ v_0,\ b=0.4,\ C_M=0.00027$
$resumption: step31$
$E_{beton}, v_{beton}, k_{beton}=2E-3\ \ applied$
$P_{w-tunnel}=0$

Figure 58. xx axial stress of the support. a) Support material impermeable
b) Support material permeable than of the ground.

5.3. Member force analysis of segment-joint lining through M+H model

The increasing use of TBM for long deep tunnels requires critical technical decisions to be made early in the design process. Therefore, it is essential to conduct well-designed, executed, and interpreted preliminary investigations to prevent inappropriate modelling, fatal design flaws, and incorrect TBM usage (Coli, Pinzani 2014).

When designing a submarine tunnel lining, water pressure is typically assumed to be the water head corresponding to the upper groundwater level outside the lining. However, this assumption is overly conservative under most construction conditions. The concrete segment lining is permeable to water, and cracks caused by construction joints or drying shrinkage can further increase its permeability. Consequently, water pressure is released due to penetration into the tunnel, meaning that the actual water pressure acting on the lining is smaller than the total head of the groundwater level. While there is still some water pressure acting on the lining, it is less than what is typically assumed.

The interaction between the tunnel excavation and the ground is one of the most important issues in tunneling. The tunnel-surrounding ground is deformed according to the effective stress in the ground, which can generate pore water pressure. The pore water pressure can infiltrate into the tunnel and affect the behavior of the lining. The convergence load ratio during tunnel excavation represents the ratio of the displacement of the excavation face to face with the deformation rate of the ground. It determines the pore water pressure and stress relief degree of the surrounding ground at the excavation stage. As the convergence load ratio increases, the pore water pressure around the excavation face also increases, negatively affecting the behavior of the lining. Therefore, it is important to control the convergence load ratio appropriately and manage the pore water pressure to maintain stable lining behavior during tunnel excavation. Sufficient ground investigation and prediction should be conducted during tunnel excavation, and appropriate technical measures such as ground reinforcement and waterproofing construction should be taken.

First, based on the geological properties data investigated in Chapter 1, we analyzed the segment joint lining model researched in CH4 and the interface (tail void) between the ground and lining using the permeability coefficient model. Although the segment lining part is a bulk volume model, it is evaluated through mechanical behavior rather than hydro-mechanical coupling behavior because the Biot value is applied as 0. However, evaluating the long-term behavior of the lining depending on the permeability coefficient of the interface between the ground and the lining requires a coupling behavior analysis as this will affect the effective stress of ground on the segment lining. Therefore, we evaluate how the Biot value affects the gap water pressure evaluation according to the tunnel excavation convergence stage of the ground and how it has an effect on long-term lining behavior.

5.3.1. Analysis model condition

In this study, we considered the case of a submarine tunnel with a radius of 6m being constructed 50m below the ground surface (groundwater level), and the analyzed ground is based on the geological properties in CH1.

The analyzed ground (Sand1, Sand2) and segment lining are modeled elastically using the Elastic model, and the Biot value is applied as the H+M bonding coefficient to the ground part. In addition, the same segment joint lining and interface model as simulated in Chapter 4 were adapted to the materials of mechanics (Table 23,24,25) (Figure 59,60). Both the interface between the ground and segment (lining) and the segment joint model were simulated as interface elements, and the influence of the gap water pressure from the external ground was researched through coupling behavior by always applying Biot=1.

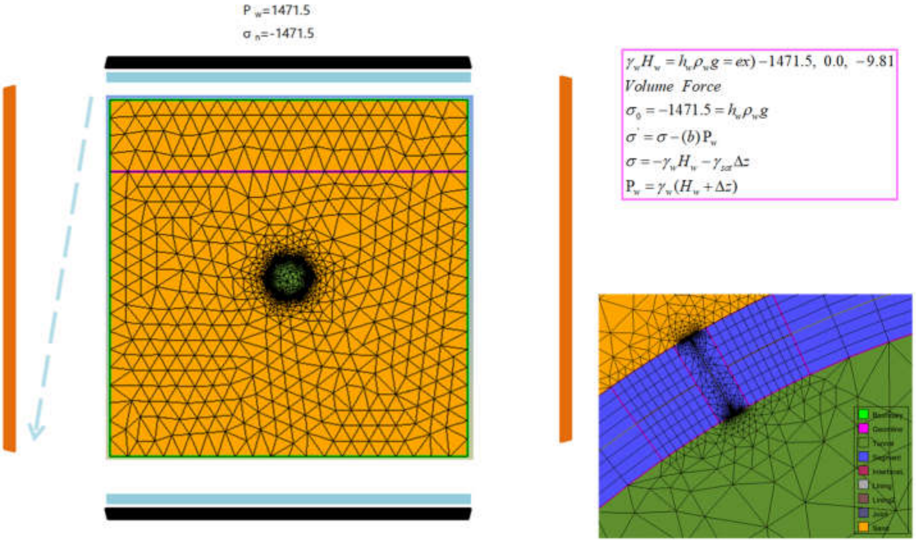

Figure 59. Initial and boundary conditions and target model geometry

In Figure 59, we adapted the water pressure corresponding to a depth of 150m at the top of the target ground and simultaneously applied the same vertical stress. For the stress analysis, we fixed the displacement of the left and right sides of the target ground and the bottom part as boundary conditions.

Moreover, as an initial load calculation, we applied the gravity-volume force ($\mathrm{K}_0 = \frac{\nu}{1-\nu}$) depending on the depth (gravitational acceleration) of the ground.

Accordingly, we set the stress and water pressure changes as the initial conditions.

The boundary condition for water pressure was analyzed under the condition of maintaining the underground water level without any changes in the top part, and we calculated the long-term behavior by assuming zero water pressure at the tunnel boundary after the tunnel excavation.

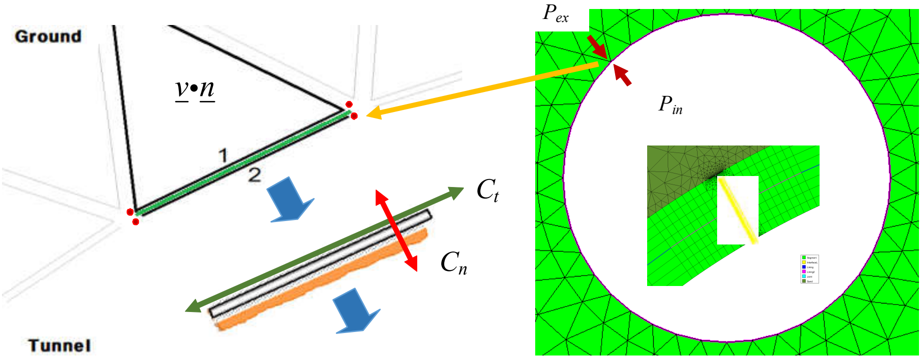

Figure 60. Interface simulation of hydraulic behavior between ground and segment lining

In Figure 60, the simulation of the behavior of the tunnel boundary's interface model described in CH2 by numerical behavior is shown. This part shows how flow results of the numerical analysis are represented by setting the interface elements between the segment lining and the ground. Then, by examining the long-term behavior after the installation of the segment lining, it sought to investigate what kind of impact such water flow has. (The parameters C_t, C_n of the Beam element are described in detail in chapter 2.2.)

Tables 23-25 show the applied parameters.

Table 23. Given properties of the sample model

	E_0 (MPa)	ν_0	n (porosity)	K_0 (MPa)	K_f (MPa)	b (biot)	k(permeability) (m/s)
Sand 1	40	0.25	0.4	26.667	2200	0.4	2E-0.8
Sand 2	40	0.25	0.4	26.667	2200	0.9	2E-0.8

Table 24. Obtained properties for drainage loading analysis

	K_s (MPa)	M (MPa)	1/M (C_M)	K_u (MPa)	B_s
Sand 1	44	5500	1.81E-7	907	2.4
Sand 2	27	486	2.057E-6	420	1.04

Table 25. Application properties before and after excavation of segment-joint lining model and interface model

Before lining	Segement		Lining Beam		Joint	Interface	
E (Kpa)	Sand	ES/1000	0	kt (kPa/m)	G/e	4705882	G/e
ν	Sand	EI/1000	0	kn (kPa/m)	H/e	82147651	H/e
k permability (m/s)	2.00E-08		2.00E-11	e (m)	0.01	0.1	
Biot	0		0	Biot	1	1	
				Ct (m^3/kPa/s)	2.00E-11	2.00E-11	
Active supports	Segement		Lining Beam		Joint	Interface	
E (Kpa)	30,000,000	ES/1000	15,000	kt (kPa/m)	168400	1.00E+07	
ν	0.2	EI/1000	312	kn (kPa/m)	730100	2.00E+07	
k permability (m/s)	2.00E-14		2.00E-17	e (m)	0.01	0.1	
Biot	0		0	Biot	1	1	
				Ct (m^3/kPa/s)	2.00E-16	2.00E-16	2.00E-03

Regarding the analysis of the tunnel lining behavior in this modelling, the influencing parameters are as follows:

First, the target ground with different Biot coefficients.

Sand1 has a Biot coefficient of 0.4, and Sand2 has a Biot coefficient of 0.9 applied. (Table 23, 24)

Second, the application pattern of tunnel excavation convergence force.

To examine the change in hydro-mechanical coupling behavior caused by tunnel excavation, two different patterns of tunnel excavation convergence stages were performed.

1) Load ratio=0.3 for initial tunnel excavation convergence force followed by Load ratio=0.7 for tunnel excavation convergence force after segment lining installation, or
2) Load ratio=0.7 for initial tunnel excavation convergence force followed by Load ratio=0.3 for tunnel excavation convergence force after segment lining installation.

The aim is to examine the effects on the effective stress of the target ground according to the application of these two different patterns of tunnel excavation force.

Third, the interface flow conductivity coefficient. A comparison analysis of long-term behavior was conducted by applying the flow conductivity coefficient value of the interface model simulated as tail void between the ground and the segment lining differently as permeability or impermeability.

5.3.2. Analysis of the Results

Figure 61 shows the axial force, moment, and radial displacement results of the tunnel lining in sand1 with a Biot value of 0.4 under the tunnel convergence pattern of "initial excavation load ratio 0.3 and load ratio 0.7 after segment installation".

Overall, when the initial tunnel convergence load ratio is low, it can be said that the load that the segment needs to support is high. In this case, the effect of changes in pore water pressure is not significant, and the effect of mechanical behavior is heavily imposed on the load that the lining needs to support.

Therefore, when looking at the results calculated for long-term behavior, the difference in lining forces between the impermeable and permeable interfaces does not give a significant influence factor.

MH Sand 1 - Biot: 0.4

$Load\ \ Ratio\ \ \alpha_1 : 0.3 \rightarrow \alpha_2 : 0.7$

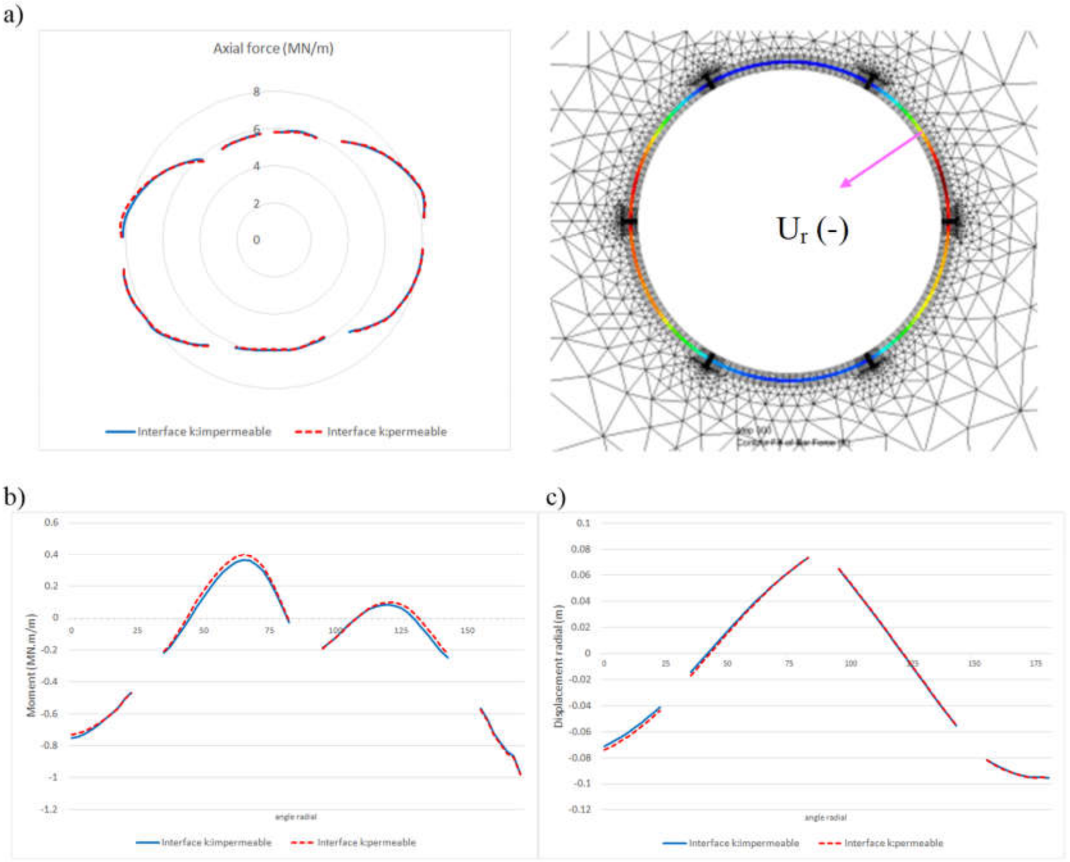

Figure 61. Sand1 (Load ratio 0.3 - 0.7 pattern) segment lining member force result. a) Axial force at tunnel rotation radius, b) Moment to 180 degrees' clockwise radius from tunnel crown point, c) Radial displacement to 180 degrees clockwise radius from tunnel crown point

On the other hand, in Figure 12, which shows a different tunnel convergence pattern, we can see a slight difference in behavior under the same conditions. In particular, when looking at the radial displacement (Figure 12c), applying a permeable interface shows larger radial displacement values near the tunnel crown (around tunnel angle radial 0 degrees) compared to when using an impermeable interface. There is no significant difference in displacement observed near the tunnel invert (around tunnel angle radial 180 degrees). This is considered to be due to a greater gap pressure in the invert section than in the crown section.

MH Sand 1 - Biot: 0.4

$Load\ \ Ratio\ \ \lambda_1 : 0.7 \rightarrow \lambda_2 : 0.3$

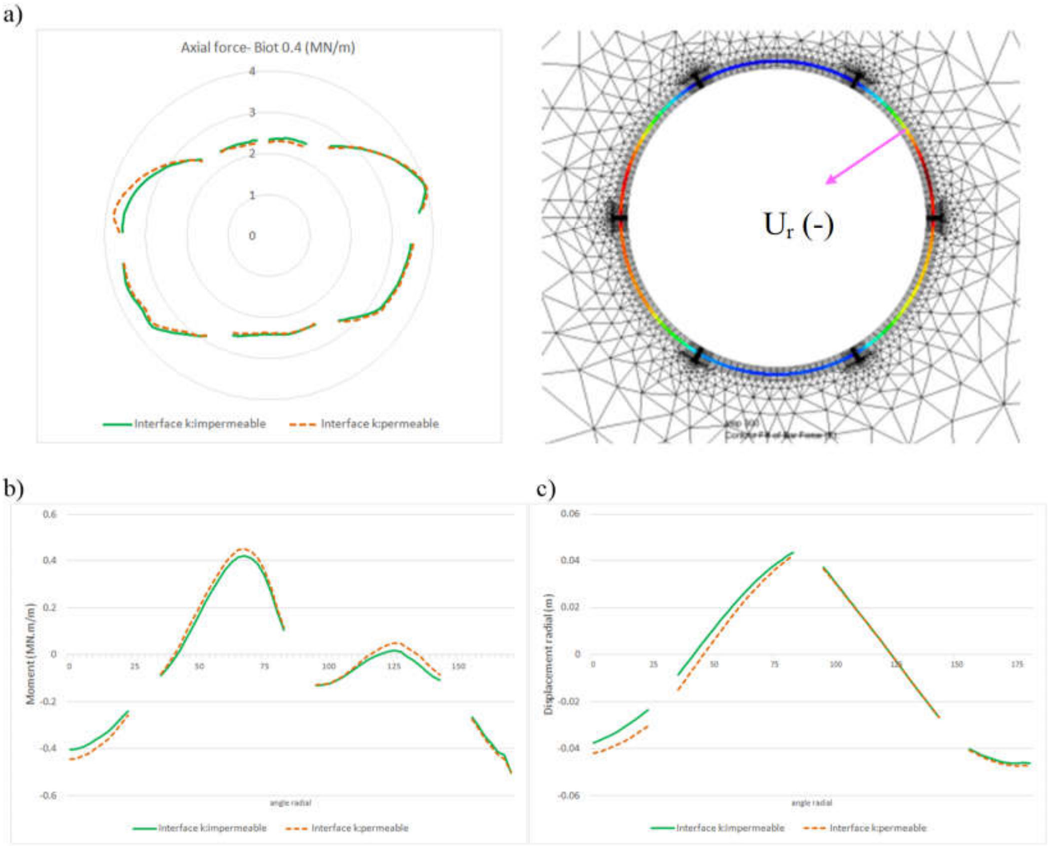

Figure 62. Sand1 (Load ratio 0.7 - 0.3 pattern) segment lining member force result. a) Axial force at tunnel rotation radius, b) Moment to 180 degrees clockwise radius from tunnel crown point, c) Radial displacement to 180 degrees clockwise radius from tunnel crown point

In Figure 63, the tunnel convergence stage was kept the same, but the Biot value of the ground varied for comparison. As a result, it can be seen that when the Biot value is higher (0.9), the influence of isotropic pressure of the gap water pressure becomes greater than when it is lower (0.4). Therefore, overall changes in the moment and radial displacement of the lining become smaller.

However, when comparing the axial force values, it was found to be smaller when the ground has a Biot value of 0.4. In evaluating the trend of axial force values, it is shown that when the ground has a higher Biot value, it shows a trend closer to an isotropic circular model, while when it has a lower Biot value, it represents a trend closer to anisotropic behavior. In this case, there is no significant difference in long-term results due to the difference in the permeability of the interface, as seen in Figure 61.

MH Sand 1 - Biot: 0.4 Vs MH Sand 2 - Biot: 0.9

Load Ratio $\lambda_1 : 0.3 \rightarrow \lambda_2 : 0.7$

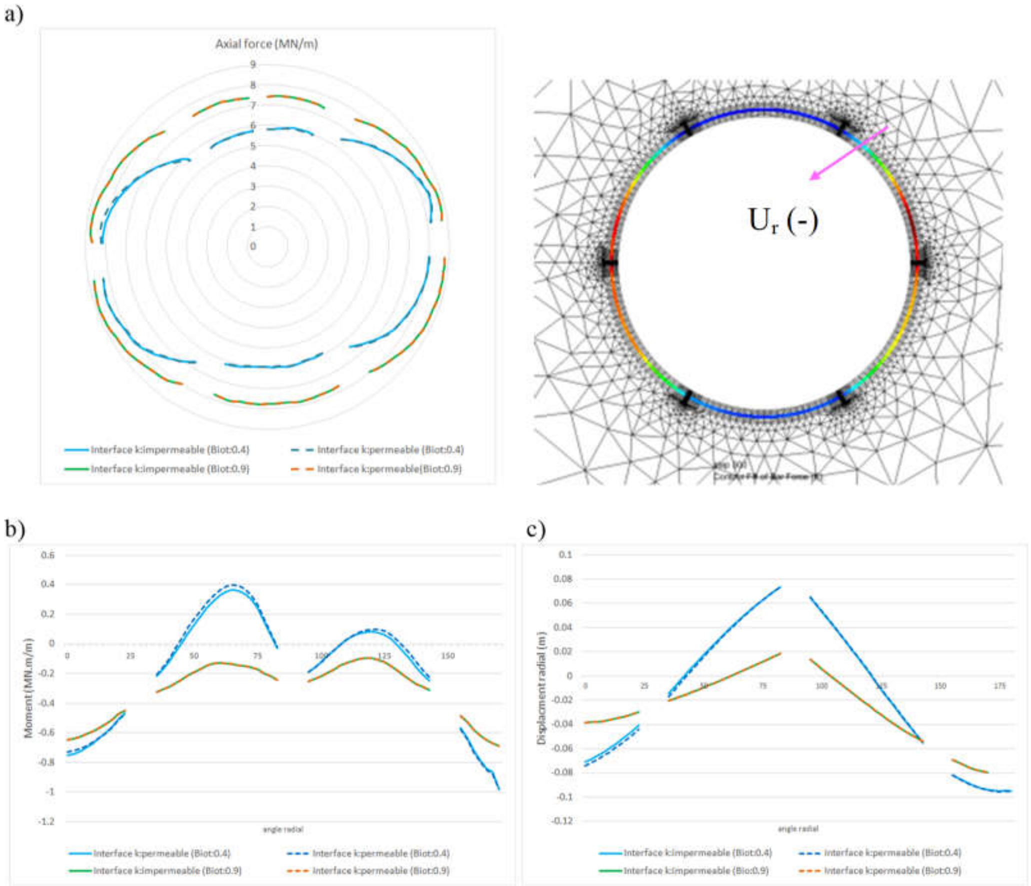

Figure 63. Comparative analysis of sand1 and sand2 (Load ratio 0.3 - 0.7 pattern). a) Axial force at tunnel rotation radius, b) Moment to 180 degrees' clockwise radius from tunnel crown point, c) Radial displacement to 180 degrees clockwise radius from tunnel crown point

5.4. Conclusion and perspective

In this chapter, we performed a segment lining behavior analysis based on a H+M coupled model.

First, long-term lining behavior changed according to the tunnel excavation convergence stage in the ground with the different values of the Biot coupling coefficient.

The change in tunnel surrounding pore pressure varies depending on the tunnel excavation convergence pattern. The greater the initial tunnel excavation convergence (load ratio), the greater the effect of hydraulic behavior. This was shown to be an analysis based on the hydraulic change factor between the ground and the lining interface.

Even if the segment lining is an impermeable material, it cannot be totally impermeable in the long term. So it reminds us why secondary grouting work is needed when examining the long-term behavior of the tunnel through hydromechanical coupling tendencies. When compared to other grounds with different Biot values, there was a difference in the tendency of stress in the lining.

This can be seen as a conflicting result of isotropic pore pressure in the H+M coupled behavior of anisotropic stress field in the ground. As the Biot value increases, the axial force value increases due to the isotropic large pore pressure, but it can be seen that the moment and radial displacement decrease.

For more advanced segment lining modelling, analysis of joints between segments is necessary. Therefore, a comparative analysis of joint effect is shown in Figure 64. Here, a comparative analysis was conducted regarding the different joint gap (e) sizes when the same ground conditions, interface conditions, and tunnel excavation patterns were applied. (Figure 64 a), b), c)).

A small joint gap (e) size means that the joint stiffness value increases slightly as nonlinear model, which also increases the stress value. However, the radial displacement result has deceased. In addition, the trend of moment change displays less dynamic change, but it represents a large moment value at the point where the maximum axial force is received. When comparing the long-term behavior of the interface, Figure 64 d) shows that when the joint stiffness value is high in the tunnel's roof section (angle 0 degrees to 90 degrees), it demonstrates less displacement.

So as the joint-segment part is also shown as an influential factor, it reminds us of the need for more in-depth research to understand this.

MH Sand 2 - Biot: 0.9 with joint stiffness

$Load\ \ Ratio\ \ \lambda_1 : 0.3 \rightarrow \lambda_2 : 0.7$

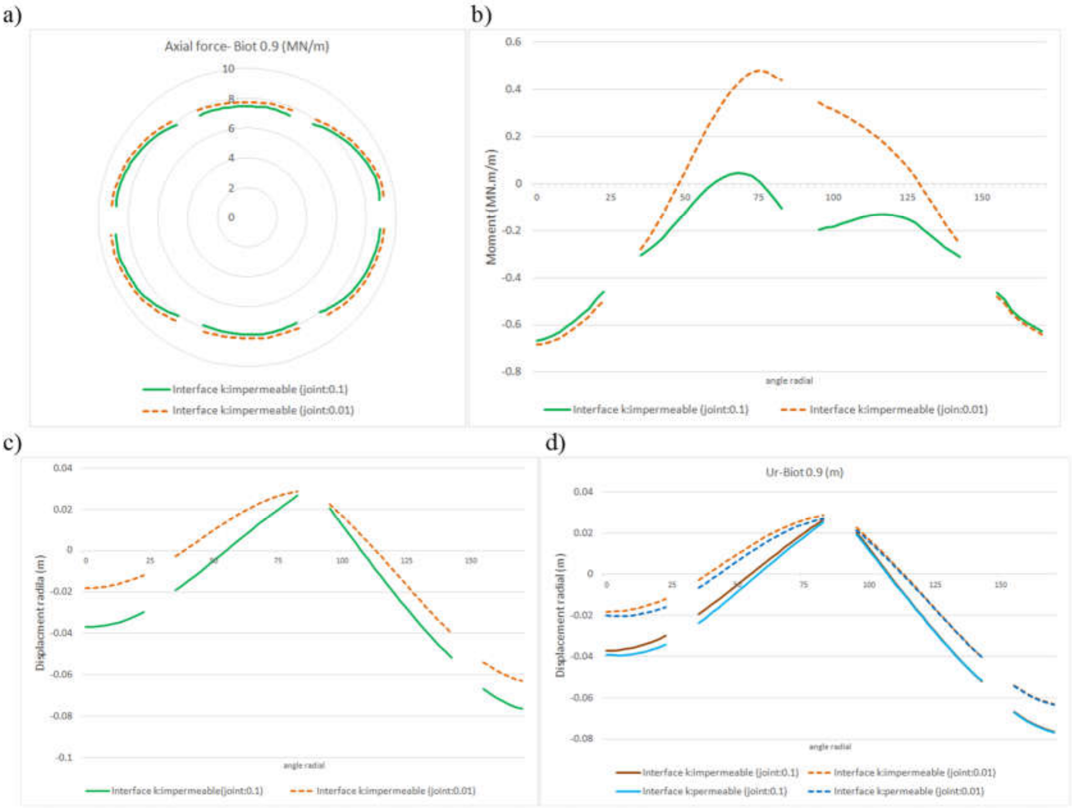

Figure 64. Analysis due to joint stiffness in segments in sand2 (Load ratio 0.3 - 0.7 pattern). a) Axial force at tunnel rotation radius, b) Moment to 180 degrees' clockwise radius from tunnel crown point, c) Radial displacement to 180 degrees' clockwise radius from tunnel crown point, d) Radial displacement to 180 degrees clockwise radius from tunnel crown point with consideration of the permeability of the interface

6. Evaluation of fault effects

6.1. Introduction

This thesis focuses on the evaluation of the behavior of a shield TBM tunnel in submarine tunnels. Specifically, the aim is to predict and evaluate various ground conditions and problems that may affect the tunnel stability during shield TBM construction under the sea ground and decrease the stability of the segment joint, in order to implement a reasonable lining model. It is particularly difficult to implement segments model that includes joints, using 2D-FEM numerical analysis in complex ground conditions.

Cho (2014, 2015) analyzed the mechanical behavior of shield TBM tunnels due to the interaction between the tunnel and excavation ground by researching appropriate numerical modeling methods. And this study analyzed the behavioral characteristics of shield TBM tunnels based on the scale of single fractures and face-to-face conditions, and the distance of backfill (grouting) injection. Borere (2002) performed staged modeling of shield TBM tunnels, taking into account the membrane pressure, backfill grouting pressure, and TBM conicity, to determine that it is possible to obtain results similar to actual field measurement values rather than 2D analysis results. Oh (2014) proposed a safe and efficient operating method for complex ground by performing reduced-scale experiments and numerical analysis to examine the stress and ground displacement that occurs during shield TBM excavation. Oh et al. (2017) performed a 3D stress-pore pressure analysis to examine the contribution of backfill injection to long-term settlement in low-permeability ground and confirmed the minimum input pressure that can limit long-term settlement. Oh et al. (2004) performed experiments by changing ground pressure conditions to investigate the effect of discontinuity surfaces in the surrounding ground of the tunnel lining behavior.

When using the shield TBM method to excavate fracture, there is a high probability of excessive internal deformation and collapse.

Lin et alet al. (2007) studied the influence of a fault movement on a shotcreted tunnel where the fault plane was parallel to the tunnel longitudinal axis. Gregor et al. (2007) studied, using a three-dimensional numerical modelling, the stability of twin tunnels crossing an oblique fault (including a normal and strike-slip fault). They showed that the soil mass and water can flow into the segmental tunnels after faulting, which causes several problems (e.g. stability problems). There is not enough study about systematic guidelines that is modeling segment-joints mode and areas that can minimize trouble when encountering special ground conditions such as faults/fracture zones during tunnel excavation. And, we know that there is a shortage long-term H+M coupling behavioral analysis study that presents segment-joints model and complex ground conditions such as faults/fracture zones during tunnel excavation. In this chapter, we attempted to perform numerical analysis of tunnel modeling under complex ground with faults using the segment-joints model we implemented in previous chapters, considering the interface (grouting) part. In addition, a comparative analysis was attempted for long-term H+M according to the Biot coefficient of the fault/fracture zone with different localization.

6.2. Numerical analysis of segment-joints tunnel model in effect of fault zone

6.2.1. Geometry modelling and parameters applied

To analyze the structural behavior of the segment-joints model according to the position of fault zone, the 2D numerical analysis was performed using the finite element analysis with FEM-Disroc.

The ground was modeled with a width of 400m, a height of 35m, and the tunnel, which was located 200m below the ground surface, had the same radius (internal diameter of 5.5m and segment thickness of 0.5m) as CH4 and CH5. An interface element was also modeled as a tail void-grouting between the ground and the segment. The initial and boundary conditions required for H+M coupling analysis were the same as CH5. There can be fault zones (Damage zone +fault interface) as the ground model differed from the previous chapter. Based on the properties of the existing investigated fault zone in CH1, a fault zone with a width of 4m and an interface element applied in the middle was modeled as core fault (Table 7: Properties of fault 2).

In Figure 66, this fault zone model was used to perform tunnel modeling at three different locations.

Figure 65 shows the geometry of the segment-joint tunnel model passing through the middle of the fault zone.

If we summarize the factors of the comparative analysis in this chapter, they include:

1) Comparative analysis between the segment-joint lining model and the continuum model of a tunnel passing through the fault zone.

2) Long-term behavior analysis according to the Biot value of the fault zone (DZ)

3) Tunnel analysis for three different fault zone positions

The applied parameters can be seen in Tables 23-26.

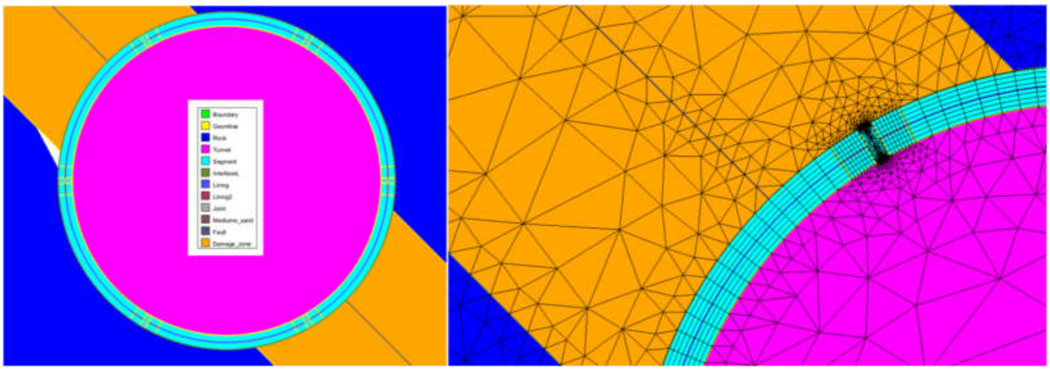

Figure 65. Segment-joint model geometry across the fault zone

Table 26. Properties applied

(C_M = 1/M (when porosity=0.4, biot :0.5~0.9) Damage zone “ 1/M: 0.0001818~0.0001819)

Medium-sand (M:31120, H:32100)			
E (kPa)	ν	k_1 Permeability (m2/kPa/s)	k_2 Permeability (m2/kPa/year)
1,500,000	0.25	2E-09	0.063

Rock (M:31120, H:32100)			
E (kPa)	ν	k_1 Permeability (m2/kPa/s)	k_2 Permeability (m2/kPa/year)
2,500,000	0.25	2E-09	0.063

Damage-zone (M:31120, H:32100)					
E (kPa)	ν	k_1 Permeability (m2/kPa/s)	k_1 Permeability (m2/kPa/year)	Biot	C_M Storage coefficient (m/kPa)
290,000	0.4	6E-08	1.9	0.9 or 0.5	0.00018

Interface-L before excavation (M:21100 H:22100)			
k_t Stiffness-t (kPa/m)	k_n Stiffness-n (kPa/m)	Ct Conductivity tangent(m^3/kPa/s)	Biot
1E+7	3E+7	2E-10	1

Interface-L after excavation (M:21200 H:22110)					
k_t Stiffness-t (kPa/m)	k_n Stiffness-n (kPa/m)	e thickness (m)	Ct (m^3/kPa/s)	Biot	Ct (m^3/kPa/year)
1E+7	2E+7	0.1	2E-15	1	6.3E-0.8

Fault (M:21220 H:22110)							
k_t Stiffness-t (kPa/m)	k_n Stiffness-n (kPa/m)	e thickness (m)	C Cohesive (kPa)	Φ Friction angle (。)	Ct Conductivity tangent (m^3/kPa/s)	Ct (m^3/kPa/year)	Biot
10,000	30,000	0.5	15	25	5E-07	15.8	1

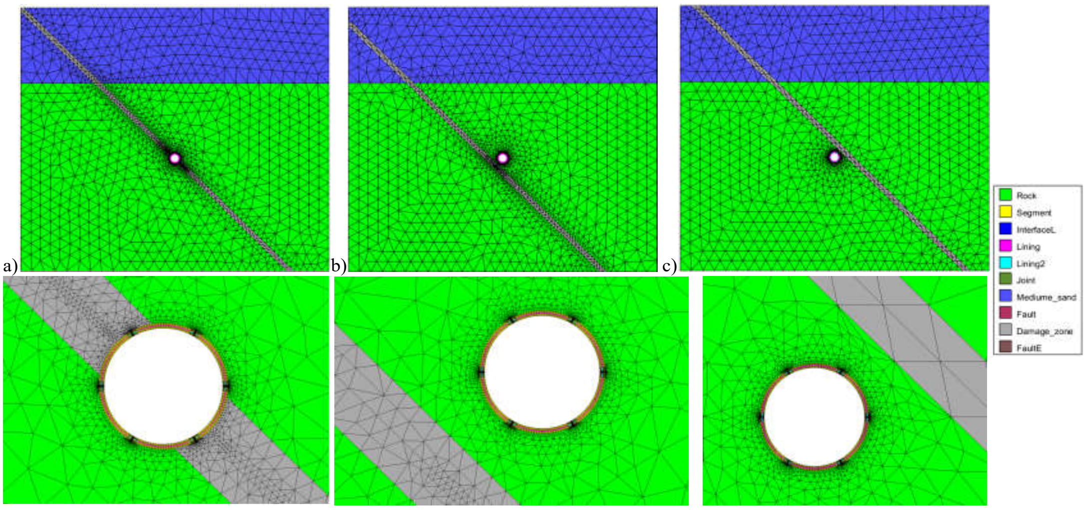

Figure 66. Segment-joint lining geometries according to three fault zone locations. a) Tunnel passing through the center of the fault zone. b) Tunnel passing through the upper part of the fault zone. c) Tunnel passing through the lower part of the fault zone.

6.2.2. Analysis of results

The comparisons between the segment-joint lining model and the continuum lining model were made in the previous chapter, but it was difficult to find significant differences under homogeneous ground conditions. Therefore, a comparison analysis of the two different types of linings was conducted on an elastic ground model that would show the largest anisotropic stress field due to the fault zone.

Figure 67 a)~c) represents the results of the comparison of member forces of the two different lining models. When comparing the two lining models in the previous chapter, the most noticeable difference was seen in the moment results. However, when looking at Figure 67 a), the axial force and radial displacement results of the segment-joint lining model are evaluated to be smaller than those of the continuum model. On the other hand, depending on the localization of fault zone, the result of moment for two lining model is similar.

Figures 68, 69, and 70 compare and analyze the segment-joint support reactions according to the Biot coefficient of the fault zone (DZ) at different positions.
In the case of a tunnel directly passing through fault zones, there is some difference in long-term behavior depending on the Biot coefficient of the fault zone (DZ). For example, Figure 68 shows that a larger Biot coefficient leads to slightly smaller

support reaction results.

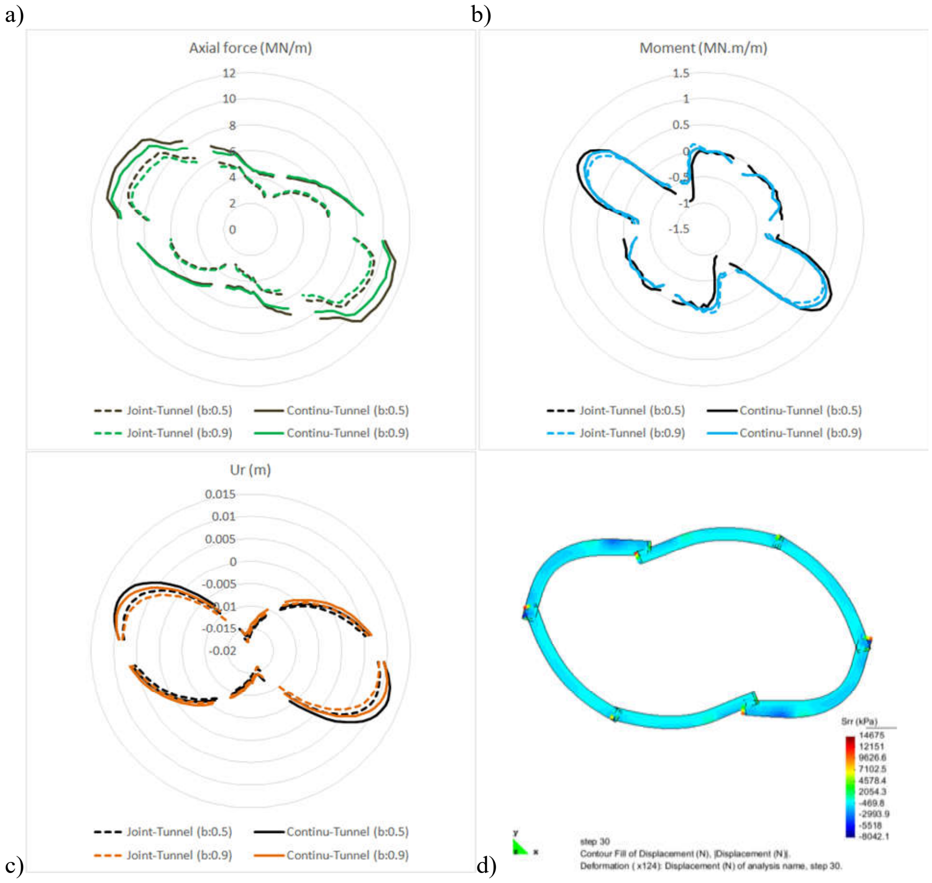

Figure 67. Comparison of member forces between the segment-joint lining model and the continuum lining model of a tunnel where fault zones pass through the center. a) Axial force comparison. b) Moment comparison. c) Radial displacement comparison. d) Radial stress in segments by post process GID.

However, when looking at the results of Figures 69 and 70, which have a fault zone at a distance from the tunnel, there is almost no difference in results according to the Biot coefficient of the fault zone (DZ). But when comparing the long-term behavior according to the location of the fault zone, a greater variation was observed when the fault zone was located in the upper part of the tunnel (Figure 70) compared to when it was located in the lower part (Figure 69).

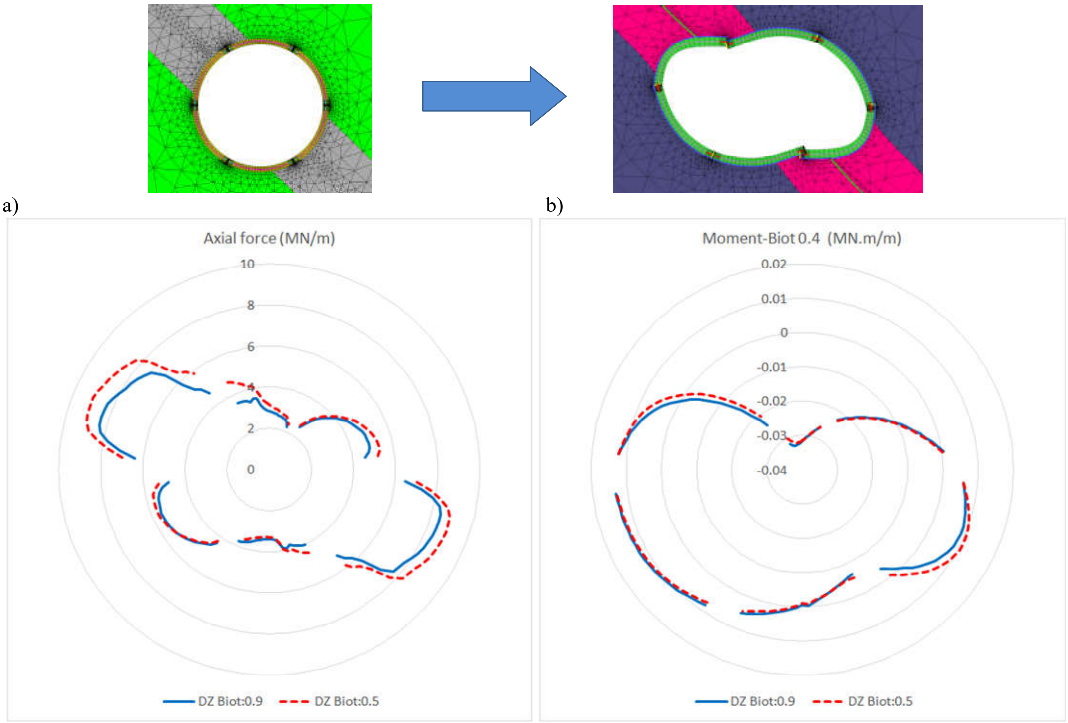

Figure 68. Member force according to the Biot coefficient of the fault zone (DZ) of the tunnel where the fault zone passes through the center of the tunnel. a) axial force comparison. b) moment comparison.

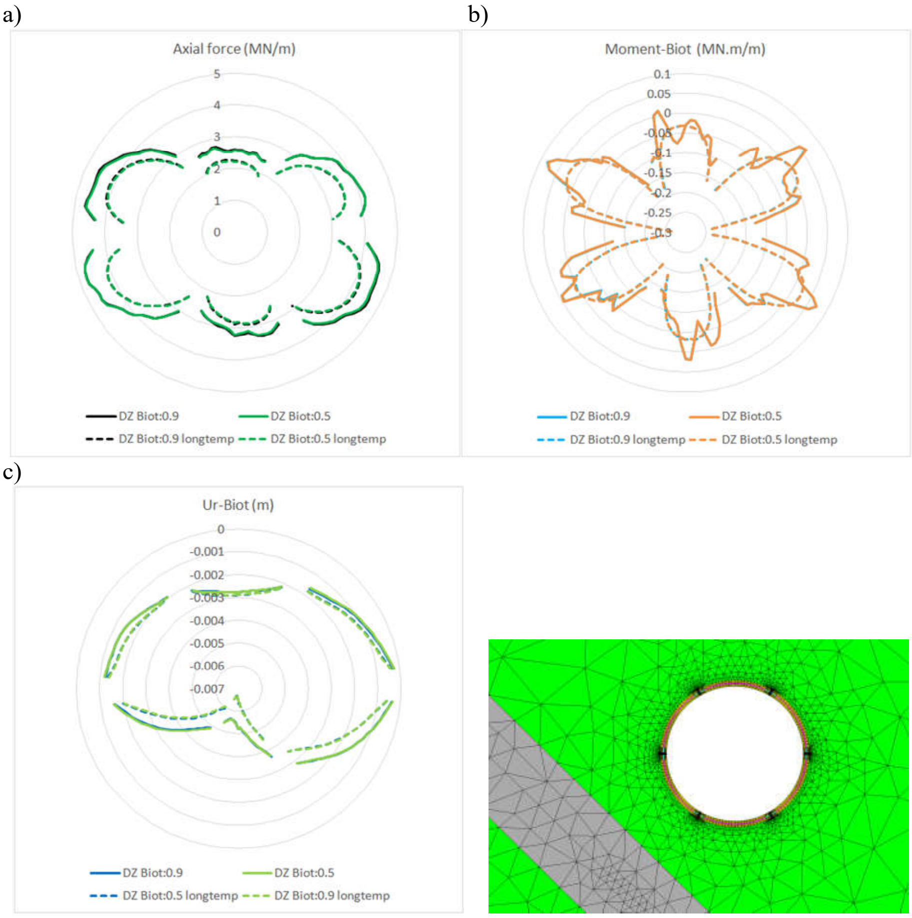

Figure 69. Member forces according to the Biot coefficient of the fault zone (DZ) of the tunnel located above of the fault zone. a) Axial force comparison. b) Moment comparison. c) Radial displacement comparison.

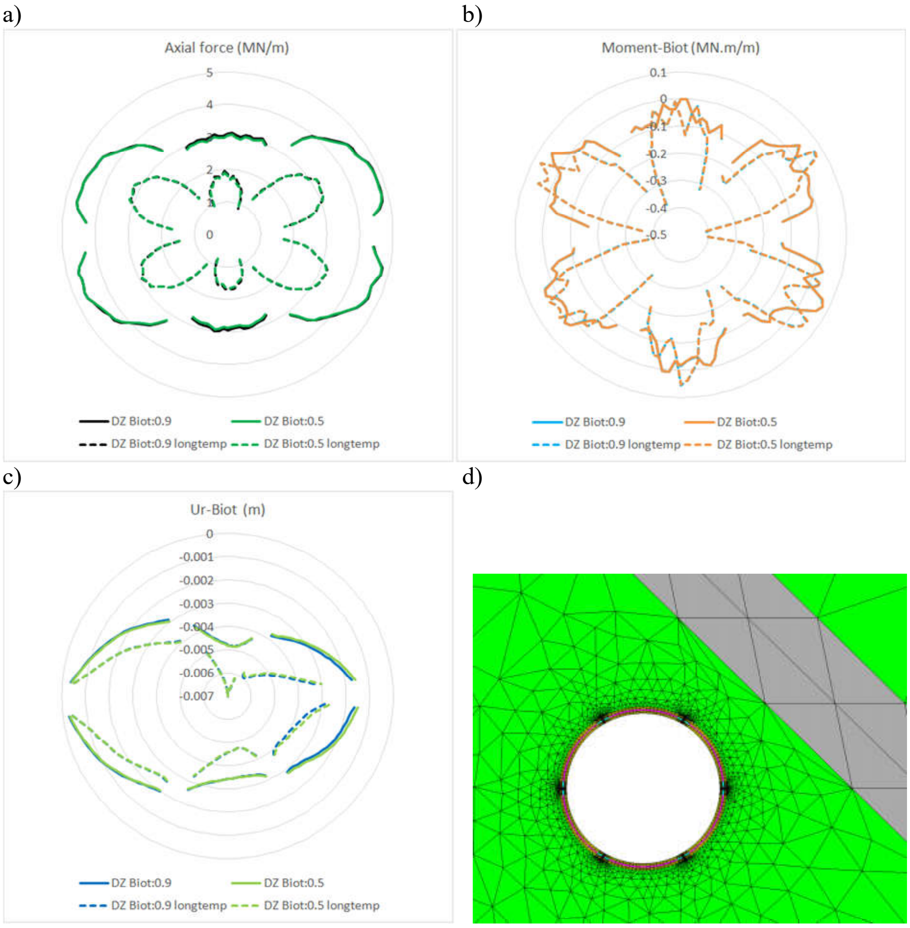

Figure 70. Member forces according to the Biot coefficient of the fault zone (DZ) of the tunnel located at the bottom of the fault zone. a) Axial force comparison. b) Moment comparison. c) Radial displacement comparison.

6.3. Conclusion and Perspective

First of all, in order to remind the necessity of segment-joint tunnel modeling once again, the continuum lining model and comparative numerical analysis were conducted. This is an analysis of tunnel behavior in the location of the fault zone with the greatest risk. (passing the fault zone)

Based on this comparative analysis, we found that the analysis of the general continuum lining model resulted in more overestimation of the lining member force than the segment-joint lining model. Because of this, we found that the more complex the ground, the more segment-joint model analysis is needed.

H+M numerical analysis was performed for the segment-joint tunnel model underground conditions at three different fault zone locations. In each fault zone, a comparative evaluation of the resulting M+H behavior was conducted through different Biot parameters.

As a result, the difference in the member force of the lining regarding the Biot coefficient of the fault zone was insignificant, but the M+H coupling long-term behavior analysis showed an overall decrease in member force.

Depending on the location of the fault zone, that is, when the fault zone passed through the top of the tunnel, the change in member force (decrease due to long-term behavior) was larger, which was judged to be due to the decrease in the hydraulic flow effect leading to the tunnel because of the fault zone with a relatively low permeability coefficient. However, there was no significant difference in the long-term behavior or the short-term behavior after excavation in the tunnel case where the fault zone penetrated.

Most studies have focused on investigating the effects of fault movements on the free field (Lin et al. 2007; Loukidis et al. 2009) and on shallow or deep foundations (Anastasopoulos and Gazetas, 2007; Anastasopoulos et al. 2008, Bransby et al. 2008a, b; Ng et al. 2014; Soomro et al. 2017).

However, given the increasing importance of seismic design for various structures, seismic analysis of the tunnel segment-joint model in the fault zone is also required. Subsea tunnel cracks caused by shield TBM tunnel segments and joints between them can lead to large-scale safety accidents due to leaks caused by joint connection defects. Therefore, more research is necessary on segment properties and joint constitutive models to simulate segments in more detail.

CONCLUSION

The research presented in this thesis aimed to design submarine tunnels more efficiently, from investigating the properties of underwater soil that must be considered, to determining the support methods in unexpected ground conditions, selecting appropriate construction methods (excavation timing), and analyzing the structure of the segment-jointed lining in the preferred TBM excavation method. By considering various problems and risks (such as hydraulic, mechanical, and geological) associated with submarine tunnel construction, parameter study cases were analyzed for unexpected ground conditions. This process is an attempt to improve the design analysis methods for constructing submarine tunnels safely.
This thesis was divided into six chapters, with each chapter focusing on a different aspect of the analysis.

Chapter 1: The expected route of the national submarine tunnel (Korea-Japan submarine tunnel, southeastern region) is difficult to investigate due to the challenging nature of the underwater soil survey, making it difficult to obtain clear information on the ground properties. Moreover, the behavior of underwater soil mechanics is different from that of terrestrial soil mechanics, so an empirical model was used to obtain the necessary local ground properties considering the relationship between the ground properties. The results were similar to the values obtained from drilling operations in Korea's East Sea region. However, the ground properties obtained through this empirical model are approximate, so core drilling is necessary for more detailed ground property investigations. If core drilling sample surveys are conducted on a large scale at the national level, the data will be valuable to geotechnical engineers.

Chapter 2: The most significant risk factor in submarine tunnel construction is hydraulic impact. Therefore, in this chapter, theoretical and numerical analyses using the Disroc software were conducted to compare the hydraulic flow analysis in submarine tunnel design, and the appropriate modelling method for numerical analysis was established. This was the cornerstone of the subsequent M+H coupling analysis.

Chapter 3: After studying the existing theoretical formula for the interaction between the existing ground and the continuous lining, a more advanced analytical solution for the ground-lining interaction was introduced. This can be considered an extension of the relationship between the ground and the lining to the linear elastic contact case. However, it suggests that this relationship is not limited to linear elastic contact, and a limit model can be applied to construct a more advanced theoretical model. Furthermore, if the model of the tunnel excavation convergence stage is shown, more efficient methods can be proposed for designing.

Chapter 4: A better geotechnical numerical analysis could be performed through modelling that simulated the volume segment lining, which is divided by joints, more closely to reality. Through this, it was possible to overcome the limitation of not being able to interpret the influence evaluation of the joint part of the lining under various ground conditions. In addition, by modelling the tail-void part between the lining and the ground as an interface element, the load area that the lining needs to support could be interpreted in various ways. However, since the segment lining performance was limited to the performed conditions, more research is necessary to apply it to actual construction sites.

Chapter 5: Submarine (underwater) tunnel modelling under unsaturated ground conditions with the segment-joint lining model simulated in the previous chapter was performed by hydraulic-mechanical coupling analysis. The H+M coupling is focused on a long-term behavior analysis. In the behavior analysis of the lining, not only the mechanical load but also the hydraulic effect was evaluated. Even in a dynamically anisotropic load field, an evaluation was conducted, in which the isotropic hydraulic effect was added due to the M+H coupled coefficient (Biot). If the segment joint model can be analyzed with a more accurate constitutive model, it is believed that the hydraulic deterioration of watertight tunnel phenomenon can be estimated in more detail.

Chapter 6: Segment lining behavior including joints was analyzed by H+M coupling analysis in complex ground. Segment-joint lining behavior underground conditions with three geographically different fault zones were analyzed. In the model in which the most risk fault zone directly passes through the tunnel, the member forces of the segment-joint model and the continuum lining model was compared and analyzed, and the segment-joint model showed relatively small member forces. The evaluation of the member strength of the lining according to the location of the fault zone, which is the soft ground, displayed different aspects, and a tendency for an overall decrease of member forces of the lining in the long-term. As the segment joint behaves elastically, it demonstrates sliding under risky ground conditions, but it does not display the failure limit behavior considering the actual frictional force and cohesion. Therefore, a study applying a model more suitable to the actual behavior is needed.

We have thus studied a number of problems related to the design of submarine tunnels. Some results that we have obtained, in particular on the "ground/lining" interaction and segment lining, go beyond the framework of submarine tunnels and are of a more general nature. We tried to show the importance of a good numerical modelling taking into account as precisely as possible the joints and the interfaces in this thesis.

In addition, this work introduced an advanced model for modelling joints in segments. However, we acknowledge that more material property data and constitutive models are needed to improve joint modelling accuracy. Note also that joints have a highly non-linear behavior. As the non-linearity of the constitutive models increase, it becomes sometimes difficult to obtain numerical convergence for complex structures. We did not present the cases where thee problems were observed and they need improved numerical methods. Also, we think that almost the maximum possible within the framework of a 2D modelling was done in the present work. Certain questions such as the influence of the excavation face and the axial layout of the segments can only be investigated further with 3D analysis methods and tools.

REFERENCE

Anastasopoulos, I. and Gazetas, G. (2007), "Foundation–structure systems over a rupturing normal fault: Part II. Analysis of the Kocaeli case histories", Bulletin of Earthquake Engineering, 5(3), 277-301.DOI: https://doi.org/10.1007/s10518-007-9030-9

Anastasopoulos, I., Callerio, A., Bransby, M., Davies, M., El Nahas, A., Faccioli, E., Gazetas, G., Masella, A., Paolucci, R. and Pecker, A. (2008), "Numerical analyses of fault–foundation interaction", Bulletin of earthquake engineering, 6(4), 645-675.DOI: https://doi.org/10.1007/s10518-008-9078-1

ANDREOTTI, Guido, CALVI, Gian Michele, SOGA, Kenichi, GONG, Chenjie and DING, Wenqi. Cyclic model with damage assessment of longitudinal joints in segmental tunnel linings. Tunnelling and Underground Space Technology, [online]. 2020, vol. 103, no. June, pp. 103472. DOI 10.1016/j.tust.2020.103472.

ARNAU, Oriol and MOLINS, Climent. Experimental and analytical study of the structural response of segmental tunnel linings based on an in situ loading test. Part 2: Numerical simulation. Tunnelling and Underground Space Technology, [online]. 2011, vol. 26, no. 6, pp. 778–788. DOI 10.1016/j.tust.2011.04.005.

ASCHE, H., IRELAND, T. Segmental lining design for large-diameter road tunnels. Proceedings Rapid Excav Tunneling Conf., [online]. 2013, pp. 866-877.

AVSETH, Per Age. Combining rock physics and sedimentology for seismic reservoir characterization of North Sea turbidite systems. Stanford University, 2000.

BAKKER, K.J. Structural design of linings for bored tunnels in soft ground. Heron, [online]. 2003, vol. 48, no. 1, pp. 33-6.

BERKOWITZ, Brian. Characterizing flow and transport in fractured geological media: A review. Advances in water resources, [online]. 2002, vol. 25, no. 8-12, pp. 861-884.

Biot, M.A., 1955. Theory of elasticity and consolidation for a porous anisotropic solid. J. Appl. Phys. 26 (2), 182–185.

Biot, M.A., 1956a. General solutions of the equations of elasticity and consolidation for a porous material. J. Appl. Phys. 78, 91–96.

Biot, M.A., 1956b. Theory of deformation of a porous viscoelastic anisotropic solid. J. Appl. Phys. 127 (5), 459–467.

Biot, M.A., 1956c. Thermoelasticity and irreversible thermodynamics. J. Appl. Phys. 27, 240–253.

Biot, M.A., 1962. Mechanics of deformation and acoustic propagation in porous media. J. Appl. Phys. 33, 1482–1498.

Biot, M.A., 1972. Theory of finite deformations of porous solids. Indiana Univ. Math. J. 21 (7), 597–620.

Biot, M.A., 1973. Nonlinear and semilinear rheology of porous solids. J. Geophys. Res. 78 (23), 4924–4937.

BLOM, C.B.M. Design philosophy of concrete linings for tunnels in soft soils. ISBN 9040723664.

Bransby, M., Davies, M. and Nahas, A.E. (2008), "Centrifuge modelling of normal fault–foundation interaction", Bulletin of Earthquake Engineering, 6(4), 585-605.DOI: https://doi.org/10.1007/s10518-008-9079-0

Bransby, M., Davies, M., El Nahas, A. and Nagaoka, S. (2008), "Centrifuge modelling of reverse fault–foundation interaction", Bulletin of Earthquake Engineering, 6(4), 607-628.DOI: https://doi.org/10.1007/s10518-008-9080-7

BRIGGS, K.B.; FISCHER, K.M. Geoacoustic model of the strait of Korea. NAVAL OCEANOGRAPHIC AND ATMOSPHERIC RESEARCH LAB STENNIS SPACE CENTER MS, [online]. 1991.

Broere, R.B.J. Brinkgreve (2002), Phased Simulation of a Tunnel Boring Processin Soft Soil, Numerical Methods in Geotechnical Engineering Mestat (ed.), Presses de lENPC/LCPC, Paris, pp. 529-536

BUSARI, Afis et MIROSLAV, Marence. A finite element model for optimum design of plain concrete pressure tunnels under high internal pressure. 2012.

Caine, J. S., Evans, J. P., and Forster, C. B. (1996). Fault zone architecture and permeability structure. Geology, 24(11), 1025-1028.

Cha, M., Cho, G., and Santamarina, J. C. (2009). Long-wavelength P-wave and S-wave propagation in jointed rock masses. Geophysics, 74(5), E205-E214.

Cho, W.S., Song, K.I., Ryu, H.H.(2014), "Analysis on the behavior of shield TBM cable tunnel: The effect of the distance of backfill grout injection from the end of skin plate", Journal of Korean Tunnelling and Underground Space Society, Vol. 16, No.2, pp. 213-224.

Cho, W.S., Song, K.I., Kim, K.Y.(2014), "The study on the effect of fracture zone and its orientation on the behavior of shield TBM cable tunnel", Journal of Korean Tunnelling and Underground Space Society, Vol. 16, No.4, pp. 403-415.

Choi, H., and Park, K. (1986). Cretaceous/Neogene stratigraphic transition and post-Gyeongsang tectonic evolution along and off the southeast coast, Korea. Journal of Asian Earth Sciences, 21(4), 281-296.

Choi, J. S., Yang, S. J., and Kim, Y. S. (2009). Fault zone classification and structural characteristics of the southern Yangsan fault in the Sangcheon-ri area, SE Korea. Journal of the Geological Society of Korea, 45(1), 9-28 (in Korean with English abstract).

Chough, S. K., Lee, H. J., and Han, S. J. (1991). Sedimentological and geotechnical properties of fine-grained sediments in part of the South Sea, Korea. Continental Shelf Research, 11(2), 183-195.

Cilingir, U., Madabhushi, S.P.G. (2011a), "A model study on the effects of input motion on the seismic behaviour of tunnels", Soil Dynamics and Earthquake Engineering, Vol. 31, No. 3, pp. 452-462.

Cilingir, U., Madabhush, S.P.G. (2011b), "Effect of depth on seismic response of circular tunnels", Canadian Geotechnical Journal, Vol. 48, No. 1, pp. 117-127.

COLI, Massimo and PINZANI, Alice, 2014. Tunnelling and hydrogeological issues: A short review of the current state of the art. Rock Mechanics and Rock Engineering. 2014. Vol. 47, no. 3, pp. 839–851. DOI 10.1007/s00603-012-0319-x.

DADASHI, E., NOORZAD, A., SHAHRIAR, K., et al. Hydro-mechanical interaction analysis of reinforced concrete lining in pressure tunnels. Tunnelling and Underground Space Technology, 2017, vol. 69, p. 125-132.

De La Fuente M, Taherzadeh R, Sulem J, Nguyen XS, Subrin D. Applicability of the Convergence-Confinement Method to Full-Face Excavation of Circular Tunnels with Stiff Support System. Rock Mech Rock Eng. 2019;52(7):2361-2376. doi:10.1007/s00603-018-1694-8

Ding Z, He SY, Zhou WH, Xu T, He SH, Zhang X. Analysis of ground deformation induced by shield tunneling considering the effects of muck discharge and grouting. Transportation Geotechnics. 2021;30:100629. doi:10.1016/j.trgeo.2021.100629

Do NA, Dias D, Oreste P, Djeran-Maigre I. 2D numerical investigation of segmental tunnel lining behavior. Tunn Undergr Sp Technol. 2013;37:115-127. doi:10.1016/j.tust.2013.03.008

Do NA, Dias D, Oreste PP, Djeran-Maigre I. Internal forces in segmental tunnel linings—a comparison between current design methods. J Min Sci. 2014;50(2):326-334.

doi:10.1134/S1062739114020161

Do NA, Oreste P, Dias D, Antonello C, Djeran-Maigre I, Livio L. Stress and strain state in the segmental linings during mechanized tunnelling. Geomech Eng. 2014;7(1):75-85. doi:10.12989/gae.2014.7.1.075

Duddeck H, Erdmann J. On structural design models for tunnels in soft soil. Undergr Sp. 1985;9(5-6):246-259. doi:10.1016/0148-9062(87)91549-x

Dvorkin J, Prasad M, Sakai A, et al. Elasticity of marine sediments: Rock physics modelling. Geophys Res Lett. 1999;26(12):1781-1784. doi:10.1029/1999GL900356

D. J. Curtis, Mott, Hay and Anderson C. Discussions: The Circular Tunnel in Elastic Ground. Geotechnique. 1976;26(1):231-237. doi:10.1680/geot.1976.26.1.231

Einstein, H.H., Schwartz CW. Simplified analysis for tunnel supports. J Geotech Eng Div. 1979;105(4):499-518.

El Tani, Mohamed. Circular tunnel in a semi-infinite aquifer. Tunnelling and underground space technology, 2003, vol. 18, no 1, p. 49-55.

El Tani, Mohamed. Helmholtz evolution of a semi-infinite aquifer drained by a circular tunnel. Tunnelling and underground space technology, 2010, vol. 25, no 1, p. 54-62.

Fernández, Gabriel. Behavior of pressure tunnels and guidelines for liner design. Journal of geotechnical engineering, 1994, vol. 120, no 10, p. 1768-1791.

Faulkner, D. R., Lewis, A. C., and Rutter, E. H. On the internal structure and mechanics of large strike-slip fault zones: Field observations of the Carboneras fault in southeastern Spain. Tectonophysics. 2003;367(3-4):235-251.

Foose, G.J., Benson, C.H. and Boscher P.J. Sand reinforced with shredded waste tire. Journal of Geotechnical Engineering. 1996;Vol. 122:760-767.

Fracsima. Disroc 2016: A Finite Element Code for modelling Thermo-Hydro-Mechanical processes in fractures porous media. http://www.fracsima.com/DISROC.

Fracsima/Disroc. Materials-Catalogue. In: . 2022. pp. 5–12.

Flügge W. Stresses in shells. Springler-Verlag Inc, New York. 1966.

Gassmann, F. Elasticity of porous media. Vierteljahrsschrder Naturforschenden Gesselschaft. 1951;96:1-23.

Goodman RE, Moye DG, Van Schalkwyk A, et al. Ground water inflows during tunnel driving. College of Engineering, University of California. 1964.

Goodman RE. Introduction to rock mechanics. New York: Wiley. 1989.

GRAZIANI, Alessandro et BOLDINI, Daniela. Influence of hydro-mechanical coupling on tunnel response in clays. Journal of geotechnical and geoenvironmental engineering, 2012, vol. 138, no 3, p. 415-418.

Gregor, T., Garrod, B. and Young, D. (2007). "Analyses of underground structures crossing an active fault in Coronado, California", Proceedings of the World Tunnel Congress.

Guan Z, Deng T, Wang G, Jiang Y. Studies on the key parameters in segmental lining design. J Rock Mech Geotech Eng. 2015;7(6):674-683. doi:10.1016/j.jrmge.2015.08.008

Gudmundsson A, Simmenes TH, Belinda L, Philipp SL. Effects of internal structure and local stress on fracture propagation, deflection, and arrest in fault zones. J Struct Geol. 2010;32(11):1643-1655.

Gustafson G, Walke L. Hydrogeology for rock engineers. Stockholm: BeFo. 2012.

Guo Z, Wu B, Jia S. An analytical model for predicting the mechanical behavior of a deep lined circular pressure tunnel by using complex variable method. Geomech Geophys Geo-Energy Geo-Resources. 2021;7(4). doi:10.1007/s40948-021-00282-1

Hamilton EL. Elastic properties of marine sediments. Journal of Geophysical Research. 1971;76(2):579-604.

Hamilton EL. Shear-wave velocity versus depth in marine sediments: A review. Geophysics. 1976;41(5):985-996.

Hamilton EL. Variations of density and porosity with depth in deep-sea sediments. Journal of Sedimentary Research. 1976;46(2):280-300.

Hamilton EL. Sound velocity–density relations in sea-floor sediments and rocks. The Journal of the Acoustical Society of America. 1978;63(2):366-377.

Hamilton EL. V p/V s and Poisson's ratios in marine sediments and rocks. The Journal of the Acoustical Society of America. 1979;66(4):1093-1101.

Hamilton EL. Geoacoustic modelling of the sea floor. The Journal of the Acoustical Society of America. 1980;68(5):1313-1340.

Heynekamp MR, Goodwin LB, Mozley PS, Haneberg WC. Controls on fault-zone architecture in poorly lithified sediments, Rio Grande Rift, New Mexico: implications for fault zone permeability and fluid flow. In: Haneberg WC, Mozley PS, Moore JC, Goodwin LB, editors. Faults and Subsurface Fluid Flow in the Shallow Crust. American Geophysical Union Geophysical Monograph. 1999;113:27-50.

Heuer RE. Estimating rock tunnel water inflow. In: Proceedings of the Rapid Excavation and Tunneling Conference. Society for Mining, Metallurgy & Exploration, Inc. 1995;p.41-60.

Huang WM, Wang JC, Yang ZX, Xu RQ. Analytical model for segmental tunnel lining with nonlinear joints. Tunnelling and Underground Space Technology. 2021;114(December 2020):103994. doi:10.1016/j.tust.2021.103994

Huangfu M, Wang MS, Tan ZS, et al. Analytical solutions for steady seepage into an underwater circular tunnel. Tunnelling and Underground Space Technology. 2010;25(4):391-396.

Holmøy KH, Nilsen B. Significance of geological parameters for predicting water inflow in hard rock tunnels. Rock Mechanics and Rock Engineering. 2014;47:853-868.

INOUE, Eiji. Geological problems on Cretaceous and Tertiary rocks in and around Tsushima-Korea Straits. United Nations ESCAP, CCOP Technical Bulletin, 1982, 15: 85-121.

JEONG, Soocheol; SEOL, Soon Jee; BYUN, Joongmoo. Effective estimation of porosity and fluid saturation using joint inversion result of seismic and electromagnetic data. Geophysics and Geophysical Exploration, 2015, 18.2: 54-63.

JUNG, Hyuksang; KIM, Hyeyang; CHUN, Byungsik. A Study on the Ground Settlement and Reinforcement Measures in the Case of Tunnelling at the Yangsan Fault. Journal of the Korean Geoenvironmental Society, 2009, 10.6: 35-48.

KANG, Byung-Yun, PARK, Hyung Keun, CHA, Jae-Hoon, et al. A study on the optimal reinforcement area for excavation of a small cross-section shield TBM tunnel in fault fracture zone through parameter analysis. Journal of Korean Tunnelling and Underground Space Association, 2020, vol. 22, no 3, p. 261-275.

KIM, Bum-Joo, JUNG, Jae-Hoon, JANG, Yeon-Soo, et al. A Study on the Lining Stability of Old Tunnel Using Groundwater Flow Modelling and Coupled Stress-Pore Water Pressure Analysis. Journal of the Korean Geotechnical Society, 2012, vol. 28, no 4, p. 101-113.

KIM, D.C., Sung, J.Y., Park, S.C., Lee, G.H., Choi, J.H., Kim, G.Y., Seo, Y.K., Kim, J.C., 2001. Physical and acoustic properties of shelf sediments, the South Sea of Korea. Marine Geology 179, 39–50.

KIM, G. Y. et KIM, D. C. Comparison and correlation of physical properties from the plain and slope sediments in the Ulleung Basin, East Sea (Sea of Japan). Journal of Asian Earth Sciences, 2001, vol. 19, no 5, p. 669-681.

Kim, G.Y., Kim, D.C., Shin, B.K., Seo, Y.K., Lee, G.H., 2005. Geoacoustic model of surface sediments in the east of Geoje Island, the South Sea of Korea. Journal of the Oceanographical Society of Korea 10, 129–138.

KIM, Gil Young, et al. Physical and geoacoustic properties of surface sediments off eastern Geoje Island, South Sea of Korea. Quaternary International, 2011, 230.1-2: 21-33.

KIM HJ, Eisenstein Z. Prediction of tunnel lining loads using correction factors. Eng Geol. 2006;85(3-4):302-312. doi:10.1016/j.enggeo.2006.03.001

KIM, Ji-Won; HONG, Eun-Soo; CHO, Gye-Chun. Assessment of elastic-wave propagation characteristics in grouting-improved rock mass around subsea tunnels. Journal of Korean Tunnelling and Underground Space Association, 2016, 18.2: 235-244.

KOCHINA, Polubarinova, et al. Theory of ground water movement. 1962.

KOLYMBAS, Dimitrios et WAGNER, Peter. Groundwater ingress to tunnels–the exact analytical solution. Tunnelling and Underground Space Technology, 2007, vol. 22, no 1, p. 23-27.

Kwak, C.W., Park, I.J. (2015), "Numerical simulation for surface settlement considering face vibration of TBM tunnelling in mixed-face condition", Journal of Korean Tunnelling and Underground Space Association, Vol. 17, No. 3, pp. 333-339.

KWAK, Chang-Won, JANG, Dong-In, PARK, Inn-Joon, et al. Seismic response analysis of virtual honam-jeju subsea tunnel. Journal of Korean Tunnelling and Underground Space Association, 2016, vol. 18, no 3, p. 319-329.

Kirsch G. Die théorie der elastizitat und die bedurfnisse fer festigkeitslehre. Published online 1898.

LEE, K. M., HOU, X. Y., GE, X. W. and TANG, Y., 2001. An analytical solution for a jointed shield-driven tunnel lining. International Journal for Numerical and Analytical Methods in Geomechanics. 2001. Vol. 25, no. 4, pp. 365–390. DOI 10.1002/nag.134.

Lee YK, Pietruszczak S. A new numerical procedure for elasto-plastic analysis of a circular opening excavated in a strain-softening rock mass. Tunn Undergr Sp Technol. 2008;23(5):588-599. doi:10.1016/j.tust.2007.11.002

Lei S (1999) An analytical solution for steady flow into a tunnel.Ground Water 37:2326

Li S cai, Wang M bin. Elastic analysis of stress-displacement field for a lined circular tunnel at great depth due to ground loads and internal pressure. Tunn Undergr Sp Technol. 2008;23(6):609-617. doi:10.1016/j.tust.2007.11.004

LI, Shu-cai, LIU, Hong-liang, LI, Li-ping, et al. Large scale three-dimensional seepage analysis model test and numerical simulation research on undersea tunnel. Applied Ocean Research, 2016, vol. 59, p. 510-520.

LI, Xiaojun, YAN, Zhiguo, WANG, Zhen and ZHU, Hehua, 2015. Experimental and analytical study on longitudinal joint opening of concrete segmental lining. Tunnelling and Underground Space Technology. Online. 2015. Vol. 46, pp. 52–63. DOI 10.1016/j.tust.2014.11.002.

Lin, M.-L., Chung, C.-F. and Jeng, F.-S. (2006), "Deformation of overburden soil induced by thrust fault slip", Engineering Geology, 88(1-2), 70-89.DOI: https://doi.org/10.1016/j.enggeo.2006.08.004

Lin, M.-L., Chung, C.-F., Jeng, F.-S. and Yao, T.-C. (2007), "The deformation of overburden soil induced by thrust faulting and its impact on underground tunnels", Engineering Geology, 92(3-4), 110-132.DOI: https://doi.org/10.1016/j.enggeo.2007.03.008

LIU, Xian, DONG, Zibo, BAI, Yun and ZHU, Yaohong, 2017. Investigation of the structural effect induced by stagger joints in segmental tunnel linings: First results from full-scale ring tests. Tunnelling and Underground Space Technology. Online. 2017. Vol. 66, no. April, pp. 1–18. DOI 10.1016/j.tust.2017.03.008.

LIU, Xiao-Xue, SHEN, Shui-Long, XU, Ye-Shuang, et al. Analytical approach for time-dependent groundwater inflow into shield tunnel face in confined aquifer. International Journal for Numerical and Analytical Methods in Geomechanics, 2018, vol. 42, no 4, p. 655-673.

Loukidis, D., Bouckovalas, G.D. and Papadimitriou, A.G. (2009), "Analysis of fault rupture propagation through uniform soil cover", Soil Dynamics and Earthquake Engineering, 29(11-12), 1389-1404.DOI: https://doi.org/10.1016/j.soildyn.2009.04.003

LUDWIG, William J.; MURAUCHI, Sadanori; HOUTZ, Robert E. Sediments and structure of the Japan Sea. Geological Society of America Bulletin, 1975, 86.5: 651-664.

LUTTIKHOLT, A. J.T., VERVUURT, A. H.J.M. and DEN UIJL, J. A., 2008. Ultimate limit state analysis of a segmented tunnel lining. Proceedings of the International FIB Symposium 2008 - Tailor Made Concrete Structures: New Solutions for our Society. 2008. Vol. 1998, pp. 267. DOI 10.1201/9781439828410.ch195.

M.J.Pender. Elastic solutions for a deep circular tunnel. Geotechnique. 1980;31(3):434-436. doi:10.1680/geot.1981.31.3.434

MAGARA, Kinji. Thickness of removed sedimentary rocks, paleopore pressure, and paleotemperature, southwestern part of Western Canada Basin. AAPG Bulletin, 1976, 60.4: 554-565.

Marwan A, Gall VE, Alsahly A, Meschke G. Structural forces in segmental linings: process-oriented tunnel advance simulations vs. conventional structural analysis. Tunn Undergr Sp Technol. 2021;111(December 2020):103836. doi:10.1016/j.tust.2021.103836

MIN, G. H. Seismic stratigraphy and depositional history of Pliocene-Holocene deposits in the southeastern shelf, Korean Peninsula. Unpublished PhD Thesis, Seoul National University, Seoul, Korea, 1994, vol. 196.

MINAMI, A. Distribution and characteristics of the sedimentary basin offshore San-in to Tsushima Island. Journal of the Japanese Association for Petroleum Technologists, 1979, 44: 321-328.

MOHD-NORDIN, Mohd Mustaqim, et al. Long-wavelength elastic wave propagation across naturally fractured rock masses. Rock mechanics and rock engineering, 2014, 47.2: 561-573.

MORGAN, H. D., 1961. A contribution to the analysis of stress in a circular tunnel. Geotechnique. 1961. Vol. 11, no. 1, pp. 37–46. DOI 10.1680/geot.1961.11.1.37.

MUIR WOOD, A. M., 1975. The Circular Tunnel in Elastic Ground. Geotechnique. 1975. Vol. 25, no. 1, pp. 115–127. DOI 10.1680/geot.1976.26.1.231.

MUSKAT, Morris. The flow of homogeneous fluids through porous media. Soil Science, 1938, vol. 46, no 2, p. 169.

Nam, K.C., Heo, Y., You, K.H. (2003), "The effects of the face reinforcement at shallow tunnels in fractured rock masses", Journal of Korean Tunnelling and Underground Space Association, Vol. 5, No. 4, pp. 323-336.

Ng, C.W.W., Soomro, M.A. and Hong, Y. (2014), "Three-dimensional centrifuge modelling of pile group responses to side-by-side twin tunnelling", Tunnelling and Underground Space Technology, 43, 350-361.DOI: https://doi.org/10.1016/j.tust.2014.05.002

NILSEN, Bjørn. Characteristics of water ingress in Norwegian subsea tunnels. Rock mechanics and rock engineering, 2014, vol. 47, p. 933-945.

OH, Dong-Wook, et al. A preliminary numerical analysis on the behaviour of tunnel under construction in fracture zone considering seismic load. Journal of Korean Tunnelling and Underground Space Association, 2019, 21.2: 279-299.

OH, Ju Young and ZIEGLER, Martin, 2014. Investigation on influence of tail void grouting on the surface settlements during shield tunneling using a stress-pore pressure coupled analysis. KSCE Journal of Civil Engineering. 2014. Vol. 18, no. 3, pp. 803–811. DOI 10.1007/s12205-014-1383-8.

Oh, J.Y., Park, H.K., Kim, D.H., Chang, S.B., Lee, S.B., Choi, H.S.(2017), "Study on the effect of tail void grouting on the short- and long-term surface settlement in the shield TBM Tunneling using numerical analysis", Journal of Korean Tunnelling and Underground Space Society, Vol. 19, No.2, pp. 265-281.

Oh, T.S.(2014), "Model Testing and Analysis on Shield TBM Excavation for Railway Tunnel in Mixed Ground", Ph.D. Thesis, Seoul National University of Science and Technology Graduate School of Railways

PARASKEVOPOULOU, Chrysothemis and DIEDERICHS, Mark, 2018. Analysis of time-dependent deformation in tunnels using the Convergence-Confinement Method. Tunnelling and Underground Space Technology. Online. 2018. Vol. 71, no. November 2016, pp. 62–80. DOI 10.1016/j.tust.2017.07.001.

PARK, C. H. A Review on Constructing Seismic Rock Physics Models Based on Gassmann's Equation for Reservoir Fluid Substitution: J. Korean Soc. Miner. Energy Resour, 2014, 51: 448-467.
PARK, Soo C. et YOO, Dong G. Depositional history of Quaternary sediments on the continental shelf off the southeastern coast of Korea (Korea Strait). Marine Geology, 1988, vol. 79, no 1-2, p. 65-75.

PARK, Kyung-Ho, OWATSIRIWONG, Adisorn, et LEE, Joo-Gong. Analytical solution for steady-state groundwater inflow into a drained circular tunnel in a semi-infinite aquifer: a revisit. Tunnelling and Underground Space Technology, 2008, vol. 23, no 2, p. 206-209.

PARK, Yong-Ahn. Late Quaternary Sedimentation on the Continental Shelf off the South-East Coast of Korea-A Further Evidence of Relict Sediments. Journal of the Oceanographical Society of Korea, 1985, vol. 20, no 3, p. 55-61.

PEILA, Daniele, BORIO, Luca and PELIZZA, Sebastiano, 2011. The behaviour of a two-component backfilling grout used in a tunnel-boring machine. Acta Geotechnica Slovenica. 2011. Vol. 8, no. 1, pp. 5–15.

PERRIER, Raymond; QUIBLIER, Jacques. Thickness changes in sedimentary layers during compaction history; methods for quantitative evaluation. AAPG Bulletin, 1974, 58.3: 507-520.

RAMONI, M., ANAGNOSTOU, G, 2010. Tunnel boring machines under squeezing conditions. Tunnelling and Underground Space Technology. 2010. Vol. 25, pp. 139–157.

Reddy JN, Wang CM, Lee KH. Relationships between bending solutions of classical and shear deformation beam theories. Int J Solids Struct. 1997;34(26):3373-3384. doi:10.1016/S0020-7683(96)00211-9

Rendulic, L., 1936. Porenziffer und Porenwasserdruck in Tonen (Void ratio and pore water pressure in clays). Der Bauingenieur 17, 559–564.

REUTER, E., KOPP, B., et LEMKE, S. Hallandsas Tunnel. Waterproofing system with a, 2000, vol. 4, p. 39-45.

SALEMI, Akbar, ESMAEILI, Morteza and SERESHKI, Farhang, 2015. Normal and shear resistance of longitudinal contact surfaces of segmental tunnel linings. International Journal of Rock Mechanics and Mining Sciences. Online. 2015. Vol. 77, pp. 328–338. DOI 10.1016/j.ijrmms.2015.04.014.

SALENCON J. Handbook of Continuum Mechanics: General Concepts Thermoelasticity. Springer Science & Business Media; 2012.

SAMARDZIOSKA, Todorka et POPOV, Viktor. Numerical comparison of the equivalent continuum, non-homogeneous and dual porosity models for flow and transport in fractured porous media. Advances in water resources, 2005, vol. 28, no 3, p. 235-255

SCHLEISS, Anton J. Design of pervious pressure tunnels. Water Power and Dam Construction, 1986, vol. 38, no 5, p. 21-26.

Shi J, Wang Y, Chen Y. A simplified method to estimate curvatures of continuous pipelines induced by normal fault movement. Can Geotech J. 2018;55(3):343-352. doi:10.1139/cgj-2017-0044

SHIN, Hee Soon. Construction of Subsea Tunnels: Overview and Status. Journal of the Korean Society of Mineral and Energy Resources Engineers, 2009, vol. 46, no 1, p. 125-133.

SHINN, Young Jae, et al. Result of CO 2 Geological Storage Site Survey for Small-scale Demonstration in Pohang Basin, Yeongil Bay, SE Korea. The Journal of Engineering Geology, 2018, 28.2: 161-174.

SONG, Gyu-Jin, YUN, Hyun-Seok, et SEO, Yong-Seok. Prediction of fault zone ahead of tunnel face using longitudinal displacement measured on tunnel face. The Journal of Engineering Geology, 2016, vol. 26, no 2, p. 187-196.

Soomro, M.A., Ng, C.W.W., Liu, K. and Memon, N.A. (2017), "Pile responses to side-by-side twin tunnelling in stiff clay: Effects of different tunnel depths relative to pile", Computers and Geotechnics, 84, 101-116.DOI: https://doi.org/10.1016/j.compgeo.2016.11.011

SULEM, J., PANET, M. and GUENOT, A., 1987. An analytical solution for time-dependent displacements in a circular tunnel. International Journal of Rock Mechanics and Mining Sciences and. 1987. Vol. 24, no. 3, pp. 155–164. DOI 10.1016/0148-9062(87)90523-7.

TEACHAVORASINSKUN, Supot, 2018. Evaluation of liner responses due to non-uniform tail void grouting pressure. Geomechanics and Geoengineering. Online. 2018. Vol. 13, no. 3, pp. 226–232. DOI 10.1080/17486025.2018.1439187.

TIMOSHENKO, S. and JNG. Theory of Elasticity. Ed Mc Graw-Hill; 1970.

Vitali OPM, Celestino TB, Bobet A. Analytical solution for tunnels not aligned with geostatic principal stress directions. Tunn Undergr Sp Technol. 2018;82(February):394-405.

doi:10.1016/j.tust.2018.08.046

VLACHOPOULOS, N. and DIEDERICHS, M. S., 2009. Improved longitudinal displacement profiles for convergence confinement analysis of deep tunnels. Rock Mechanics and Rock Engineering. 2009. Vol. 42, no. 2, pp. 131–146. DOI 10.1007/s00603-009-0176-4.

VONK, M, 2020. Grouting the tail void. . 2020.

VU, Minh Ngan, BROERE, Wout and BOSCH, Johan, 2016. Volume loss in shallow tunnelling. Tunnelling and Underground Space Technology. Online. 2016. Vol. 59, pp. 77–90. DOI 10.1016/j.tust.2016.06.011.

YOO, C. Investigation on tunneling and groundwater interaction using a 3D stress-pore pressure coupled analysis. Journal of the Korean Geotechnical Society, 2004, vol. 20, no 3, p. 24-32.

YOO, Dong-Geun et PARK, Soo-Chul. High-resolution seismic study as a tool for sequence stratigraphic evidence of high-frequency sea-level changes: latest Pleistocene-Holocene example from the Korea Strait. Journal of Sedimentary Research, 2000, vol. 70, no 2, p. 296-309.

YOO, Dong-Geun, et al. Seismic stratigraphic reconstruction of Plio-Quaternary depositional sequences on the continental shelf of Korea Strait. Quaternary International, 2017, 459: 116-132.

ZHANG, Jiao Long, SCHLAPPAL, Thomas, YUAN, Yong, MANG, Herbert A. and PICHLER, Bernhard, 2019. The influence of interfacial joints on the structural behavior of segmental tunnel rings subjected to ground pressure. Tunnelling and Underground Space Technology. Online. 2019. Vol. 84, no. August 2018, pp. 538–556. DOI 10.1016/j.tust.2018.08.025.

ZHANG, L. et FRANKLIN, J. A. Prediction of water flow into rock tunnels: an analytical solution assuming an hydraulic conductivity gradient. In : International journal of rock mechanics and mining sciences & geomechanics abstracts. Pergamon, 1993. p. 37-46.

ZHOU, Yafeng, SU, Kai, et WU, Hegao. Hydro-mechanical interaction analysis of high pressure hydraulic tunnel. Tunnelling and Underground Space Technology, 2015, vol. 47, p. 28-34.

ZIEGLER, Martin and OH, Ju-young, 2014. Effect of tail void grouting on the surface settlements in soil of low permeability. . 2014. No. September 2016.